AFRL-VS-HA-TR-2006-1143

Quantum Algorithms for Computational Physics:
Volume III of Lattice Gas Dynamics

Jeffrey Yepez

3 January 2007

AIR FORCE RESEARCH LABORATORY
Space Vehicles Directorate
29 Randolph Rd
AIR FORCE MATERIEL COMMAND
Hanscom AFB, MA 01731-3010

AFRL-VS-HA-TR-2006-1143

This technical report has been reviewed and is approved for publication.

/signed/
Steven L. Clark, Acting Chief
Battlespace Environment Division

/signed/
Frank H. Ruggiero
Battlespace Surveillance Innovation Center

/signed/
Brian Griffith, Maj, USAF, Chief
Battlespace Surveillance Innovation Center

REPORT DOCUMENTATION PAGE

Form Approved
OMB No. 0704-01-0188

PLEASE DO NOT RETURN YOUR FORM TO THE ABOVE ADDRESS.

1. REPORT DATE *(DD-MM-YYYY)*	2. REPORT TYPE	3. DATES COVERED *(From - To)*
16-03-2007	Scientific, Final	1 Oct 1999-15 Mar 2007

4. TITLE AND SUBTITLE
Quantum Algorithms for Computational Physics:
Volume III of Lattice Gas Dynamics

5a. CONTRACT NUMBER

5b. GRANT NUMBER

5c. PROGRAM ELEMENT NUMBER
61102F

6. AUTHORS
Jeffrey Yepez

5d. PROJECT NUMBER
2304

5e. TASK NUMBER
OT

5f. WORK UNIT NUMBER
B1

7. PERFORMING ORGANIZATION NAME(S) AND ADDRESS(ES)
Air Force Research Laboratory /VSBYA
29 Randolph Road
Hanscom AFB, MA 01731-3010

8. PERFORMING ORGANIZATION REPORT NUMBER
AFRL-VS-HA-TR-2006-1143

9. SPONSORING/MONITORING AGENCY NAME(S) AND ADDRESS(ES)

10. SPONSOR/MONITOR'S ACRONYM(S)
AFRL/VSBYA

11. SPONSOR/MONITOR'S REPORT NUMBER(S)

12. DISTRIBUTION/AVAILABILITY STATEMENT
Approved for Public Release; distribution unlimited.

13. SUPPLEMENTARY NOTES

14. ABSTRACT

This report is divided into two tracks, an introductory track and a technical track. Ths introductory track includes a general introduction and background, introductions to two types of analog (and parallel) quantum computing, and an overview oriented conclusion. The technical track includes sections on quantum memory, conservative quantum logic, and quantum algorithm types, including quantum algorithms for the Dirac and Schroedinger quantum mechanical wave equations, the mesoscopic scale quantum Boltzmann equation, and the quantum algorithms for the diffusion equation, Burgers equation, magnetohydrodynamic Burgers equations, and the Navier-Stokes fluid equation.

15. SUBJECT TERMS
Quantum computer Qubit Quantum lattice gas Quantum simulation Electron gas Decoherence
Spin Full adder Fermions Physical modeling Physical quantum algorithms

16. SECURITY CLASSIFICATION OF:			17. LIMITATION OF ABSTRACT	18. NUMBER OF PAGES	19a. NAME OF RESPONSIBLE PERSON
a. REPORT	b. ABSTRACT	c. THIS PAGE			Jeffrey Yepez
UNCL	UNCL	UNCL			19B. TELEPHONE NUMBER *(Include area code)*

Contents

List of Figures

List of Tables

Abstract

Presented is a review of quantum algorithms for computational physics applications and a review of two types of analog quantum computing methodologies, referred to as type-I and type-II quantum computing.

The material contained in this review covers the theoretical developments that have occurred over a dozen years while I have been the principal investigator of a quantum computing research project conducted at the Air Force Research Laboratory and supported by the Air Force Office of Scientific Research, beginning with my first four year grant betweeen 1992 and 1995 entitled "Novel Parallel Computing Strategies," a three year grant between 1996 and 1998 entitled "New models of Computation: Lattice-Based Quantum Computation," and a five year (plus one) grant from 1999 to 2005 entitled "Quantum Computation for Physical Modeling"

The report is divided into two tracks, an introductory track and a technical track. The introductory track includes a general introduction and background, introductions to two types of analog (and parallel) quantum computing, and an overview oriented conclusion. The technical track include sections on quantum memory, conservative quantum logic, and quantum algorithm types, quantum algorithms for the Dirac and Schroedinger quantum mechanical wave equations, the mesoscopic scale quantum Boltzmann equation, and the quantum algorithms for the diffusion equation, Burgers equation, magnetohydrodynamic Burgers equations, and the Navier-Stokes fluid equation, and their respective appendices.

The report does not cover experimental implementation details of our operational quantum computer prototype, our spatial nuclear magnetic resonance spectrometer, developed over the last four years in collaboration with the MIT Nuclear Engineering Department, nor does it survey the innovative experimental approaches that were under investigation by Air Force supported university researchers, for example quantum information processing using Josephson junction-based superconducting electronics, a main technology push by our group.

Preface

This review of quantum algorithms for computational physics is meant to provide a detailed description of a new approach in numerical methods. Anyone interested in this field of research should find ample nourishment in the following pages and gain a sufficient fill of knowledge to produce their own versions of these algorithms, and hopefully, to extend those reviewed here and find altogether new physical modeling applications. The field of quantum algorithms for computational physics is a specialty area within the broader subject area of quantum computing or quantum information processing. Hence, this review covers only a small slice of quantum information science. Furthermore, since this narrow subject area is not very well known (as far as I know there exists no other dedicated reviews of this subject), it may be difficult for the reader to learn the art of developing quantum algorithms for computational physics simply by reading a review written from only one point-of-view.

This review is also meant to convey the essence of the approach to those who are not researchers in this field (nor want to be), but who nevertheless have either a need or desire to understand the approach to effectively judge its merits and determine for themselves whether it is a worthwhile pursuit. Since the work presented herein was mostly conducted at a governmental research facility (or through collaborative governmental grants), there are certainly federal employees and managers who fall into this second category of readers. Yet, quantum computing has become so popular that most likely there will be many more who fall into this second category as well. Consequently, I have divided the subject material into two tracks, and *introductory track* and a *technical track*, and recommend the former track to this second group of readers. In the introductory track, which includes the general introduction in Chapter 1, introductions to the two types of analog quantum computing in Chapter 3 and Chapter 6, and the conclusion in Chapter 12, I have avoided the use of detailed mathematical descriptions and mathematical developments. Any mathematics that is presented in the introductory track is separated from the main body of text by the use of italicized print, and therefore can be easily skipped over.

In contrast, in all the remaining chapters I have extensively relied on mathematical descriptions and developments. I have favored analytical formalisms over strictly computational

ones and so have taken the point-of-view of a theorist. To the group of readers practicing the art of developing analog quantum algorithms, I recommend skipping the introductory material altogether and reading only the relevant technical chapters, which include material on quantum memory, conservative quantum logic, and quantum algorithm types in Chapter 2, quantum algorithms for the Dirac and Schroedinger quantum mechanical wave equations in Chapter 4 and Chapter 5, the mesoscopic scale quantum Boltzmann equation description in Chapter 7, and the quantum algorithms for the diffusion equation in Chapter 8, Burgers equation in Chapter 9, magnetohydrodynamic Burgers equations in Chapter 10, and the Navier-Stokes fluid equation in Chapter 11, and their respective appendices. As I have already alluded to, some researchers who are more computationally oriented may be disappointed with the overall theoretical viewpoint. To help in this regard, I have tried to include numerical simulation results within the technical chapters, which also serve as a confirmation of the analytical developments.

The material contained in this review covers the developments that have occurred over a dozen years while I was the principal investigator of a quantum computing research project conducted at the Air Force Research Laboratory and supported by the Air Force Office of Scientific Research, beginning with my first four year grant between 1992 and 1995 entitled "Novel Parallel Computing Strategies," a three year grant between 1996 and 1998 entitled "New Models of Computation: Lattice-Based Quantum Computation," a four year grant from 1999 to 2003 entitled "Quantum Computation for Physical Modeling," as well as my ongoing research this year at the laboratory. Because of a limitation of space to print this review, as well as the time available for its preparation, I had to make the difficult decision to leave out chapters on the quantum algorithms for solitons, superfluids, Bose-Einstein condensates, and the Hubbard model, all applications I am very fond of (hopefully, all these will be included in some future edition).

Finally, this review is the one part of a two part review. It does not cover any of the experimental implementation details of our operational quantum computer prototype (e.g spatial nuclear magnetic resonance spectrometer) that has been developed over five years in collaboration with the MIT Nuclear Engineering Department, nor does it survey all the innovative experimental approaches that are presently under investigation by Air Force researchers and grantees across the country.

Acknowledgements

Primarily, I would like to acknowledge the leaders in the Air Force Office of Scientific Research, particularly Clifford E. Rhoades. The AFOSR Novel Strategies for Parallel Computing Initiative launched in 1992, and two subsequent AFOSR quantum computing research projects launched in 1996 and 2000, allowed for the development of a firm foundation theoretically, experimentally, and numerically for quantum lattice gas model of quantum and classical nonlinear dynamical systems suited for both parallel supercomputers and quantum computers.

I would like to thank Norman Margolus for introducing me to the subject of quantum computing. I would like to thank Bruce Boghosian for his collaboration over the years on the subject of lattice gases. I would also like to thank George Vahala for his continual valuable collaboration and indispensable support running codes on the supercomputers.

Computational simulation work was supported in part by a grant of computer time from the defense department High Performance Computing Modernization Program, with computational support from the Major Shared Resource Centers: the Naval Oceanographic Office and the US Army Engineer Research and Development Center.

Chapter 1

Introduction

1.1 Digital computing

The architecture of modern digital computers was born in government projects of the United States and Great Britian during the Second World War. There were two analytically intractable problems whose timely solutions were crucial for victory: code-breaking and ballistic aerodynamics. The Department of Communications in Great Britain and the precursor to the United States National Security Agency were compelled to decipher German naval communications encrypted on the "unbreakable" Enigma machine. With the guidance of the computer scientist Alan Turing at Bletchley Park, the world's first digital calculator, the Colossus, was constructed first in Britain and subsequently in the United States after British resources dwindled. It used an optical paper tape reader streaming at sixty miles per hour and used gas-filled triodes called thyratrons to store bits. Contemporaneously, the United States War Department, computed extensive ballistic trajectory tables using the world's second large-scale digital calculator, the Electronic Numerical Integrator And Computer (ENIAC), that outperformed and obsoleted the hundreds of human "computers" at the Army's Ballistic Research Laboratory. It had an unwieldy eighteen thousand vacuum tubes, another historic milestone launching the information revolution.

To overcome the limitations of the hard-wired and switch-programmed Colossus and ENIAC computers, a smaller and more programmable digital computer was commissioned by the US Army's Ballistic Research Laboratory, called the Electronic Discrete Variable Automatic Calculator (EDVAC) using mercury acoustic delay memory. Here a single bit of information was temporarily embodied as an acoustic shock wave traveling down a column of mercury. The American pioneer of the first general-purpose programmable computer was John von Neumann, whose instruction-based programmable architecture has remained the standard up until today in all modern general-purpose computers.

Over a half century later, both decryption and aerodynamics remain analytically in-

tractable and our quest for their solutions has pushed us into the new age of quantum information processing. Thousands of new articles and dozens of recently published books are now available covering the subject of quantum encryption and code-breaking [Chuang and Nielsen, 2000, Bouwmeester et al., 2001], so I need not discuss this subject matter here. However, the nascent field of efficient quantum computation of aerodynamics, as well as the application of quantum computing to other important physical dynamics, deserves attention.

Going beyond computational aerodynamics, I would like to discuss quantum computing by addressing a broader agenda related to quantum computers used to model dynamical physical systems. Just a decade ago, the classical von Neumann architecture was so intrenched that it seemed inconceivable another architecture for computing might emerge as a new dominant standard. Today it is widely understood that the classical computing standard will be replaced by a quantum computing standard. I will argue that a pathway for achieving a new standard may be through quantum computers with an architecture designed to specifically solve physical modeling problems. These quantum computers will not be general purpose and will not be able to run Shor's quantum algorithm for factoring [Shor, 1994], and therefore will not be able to be used to decrypt messages. Nevertheless, special-purpose quantum computers built to solve physical modeling problems can have a substantial impact on the supercomputing industry. A case in point is Japan's Earth Simulator [Sato, 2003], presently the fastest classical supercomputer in the world. This special-purpose and massively parallel computer, custom designed for computational fluid dynamics applications and other related geophysical modeling applications, typifies how the quest for physical modeling through numerical simulation is driving the supercomputer industry today.

Modeling the dynamical behavior of physical systems is an extremely difficult technical challenge from a quantum algorithmic point-of-view. However, preliminary steps have already successfully been taken in this direction [Yepez, 1998, Yepez, 1999, Yepez, 2001a, Yepez, 2001b, Yepez, 2002c, Yepez 2002a, Vahala et al., 2003c, Vahala et al., 2003b, Vahala et al., Yepez, 2003, Vahala et al., 2004b, Vahala et al., 2004a]. I believe that one of the most important first applications of quantum technology to information processing will be the quantum computation of fluid dynamics curcial to the design of future advanced Air Force aircraft and propulsion systems. Modeling turbulent Navier-Stokes fluids is a grand challenge problem for which we have already developed candidate quantum algorithms. These algorithms will serve as templates that can be modified and extended to handle more complex hydrodynamic problems and subsequently more general physical modeling problems.

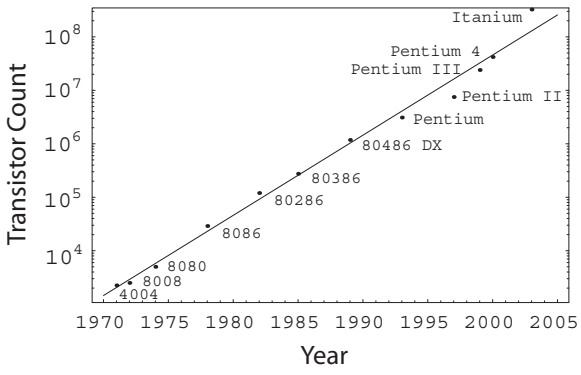

Figure 1.1: Moore's law: Exponential growth law for integrated circuits, the well-known as Moore's law, has remained a steady trend over the years.

1.2 Exponential growth

In 1965 Gordon Moore, the director of the Research and Development Laboratories of Fairchild Semiconductor, made some astonishingly accurate predictions about the future of integrated electronics. He predicted the home computer, the palm-top computer, cruise control for automobiles, the electronic wrist-watch, adaptive phased-array radars, and integrated radio and microwave frequency amplifiers and receivers using gallium arsenide based integrated circuits for communications [Moore, 1965]–which is the basic technology used for cell phones today nearly a half century later. He also foresaw silicon oxide as the primary substrate for integrated circuits. Of all these remarkable predictions, the most famous one was his observation and prediction of the continued exponential growth in the number of components per integrated function versus time by plotting five data points obtained over the years 1959 to 1965.

Figure 1.1 shows the continued manifestation of Moore's law for the popular models of central processing units sold over the last three decades by Intel Corporation. This log-linear plot shows the trend for the number of transistors in a single integrated circuit for the popular models of the Intel central processing units. The best-fit regression line indicates a doubling of the transistor count occurring every two years. The latest data point is for the newest Intel processor architecture, the 64-bit Itanium chip, with 325 million transistors. Although the data point for the Itanium chip lies far above the best-fit regression line, actually only 25 million of its transistors are dedicated to information processing. The remaining 300 million of them are dedicated to merely information storage, a large and fast on-chip cache of static random access memory.

What Moore didn't realize is that this exponential growth law applied not only to integrated circuits, but to all types of computing devices in the distant past long before the

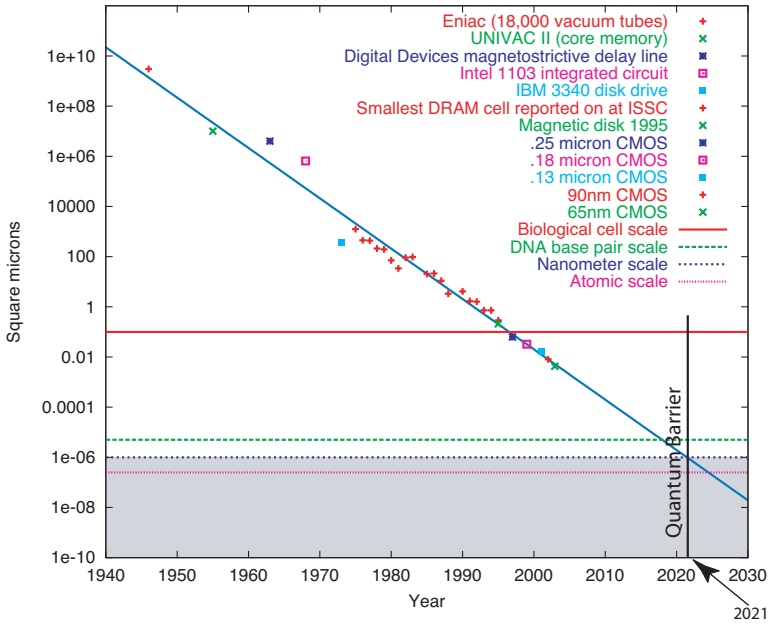

Figure 1.2: General exponential growth law manifested by the shrinking areal bit size spanning a variety of classical computing device technologies. The gray area is the sub-nanometer regime.

invention of integrated circuits, as shown in Figure 1.2. I believe this exponential growth law, with a fixed doubling time, will continue to apply long into the far distant future when integrated circuit technology based on the principles of classical electrical circuit theory will be obsolete–the historical trend of the exponential growth law for areal bit size has remained a steady trend over the past fifty years. Figure 1.2 shows the size of a classical bit measured in square microns on a log-linear plot over the years for a variety of technologies. The best-fit regression line plotted here as the dashed red line was first determined by our group at the Air Force Research Laboratory in 1994 by Norman Margolus and this has remained a faithful prediction over the past nine years. The slope of this line indicates that the areal bit size halves about every 2.16 years. This corresponds to the feature size of a bit halving every 17.65 months. The shaded gray rectangular region below the nanometer scale represents a regime where device physics is purely quantum mechanical. The transition point between the classical regime and this quantum regime occurs in the summer of the year 2021. This is the time after which any commercial grade high-performance computers cannot be designed using classical physics, and hence demarcates a *quantum barrier*.

a	b	AND(a,b)
0	0	0
0	1	0
1	0	0
1	1	1

a	NOT(a)
0	1
1	0

a	b	NAND(a,b)
0	0	1
0	1	1
1	0	1
1	1	0

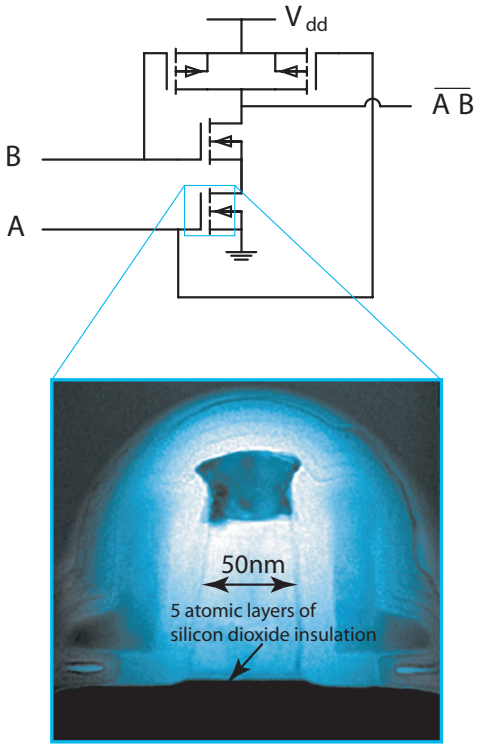

Figure 1.3: Circuit diagram for the common NAND gate comprising four complementary metal oxide transistors (CMOS) and a scanning electron micrograph of a CMOS transistor produced by Intel's 90-nm process [Geppert, 2002].

1.3 Logical gates

All computation is decomposable into a sequence of logical gate operations that either act on two input bits at a time to produce a single output bit, such as the AND gate which multiplies the two input bits together to produce its output bit, or act on a single input bit to produce a single output bit, such as the NOT gate which inverts, or negates, the input bit. Connecting these two gates together so that the output bit of the AND gate is negated by the action of a NOT gate, one obtains the universal NAND gate which is the most common gate used to make most logical functions in chip fabrication today, usually implemented with four transistors as shown in Figure 1.3.

What is the reason behind Moore's first law? The answer to this question is quite simple. Despite the abstract simplicity of logic gates, so far in the history of computing all physical implementations of these fundamental logical gates have been extremely inefficient ones and have been realized at very coarse spatial and temporal scales.

In contrast, nature processes information efficiently at very small spatial and temporal scales characterized by the dynamics and interactions of the fundamental particles. So far in the history of computing all of our physical implementations of logical gates rely on governing principles that are deterministic in nature and intuitive using common sense. Such governing principles are within the realm of classical physics which deals with the behavior of tangible objects that are extremely large compared to the size of the fundamental particles in nature. Yet the true governing principles at the very bottom of things are not intuitive nor commonsensical at all. The true governing principles that describe the behavior and interactions of the fundamental particles, collectively called quantum mechanics, involves two exotic characteristics of our universe, entanglement and wave function collapse. To quote Richard Feynman at a lecture he gave the American Physical Society in 1959, so long as there is sufficient "room at the bottom," our inefficient physical implementations of logical gates can continually be improved upon [Feynman, 1960]. We quantify the rate of improvement by the time it takes to reduce by a factor of two the size of the fundamental building blocks of logic gates and logical bits. According to Figure 1.2 this folding time has remained constant over the history of computing.

1.4 Expensive reduction

The data for the Intel processors plotted in Figure 1.1 is consistent with a total transistor count doubling approximately every two years. This is a good trend. But there is a flip-side to Moore's law, called Moore's second law, which states that the cost of building new

foundries continually doubles as well and this is a bad trend. In 1970 it cost Intel under five million dollars to build a large fabrication facility for integrated circuits. Today, the cost for the newest generation fabrication facility has exceeded five billion dollars, and these costs are growing faster than the growth of revenues from the sale of complex semiconductors. This has pushed the semiconductor industry to fabricate small chips in large quantity, such as those found in cellular telephones or hand-held computing devices like personal data assistants.

What is the reason behind Moore's second law? The answer to this question is more difficult. Since classical physics is usually a very good approximation of quantum mechanical physics so long as the spatial, temporal, and energy scales one is dealing with are sufficiently large compared to the small scales corresponding the individual fundamental particles, it has been practical to engineer the behavior of fundamental computing devices using the language of classical physics. This is certainly the case for the earliest types of computing devices, the abacus, rotary cogs, mechanical relays, electromechanical switches, vacuum tubes, point contact transistor, and the field-effect transistor. Actually, the field-effect transistor, as shown in Figure 1.3, the staple in our present-day computing diet, requires at least semi-classical physics to describe its behavior, that is, a description of processes part way between classical and quantum mechanical physics. As the size of logic gates approach atomic scales, it necessarily becomes ever more expensive to implement those gates using engineering practices based on classical physics.

To use a characteristic New England example, this is very much the same as it would be more difficult, and hence more expensive, to build a two foot high hand-packed rock wall at the boundary line of your back yard using individual pebbles than it would be using large field stones. Just image trying to build the same rock wall using individual grains of sand instead of pebbles. To be even more absurd, imagine using individual silicon dust flecks instead of sand grains to build the wall. The same reasoning may apply to building integrated circuits with ever smaller feature sizes. It remains an open issue whether Moore's second law can be overcome by the invention of new quantum mechanical technologies.

1.5 Computer metamorphosis

By looking at historical trends in computing, one is driven to consider the prospect that, within our lifetime, the technologies driving the information revolution may undergo a radical metamorphosis and consequently we may face an awesome technological barrier, what I have called the quantum barrier, where all classical computing technologies saturate and become incapable of sustaining the information revolution. What is at stake is the economic welfare,

both nationally and internationally, of the pervasive computer industry. Furthermore, the stakes could be much higher, at least to the extent that growth in the newly globalized economies of our world is dependent upon the rapid expansion afforded by the information revolution and consequent high-technology advancements driven by the continued doubling of information processing cutting across all manufacturing and service sectors.

1.6 Quantum processes

In this section I give give a description of quantum entanglement and wave function collapse for the layman.

1.6.1 Entanglement and collapse

Quantum objects can exist in multiple states simultaneously, such as being located at two or more places in space at the same time. This is called *quantum superposition*. Observing a quantum object that is in a superposition of states necessarily causes that object to randomly jump into only one of those states. This is called *wave function collapse* and it occurs stochastically. Quantum mechanics does not predict which state will be selected during wave function collapse. Instead it predicts with remarkable accuracy the probability with which any of the possible states are selected. This interpretation of quantum mechanics is called the *Copenhagen interpretation*. There are other interpretations, but they are not needed for our purposes.

Quantum entanglement is a characteristic property of two or more quantum objects, which occurs when each of them is existing in a superposition of states, and where the quantum objects are strongly correlated in such a way that an observation causing one of the participating quantum objects to collapse into a particular state causes the other participating quantum object to simultaneously, and deterministically, collapse into an associated "correlated" state.

The manipulation of two entangled quantum objects is sufficient to represent all logical functions that one may need in any computation [Barenco et al., 1995]. Naturally occurring physical processes may couple these two quantum objects causing them to become entangled. For example, one nucleus inside an atom of some molecule can be be entangled with the nucleus of another atom within that molecule because the two atoms are chemically bonded together and intermediary electrons within the molecule become correlated with both nuclei. This process of quantum entanglement can be controlled experimentally using nuclear magnetic resonance spectroscopy, and therefore can serve as the basis of quantum logical gates [Cory et al., 1998]. There are a myriad of ways to control entanglement and more and more

quantum computing and quantum information research groups around the world are now racing toward achieving experimental results in this area.

Just as the output bit of the classical AND gate conditionally depends on the states of the two input bits, the collapsed state of two previously input quantum objects conditionally depends on their entanglement. Engineering entanglement is therefore a way to perform logical gate operations.

I would like to begin with a concrete example using a quantum mechanical system called a *quantum spin system* to illustrate the physical properties of quantum entanglement and wave function collapse. Yet the subject of quantum spin systems is esoteric, so I will first attempt to explain what this is. As a prerequisite, I will begin by discussing its baby sister the *classical spin system*.

1.6.2 Simplest spin system

We shall consider a *system* of spins that reside on the nodes of a regular lattice. The lattice is an array of points (which is also referred to as *sites* or *nodes*), arranged in a regular crystallographic fashion, and the lattice appears exactly the same from whichever of the points the array is viewed. This kind of lattice is called a *Bravais lattice*. At any particular moment in time, every spin has two intrinsic properties: it has a spatial location, which coincides with one of the lattice nodes, and it has an internal orientation. At any particular node reside either zero, one, or two spins. If a lattice node has no resident spins, it is referred to as an *empty* node. And if a node has all its resident spins present, it is called a *full* node.

In classical spin systems, the spin's orientation is specified by a vector on the unit sphere. In the simplest case, the spin vector is either up or down, which may be encoded on a computer using one bit of information. These internal spin states are called the *spin-up* and *spin-down* states. The particular node where that bit is located on the lattice specifies the spin's spatial location. A well known classical spin system is the Ising lattice-gas model of ferromagnetism (or anti-ferromagnetism). This spin system is the simplest model of a magnet, where the spin system is constrained to have only one binary spin per node and each spin is fixed at one node of the lattice. Corresponding to a system with only nearest neighbor bonds, the computational algorithm that governs the behavior of the spin system is usually applied using a local stencil that includes the neighbors of a central node. A bond is defined between two spins and is called ferromagnetic if the spins are aligned or called anti-ferromagnetic if the spins are anti-aligned. The spin at the central node is flipped to reduce the total bond energy which is computed using an energy function, called the *Ising Hamiltonian*, that counts one unit of energy for each bond. Usually, the microscopic evolution is based either on on-site-single-spin-flip Glauber dynamics [Glauber, 1963] or two-

site-two-spin-exchange Kawasaki dynamics [Kawasaki, 1972].

A microscopic Hamiltonian and its macroscopic effective field theory: The Ising Hamiltonian is

$$H = -J \sum_{\langle ij \rangle} s_i s_j,$$

where $\langle ij \rangle$ *denotes the set of nearest neighbor bonds between spins,* s_i *and* s_j*, on the lattice and where the energy of the spin-spin coupling is modeled by the parameter* J*. If* $\varphi(r,t)$ *is a coarse-grained macroscopic spin-magnetization variable, then the nonconservative large-scale spin dynamics is governed by the effective field theory*

$$\partial_t \varphi = \nu \nabla^2 \varphi + \frac{dV(\varphi)}{d\varphi},$$

where ν *is the diffusivity and* $V(\varphi)$ *is an effective interaction potential. It is a double well potential with each minima corresponding to the spin-up and spin-down ordered phases of the magnetization.*

There is a mapping between the thermodynamic variables for fluids and magnets—a fluid's density is analogous to a spin system's magnetization, a fluid's compressibility is analogous to a spin system's magnetic susceptibility, and a fluid's liquid and gas phases are analogous to a spin system's ordered (all spins aligned) and disordered phases (random spin orientations). The phase change between the ordered and disordered phases occurs at a critical temperature, $T_c = 2/\log(1+\sqrt{2})$*, which is expressed in units of the spin-spin coupling energy divided by the Boltzmann constant. The Ising model captures the equilibrium thermodynamic behavior of these two phase order-disorder systems in an elegant way. The Ising model manifests many universal properties: an order-disorder phase transition [Binder, 1987], scaling [Binder, 1981] that relates critical-point exponents [Hohenberg and Halperin, 1977], and critical slowing down. The numerical techniques applied to it appear to be endless: the Monte Carlo Metropolis algorithm, microcanonical cluster Monte Carlo [Creutz, 1992], Ising cellular automata [Vichniac, 1984, Toffoli and Margolus, 1987, Creutz, 1992], deterministic heat-bath [Hede and Herrmann, 1991, MacIssac et al., 1991], parallel Monte Carlo [Schleier et al., 1992], multispin encoding [Zhang, 1989], multigrid techniques [Kandel et and the Monte Carlo renormalization group [Ma, 1976, Swendsen, 1979].*

In this present case, it is rather difficult to analytically derive the macroscopic effective field theory from a microscopic spin dynamics that minimizes the energy given by the Ising Hamiltonian. The art of quantum computational physics is to engineer microscopic Hamiltonians for which it is analytically possible to derive a corresponding macroscopic-scale effective

field theory. It is in this sense that an engineered microscopic quantum mechanical system can numerically solve a particular "macroscopic" partial differential equation.

One can try to model how a physical system, initially in a non-equilibrium configuration, approaches equilibrium–how the system changes over time as it dynamically moves towards its thermodynamic equilibrium configuration. In kinetic spin models, in addition to Glauber or Kawasaki dynamics, each spin can move or "hop" from lattice site to lattice site. For example, it is possible to merge the Ising spin model with a simple lattice gas model [Frisch et al., 1986], as had been done by Chen *et al.* in 1989 [Chen et al., 1989], which is described by macroscopic equations for the long wavelength modes related to the collective motions of the spins as well as a macroscopic fluidic equation of motion.

Regardless of these particularities, in all spatially discrete models, time remains a continuous quantity. Yet successive configurations of the system may be sampled at discrete time intervals. That is, at every time step interval, there exists a particular configuration of spins. At the next time step interval, there exists a different configuration of spins. Each configuration at each and every time step is unique and derivable by applying the set of deterministic rules to the configuration of the previous time step. The deterministic rules underlying the dynamics of the system are subject to the following four constraints: locality, conservation, detailed-balance or invertibility, and invariance.

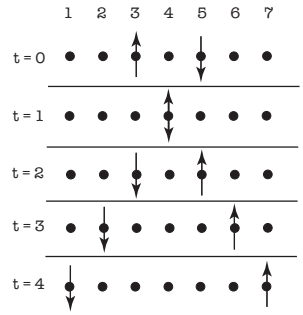

Figure 1.4: Simple noninteracting spin system on a one-dimensional lattice with seven nodes. The spin-up hops to the right while the spin-down hops to the left.

As a simple example, let us consider a one-dimensional system where initially at the zeroth time step a spin-up is located at node 3 and is moving to the right (hopping one lattice cell length at every time step) and a spin-down is located at node 5 moving to the left at the same speed, as depicted in Figure 1.4. This simple classical spin system has no interactions. The spins are seen to pass through each other just after the first time step.

We can add a simple rule to effectively induce an "elastic collision" into the dynamics of the model, as illustrated in Figure 1.5. The local interaction rule is this: whenever two

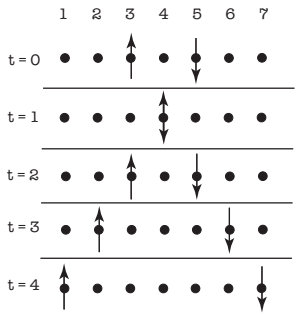

Figure 1.5: Simple interacting spin system again with a system of two spins. Initially, the spin-up hops to the right, then collides with a spin-down that was hopping to the left. As a result of a local spin-exchange interaction, one can describe the dynamics as possessing a kinetic bounce-back collision where the spins reverse the direction of their original motion.

spins arrive at the same node, they swap their spin orientations. With the addition of this interaction rule, the resulting dynamics can be interpreted as a momentum-conserving elastic collision causing the two "particles" to bounce off of each other at node 4. This second interpretation implies that a kinematic scattering event can be modeled by local spin-spin interactions. It is in this sense we think of using spins to encode kinetic particle dynamics.

1.6.3 Quantum spins

Like classical spins, quantum spins also possess two intrinsic properties: a spatial location and an internal spin orientation. Again, we shall consider quantum spins whose spatial locations coincide with the nodes of a lattice. Upon measurement we can only observe one of two internal spin states: spin-up and spin-down-states; they are orthogonal states, even though the usage of the words "up" and "down" does not connote this fact. Perhaps a better notation is to think of the spin-up state as physically related to a quantum object rotating clockwise, whereas the spin-down state represents it rotating counter-clockwise. In any case, a quantum spin's internal orientation is specified using two complex numbers, instead of a single bit sufficient to specify the orientation of a classical spin. These complex numbers are called *amplitudes*, and have a magnitude and phase which are both real numbers. The square of an amplitude's magnitude is a probability. The magnitude squared of one amplitude gives the probability that the quantum spin is up and similarly the magnitude squared of the other amplitude gives the probability that the quantum spin is down. The sum of these two probabilities equals one.

In a quantum spin system, a spin may simultaneously exist in both its up and down states at any particular time. This is fundamentally different from the way classical spins behave since occupancy of the up or down state is mutually exclusive there. Quantum superposition

is a striking property of quantum spins, yet superposition is quite commonly experienced in everyday life, although people usually do not link the cause of these experiences to quantum superposition.

1.6.4 Interference

The best example of this phenomenon is the superposition of light waves, which can be either constructive or destructive. For example, soap bubbles have color even though the soapy liquid in the membrane might generally be colorless. The reason is that visible light entering our eyes from a soap bubble reflects off of the front and back surface of the film membrane. Depending on the thickness of the film, some wavelengths in the visible spectrum will constructively interfere during their superposition while other wavelengths will destructively interfere. Hence, the bubble will take on the hue of the constructively interfering light.

Diffraction is also commonly seen, for example the diffraction of sun light by water droplets in the atmosphere following a rainstorm as the drops act like an array of small prisms collectively causing a large rainbow that beautifully illustrates to the naked eye that the visible light coming from the sun, which usually looks white, is really a superposition of red, yellow, green, blue, and violet colored light. Advancing his view that light consisted of small particles or *corpuscles*, Sir Isaac Newton, in the mid 1660's, confirmed the diffraction effect by splitting a narrow beam of sunlight into its spectral components employing a thin glass prism and then re-superposed the spectral components back into a white sunlight beam using a second glass prism.

Furthermore, Newton discovered an amazing interference pattern caused by superposing a beam of monochromatic light as it reflects off of the top flat surface of a hemisphere while simultaneously reflecting off of the bottom curved surface to the same hemisphere. The resulting interference pattern caused by concentric regions of destructive and constructive superposition are called *Newton's rings*.

These few examples help bring the notion of superposition to mind. All these examples, and many others that could also be mentioned, do not necessarily prove that light is indeed made of particles, nor that any one photon in a beam of light may actually exist in two or more states simultaneously. To the contrary, these examples of superposition could involve different photons in superposition (that is two or more photons simultaneously occupying the same location in space such as red, yellow, green, blue, and violet photons in a beam of white light). To prove that a single photon can indeed exist in superposition, one must leap forward in time from the seventeenth century to the dawn of the twentieth when it first became possible to perform experiments with weak beams of light made up of a stream of single photons.

In 1909 Geoffrey Ingram Taylor conducted a historic two-slit interference experiment using a extremely weak light source like that from "a candle burning at a distance slightly exceeding a mile" so that very few photons where present at one time. He collected a resulting image over several months of exposure on a photographic plate and discovered the same interference fringes that occur using an intense light source. This led Paul Dirac, the discoverer of the relativistic quantum mechanical wave equation, to believe that "each photon then interferes only with itself." It is a most remarkable feature of the quantum mechanical nature of light (and matter) that identical interference patterns emerge from either intense beams or extremely weak beams made of a timed sequence of individual particles.

1.6.5 Wave function collapse

Although I have argued that we should not be surprised with the quantum mechanical principle of superposition, any rational person should certainly be alarmed by the quantum mechanical principle of wave function collapse. If a quantum object exists in a superposition of states, for example a quantum spin's internal state being equally balanced in both the up and down states, then as one measures the state of a quantum object, the outcome is a classical result. Upon measurement, the internal spin will be either up or down, and not a combination. This elusive process of "losing" all phase information is called *wave function collapse*. A quantum object in a superposition of states collapses into one classical state upon observation as one complex amplitude vanishes and the other amplitude becomes unity. Therefore, the most information we can extract from a quantum spin is a binary value, one bit of information.

To see why wave function collapse is so disturbing, let us consider a situation when two quantum spins are both in superposition, where they are highly correlated, so that a measurement of one spin causes a collapse of the entire pair. We shall consider an example of the well known paradox discovered by Albert Einstein, Boris Podolsky, and Nathan Rosen, first posited in 1935 to bring to light a troubling consequence of entanglement and wave function collapse in the theory of quantum mechanics [Einstein et al., 1935]. As the measured quantum spin collapses into a classical state, without directly touching the second spin and regardless of where it is located, either nearby or far away, the second spin of the pair also collapses into an associated classical state. When quantum spins are correlated in this way they are said to be *entangled*.

Figure 1.6 shows a simple one-dimensional quantum spin system that illustrates both entanglement and wave function collapse. The situation is a generalization of the classical spin systems presented above and shown in Figures 1.4 and 1.5. In the quantum case, the local interaction rule is the following: whenever two spins arrive at the node, they $\sqrt{\text{swap}}$

their spin orientations. This rule is very similar to the collision rule for the interacting classical spin system which swapped the orientations whenever spins meet at a common node. The difference here of course is that I have placed a square root symbol over the swap operation.

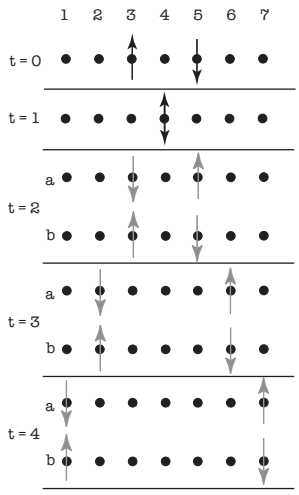

Figure 1.6: A simple quantum spin system example. The collision process causes the pair of spins to become entangled. The spins are simultaneously swapped and left intact. The resulting two alternatives, a and b, are shown.

The $\sqrt{\text{swap}}$ operation is defined as the operation which when it is applied twice in sequence, results in the overall effect that is identical to the original swap operation. So the $\sqrt{\text{swap}}$ is like the swap operation but it only goes "half way" so to speak. The result of the $\sqrt{\text{swap}}$ operation is that the two states of the interacting quantum spins are left both intact and swapped, as illustrated in Figure 1.6. The outcome of the $\sqrt{\text{swap}}$ operation is that the spins are left in an entangled superposition of states.

1.6.6 Square Roots

The first person to have attempted to compute a square root was probably an ancient Egyptian perhaps around 3400BC in the classic problem of squaring the circle, which is equivalent to finding the square with area matching that of a circle. After 500BC, the square root took on its modern definition given by the "divine" Greek mathematician Pythagoras. Today, most people normally think of the square root operation as it applies to a positive number.

Yet over time, the square root has been generalized in all sorts of ways. In 1777, Leonhard Euler introduced the imaginary number $\sqrt{-1}$, which is denoted by the symbol i. Euler's work ushered in the sweeping new field of complex analysis and this was by no means the

greatest of his achievements. For example he pioneered a mathematical field called calculus of variations, which centuries later is considered pivotal to modern quantum physics, as he attempted to prove the age old isoperimetric theorem of geometry. It may be loosely stated as, a circle is the optimal closed curve, because of the set of all closed curves with a fixed perimeter, a circle encloses the greatest area. Likewise a sphere is an isoperimetric surface because, of the set of all closed and bounded surfaces with fixed area, it encloses the greatest volume. Soap bubbles are again illustrative here because they employ a "calculus of variations." For a fixed amount of liquid, spread over a thin membrane film, a bubble "wants" to enclose the greatest volume so as to reduce its curvature as it strives to equalize the pressure of the air inside the bubble to the ambient outside air pressure. In this way, it also minimizes its surface tensions (the energy arising from bonds in the membrane with the air at the film's interface), to achieve an optimal and stable equilibrium configuration. In Section 4, we review a form of calculus of variations called a *path integral* as we describe how one uses a system of spins to model the kinematic dynamics of relativistic quantum particles.

A square root example related to idempotent Hamiltonians and their associated unitary operators of Section 2 on conservative quantum logic gates: If δ is a boolean number with value either 0 or 1, then

$$\sqrt{1-2\delta} = 1 + (i-1)\delta,$$

which is the positive root. Using the Taylor expansion

$$\begin{aligned} e^{z\delta} &= 1 + z\delta + \frac{1}{2!}(z\delta)^2 + \frac{1}{3!}(z\delta)^3 + \cdots & (1.1)\\ &= 1 + (e^z - 1)\delta, & (1.2) \end{aligned}$$

it follows that $e^{i\pi\delta} = 1 - 2\delta$, and in turn the positive root of this is

$$e^{i\frac{\pi}{2}\delta} = \sqrt{1-2\delta} = 1 + (i-1)\delta. \quad (1.3)$$

The negative root is a bit more tricky.

It is also possible to take a square root of a matrix, an array of numbers ordered with an equal number of rows and columns. One first derives an associated matrix, called the *matrix of eigenvectors*, from the original matrix and subsequently uses this second matrix to diagonalize the original matrix. Diagonalizing a matrix entails tranforming it so as to render all of the components of the matrix to be zero except that new components are left along the central diagonal slice of the matrix. The remaining new components along the diagonal

are called the *eigenvalues* of the matrix. This processes of diagonalizing a matrix using the matrix of eigenvectors is technically called a *similarity transformation*.

We can take the square root of a diagonal matrix: the result is simply another diagonal matrix whose components are the square roots of the original eigenvalues. Therefore, to take the square root of any non-diagonal matrix first one diagonalizes it with the appropriate similarity transformation, then one takes the square root of the associated diagonal matrix of eigenvalues, and finally one applies the inverse of the similarity transformation. In this way, one obtains a matrix that when multiplied times itself yields the original matrix.

Here is a simple example of an off-diagonal matrix, which is called the Pauli σ_x matrix (1-qubit NOT gate), expressed in terms of its square root:

$$\begin{pmatrix} 0 & 1 \\ 1 & 0 \end{pmatrix} = \begin{pmatrix} \frac{1}{2} - \frac{i}{2} & \frac{1}{2} + \frac{i}{2} \\ \frac{1}{2} + \frac{i}{2} & \frac{1}{2} - \frac{i}{2} \end{pmatrix} \cdot \begin{pmatrix} \frac{1}{2} - \frac{i}{2} & \frac{1}{2} + \frac{i}{2} \\ \frac{1}{2} + \frac{i}{2} & \frac{1}{2} - \frac{i}{2} \end{pmatrix}.$$

It is possible to express the 2-qubit swap operation in matrix form

$$\text{swap} = \begin{pmatrix} 1 & 0 & 0 & 0 \\ 0 & 0 & 1 & 0 \\ 0 & 1 & 0 & 0 \\ 0 & 0 & 0 & -1 \end{pmatrix}.$$

Then taking the square root of this, we have the $\sqrt{\text{swap}}$ operation in a matrix form representation

$$\sqrt{\text{swap}} = \begin{pmatrix} 1 & 0 & 0 & 0 \\ 0 & \frac{1}{2} - \frac{i}{2} & \frac{1}{2} + \frac{i}{2} & 0 \\ 0 & \frac{1}{2} + \frac{i}{2} & \frac{1}{2} - \frac{i}{2} & 0 \\ 0 & 0 & 0 & i \end{pmatrix}.$$

Here is another example of an off-diagonal matrix, which is the imaginary number i times the Pauli σ_y matrix, expressed in terms of its square root:

$$\begin{pmatrix} 0 & -1 \\ 1 & 0 \end{pmatrix} = \begin{pmatrix} \frac{1}{\sqrt{2}} & -\frac{1}{\sqrt{2}} \\ \frac{1}{\sqrt{2}} & \frac{1}{\sqrt{2}} \end{pmatrix} \cdot \begin{pmatrix} \frac{1}{\sqrt{2}} & -\frac{1}{\sqrt{2}} \\ \frac{1}{\sqrt{2}} & \frac{1}{\sqrt{2}} \end{pmatrix}.$$

This matrix and its square root are *antisymmetric* because the off-diagonal components are the negative of each other. It is possible to express a 2-qubit antisymmetric swap operation as a matrix:

$$\text{antisymmetric swap} = \begin{pmatrix} 1 & 0 & 0 & 0 \\ 0 & 0 & -1 & 0 \\ 0 & 1 & 0 & 0 \\ 0 & 0 & 0 & -1 \end{pmatrix}.$$

Then taking the square root of this, we have the antisymmetric $\sqrt{\text{swap}}$ operation in a matrix

form representation

$$\sqrt{\text{antisymmetric swap}} = \begin{pmatrix} 1 & 0 & 0 & 0 \\ 0 & \frac{1}{\sqrt{2}} & -\frac{1}{\sqrt{2}} & 0 \\ 0 & \frac{1}{\sqrt{2}} & \frac{1}{\sqrt{2}} & 0 \\ 0 & 0 & 0 & i \end{pmatrix}.$$

Almost all the quantum algorithms that we know of today for modeling physical systems are decomposable into "quantum circuits" made up of swap and symmetric and antisymmetric $\sqrt{\text{swap}}$ quantum gates.

1.6.7 Measurement of entangled states

Referring to Figure 1.6, suppose initially at $t = 0$ we prepare two quantum spins in a well defined classical state, just as we did in our previous two examples of a classical spin system. If we attempt to measure whether a quantum spin exists at node 1 say, we will find nothing there initially at $t = 0$ nor at the later times $t = 1$, $t = 2$ and $t = 3$. Our attempt to measure the state of a spin would have no bearing whatsoever on the quantum spin system. Of course we are presuming that our quantum measurement apparatus is a delicate one that affects a tiny region no bigger than size of a single node itself and that when we run our detector at that particular node it only interacts with spins on that node and the measurement does not in any way "leak" into neighboring nodes, next nearest neighboring nodes, and so forth. So we suppose we have a perfect detector. (One advantage of taking a theorist's viewpoint in this review is that we do not have to describe an actual detector. In the next part of this review where we include all the experimental details, we do not have this luxury.)

However, if we apply our detector at node 1 at time step $t = 4$, we will indeed discover a spin there. Either we will find the that it is spin down or up. If the first alternative presents itself, then we know that we are sampling the state of the system that corresponds to the case when the two spins passed each other at time $t = 1$ and did not interact (alternative a). Because of this we know that if we then attempt to observe the other spin, we must find it definitely in a spin up state. Conversely, if the alternative b presents itself instead, then we know we sampled the state of the system corresponding to the case where the spins interacted at node 4 and exchanged their spins at time $t = 1$. Consequently, if we attempt to observe the other spin we would definitely find it in a spin down state. This is a manifestation of entanglement. It is rather straightforward to comprehend.

What is unnerving is that entanglement does not depend on how big the lattice might be nor how far apart the quantum spins might be at the moment of our observation. This appears to violate our notions of locality in physics because whether we perform our mea-

surement at time step 4 or time step one trillion, still only a type a or type b alternative materializes.

A result from Section 2: The following number operators, called entanglement operators, count units of entanglement between qubits $|q_\alpha\rangle$ and $|q_\beta\rangle$ as if the entanglement were a physical resource:

$$\frac{1}{2}\left(\hat{a}_\alpha^\dagger \pm \hat{a}_\beta^\dagger\right)\left(\hat{a}_\alpha \pm \hat{a}_\beta\right) + (\delta - 1)\hat{n}_\alpha \hat{n}_\beta,$$

where $\hat{a}_\alpha^\dagger$ and $\hat{a}_\alpha$ are creation and annihilation operators for the αth qubit, where the number operators are $\hat{n}_\alpha = \hat{a}_\alpha^\dagger \hat{a}_\alpha$, and where $\delta = 0$ for bosonic particles and $\delta = 1$ for fermionic particles.

1.6.8 Hilbert space

Only two amplitudes are ever physically pertinent in our simple example, the amplitude for alternative a and the amplitude for alternative b. The collapse is characterized by one amplitude jumping to unity as the other one vanishes and this can occur essentially instantaneously (in some sense, these two amplitudes are physically "close" to one another in the space of amplitudes). What I am calling the "space of amplitudes" is foundational in quantum mechanics and is called the *Hilbert space*. For each classical state of the system, which for our spin system includes all spatial configurations of the set of spins as well as all their internal orientations, there is an associated dimension in the Hilbert space. Consequently, this is a very high-dimensional space. Let's enumerate all the configurations for our simple example.

In our previous example in Figure 1.6, we had two spins with a total zero spin along the vertical direction, which is typically called the direction of the z-axis. The total spin along the z-axis direction vanishes because the spin-up of the first spin cancels the spin-down of the second spin. Some of the possible classical configurations are shown in Figures 1.4 and 1.5, but what is the total number in this case? The answer is the number of nodes squared. With 7 nodes, the answer is 49 states with two opposite spin spins because there are 7 places to put the first spin and independently also 7 places to put the second spin.

However, suppose both spins are spin-up say, so the total spin along the z-axis is 2 instead of 0. Then how many configurations are there? The answer is 21, which is lower than the number of configurations for the previous case because now we cannot include configurations with two spins per node. Our quantum spins obey the *Pauli exclusion principle*, which states that two or more them cannot reside at the same point in space in the same spin state. The

	-7	-6	-5	-4	-3	-2	-1	0	1	2	3	4	5	6	7
0	0	0	0	0	0	0	0	1	0	0	0	0	0	0	0
1	0	0	0	0	0	0	7	0	7	0	0	0	0	0	0
2	0	0	0	0	0	21	0	49	0	21	0	0	0	0	0
3	0	0	0	0	35	0	147	0	147	0	35	0	0	0	0
4	0	0	0	35	0	245	0	441	0	245	0	35	0	0	0
5	0	0	21	0	245	0	735	0	735	0	245	0	21	0	0
6	0	7	0	147	0	735	0	1225	0	735	0	147	0	7	0
7	1	0	49	0	441	0	1225	0	1225	0	441	0	49	0	1
8	0	7	0	147	0	735	0	1225	0	735	0	147	0	7	0
9	0	0	21	0	245	0	735	0	735	0	245	0	21	0	0
10	0	0	0	35	0	245	0	441	0	245	0	35	0	0	0
11	0	0	0	0	35	0	147	0	147	0	35	0	0	0	0
12	0	0	0	0	0	21	0	49	0	21	0	0	0	0	0
13	0	0	0	0	0	0	7	0	7	0	0	0	0	0	0
14	0	0	0	0	0	0	0	1	0	0	0	0	0	0	0

Table 1.1: Sector of Hilbert space: Number of configurations given the number of spins (left most column) versus the total spin along the z-axis (top most row).

way to count the number of configurations in this case is simple. With the first spin at node 1, the second spin can be on any of the six remaining nodes, so this contributes 6 configurations. With the first spin at node 2, the second spin can be on any of the remaining nodes except node 1 since we counted this case already. So this contributes 5 configurations. With the first spin at node 3, the second spin can be on any of the remaining nodes except nodes 1 and 2 since we counted these already. So this contributes 4 configurations. We can continue this until we are left with one last configuration with the first spin on node 6 and the second spin on node 7, whence we obtain the final result 21=7+6+5+4+3+2+1.

Table 1.1 gives the number of configurations for all the possible cases of spin number and total spin-z component. The cases we just worked out by hand are shown in the table along the row labeled 2.

The entries in Table 1.1 can be obtained using the generating function

$$\left(\sum_{p=0}^{1}\sum_{m=0}^{1} n^{p+m} s_z^{p-m}\right)^{\frac{Q}{2}},$$

for $Q = 14$ and where n denotes total number of spins and s_z denotes the total spin along the z-axis (total magnetization). This simple generating function works for any number of qubits $Q = 2L$, where L is the number of nodes in the lattice. See Appendix B for the polynomial that is equivalent to Table 1.1. This way of counting the size of the Hilbert space sectors is used in numerical simulations of the many-body quantum systems governed by the Schroedinger equation in Section 5.

An important point to observe is that if we sum along the rows we can find the total number of configurations given a specified number of spins. The result is 1,14, 91, 364, 1001, 2002, 3003, 3432, 3003, 2002, 1001, 364, 91, 14, 1 configurations for 0 up to 14 spins. This is a *binomial distribution* and it is plotted in Figure 1.7. The solid bell-shaped curve plotted in

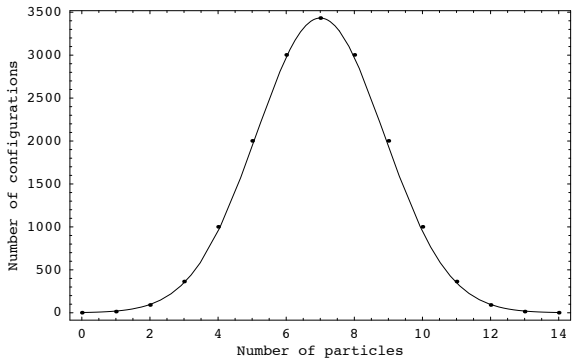

Figure 1.7: Bell shaped distribution: Binomial distribution plotted as the black circles. The solid curve is the normal distribution.

Figure 1.7 is a Gaussian distribution, sometimes called the normal distribution. It becomes a better approximation of the binomial distribution as the number of nodes increases. If we add together all the configurations, we get 16384 of them in this case. Each of these configurations is called a *basis state*. This number can be written in exponential form as $16384 = 2^{14}$. This is the total number of dimensions in the Hilbert space of a quantum spin system on a lattice with 7 nodes where the spins obey the Pauli exclusion principle. Why is the size of the Hilbert space such a simple number? Let L denote the number of

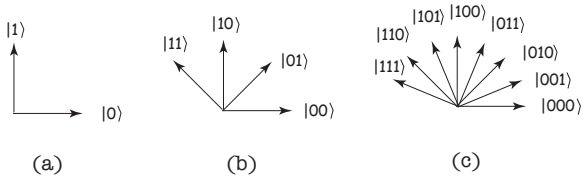

Figure 1.8: Hilbert space: (a) single qubit, (b) two qubits, and (c) three qubits.

nodes. If we let $Q = 2 \times L$, so as to account for up to two spins per node, then the size of the Hilbert space is 2^Q and this is a generally true for any lattice with L nodes. The number Q is the total number of qubits needed to encode all the possible basis states, and hence all possible combinations of all the classical configurations in superposition. With one qubit, $Q = 1$, there are two orthogonal basis states: true $|1\rangle$ and false $|0\rangle$, as depicted in Figure 1.8a. With two qubits, $Q = 2$, there are four orthogonal basis states: $|00\rangle$, $|01\rangle$, $|10\rangle$,

and $|11\rangle$, as depicted in Figure 1.8b, although it is not possible on a flat piece of paper to draw these four states to all appear orthogonal to one another. With three qubits, there are eight basis states, and so on and so forth. As Q get larger, the orthogonal axes of the Hilbert space begin to look porcupine-like. And as Q increases, the Hilbert space quickly becomes unwieldy because adding a single qubit doubles the number of quills.

Chapter 2

Quantum memory, conservative quantum gates, and quantum algorithm types

2.1 A fermionic quantum bit

A fundamental unit of information is the coherent time-dependent state $|q(t)\rangle$ of a two-energy level quantum mechanical system, which is a *fermionic qubit* and is governed by the Schroedinger wave equation

$$-i\hbar\frac{\partial}{\partial t}|q(t)\rangle = \mathbf{H}|q(t)\rangle, \tag{2.1}$$

where the Hamiltonian is

$$\mathbf{H} = \mathcal{E}\sigma_z = \mathcal{E}\begin{pmatrix}1 & 0\\ 0 & -1\end{pmatrix}, \tag{2.2}$$

and where the energy eigenvalues are $\pm\mathcal{E}$, σ_z is a Pauli matrix, and energy eigenstates are

$$|g\rangle \equiv \begin{pmatrix}0\\1\end{pmatrix} \qquad |e\rangle \equiv \begin{pmatrix}1\\0\end{pmatrix}, \tag{2.3}$$

where $|g\rangle$ is the ground state and $|e\rangle$ is the excited state of the qubit. In terms of the angular Rabi frequency $\Omega \equiv \frac{\mathcal{E}}{\hbar}$, the time-dependent qubit is

$$|q(t)\rangle = \mathcal{A}(0)e^{-i\Omega t}|g\rangle + \mathcal{A}(1)e^{i\Omega t}|e\rangle, \tag{2.4}$$

where the complex probability amplitudes satisfy $|\mathcal{A}(0)|^2 + |\mathcal{A}(1)|^2 = 1$. The two-level quantum system is realized using nuclear magnetic resonance of a spin-$\frac{1}{2}$ atomic nucleus, optical resonance of a two-level atom, or spin state of an electron. It is also possible that the two-level quantum system is realized by a mesoscopic-scale superconductive circuit with Josephson junctions–there are a variety of configurations under investigation using either charge states, flux states, or phase.

Table 2.1: Symbols

Symbol	Description
t	time
B	number of qubits per quantum node
L	number of quantum nodes
Q	total number of qubits in the quantum computer
N	ensemble size
x, y, z	spatial dimensions
i, j, k	spatial indices $(i, j, k) = (x, y, z)$
$\mathcal{A}$	probability amplitude
n	bit (0 or 1)
$\|n\rangle$	number ket or bit ket ($\|0\rangle$ or $\|1\rangle$)
$\|q\rangle$	qubit ket
α	qubit index ($1 \leq \alpha \leq Q$)
S	binary encoded state index ($0 \leq S \leq 2^Q - 1$)
$\|S\rangle$	numbered basis state
$\|\psi\rangle$	on-site ket of size 2^B
$\|\Psi\rangle$	total system ket of size 2^Q

2.2 The quantum state in the number representation

From the previous section, a time-dependent qubit may be written

$$|q(t)\rangle = \sum_{n=0}^{1} \mathcal{A}(n,t)|n\rangle, \tag{2.5}$$

where $\mathcal{A}(0,t) \equiv \mathcal{A}(0)e^{-i\Omega t}$ and $\mathcal{A}(1,t) \equiv \mathcal{A}(1)e^{i\Omega t}$ and where $|0\rangle \equiv |g\rangle$ and $|1\rangle \equiv |e\rangle$. We introduce the bit numbers, denoted n_α for $1 \leq \alpha \leq Q$, that are either zero or one (they are commonly referred to as *fermionic number variables* or *Grassman variables* in the literature on the second quantized representation of many-body quantum mechanics). Each tensor product state, $|n_1\rangle \otimes \cdots \otimes |n_Q\rangle$, is a basis state in the number representation. The initial quantum state $|\Psi_\circ\rangle$ at time $t_\circ$ is a tensor product state

$$|\Psi_\circ\rangle = \bigotimes_{\alpha=1}^{Q} \left(\sum_{n_\alpha=0}^{1} \mathcal{A}(n_\alpha, t_\circ)|n_\alpha\rangle \right). \tag{2.6}$$

The symbol $\bigotimes$ represents the tensor product operation, which in this case is a Q-fold tensor product. Let $\{n_1, \ldots, n_Q\}$ denote the set of size 2^Q of all the combinations of the bit variables. Hence, the initial quantum state can also be written as a superposition of all the basis states

$$|\Psi_\circ\rangle = \sum_{\{n_1,\ldots,n_Q\}} \left(\prod_{\alpha=1}^{Q} \mathcal{A}(n_\alpha, t_\circ) \right) |n_1\rangle \otimes \cdots \otimes |n_Q\rangle. \tag{2.7}$$

This is said to be a *separable* state, because the qubits are prepared individually and independently. This is seen by the form of (2.6).

An arbitrary quantum state is a linear combination over all these numbered basis states

$$|\Psi(t)\rangle = \sum_{\{n_1,\ldots,n_Q\}} \mathcal{A}(n_1,\ldots,n_Q,t)|n_1\rangle \otimes \cdots \otimes |n_Q\rangle, \tag{2.8}$$

which not only accounts for superposition but also entanglement since the coefficients $\mathcal{A}(n_1,\ldots,n_Q,t)$ cannot, in general, be written in separable form $\mathcal{A}(n_1,t)\mathcal{A}(n_2,t)\ldots\mathcal{A}(n_Q,t)$.

2.3 The density matrix

If we consider an ensemble of quantum computers of size N, then it is useful to define the density matrix ϱ for this ensemble as

$$\varrho \equiv \sum_{r=1}^{N} P_r |\Psi_r\rangle\langle\Psi_r|, \tag{2.9}$$

where the probability distribution P_r over the ensemble members is normalized

$$\sum_{r=1}^{N} P_r = 1. \tag{2.10}$$

Note, if each quantum state within the ensemble of states is normalized, then the scalar (or inner) product of the bra $\langle\Psi_r|$ and the ket $|\Psi_r\rangle$ is unity, $\langle\Psi_r|\Psi_r\rangle = 1$. In (2.9), we used the tensor (or outer) product of the ket $|\Psi_r\rangle$ and the bra $\langle\Psi_r|$. Therefore, ϱ is represented by an $N \times N$ matrix.

Now suppose the system is in the entangled state $|\Psi_r(t)\rangle = \sum_{S=0}^{2^Q-1} \mathcal{A}_r(S,t)|S\rangle$, where we use the Q-digit binary encoded numbers $0 \leq S \leq 2^Q - 1$ to denote the numbered basis states. Then the density matrix is

$$\begin{aligned} \varrho(t) &= \sum_{r=1}^{N} P_r \sum_{S=0}^{2^Q-1} \sum_{S'=0}^{2^Q-1} \mathcal{A}_r^*(S,t)\mathcal{A}_r(S',t)|S\rangle\langle S'| \\ &= \sum_{SS'} \mathcal{C}_{SS'}(t)|S\rangle\langle S'| \end{aligned} \tag{2.11}$$

where

$$\mathcal{C}_{SS'}(t) \equiv \sum_{r=1}^{N} P_r \mathcal{A}_r^*(S,t)\mathcal{A}_r(S',t). \tag{2.12}$$

Because of two main uncontrollable physical mechanisms, the total state of the quantum computer decoheres:

(1) It loses coherence by an internal dephasing process occurring strictly within the quantum computer itself that causes the off-diagonal elements of the density matrix to be randomized. The dephasing time, denoted τ_2, is short and occurs because the Rabi frequencies $\Omega = \frac{\mathcal{E}}{\hbar}$ of the qubits differ. This dephasing is reversible (usually by application of a π-pulse) and gives rise to echo phenomena.

(2) Also, it relaxes to thermal equilibrium by spontaneous and dissipative coupling to its external environment causing the density matrix to be diagonalized. The relaxation time, denoted τ_1, is longer and is an irreversible process because the off-diagonal complex numbers $\mathcal{C}_{SS'}(t)$ vanish for all $S \neq S'$

$$\mathcal{C}_{SS'}(t) \longrightarrow \mathcal{C}_{SS}(t)\delta_{SS'} = \delta_{SS'} \sum_{r=1}^{N} P_r \left(\prod_{\alpha=1}^{Q} |\mathcal{A}(n_\alpha, t)|^2 \right), \tag{2.13}$$

where n_α is the αth bit of the state number S. We have written the relaxation process as rendering the density matrix as a classical average (over the ensemble) of a product of occupation probabilities. Correlations are lost, since the 2^Q diagonal components depends only on Q quantities as the product of independent averages

$$\mathcal{C}_{SS}(t) \longrightarrow \prod_{\alpha=1}^{Q} \left(\sum_{r=1}^{N} P_r |\mathcal{A}(n_\alpha)|^2 \right). \tag{2.14}$$

2.4 Mixed ensemble

The single-qubit number operator for "particles" (state $|1\rangle$) is $\mathbf{n} \equiv \frac{1}{2}(\mathbf{1} + \sigma_z)$ and for "holes" (state $|0\rangle$) is $\bar{\mathbf{n}} \equiv \frac{1}{2}(\mathbf{1} - \sigma_z)$. Note that the particle and hole number operators are complementary $\mathbf{n} = \mathbf{1} - \bar{\mathbf{n}}$. The generalized number operator $\mathbf{n}_\alpha$ acting on the αth qubit is

$$\mathbf{n}_\alpha \equiv \bigotimes_{\beta=1}^{Q} \left[\mathbf{1} - \bar{\mathbf{n}}\delta_{\alpha\beta} \right], \tag{2.15}$$

where the Kronecker delta $\delta_{\alpha\beta}$ is 1 when $\alpha = \beta$, and 0 otherwise. Remember, the symbol $\bigotimes$ represents the tensor product operation. A matrix representation of the generalized number operator is given in Appendix D.

We shall define the *occupation probability* of the αth qubit, $|q_\alpha\rangle$, as the quantum mechanical expectation value of the number operator, denoted $\langle \mathbf{n}_\alpha \rangle$, for the system at temperature T.

$$\mathrm{Tr}\left(\varrho \mathbf{n}_\alpha\right) = \sum_{S=0}^{2^Q-1} \left[\prod_{\alpha=1}^{Q} \left(\sum_{r=1}^{N} P_r |\mathcal{A}(n_\alpha)|^2 \right) \right], \tag{2.16}$$

where $\mathrm{Tr}(\bullet)$ is the trace operation.

2.5 Fermi-Dirac distribution

The mesoscopic-scale occupation probability of a qubit is expressible using the Fermi-Dirac function $F(x) = \frac{1}{e^x+1}$

$$\langle \mathbf{n}_\alpha \rangle = F(\beta\mathcal{E}) \tag{2.17}$$

$$\langle \bar{\mathbf{n}}_\alpha \rangle = F(-\beta\mathcal{E}), \tag{2.18}$$

where $\beta \equiv k_B T$. To analytically predict the effective field theory describing the behavior of a qubit computer comprised of two-state qubits, it is necessary to use this Fermi-Dirac function. In the Burgers equation derivation, the Fermi-Dirac function is used in Section 9.3.2. In the Navier-Stokes equation derivation, the Fermi-Dirac function is used in Section 11.5.2 which, in turn, is expanded in Mach number, as is given in Appendix I.

2.6 Second quantized representation

We shall represent the basic quantum gate operations in terms of the fermionic *qubit creation* and *qubit annihilation* operators in the number representation, denoted $\hat{a}_\alpha^\dagger$ and $\hat{a}_\alpha$ respectively, and use this approach as the basis for a general computational formulation applicable to any quantum algorithm. A classic text by Fetter and Walecka on solid-state physics uses second quantization and contains detailed information on creation and annihilation operators [Fetter and Walecka, 1971]. Acting on a system of Q qubits, $\hat{a}_\alpha^\dagger$ and $\hat{a}_\alpha$ create and destroy a "fermionic particle" encoded in the αth qubit

$$\hat{a}_\alpha^\dagger |n_1 \dots n_\alpha \dots n_Q\rangle = \begin{cases} 0 & , \ n_\alpha = 1 \\ \epsilon \, |n_1 \dots 1 \dots n_Q\rangle & , \ n_\alpha = 0 \end{cases} \tag{2.19}$$

$$\hat{a}_\alpha |n_1 \dots n_\alpha \dots n_Q\rangle = \begin{cases} \epsilon \, |n_1 \dots 0 \dots n_Q\rangle & , \ n_\alpha = 1 \\ 0 & , \ n_\alpha = 0 \end{cases}, \tag{2.20}$$

where the phase factor is $\epsilon = (-1)^{\sum_{i=1}^{\alpha-1} n_i}$. The fermionic creation and annihilation operators satisfy the anti-commutation relations

$$\begin{aligned} \{\hat{a}_\alpha, \hat{a}_\beta^\dagger\} &= \delta_{\alpha\beta} \\ \{\hat{a}_\alpha, \hat{a}_\beta\} &= 0 \\ \{\hat{a}_\alpha^\dagger, \hat{a}_\beta^\dagger\} &= 0. \end{aligned} \tag{2.21}$$

The number operator $\hat{n}_\alpha \equiv \hat{a}_\alpha^\dagger \hat{a}_\alpha$ has eigenvalues of 1 or 0 in the number representation when acting on a pure state, corresponding to the αth qubit being in state $|1\rangle$ or $|0\rangle$ respectively.

The Hilbert space for a two-qubit system is four dimensional, and we choose the following basis kets in the number representation:

$$|v\rangle = |00\rangle = \begin{pmatrix}1\\0\\0\\0\end{pmatrix}, \qquad |\downarrow\rangle = |01\rangle = \begin{pmatrix}0\\1\\0\\0\end{pmatrix},$$
$$|\uparrow\rangle = |10\rangle = \begin{pmatrix}0\\0\\1\\0\end{pmatrix}, \qquad |\uparrow\downarrow\rangle = |11\rangle = \begin{pmatrix}0\\0\\0\\1\end{pmatrix} \tag{2.22}$$

to represent fermionic states in terms of qubits. In this basis, where qubits $|q_1\rangle$ and $|q_2\rangle$ are ordered left to right $|q_1 q_2\rangle$, the two number operators can be expressed in terms of the singleton number operator $\hat{n} = \begin{pmatrix}0 & 0\\0 & 1\end{pmatrix}$ as follows:

$$\hat{n}_1 = \hat{n} \otimes \mathbf{1} = \begin{pmatrix}0&0&0&0\\0&0&0&0\\0&0&1&0\\0&0&0&1\end{pmatrix}, \qquad \hat{n}_2 = \mathbf{1} \otimes \hat{n} = \begin{pmatrix}0&0&0&0\\0&1&0&0\\0&0&0&0\\0&0&0&1\end{pmatrix}. \tag{2.23}$$

In this basis, the creation operators are

$$\hat{a}_1^\dagger = \begin{pmatrix}0&0&0&0\\0&0&0&0\\1&0&0&0\\0&1&0&0\end{pmatrix}, \qquad \hat{a}_2^\dagger = \begin{pmatrix}0&0&0&0\\1&0&0&0\\0&0&0&0\\0&0&-1&0\end{pmatrix}. \tag{2.24}$$

Since $\hat{a}_1^\dagger$ and $\hat{a}_2^\dagger$ have real components, the annihilation operators are the transposes of the matrices given in (2.24), $\hat{a}_1 = (\hat{a}_1^\dagger)^T$ and $\hat{a}_1 = (\hat{a}_1^\dagger)^T$:

$$\hat{a}_1 = \begin{pmatrix}0&0&1&0\\0&0&0&1\\0&0&0&0\\0&0&0&0\end{pmatrix}, \qquad \hat{a}_2 = \begin{pmatrix}0&1&0&0\\0&0&0&0\\0&0&0&-1\\0&0&0&0\end{pmatrix}. \tag{2.25}$$

2.7 Qubit interchange operator

All permutations of qubits (here taken to be fermionic in nature) may be implemented by successive application of an "interchange operator," or $\sqrt{\text{SWAP}}$ gate, which we denote by $\hat{\chi}_{\alpha\beta}$ and which interchanges the αth and βth qubits. We construct an interchange operator that correctly handles any necessary phase change due to the anti-commutation relations (2.21) and we do so using the qubit creation and annihilation operators (2.24) and (2.25) with only quadratic products of $\hat{a}$ and $\hat{a}^\dagger$ [Pendleton, 1991].

We require that $\hat{\chi}$ be:

1. unitary ($\hat{\chi}_{\alpha\beta}\hat{\chi}^{\dagger}_{\alpha\beta} = \mathbf{1}$);

2. conserve number density ($[\hat{\chi}_{\alpha\beta}, \hat{n}_{\alpha} + \hat{n}_{\beta}] = 0$); and

3. maintain the vacuum state ($\hat{\chi}_{\alpha\beta}|v\rangle = |v\rangle$).

Let us assume we have a "one-particle" state $|\gamma\rangle = \hat{a}^{\dagger}_{\gamma}|v\rangle$, where $\gamma = \alpha$ or β. A first guess at the form of the interchange operator between sites is

$$\hat{\chi}_{\alpha\beta} = \hat{a}^{\dagger}_{\alpha}\hat{a}_{\beta} + \hat{a}^{\dagger}_{\beta}\hat{a}_{\alpha}. \tag{2.26}$$

This acts correctly on $|\gamma\rangle$. The problem with (2.26) is its application on the vacuum state $|v\rangle$ causing it to vanish into oblivion and therefore violating our last requirement that $\hat{\chi}|v\rangle = |v\rangle$. This is remedied easily enough by slightly modifying our first guess

$$\hat{\chi}_{\alpha\beta} = \hat{a}^{\dagger}_{\alpha}\hat{a}_{\beta} + \hat{a}^{\dagger}_{\beta}\hat{a}_{\alpha} + \mathbf{1}. \tag{2.27}$$

Although (2.27) repairs the vacuum problem, now its application onto $|\gamma\rangle$ interchanges qubits but incorrectly gives back the interchanged state along with the original state $|\gamma\rangle$. To administer a remedy, we must include two more terms that subtract off the original state. The interchange operator then takes the final form:

$$\hat{\chi}_{\alpha\beta} = \hat{a}^{\dagger}_{\alpha}\hat{a}_{\beta} + \hat{a}^{\dagger}_{\beta}\hat{a}_{\alpha} + \mathbf{1} - \hat{a}^{\dagger}_{\alpha}\hat{a}_{\alpha} - \hat{a}^{\dagger}_{\beta}\hat{a}_{\beta}. \tag{2.28}$$

Although we have constructed (2.28) by considering only "one-particle" states, (2.28) works on any arbitrary state.

Let us test the properties of $\hat{\chi}$ further. We rewrite (2.28) by factoring the creation operators,

$$\hat{\chi}_{\alpha\beta} = \mathbf{1} + \hat{a}^{\dagger}_{\beta}\left(\hat{a}_{\alpha} - \hat{a}_{\beta}\right) - \hat{a}^{\dagger}_{\alpha}\left(\hat{a}_{\beta} - \hat{a}_{\alpha}\right), \tag{2.29}$$

which leads to

$$\hat{\chi}_{\alpha\beta} = \mathbf{1} - \left(\hat{a}^{\dagger}_{\alpha} - \hat{a}^{\dagger}_{\beta}\right)\left(\hat{a}_{\alpha} - \hat{a}_{\beta}\right). \tag{2.30}$$

Now of course, one is motivated to define the following "two-point" creation, annihilation, and number operators

$$\hat{a}_{\alpha\beta} \equiv \frac{1}{\sqrt{2}}\left(\hat{a}_{\alpha} - \hat{a}_{\beta}\right) \tag{2.31a}$$

$$\hat{a}^{\dagger}_{\alpha\beta} \equiv \frac{1}{\sqrt{2}}\left(\hat{a}^{\dagger}_{\alpha} - \hat{a}^{\dagger}_{\beta}\right) \tag{2.31b}$$

$$\hat{n}_{\alpha\beta-} \equiv \hat{a}^{\dagger}_{\alpha\beta}\hat{a}_{\alpha\beta} \tag{2.31c}$$

so that (2.30) may be written as

$$\hat{\chi}_{\alpha\beta} = \mathbf{1} - 2\hat{n}_{\alpha\beta-}. \tag{2.32}$$

Our two-point operators form superposition states

$$\hat{a}^{\dagger}_{\alpha\beta}|v\rangle = \frac{1}{\sqrt{2}}\left(|\ \alpha\rangle - |\ \beta\rangle\right). \tag{2.33}$$

The two-point number operator is idempotent ($\hat{n}^2_{\alpha\beta} = \hat{n}_{\alpha\beta}$) and hermitian ($\hat{n}^{\dagger}_{\alpha\beta} = \hat{n}_{\alpha\beta}$). In turn the interchange operator is hermitian ($\hat{\chi}^{\dagger}_{\alpha\beta} = \hat{\chi}_{\alpha\beta}$) and consequently we have

$$\hat{\chi}^2_{\alpha\beta} = (\mathbf{1} - 2\hat{n}_{\alpha\beta-})^2 = \mathbf{1} - 4\hat{n}_{\alpha\beta-} + 4(\hat{n}_{\alpha\beta-})^2 = \mathbf{1}, \tag{2.34}$$

satisfying the unitarity requirement of involution. The interchange operator can be written in exponential form

$$\hat{\chi}_{\alpha\beta} = e^{z\hat{n}_{\alpha\beta-}} = \mathbf{1} + z\hat{n}_{\alpha\beta-} + \frac{z^2}{2!}(\hat{n}_{\alpha\beta-})^2 + \cdots = \mathbf{1} + \left(z + \frac{z^2}{2!} + \cdots\right)\hat{n}_{\alpha\beta-} \tag{2.35}$$

or

$$\hat{\chi}_{\alpha\beta} = \mathbf{1} + \left(1 - e^{-z}\right)\hat{n}_{\alpha\beta-}. \tag{2.36}$$

Comparing (2.32) with (2.36), allows us to choose $z = i\pi$, so we have a manifestly unitary interchanger,

$$\hat{\chi}_{\alpha\beta} = e^{i\pi\hat{n}_{\alpha\beta-}} = -1^{\hat{n}_{\alpha\beta-}}, \tag{2.37}$$

appearing as a rotation by 180°. To add a measure of concreteness, it is useful to show $\hat{\chi}_{\alpha\beta}$ in its matrix representation. For a two qubit system, we have

$$\hat{\chi}_{12} = \begin{pmatrix} 1 & 0 & 0 & 0 \\ 0 & 0 & 1 & 0 \\ 0 & 1 & 0 & 0 \\ 0 & 0 & 0 & -1 \end{pmatrix} = \exp\left[i\pi \begin{pmatrix} 0 & 0 & 0 & 0 \\ 0 & \frac{1}{2} & -\frac{1}{2} & 0 \\ 0 & -\frac{1}{2} & \frac{1}{2} & 0 \\ 0 & 0 & 0 & 1 \end{pmatrix} \right]. \tag{2.38}$$

2.8 General two-qubit conservative quantum logic gate

The quantum gates that we deal with in our quantum algorithms for computational physics are called *conservative quantum gates* in the sense that they do not alter the total "particle count" in the number representation of the qubit system (i.e. the total spin magnetization of a spin-$\frac{1}{2}$ system). When conservative quantum gates serve as the basic operators of a quantum algorithm, then the macroscopic scale dynamics of the quantum system are ultimately constrained by a continuity equation. Since we are interested in modeling various types of hydrodynamic fluids, it is essential that the macroscopic scale dynamics of the

quantum system obey the continuity equation. Therefore, conservative quantum gates are the type of quantum logic gates suited for our computational physics agenda.

The interchange operator $\hat{\chi}$ treated in the previous section is the simplest example of a conservative gate. In the most general situation, it is sufficient to consider only a block diagonal matrix that has a 2×2 sub-block, which causes entanglement and is a member of the special unitary group SU(2). We can neglect the overall phase factor because this does not affect the quantum dynamics and therefore our sub-block need not be a member of the more general unitary group U(2). If $\hat{U}$ is a member of SU(2), it can be parameterized using three real numbers, ξ, ζ, and θ, as follows

$$\hat{U} \equiv \begin{pmatrix} e^{i\xi}\cos\theta & -e^{i\zeta}\sin\theta \\ -e^{-i\zeta}\sin\theta & -e^{-i\xi}\cos\theta \end{pmatrix}. \tag{2.39}$$

We can represent a general conservative quantum logical gate by the 4×4 unitary matrix

$$\hat{\Upsilon} = \begin{pmatrix} 1 & 0 & 0 & 0 \\ 0 & A & B & 0 \\ 0 & C & D & 0 \\ 0 & 0 & 0 & E \end{pmatrix}. \tag{2.40}$$

We choose this form for $\hat{\Upsilon}$ because we want to entangle only two of the basis states, $|01\rangle$ with $|10\rangle$, so as to conserve particle number, and that is why we call $\hat{\Upsilon}$ a *conservative* quantum gate. The component in the top-left corner is set to unity because we do not want $\hat{\Upsilon}$ to alter the vacuum state $|00\rangle$ in any way. However, we must allow the component in the bottom-right corner to be arbitrary. We will see that the value of this component will depend on the particle statistics, reflecting whether the particles are bosons or fermions.

Consider the following five operators:

$$\hat{a}_1^\dagger \hat{a}_2 = \begin{pmatrix} 0 & 0 & 0 & 0 \\ 0 & 0 & 0 & 0 \\ 0 & 1 & 0 & 0 \\ 0 & 0 & 0 & 0 \end{pmatrix} \qquad \hat{a}_2^\dagger \hat{a}_1 = \begin{pmatrix} 0 & 0 & 0 & 0 \\ 0 & 0 & 1 & 0 \\ 0 & 0 & 0 & 0 \\ 0 & 0 & 0 & 0 \end{pmatrix} \tag{2.41}$$

along with the compound number operators

$$\begin{gathered} \hat{n}_1(\mathbf{1} - \hat{n}_2) = \begin{pmatrix} 0 & 0 & 0 & 0 \\ 0 & 0 & 0 & 0 \\ 0 & 0 & 1 & 0 \\ 0 & 0 & 0 & 0 \end{pmatrix} \qquad (\mathbf{1} - \hat{n}_1)\hat{n}_2 = \begin{pmatrix} 0 & 0 & 0 & 0 \\ 0 & 1 & 0 & 0 \\ 0 & 0 & 0 & 0 \\ 0 & 0 & 0 & 0 \end{pmatrix} \\ \hat{n}_1 \hat{n}_2 = \begin{pmatrix} 0 & 0 & 0 & 0 \\ 0 & 0 & 0 & 0 \\ 0 & 0 & 0 & 0 \\ 0 & 0 & 0 & 1 \end{pmatrix}. \end{gathered} \tag{2.42}$$

As a generalization of (2.28), the quantum gate (2.40) can be expressed in terms of the operators (2.41) and (2.42) given above:

$$\begin{aligned}\hat{\Upsilon} &= \mathbf{1} + (A-1)(\mathbf{1}-\hat{n}_1)\hat{n}_2 + B\hat{a}_2^\dagger\hat{a}_1 + C\hat{a}_1^\dagger\hat{a}_2 + (D-1)\hat{n}_1(\mathbf{1}-\hat{n}_2) + (E-1)\hat{n}_1\hat{n}_2 \\ &= \mathbf{1} + (A-1)\hat{n}_2 + B\hat{a}_2^\dagger\hat{a}_1 + C\hat{a}_1^\dagger\hat{a}_2 + (D-1)\hat{n}_1 - (A+D-E-1)\hat{n}_1\hat{n}_2. \end{aligned} \tag{2.43}$$

We would like to find the Hamiltonian, denoted $\hat{H}$, associated with $\hat{\Upsilon}$. Letting z denote a complex number, we begin by parametrizing (2.43) in terms of z

$$\hat{\Upsilon}(z) = e^{z\hat{H}}, \tag{2.44}$$

and then we solve for $\hat{H}$. To do this, we series expand in the parameter z:

$$\hat{\Upsilon}(z) = \mathbf{1} + z\hat{H} + \frac{z^2}{2}\hat{H}^2 + \cdots. \tag{2.45}$$

There are two cases of interest. In the first case, when the Hamiltonian is idempotent, $\hat{H}^2 = \hat{H}$, then (2.45) reduces to

$$\hat{\Upsilon}(z) = \mathbf{1} + (e^z - 1)\hat{H}. \tag{2.46}$$

In the second case, when $\hat{H}^3 = \hat{H}$ and $\hat{H}^4 = \hat{H}^2$, then (2.45) reduces to

$$\hat{\Upsilon}(z) = \mathbf{1} + \sinh z\,\hat{H} + (\cosh z - 1)\hat{H}^2. \tag{2.47}$$

These two cases are treated in Appendix A. The most general conservative quantum logic gate $\hat{\Upsilon}(z) = e^{z\hat{H}_\delta(\xi)}$ has the form

$$e^{z\hat{H}_\delta(\xi)} = \begin{pmatrix} 1 & 0 & 0 & 0 \\ 0 & \frac{1}{2}(e^z+1) & -\frac{1}{2}(e^z-1)e^{-i\xi} & 0 \\ 0 & -\frac{1}{2}(e^z-1)e^{i\xi} & \frac{1}{2}(e^z+1) & 0 \\ 0 & 0 & 0 & 1+(e^z-1)\delta \end{pmatrix} \tag{2.48a}$$

$$= \mathbf{1} + (e^z-1)\left[\frac{1}{2}\left(\hat{a}_1^\dagger - e^{-i\xi}\hat{a}_2^\dagger\right)\left(\hat{a}_1 - e^{i\xi}\hat{a}_2\right) + (\delta-1)\hat{n}_1\hat{n}_2\right]. \tag{2.48b}$$

where δ is a boolean number with value either 0 or 1, and where the Hamiltonian is the idempotent ($\hat{H}^2 = \hat{H}$) matrix

$$\hat{H}_\delta(\xi) = \begin{pmatrix} 0 & 0 & 0 & 0 \\ 0 & \frac{1}{2} & -\frac{1}{2}e^{-i\xi} & 0 \\ 0 & -\frac{1}{2}e^{i\xi} & \frac{1}{2} & 0 \\ 0 & 0 & 0 & \delta \end{pmatrix} \tag{2.49a}$$

$$= \frac{1}{2}\left(\hat{n}_1 + \hat{n}_2 - \hat{a}_1^\dagger\hat{a}_2 e^{i\xi} - \hat{a}_2^\dagger\hat{a}_1 e^{-i\xi}\right) + (\delta-1)\hat{n}_1\hat{n}_2. \tag{2.49b}$$

This is demonstrated in Appendix A. (2.49) parametrizes a class of quantum logic gates using a complex number ξ for a given binary value of δ, where $\delta = 1$ for the case of Fermi-Dirac statistics and $\delta = 0$ otherwise.

2.9 Entanglement operators

Without loss of generality, let us consider two qubits: $|q_\alpha\rangle$ and $|q_\beta\rangle$. Following the form of (2.31), let us define the following generalized creation and annihilation operators

$$\hat{a}^\dagger_{\alpha\beta}(\xi) \equiv \frac{1}{\sqrt{2}}\left(\hat{a}^\dagger_\alpha - e^{-i\xi}\hat{a}^\dagger_\beta\right) \qquad \hat{a}_{\alpha\beta}(\xi) \equiv \frac{1}{\sqrt{2}}(\hat{a}_\alpha - e^{i\xi}\hat{a}_\beta). \tag{2.50}$$

The corresponding generalized number operator is

$$\begin{aligned}
\hat{n}_{\alpha\beta}(\xi) &\equiv \hat{a}^\dagger_{\alpha\beta}(\xi)\hat{a}_{\alpha\beta}(\xi) && (2.51)\\
&= \frac{1}{2}\left(\hat{a}^\dagger_\alpha - e^{-i\xi}\hat{a}^\dagger_\beta\right)\left(\hat{a}_\alpha - e^{i\xi}\hat{a}_\beta\right) && (2.52)\\
&= \frac{1}{2}\left(\hat{n}_\alpha + \hat{n}_\beta - e^{i\xi}\hat{a}^\dagger_\alpha\hat{a}_\beta - e^{-i\xi}\hat{a}^\dagger_\beta\hat{a}_\alpha\right) && (2.53)
\end{aligned}$$

With the generalized number operator, the idempotent Hamiltonian (2.49b) takes the simple form:

$$\hat{H}_{\alpha\beta}(\xi) = \hat{n}_{\alpha\beta}(\xi) + (\delta - 1)\hat{n}_\alpha\hat{n}_\beta. \tag{2.54}$$

For some state $|\ldots\alpha\ldots\beta\ldots\rangle$, with two qubits of interest located at α and at β, we will use a short-hand notation for this state and write it as if it were only a two-qubit state $|\alpha\beta\rangle$. Remember, the operators written below can apply to any pair of qubits, regarless of their location. We have the "singlet" state $\frac{1}{\sqrt{2}}(|01\rangle - |10\rangle)$ and the "triplet" states $\frac{1}{\sqrt{2}}(|01\rangle + |10\rangle)$ and $\frac{1}{\sqrt{2}}(|11\rangle \pm |00\rangle)$. The action of $\hat{H}_{\alpha\beta}(\xi)$ on these entangled states is the following:

$$\hat{H}_{\alpha\beta}(\xi)\left(|01\rangle \pm |10\rangle\right) = \frac{1}{2}(1 \mp e^{-i\xi})|01\rangle - \frac{1}{2}\left(1 \pm e^{i\xi}\right)|10\rangle \tag{2.55a}$$

$$\hat{H}_{\alpha\beta}(\xi)(|11\rangle \pm |00\rangle) = \delta|11\rangle. \tag{2.55b}$$

We are concerned with two special cases, $\xi = \pi$ and $\xi = 0$, which we denote as follows ($+ = \pi$ for the singlet and $- = 0$ for the triplet):

$$\hat{e}_{\alpha\beta\pm} = \hat{n}_{\alpha\beta\pm} + (\delta - 1)\hat{n}_\alpha\hat{n}_\beta, \tag{2.56}$$

where

$$\begin{aligned}
\hat{n}_{\alpha\beta+} &\equiv \frac{1}{2}\left(\hat{a}^\dagger_\alpha + \hat{a}^\dagger_\beta\right)\left(\hat{a}_\alpha + \hat{a}_\beta\right) && (2.57)\\
\hat{n}_{\alpha\beta-} &\equiv \frac{1}{2}\left(\hat{a}^\dagger_\alpha - \hat{a}^\dagger_\beta\right)\left(\hat{a}_\alpha - \hat{a}_\beta\right). && (2.58)
\end{aligned}$$

The hermitian operator (2.56) counts one bit of the pairwise entanglement, so it is called an *e-bit number operator*. The sum of the e-bit operators reduces to the standard number operators:

$$\hat{e}_{\alpha\beta+} + \hat{e}_{\alpha\beta-} = \hat{n}_\alpha + \hat{n}_\beta + 2(\delta - 1)\hat{n}_\alpha \hat{n}_\beta. \tag{2.59}$$

The e-bit number operator $\hat{e}_-$ has an eigenvalue of 1 for the singlet state:

$$\hat{e}_-(|01\rangle - |10\rangle) = |01\rangle - |10\rangle \tag{2.60a}$$

$$\hat{e}_-(|01\rangle + |10\rangle) = 0 \tag{2.60b}$$

$$\hat{e}_-(|11\rangle \pm |00\rangle) = \delta|11\rangle. \tag{2.60c}$$

For fermionic particles ($\delta = 1$), the doubly occupied site $|\uparrow\downarrow\rangle = |11\rangle$ is an eigenvector of $\hat{e}_-$ with unity eigenvalue. Conversely, the e-bit number operator $\hat{e}_+$ has an eigenvalue of 0 for the singlet state:

$$\hat{e}_+(|01\rangle - |10\rangle) = 0 \tag{2.61a}$$

$$\hat{e}_+(|01\rangle + |10\rangle) = |01\rangle + |10\rangle \tag{2.61b}$$

$$\hat{e}_+(|11\rangle \pm |00\rangle) = \delta|11\rangle, \tag{2.61c}$$

and $|11\rangle$ is an eigenvector of $\hat{e}_+$ with unity eigenvalue as well when $\delta = 1$.

Defining the pairwise entangled states with qubits of interest at locations α and β as

$$\psi_+ \equiv |\ldots 0 \ldots 1 \ldots\rangle + |\ldots 1 \ldots 0 \ldots\rangle \tag{2.62}$$

$$\psi_- \equiv |\ldots 0 \ldots 1 \ldots\rangle - |\ldots 1 \ldots 0 \ldots\rangle, \tag{2.63}$$

then these entangled states are eigenvectors of the e-bit number operators (with unity eigenvalue):

$$\hat{e}_{\alpha\beta\pm}\psi_\pm = \psi_\pm. \tag{2.64}$$

2.10 The site-dependent total-spin operator and the Heisenberg Hamiltonian operator

We shall denote the *spin creation* and *spin annihilation* operators by $\hat{a}^\dagger_{i\mu}$ and $\hat{a}_{i\mu}$, respectfully, which act on the spin state located at spatial position i with spin orientation $\mu =\uparrow$ or $\mu =\downarrow$, for $1 \leq i \leq L$, where L is the number of nodes in the lattice. In turn, the site-specific total-spin operator $\vec{S}_i$ is compactly written in terms of the spin creation and annihilation operators and the Pauli spin matrices as

$$\vec{S}_i = \frac{1}{2}\hat{a}^\dagger_{i\mu}\vec{\sigma}_{\mu\nu}\hat{a}_{i\nu}, \tag{2.65}$$

where $\vec{\sigma} = (\sigma_x, \sigma_y, \sigma_z)$, and

$$\sigma_x = \begin{pmatrix} 0 & 1 \\ 1 & 0 \end{pmatrix} \quad \sigma_y = \begin{pmatrix} 0 & -i \\ i & 0 \end{pmatrix} \quad \sigma_z = \begin{pmatrix} 1 & 0 \\ 0 & -1 \end{pmatrix}. \tag{2.66}$$

Normally, the spin operators are in units of Planck's constant, but here we take $\hbar = 1$. The components of (2.65) are then

$$\hat{S}_{ix} = \tfrac{1}{2}\hat{a}^\dagger_{i\mu}\sigma^x_{\mu\nu}\hat{a}_{i\nu} = \frac{1}{2}(\hat{a}^\dagger_{i\uparrow}\hat{a}_{i\downarrow} + \hat{a}^\dagger_{i\downarrow}\hat{a}_{i\uparrow}) \tag{2.67}$$

$$\hat{S}_{iy} = \tfrac{i}{2}\hat{a}^\dagger_{i\mu}\sigma^y_{\mu\nu}\hat{a}_{i\nu} = \frac{1}{2}(\hat{a}^\dagger_{i\downarrow}\hat{a}_{i\uparrow} - \hat{a}^\dagger_{i\uparrow}\hat{a}_{i\downarrow}) \tag{2.68}$$

$$\hat{S}_{iz} = \tfrac{1}{2}\hat{a}^\dagger_{i\mu}\sigma^z_{\mu\nu}\hat{a}_{i\nu} = \frac{1}{2}(\hat{a}^\dagger_{i\uparrow}\hat{a}_{i\uparrow} - \hat{a}^\dagger_{i\downarrow}\hat{a}_{i\downarrow}). \tag{2.69}$$

where the total-spin operator is the vector

$$\vec{S}_i = \left(\hat{S}_{ix}, \hat{S}_{iy}, \hat{S}_{iz}\right). \tag{2.70}$$

We can implement quantum logic gates by exploiting an isomorphism between the qubit creation and annihilation operators, $\hat{a}^\dagger_\alpha$ and $\hat{a}_\alpha$ for the αth qubit, and the site-specific spin creation and annihilation operators, $\hat{a}^\dagger_{i\mu}$ and $\hat{a}_{i\mu}$ for the spin component (say along the z-axis) of value μ at the ith lattice node. Two qubits are required to encode one site-specific quantum spin, both having four basis states as given in (2.22). The isomorphism between these two sets of operators are mapped as follows ($i = 1, \ldots, L$):

$$\begin{aligned} \text{spin} &\leftrightarrow \text{qubit} \\ \hat{a}^\dagger_{i\uparrow} &\leftrightarrow \hat{a}^\dagger_{2i-1} && (2.71a) \\ \hat{a}_{i\uparrow} &\leftrightarrow \hat{a}_{2i-1} && (2.71b) \\ \hat{a}^\dagger_{i\downarrow} &\leftrightarrow \hat{a}^\dagger_{2i} && (2.71c) \\ \hat{a}_{i\downarrow} &\leftrightarrow \hat{a}_{2i}, && (2.71d) \end{aligned}$$

and in turn we have

$$\hat{S}_{ix} = \frac{1}{2}\left(\hat{a}^\dagger_{i\uparrow}\hat{a}_{i\downarrow} + \hat{a}^\dagger_{i\downarrow}\hat{a}_{i\uparrow}\right) = \frac{1}{2}\left(\hat{a}^\dagger_{2i-1}\hat{a}_{2i} + \hat{a}^\dagger_{2i}\hat{a}_{2i-1}\right) \tag{2.72a}$$

$$\hat{S}_{iy} = \frac{1}{2}\left(\hat{a}^\dagger_{i\downarrow}\hat{a}_{i\uparrow} - \hat{a}^\dagger_{i\uparrow}\hat{a}_{i\downarrow}\right) = \frac{1}{2}\left(\hat{a}^\dagger_{2i}\hat{a}_{2i-1} - \hat{a}^\dagger_{2i-1}\hat{a}_{2i}\right) \tag{2.72b}$$

$$\hat{S}_{iz} = \frac{1}{2}\left(\hat{a}^\dagger_{i\uparrow}\hat{a}_{i\uparrow} - \hat{a}^\dagger_{i\downarrow}\hat{a}_{i\downarrow}\right) = \frac{1}{2}\left(\hat{a}^\dagger_{2i-1}\hat{a}_{2i-1} - \hat{a}^\dagger_{2i}\hat{a}_{2i}\right). \tag{2.72c}$$

Notice in (2.22), and likewise in (2.71), there is a particular ordering with *spin up* encoded by the *left* qubit and *spin down* encoded by the *right* qubit. This ordering has a physical manifestation as explained in Section 3 on type-I quantum algorithms, particularly in the context of the quantum algorithm for the Dirac equation.

2.11 Spin interchange operator

The spin interchange operator that exchanges the σth spin between the ith node and the jth node of the lattice can be written in the same form as (2.30):

$$\hat{\chi}_{ij\mu} = \mathbf{1} - \left(\hat{a}^\dagger_{i\mu} - \hat{a}^\dagger_{j\mu}\right)\left(\hat{a}_{i\mu} - \hat{a}_{j\mu}\right), \tag{2.73}$$

where $\mu =\uparrow$ or $\downarrow$. In terms of the qubit operators, it is the following:

$$\hat{\chi}_{ij\sigma} = \begin{cases} \mathbf{1} - \left(\hat{a}^\dagger_{2i-1} - \hat{a}^\dagger_{2j-1}\right)\left(\hat{a}_{2i-1} - \hat{a}_{2j-1}\right), & \sigma =\uparrow \\ \mathbf{1} - \left(\hat{a}^\dagger_{2i} - \hat{a}^\dagger_{2j}\right)\left(\hat{a}_{2i} - \hat{a}_{2j}\right), & \sigma =\downarrow . \end{cases} \tag{2.74}$$

We make use of the spin interchange operator (2.74) to perform essential symmetry operations, as explained in Section G.

2.12 $\sqrt{SWAP}$ gate

2.12.1 Symmetric gate

Using (2.70), the Heisenberg Hamiltonian operator is readily constructed

$$\hat{H} = \sum_{\langle ij\rangle} J_{ij}\vec{S}_i \cdot \vec{S}_j, \tag{2.75}$$

where $\langle ij\rangle$ indicates a sum over all the bonds of the lattice with coupling constants J_{ij} for each of the respective bonds. Let us consider a Heisenberg spin system with two coupled spins according to (2.75):

$$\hat{H} = J\vec{S}_1 \cdot \vec{S}_2. \tag{2.76}$$

We can work out the the matrix representation of $\hat{H}$ by applying it to each ket in the number basis. We use the following rules: the operator $\hat{S}_{nx}$ flips the nth spin, the operator $\hat{S}_{nz}$ flips the phase of the state (multiplies the amplitude by -1) if the nth spin is down and does nothing otherwise, whereas the operator $\hat{S}_{ny}$ both flips the nth spin and flips the phase of the state if the nth spin is down and also multiplies the amplitude by i since $\hat{S}_{ny} = i\hat{S}_{nz}\hat{S}_{nx}$. The action of these spin operators on the basis states is tabulated in Appendix C. So in the

number basis, we compute the matrix representation of the 2-spin Heisenberg Hamiltonian (2.76) by finding its matrix elements

$$H = J \begin{pmatrix} \frac{1}{2} & 0 & 0 & 0 \\ 0 & -\frac{1}{2} & 1 & 0 \\ 0 & 1 & -\frac{1}{2} & 0 \\ 0 & 0 & 0 & \frac{1}{2} \end{pmatrix}. \tag{2.77}$$

The eigenvalues of (2.77) are

$$\lambda_1 = -\frac{3J}{2} \qquad \lambda_2 = \frac{J}{2} \qquad \lambda_3 = \frac{J}{2} \qquad \lambda_4 = \frac{J}{2} \tag{2.78}$$

and the respective eigenvectors of (2.77) are

$$\begin{array}{ll} |1\rangle = \frac{1}{\sqrt{2}}(|\uparrow\downarrow\rangle - |\downarrow\uparrow\rangle) & |2\rangle = |\uparrow\uparrow\rangle \\ |3\rangle = \frac{1}{\sqrt{2}}(|\uparrow\downarrow\rangle + |\downarrow\uparrow\rangle) & |4\rangle = |\downarrow\downarrow\rangle \end{array} \tag{2.79}$$

Now the evolution operator $\hat{U} = e^{-i\hat{H}\tau/\hbar}$ can be expressed in matrix form using these eigenvalues and eigenvectors as follows

$$U = \begin{pmatrix} \langle 1| \\ \langle 2| \\ \langle 3| \\ \langle 4| \end{pmatrix} \begin{pmatrix} e^{-i\lambda_1\tau/\hbar} & 0 & 0 & 0 \\ 0 & e^{-i\lambda_2\tau/\hbar} & 0 & 0 \\ 0 & 0 & e^{-i\lambda_3\tau/\hbar} & 0 \\ 0 & 0 & 0 & e^{-i\lambda_4\tau/\hbar} \end{pmatrix} \begin{pmatrix} |1\rangle & |2\rangle & |3\rangle & |4\rangle \end{pmatrix}, \tag{2.80}$$

where $\begin{pmatrix} |1\rangle & |2\rangle & |3\rangle & |4\rangle \end{pmatrix}$ is the 4×4 matrix with columns that are the eigenvectors of U. The result for the evolution matrix is

$$U = e^{-i\frac{J\tau}{2\hbar}} \begin{pmatrix} 1 & 0 & 0 & 0 \\ 0 & \frac{1}{2} + \frac{e^{2iJ\tau/\hbar}}{2} & \frac{1}{2} - \frac{e^{2iJ\tau/\hbar}}{2} & 0 \\ 0 & \frac{1}{2} - \frac{e^{2iJ\tau/\hbar}}{2} & \frac{1}{2} + \frac{e^{2iJ\tau/\hbar}}{2} & 0 \\ 0 & 0 & 0 & 1 \end{pmatrix}. \tag{2.81}$$

Hence, the Heisenberg Hamiltonian (2.76) can be used to model the conservative quantum logic gate (2.48a) for the bosonic case ($\delta = 0$). Now if we allow the two-spin system to evolve for the duration of $\tau = \frac{\pi}{4}\frac{\hbar}{J}$, which we may refer to as a *quarter π-evolution*, then U becomes the $\sqrt{\text{swap}}$ gate used to model the microscopic particle-particle collisional dynamics in the context of a quantum lattice-gas system

$$U = e^{-i\frac{\pi}{8}} \begin{pmatrix} 1 & 0 & 0 & 0 \\ 0 & \frac{1}{2} + \frac{i}{2} & \frac{1}{2} - \frac{i}{2} & 0 \\ 0 & \frac{1}{2} - \frac{i}{2} & \frac{1}{2} + \frac{i}{2} & 0 \\ 0 & 0 & 0 & 1 \end{pmatrix}. \tag{2.82}$$

For example, this is used in quantum algorithm for the Schroedinger equation in Section 5 and the quantum algorithm for the diffusion equation in Section 8. The only underlying

difference in the modeled sub-scale dynamics between the quantum mechanical Schrodinger wave equation case and the classical diffusion equation case is that in the latter case there is a loss of phase coherence due to periodic state reduction (*e.g.* wave function collapse by measurement) of all the qubits.

2.12.2 Antisymmetric gate

Another important gate that conserves spin is the following gate:

$$U = \begin{pmatrix} 1 & 0 & 0 & 0 \\ 0 & \cos\theta & -\sin\theta & 0 \\ 0 & \sin\theta & \cos\theta & 0 \\ 0 & 0 & 0 & 1 \end{pmatrix}. \tag{2.83}$$

We can build this gate using the following Hamiltonian

$$\hat{H} = J(\hat{S}_{2x}\hat{S}_{1y} - \hat{S}_{1x}\hat{S}_{2y}). \tag{2.84}$$

The matrix representation of this Hamiltonian in the number basis is

$$H = J \begin{pmatrix} 0 & 0 & 0 & 0 \\ 0 & 0 & \frac{i}{2} & 0 \\ 0 & -\frac{i}{2} & 0 & 0 \\ 0 & 0 & 0 & 0 \end{pmatrix}. \tag{2.85}$$

The eigenvalues of (2.85) are

$$\lambda_1 = 0 \qquad \lambda_2 = 0 \qquad \lambda_3 = -\tfrac{J}{2} \qquad \lambda_4 = \tfrac{J}{2} \tag{2.86}$$

and the respective eigenvectors of (2.85) are

$$\begin{array}{cc} |1\rangle = |\downarrow\downarrow\rangle & |2\rangle = |\uparrow\uparrow\rangle \\ |3\rangle = \frac{1}{\sqrt{2}}(|\uparrow\downarrow\rangle - i|\downarrow\uparrow\rangle) & |4\rangle = \frac{1}{\sqrt{2}}(|\uparrow\downarrow\rangle + |\downarrow\uparrow\rangle) \end{array} \tag{2.87}$$

Using (2.80) but now with these new eigenvalues and eigenvectors, the result for the evolution matrix is the matrix

$$U = \begin{pmatrix} 1 & 0 & 0 & 0 \\ 0 & \cos\frac{J\tau}{2\hbar} & -\sin\frac{J\tau}{2\hbar} & 0 \\ 0 & \sin\frac{J\tau}{2\hbar} & \cos\frac{J\tau}{2\hbar} & 0 \\ 0 & 0 & 0 & 1 \end{pmatrix}. \tag{2.88}$$

Now if we allow this two-spin system to evolve for the duration of $\tau = \frac{\pi}{2}\frac{\hbar}{J}$, then U becomes the gate for modeling the Burgers equation in the context of a quantum lattice-gas method [Yepez, 2002c]

$$U = \begin{pmatrix} 1 & 0 & 0 & 0 \\ 0 & \frac{1}{\sqrt{2}} & -\frac{1}{\sqrt{2}} & 0 \\ 0 & \frac{1}{\sqrt{2}} & \frac{1}{\sqrt{2}} & 0 \\ 0 & 0 & 0 & 1 \end{pmatrix}, \tag{2.89}$$

and is used in the type-II quantum algorithms for the Burgers equation in Section 9 and the magnetohydrodynamics equations in Section 10.

2.13 Hilbert space sectors

Because of conservation of number density (number of spins over the lattice) and the spin-z component (net magnetization s_z), as well as other possible conserved quantities (such as symmetries of the quantum state arising from the finite-point group associated with a two or three dimensional spatial lattice), the number of quantum states that can become occupied (through superposition) is much less than the total number of basis states of the entire Hilbert space. Since $\hat{s}_z$ commutes with any Hamiltonian built out of conservative quantum logic gates, it is convenient to work with a set of basis states in the number representation having a given fixed magnetization s_z because by inspection one can immediately determine s_z for any such state. Given a lattice of size L with n particles, we can determine the Hilbert space sectors using a generating function

$$\left(\sum_{p=0}^{1} \sum_{m=0}^{1} n^{p+m} s_z^{p-m} \right)^{\frac{Q}{2}}, \tag{2.90}$$

where the number of qubits is $Q = 2L$ for a system with 2 qubits/node, as mentioned in the introduction. In the summation (2.90), p denotes spin-up and m denotes spin-down. In our case example above in Table 1.1, the largest sector of the total Hilbert space is 1225 and occurs if there are six spins or eight spins with $s_z = 0$, and also occurs at half-filling with 7 spins when $s_z = \pm 1$.

Another relevant issue is the finite-point group symmetry of the spatial lattice. Let us denote an *s_z-basis state* by the symbol ϕ_n. It is possible to determine a representation of the finite point group operators in the $\{\phi_n\}$ basis. This is accomplished by successively employing a site-interchange operator, here denoted $\hat{\mathcal{X}}$. Using (2.74), we can interchange all the spins at the ith node of the lattice with the spin at the jth node of the lattiice:

$$\hat{\mathcal{X}}_{ij} \equiv \hat{\chi}_{ij\uparrow} \hat{\chi}_{ij\downarrow}. \tag{2.91}$$

Let us denote the various finite-point group operations by the generic symbol R and let us denote their ith irreducible representations by Γ_i^R. Using (2.91) we can rotate or reflect any particular state by implementing any desired group operation R in terms of $\mathcal{X}$ (a couple of examples are given in Appendix G).

Given that we have constructed a *reducible* matrix representation, denoted $\{M_{mn}^R\}$, of the symmetry group in our $\{\phi_n\}$ basis, we may then construct projection operators, denoted $P_{mn}^{\Gamma_i}$, for each of the irreducible representations of the group [Reich and Falicov, 1988,

Chen et al., 1988, Freericks et al., 1991, Freericks and Falicov, 1991, Falicov, 1966]. This is done as follows

$$P^{\Gamma_i}_{mn} = \sum_R \mathrm{Tr}(\Gamma^R_i) M^R_{mn}, \tag{2.92}$$

where $\mathrm{Tr}(\Gamma^R_i)$ is the character or trace listed in the ith row and Rth column of the character tables. We can also determine the number of times the Γ^R_i irreducible representation occurs in M^R_{mn} by knowing the character, $\mathrm{Tr}(M^R_{mn})$ [Cotton, 1964]. In practice the useful quantity b_i is determined by

$$b_i = \sum_R \mathrm{Tr}(\Gamma^R_i)\mathrm{Tr}(M^R_{mn}), \tag{2.93}$$

giving the size of the ith block of the resulting block-diagonalized Hamiltonian matrix of elements.

The third step is to apply $P^{\Gamma_i}_{mn}$ onto the $\{\phi_n\}$ basis to find linear combinations that possess a definite symmetry

$$\psi^{\Gamma_i}_m = \sum_n P^{\Gamma_i}_{mn}\phi_n. \tag{2.94}$$

We shall denote the *symmetry basis* set by $\{\psi^{\Gamma_i}_n\}$.

The fourth step is to try to block diagonalize the Hamiltonian still further by calculating the matrix of elements of the total-spin-squared operator, $\hat{S}^2$, in each $\{\psi^{\Gamma_i}_m\}$ sub-basis and diagonalizing this matrix to determine linear combinations of the $\psi^{\Gamma_i}_m$ states that have a definite total-spin, that is, we find eigenvectors of $\hat{S}^2$. Let us denote these eigenvectors of $\hat{S}^2$ as $\varphi^{\Gamma_i,S}_m$. These define a *total-spin sub-basis* $\varphi^{\Gamma_i,S}_m$. Since $\hat{S}^2$ commutes with the Hamiltonian we thereby partition each symmetry block into smaller blocks, each having a definite total-spin.

For small lattices, as a final step we analytically find the eigenvalues and eigenvectors of each resulting *spin-and-symmetry block* and thereby determine the solution by calculating the Hamiltonian matrix elements in the $\{\varphi^{\Gamma_i,S}_m\}$ symmetry and total-spin sub-basis. However, for arbitrarily large lattices the only possible solution is a numerical one achieved on a quantum computer. The quantum computation is carried out in a particular $\varphi^{\Gamma_i,S}_m$ sub-basis.

2.14 Efficiency

In the Hilbert space of a system with $\frac{Q}{2}$ nodes, whatever sector is chosen, only Q qubits are needed here and this is the crux of efficient quantum mechanical encoding. Furthermore, wave functions spanning multiple sectors of the Hilbert space may still be encoded using only these Q qubits because of the principle of quantum mechanical superposition, yet because of conservation of number of spins and the spin-z component, total spin, and state symmetries,

these are unphysical superpositions. Each basis state is a member of only one of the sectors of the full Hilbert space, and its probability of outcome depends only on its entanglement with the other basis states in that particular sector.

The initial state of every quantum computer has no entanglement, which is a quantifiable physical resource that must be "input" into the quantum computer to cause the qubits to become quantum mechanically correlated. The Hamiltonian (2.49) for the conserative quantum gate is the generator of entanglement. Think of the programmer (e.g. experimental physicist) having access to a "high entanglement" reservoir and think of a quantum computer as an engine driven by entanglement transfer.

At the final stage of the computation, an *output register* (a subset of the qubits) contains the desired answer to a difficult problem. This answer can be reliably extracted because each qubit of the output register is put into a classical binary state, $|0\rangle$ or $|1\rangle$, as all the entanglement is transferred onto the remaining qubits. By measuring the register, the desired binary information (one bit for each qubit in the register) is obtained. This is accomplished without any wave function collapse since this register is in a purely classical state. However, during this final measurement stage, all the remaining entangled qubits in the system undergo decoherence whereby all the residual entanglement escapes to a "low entanglement" reservoir, the external environment. Quantum mechanics, a theory to accurately and deterministically predict the evolution of probability amplitudes, is turned on its head and used as an engine for computational work as entanglement is transferred from a source reservoir to a sink reservoir. This is reminiscent of the thermodynamic heat engine but at the microscpic scale where *computational work* (e.g. rotating a nuclear spin) takes the place of *work* and transference of *entanglement* (e.g. correlating and de-correlating pairs of spins) takes the place of the transference of *heat* between reserviors.

As an alternative to the quantum computing engine described above, it is possible to use all the qubits as the output register. The quantum computer is driven by the transference of entanglement from a source to a sink, but information is now extracted by employing wave function collapse through measurement. This alternative may be classified as *analog quantum computing* since the physical microscopic system embodied in the quantum computer may be efficiently used to model a different physical system. A further sub-classification emerges because there are two ways to use entanglement in analog quantum computers: (1) in a global long-range and long-lived way (requiring quantum error correction in its experimental implementation); or (2) in localized short-range and short-lived way (mitigating the need for quantum error correction). This distinction leads to two types of analog quantum computers, here labeled *type-I* and *type-II*, and respectively introduced in Section 3 and Section 6.

2.15 Quantum algorithmic paradigm

Developing analog quantum algorithms amounts to unfolding the quantum mechanical evolution operator into an ordered sequence of 2-qubit quantum gate operations. Let $\hat{G}$ denote an arbitrary 2-qubit quantum gate and let $\hat{H}_{\text{eff}}$ denote the effective Hamiltonian for a quantum spin system embodying the quantum computer with Q qubits. The quantum mechanical evolution operator that evolves the state of the system is:

$$\begin{aligned} e^{-i\hat{H}_{\text{eff}}\tau/\hbar} &= e^{-i\hat{H}_N\Delta t/\hbar}\cdots e^{-i\hat{H}_1\Delta t/\hbar}e^{-i\hat{H}_0\Delta t/\hbar} \\ &= \hat{G}_N\cdots\hat{G}_1\hat{G}_0. \end{aligned} \tag{2.95}$$

Here each 2-qubit gate operation, $\hat{G}_n = e^{-i\hat{H}_n\Delta t/\hbar}$, is represented by a $2^Q \times 2^Q$ matrix, for $0 \leq n \leq N$ with gates applied in series ($\tau = (N+1)\Delta t$) or in parallel ($\tau = \Delta t$). The quantum mechanical evolution equation in product form is

$$|\Psi(t+\tau)\rangle = \hat{G}_N\cdots\hat{G}_2\hat{G}_1\hat{G}_0|\Psi(t)\rangle. \tag{2.96}$$

In general, it is not possible to analytically express the the quantum mechanical evolution equation in Heisenberg form

$$|\Psi(t+\tau)\rangle = e^{-i\hat{H}_{\text{eff}}\tau/\hbar}|\Psi(t)\rangle \tag{2.97}$$

because $\hat{H}_{\text{eff}}$ is has an infinite number of terms due to the noncommutability of the quantum gates ($[\hat{H}_n, \hat{H}_m] \neq 0$), as shown by the Campbell-Baker-Hausdorff theorem. Nevertheless, in certain special cases (type-I quantum algorithms) we are able to analytically determine an accurate approximation of $\hat{H}_{\text{eff}}$.

Equation (2.96) can be decomposed into a set of equations, one for each gate operation, using N intermediate states $|\Psi_n\rangle$, for $0 \leq n \leq N$

$$\begin{aligned} |\Psi_1\rangle &= \hat{G}_0|\Psi(t)\rangle \\ |\Psi_2\rangle &= \hat{G}_1|\Psi_1\rangle \\ |\Psi_3\rangle &= \hat{G}_2|\Psi_2\rangle \\ \vdots &\ \vdots\ \vdots \\ |\Psi(t+\tau)\rangle &= \hat{G}_N|\Psi_N\rangle. \end{aligned} \tag{2.98}$$

It is customary that each intermediate state in (2.98) be depicted by a stage in a "quantum circuit diagram" where qubits are drawn as "leads" and each gate $\hat{G}_n$ is drawn as a transfer function usually with two input leads and two output leads. (There are also single qubit gates that rotate the phase of the qubit). In our treatment of quantum algorithms for

computational physics, we generally have no need for this type of diagrammatic approach, however for pedagogical purposes I do draw some "periodic" quantum circuits in the introductory section to the type-II quantum computer in Section 6. The graphical approach can be found in most other reviews of quantum computing, for example in the comprehensive book by Nielsen and Chuang [Chuang and Nielsen, 2000].

Equation (2.98) expresses a quantum algorithmic approach where each gate operation is accomplished in series, one after the other, and the final result of the computation is obtained by measuring all Q qubits (a classical bit string of length Q). Of course this is overly restrictive since it is possible to apply quantum gates in parallel to different and non-overlapping pairs of qubits. Actually the other case where the maximum possible number of quantum gates are accomplished in parallel, in an attempt to save physical time in the actual implementation, is the most relevant to quantum algorithms for computational physics. Hence, qubits are partitioned into small groups, called *quantum nodes*, and the gates are distributively applied over the nodes. The initial state of a quantum node is an unequally weighted superposition of states over the Hilbert space of that node, generated by tipping, or rotating, each qubit of the quantum node independently. Such parallel cases are discussed immediately below in Section 2.16.

Finally, any quantum algorithm that requires very many qubits to remain phase-coherent and globally entangled over the entire course of the quantum computation, employing either serialized or parallelized quantum gate protocols, requires the use of extra qubits to correct for bit-flip and phase errors [Shor, 1995, Knill et al., 1998]. The use of quantum error correction codes is an intrinsic part of type-I quantum algorithms.

Analog quantum computers have the following characteristics: finegrained; systolic; based on conservative quantum logic (2.48a); and described by a mesoscopic *quantum Boltzmann equation* for $f(\vec{x},\vec{p},t) = \langle\Psi(t)|\hat{n}_\alpha|\Psi(t)\rangle$ (as presented in (7.27) in Section 7):

$$\frac{df(\vec{x},\vec{p},t)}{dt} = \lim_{\tau\to 0}\frac{1}{\tau}\langle\Psi(t)|\hat{C}^\dagger\hat{n}_\alpha\hat{C} - \hat{n}_\alpha|\Psi(t)\rangle,$$

where the αth qubit encodes a particle at location $\vec{x}$ with momentum $\vec{p}$ and $|\Psi(t)\rangle$ is the quantum state of the entire quantum computer.

2.16 Formal distinction between analog quantum algorithms

2.16.1 Type-I quantum algorithms

The crucial feature of a type-I quantum algorithm is its tractability in the sense that it is possible to analytically derive an accurate approximation of $\hat{H}_{\text{eff}}$ so that (4.109) emerges as an

effective field theory. It is possible to choose a protocol of gate operations so that the effective field theory (4.109) becomes the relativistic Dirac equation with $H_{\text{eff}} = \sigma_z \otimes \vec{\sigma} \cdot \vec{p}c + \sigma_x \otimes \mathbf{1} mc^2$, with momentum $\vec{p} = (p_x, p_y, p_z)$ and the Pauli spin matrices $\vec{\sigma} = (\sigma_x, \sigma_y, \sigma_z)$, or the effective field theory for the non-relativistic Schroedinger equation with $H_{\text{eff}} = \frac{p^2}{2m}$.

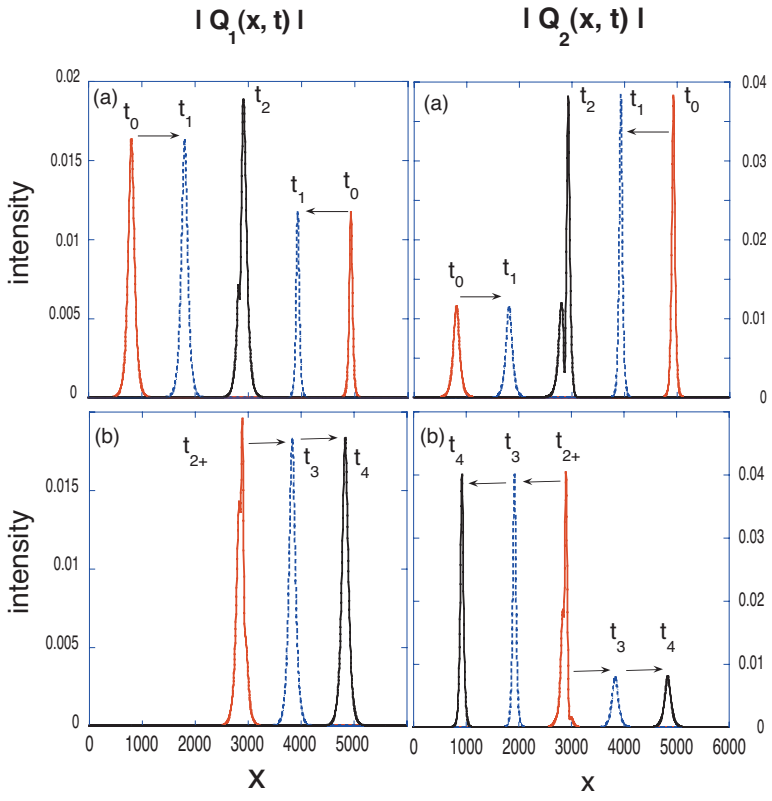

Figure 2.1: Soliton collisions: The propagation of an initial ($t_0 = 0$) exact 2-soliton vector solution to the Manakov system for polarization modes: $|Q_1|$ (on left) and $|Q_2|$ (on right). (a) The solitons propagate toward each other $t_1 = 25K\tau$ and undergo their first collision at $t_1 = 50K\tau$. (b) The post-collision polarization modes with the soliton parameters chosen so there is no left-propagating soliton for mode Q_1 ($t_{2+} = 51K\tau$, $t_3 = 75K\tau$, and $t_4 = 100K\tau$). The intensity of each mode $\int dx |Q_i(x,t)|^2 = \text{const.}$ is preserved to better than one part in 10^{-17}. Within each mode, there is a redistribution of the intensity in the outgoing asymptotic 1-soliton states. These simulations were carried out by collaborators George and Linda Vahala.

Furthermore, we can add a scalar potential into $\hat{H}_{\text{eff}}$. When this potential depends on the wave function itself, we can model nonlinear soliton dynamics governed by the nonlinear Schroedinger equation and the Korteweg de Vries equation [Vahala et al., 2003b, Vahala et al., 2003a], and very recently dark solitons [Vahala et al., 2004b] and elastic soliton collision of optical pulses in birefringent optical telecom fibers governed by the Manakov equations [Vahala et al., 2004a], see Figure 2.1.

The discrete amplitude field dynamically changes over time through a process of "local collisions" at each lattice node and "local translations" between neighboring lattice nodes:

1. A local collision at a lattice node is defined by the action of a unitary operator on the amplitudes at that lattice node. This unitary operator is uniformly and spatially homogeneously applied to the lattice-based amplitude field.

2. A local translation is defined by that action of another unitary operator that exchanges two particles between nearest neighboring lattice nodes. Again, this unitary operator is uniformly and spatially homogeneously applied to the lattice-based amplitude field between all lattice node pairs in a prescribed fashion that depends on whether the model is a non-relativistic or relativistic one and also depends on the spatial dimension of the modeled quantum mechanical system; either one, two, or three dimensional.

Therefore, for a quantum lattice gas the quantum algorithm can be expressed in a form like (2.98), with an intermediate state $|\Psi'\rangle$:

$$|\Psi'\rangle = \hat{C}|\Psi(\vec{x}_1, \ldots, \vec{x}_L; t)\rangle \tag{2.99a}$$

$$|\Psi(\vec{x}_1, \ldots, \vec{x}_L; t+\tau)\rangle = \hat{S}|\Psi'\rangle, \tag{2.99b}$$

where $|\Psi\rangle$ is explicitly notated to make it clear that the qubits are partitioned into a lattice arrangement with L quantum nodes labeled by the spatial vectors $\vec{x}_1$, $\vec{x}_2$, $\ldots$, $\vec{x}_L$. These vectors point to the centroid of each respective quantum node. Each qubit is also associated with a particular lattice vector, $\hat{v}$, or *displacement* vector. Furthermore, according to (2.5), the *occupancy probability* of finding a "particle" at time t at a location $\vec{x}$ hopping with unit speed along direction $\hat{v}$ is defined to be probability $|\mathcal{A}(1,t)|^2$ for the particular qubit at that quantum node which is associated with that displacement direction.

The unitary operator $\hat{C}$ changes the occupancy probabilities on each node independently. It causes local collisional scattering of particles at each node in the system independently, and therefore, can be written as a L-fold tensor product over the lattice nodes

$$\hat{C} = \bigotimes_{x=1}^{L} \hat{U}, \tag{2.100}$$

where $\hat{U}$ is a "local" unitary transformation constructed using a sequence of one or more conservative quantum gates

$$\hat{U} = \Upsilon_N \cdots \Upsilon_2 \Upsilon_1. \tag{2.101}$$

With B qubits per node, $\hat{U}$ is represented by a $2^B \times 2^B$ size matrix. All the gate operations needed to implement $\hat{C}$ are homogeneously applied on a node-by-node basis causing local superposition and entanglement within each node.

In general $\hat{U}$ is represented by a block diagonal matrix, where each block mixes local on-site configuration that have the same additive conserved quantities. For the simplest

one dimensional quantum lattice-gas models presented Section 8 and Section 9, each $\hat{U}$ is implemented by a single quantum gate operation. For more complex models, $\hat{U}$ would be implemented by a sequence of quantum gates and is block diagonal over the sectors of the Hilbert space as in the three-dimensional quantum lattice-gas fluid model presented in Section 11.

In our investigation of a suitable local unitary collision operator we have found that one quantum gate in particular, the $\sqrt{\text{swap}}$ gate, is especially useful for modeling the Schroedinger wave equation because there exists a local equilibrium configuration that is an eigenket of this gate and has unity eigenvalue. This local equilibrium is defined in Section 5.2.1. Therefore, we have selected the $\sqrt{\text{swap}}$ gate as our model quantum gate. It holds the same status for analog quantum computers that the classical NAND gate holds for our present day digital-electronics-based computers. When used in the appropriate fashion, this quantum gate leads to quantum algorithms with an overall modeling error that is second-order in the temporal discretization and fourth-order in the spatial discretization.

The unitary operator $\hat{S}$ shifts the occupancy probabilities between nodes, but otherwise does not change them. The streaming operator $\hat{S}$ is constructed using a sequence of interchange operators of the form (2.37). It causes "particle" movement and is represented by an orthogonal permutation matrix; it would otherwise cause strictly classical data movement if there were not superposed or entangled on-site qubits. In a type-I quantum algorithm, the application of the streaming operator $\hat{S}$ spreads quantum correlations across the lattice.

A detailed treatment of a globally phase-coherent quantum lattice has shown that quantum correlations can significantly alter the macroscopic scale transport properties of the system [Yepez, 2001a].

2.16.2 Type-II quantum algorithms

A type-II quantum computer is a new type of quantum computing device with a variety of computational physics applications now in the literature. The qubits within a type-II quantum computer are partitioned into quantum nodes just as in the type-I case. In general, all qubits can be initialized with independent tipping angles $|q_\alpha\rangle = \cos\varphi_\alpha|1\rangle + \sin\varphi_\alpha|0\rangle$, for $\alpha = 1, 2, \ldots, Q$, where Q is the number of qubits. The crucial features of a type-II quantum algorithm are the following:

1. its periodically repeated measurement of the qubits; and

2. its tractability in the sense that it is possible to analytically derive a classical effective field theory, a partial differential equation that includes dissipative terms.

The main difference between the type-I and type-II quantum algorithms is that for the second case no effective Hamiltonian description, $\hat{H}_{\rm eff}$, exists because of the non-unitary action of the measurement process. Nevertheless, an emergent Hamiltonian-based effective field theory does exist but it is classical and dissipative in nature. The effective field theory is represented by a partial differential equation description.

The collision function on the R.H.S. of quantum lattice Boltzmann equation (7.27) is simplified in the type-II case because of short-range and short-lived entanglement. Consequently, there exists a unique entropy function:

$$\mathcal{H} = -\sum_{a=1}^{B} \left[f_a \ln(\gamma_a f_a) + (1 - f_a) \ln(1 - f_a) \right], \tag{2.102}$$

where γ_a depends on gate protocol using successive applications of conservative quantum logic gates of the form (2.48a). As an extremum of (2.102) subject to the constraint of conservation of E_a (the qubit energy eigenvalues), $\frac{\partial \mathcal{H}}{\partial f_a} = 0$, we find the Fermi-Dirac equilibrium occupation probability:

$$f_a^{\rm eq} = \frac{1}{\frac{1}{\gamma_a} e^{\beta E_a} + 1} = \frac{1}{e^{\beta(E_a + \Delta E_a)} + 1}. \tag{2.103}$$

Traditional computational physics models obey the first law of thermodynamics (conservation law) and neglect the second law. We have pioneered algorithms that also obey the second law of thermodynamics by using an entropy function [Boghosian et al., 2003, Boghosian et al., 2004b]. For type-II quantum algorithms, the mesoscopic $\mathcal{H}$ function is determined by averaging the microscopic dynamics.

A simple unitary transformation $\hat{C}$, applied homogeneously to all the quantum nodes, causes short-range entanglement that is relatively short-lived. The transformation is close to the naturally occurring one that couples the quantum objects embodying the qubits in the quantum computer, for example generated by an nuclear magnetic resonance Hamiltonian $\frac{1}{2} \sum_{i=1}^{B} \sum_{j=1}^{B} J_{ij} \hat{\sigma}_{zi} \hat{\sigma}_{zj}$, where J_{ij} is the energy of the spin-spin coupling between the ith and jth spins, and B is the number of qubits per quantum node. For this reason, the unitary transformation obeys all physical conservation laws, conserving the total spin for example. The engineering needed to employ such a unitary transformation is manageable and is limited only by the number of J-coupling resonances that are experimentally accessible.

In the type-II quantum algorithmic procedure, entanglement once generated is promptly destroyed by measurement. At the node-level, we exploit the inherent nonlinearity that naturally occurs during wave function collapse and map this nonlinearity onto some nonlinear function to perform beneficial computational work. Following the measurement step, all the qubits are in a classical state. The resulting measurements can be accumulated, either by coarse-grain averaging or ensemble averaging over a sample. Probabilities are estimated

by frequency of occurrence: counting the number of 1's in the sample and dividing by the sample size.

The spin system's quantum state is always factored into a tensor product state over the nodes of the lattice

$$|\Psi(\vec{x}_1, \ldots, \vec{x}_L; t)\rangle = |\psi(\vec{x}_1, t)\rangle \otimes |\psi(\vec{x}_2, t)\rangle \otimes \cdots \otimes |\psi(\vec{x}_L, t)\rangle. \tag{2.104}$$

With B qubits per lattice node, the *on-site ket* $|\psi(\vec{x}, t)\rangle$ resides in a Hilbert space of size $2^B \times 2^B$. The outcome of a computation is determined by measuring the probability of qubit occupancies on all nodes of the array using either an ensemble or coarse-grain averaging technique. That is, the probability of occupancy of a qubit $|q\rangle$ located at coordinate $\vec{x}$ and corresponding to lattice vector $\vec{v}$ is determined by computing the following trace

$$f(\vec{x}, \vec{v}, t) = \mathrm{Tr}\left[|\Psi(\vec{x}_1, \ldots, \vec{x}_L; t)\rangle\langle\Psi(\vec{x}_1, \ldots, \vec{x}_L; t)|\hat{n}_q\right], \tag{2.105}$$

where $\hat{n}_q$ is the number operator associated with qubit $|q\rangle$ at position $\vec{x}$ encoding a particle moving with velocity $\vec{v}$.

In a factorized quantum lattice gas, the quantum algorithm is also expressed in a form like (2.98), but with two intermediate states $|\Psi'\rangle$ and $|\Psi''\rangle$

$$|\Psi'\rangle = \hat{C}|\Psi(\vec{x}_1, \ldots, \vec{x}_L; t)\rangle \tag{2.106a}$$

$$|\Psi''\rangle = \hat{\Gamma}|\Psi'\rangle \tag{2.106b}$$

$$|\Psi(\vec{x}_1, \ldots, \vec{x}_L; t + \tau)\rangle = \hat{S}|\Psi''\rangle. \tag{2.106c}$$

The additional operation, denoted by $\hat{\Gamma}$, is required to control the system wave function so that it remains a tensor product over the on-site submanifolds after application of the streaming operator $\hat{S}$. The operator $\hat{\Gamma}$ is a *projection operator* and is applied homogeneously across the nodes of the lattice and acts on all the qubits at each node. Therefore, it can be expressed as a tensor product, $\hat{\Gamma} = \bigotimes_{x=1}^{L} \hat{\Gamma}_x$. That is, $\hat{\Gamma}_x$ acts on the on-site ket $|\psi'(\vec{x}, t)\rangle$ independently. It corresponds to state reduction, such as a measurement of the occupancy probabilities of each qubit as specified in (2.105), and causes a collapse of the system wave function and hence is non-unitary

$$|\psi''(\vec{x}, t)\rangle = \hat{\Gamma}_x|\psi'(\vec{x}, t)\rangle = \bigotimes_{a=1}^{B} |q_a\rangle. \tag{2.107}$$

The state reduction or measurement procedure specified by the application of $\hat{\Gamma}$ keeps all the occupancy probabilities conserved, keeps each on-site ket (and in turn, the system wave

function) unit normal, and in the context of the lattice-gas method obeys the principle of detailed-balance. That is, after the application of $\hat{\Gamma}$, we require that

$$f''(\vec{x}, \vec{v}, t) = f'(\vec{x}, \vec{v}, t), \tag{2.108}$$

for all $\vec{x}$ and $\vec{v}$. The mesoscopic description in Section 7 of a locally phase-coherent quantum lattice has a nontrivial projection operator consistent with (2.105) that both satisfies the requirement given by (2.108) and the requirement of the principle of detailed-balance.

The repeated state reduction or measurement procedure specified by the application of the projection operator $\hat{\Gamma}$ during each time step evolution of the quantum computer wave function is a distinguishing characteristic of a type-II quantum computer. This step prevents uncontrolled bit-flip and phase errors for all the qubits in the system.

Chapter 3

Introduction to Type I analog quantum computing

A type I analog quantum computer is used to model one or more quantum particles governed by a quantum mechanical wave equation, such as the Schroedinger equation, Weyl equation, or Dirac equation. We say the quantum computer preforms analog computation because it relies on one physical quantum mechanical system (a quantum spin system with an inherent physical interaction Hamiltonian) to model another physical quantum mechanical system (a quantum system with a modeled many-body interaction Hamiltonian). Each qubit contained within the quantum computer is embodied by a fermionic spin-$\frac{1}{2}$ particle, or some other mathematically equivalent two-level quantum system. Every logical operation between qubit pairs is embodied by an interaction Hamiltonian describing the spin-spin coupling. For example, in nuclear magnetic resonance there exists a direct vector dipolar coupling of the magnetic dipoles associated with the two spins that averages to zero because of the molecular free rotation, and there also exists an indirect scalar coupling mediated by correlated electrons binding the molecule together between the measurable components of the two spins. Quantum logical operations are embodied in the scalar coupling mechanism, or some other mathematically equivalent two-qubit coupling mechanism appropriate to the particular experimental realization. The form of the scalar coupling Hamiltonian can be effectively altered by applying appropriately timed spin rotations using externally applied electromagnetic pulses, whose frequency, strength, polarization, and pulse duration depend on the particular experimental realization, so that the natural coupling along with the program of externally applied pulses together cause the desired quantum logic operation between qubit-pairs.

Since the quantum spin system is lattice based, its representation is naturally spatially discrete. In contrast, the modeled quantum particle system's wave function may be spatially continuous. Therefore, the quantum spins can only be used to approximately describe the

modeled quantum particle's wave function and I provide an overview of how this is done.

3.1 Reversible quantum lattice gas algorithms

A characteristic feature of all quantum algorithms used to model the dynamical behavior of a system of either relativistic or non-relativistic quantum particles is that a spatially continuous wave function must be approximated using a numerical grid with finite resolution. From the point-of-view of the modeler, there exists a small numerical "sub-scale" where unitary dynamical rules are locally applied in a discretized fashion and time advances forward in incremental units in a "programmed" way. Furthermore, this sub-scale is below the physical microscopic scale of the modeled quantum mechanical system.

Let me first describe how a one-body quantum particle governed by either the Schroedinger equation or Dirac equation is modeled. The basic approach is to use a customized quantum spin system (an externally controlled array of qubits as described above) to encode the quantum wave function of the modeled quantum system as well as its time-dependent behavior. At the small sub-scale (characterized by the lattice cell size) one imagines a sub-system of fermionic spins, each one of which encodes the possible presence of the modeled quantum particle at the location of that spin. That is, each of the fermionic spins encodes the local spatial occupancy, with a certain probability amplitude, of the modeled quantum particle at a specific lattice node where the spin is located.

The probability of finding the modeled quantum particle at the location of the spin is set equal to the probability that the spin is in its excited state, say spin-up. All the possible locations of the actual physical quantum particle are effectively modeled by the interfering set of probability amplitudes associated with this sub-system of fermionic spins. All these probability amplitudes, considered as an ordered finite set of complex numbers, constitute a discrete amplitude field. We use a discrete two-component amplitude field to model a wave function governed by the Schroedinger equation and we use a discrete four-component amplitude field to model a wave function governed by the Dirac equation. That is, on a type I analog quantum computer, two qubits are used per lattice node to model the Schroedinger equation and four qubits are used per lattice node to model the Dirac equation.

Perhaps the most remarkable characteristic of the quantum algorithm to model a many-body system of quantum particles governed by a set of coupled quantum wave equations is that we use the same protocol for local collisions and local translations that we use in the quantum algorithm to model the dynamical behavior of the one-body problem governed by either the Schrodinger equation or Dirac equation. Therefore, the computational overhead associated with the action of the unitary operators is fixed for both the one-body and many-

body cases. What differs is the number of configurations of the respective sub-system of fermionic spins that must be dealt with in the numerical simulation.

Through the combined actions of the unitary collision and translation operators, all the quantum mechanical pathways of the possible motions of the modeled quantum particles are numerically treated in simultaneous fashion. The numerical model can be viewed as a kind of kinetic system of locally interacting spins on the small sub-scale. There also exists a large "super-scale," which corresponds to the long wavelength limit of the dynamical modes in the discrete spin system. This numerical super-scale is equivalent to the physical microscopic scale where the many-body wave function of the modeled quantum mechanical system in question is well defined. Its continuous wave function is accurately approximated as one approaches the continuum limit where the grid resolution of the spatial lattice becomes infinite (the lattice cell size approaches zero). At this super-scale, the dynamical amplitude field is both continuous and differentiable in space and time [1].

At this super-scale, one can characterize the behavior of the quantum algorithm by an emergent effective field theory, cast as a partial differential equation of infinite order, for the dynamical amplitude field. Only the low-order time and space partial derivatives are numerically relevant and all the higher order partial derivatives are considered error terms. The lower order terms are equivalent to either the Schroedinger equation or the Dirac equation, depending on the construction. The physical wave function of the modeled quantum mechanical system and its dynamical behavior accurately obeys the appropriate physical quantum mechanical equations of motion in this sense. The quantum algorithm must have a sufficiently high degree of numerical convergence. To be a practical and useful algorithm, it must have at least second-order convergence which means that decreasing the grid cell size by a factor of two causes the numerical error inherent in the algorithm to decrease by a factor of four.

In summary, we model the evolution of the physical wave function by the collective motion of an engineered kinetic system of quantum spins. We expect that there exists a *local equilibrium configuration of spins* at each node of the numerical lattice. We require that this configuration be an eigenket, with unity eigenvalue, of the local unitary collision operator.

For classical many-body kinetic systems, there exists a global thermodynamic equilibrium which is a maximal entropy configuration. Classical kinetic systems relax towards this thermodynamic equilibrium through dissipative processes where observable information

[1] Another point regarding the $\sqrt{\text{swap}}$ gate is that when measurements are periodically made of the state of qubits in the system (this is done in the type II quantum algorithms described in Section 6), which destroys quantum superpositions and entanglements in the system, the super-scale behavior of the quantum lattice gas system is governed by the classical diffusion equation [Yepez, 2001b].

embodied within spatial correlations is transferred through spin-spin interaction into non-observable information embodied within spin-spin correlations. In the present case of our numerical quantum many-body kinetic spin system, our quantum lattice gas system, more than one global thermodynamic equilibrium exists, and this is to be expected because of its unitary evolution. The global configuration of quantum spins does not relax to a single steady-state equilibrium. Instead, there are many "steady-state configurations" that can exist in superposition. Each one of these configurations corresponds to an energy eigenstate of the modeled quantum mechanical equation of motion at the super-scale. If the quantum lattice gas system is initialized in a configuration corresponding to any one of the energy eigenstates, the super-scale spatial configuration of the system will remain fixed in time. Given a finite size lattice used for modeling purposes, the quantum state of each sub-scale configuration oscillates in time with a sinusoidal phase $e^{iEt/\hbar}$, where the energy eigenvalue of the super-scale configuration is E.

The quantum lattice gas method is equivalent to the Feynman path integral method. This is demonstrated in Section 4. The path integral is accurately recast as a kinetic dynamical process and efficiently computed in parallel on a space-time lattice arrangement of quantum bits in the idealized analog quantum computer.

3.2 Difficulty of type I quantum computing

In principle, a quantum computer can efficiently simulate, with fixed computational overhead, the behavior of another many-body quantum mechanical system where the number of modeled quantum particles ranges from one to half the number of qubits in the quantum computer. Of course, we have to qualify our claim for the efficiency of the quantum algorithm by saying that this is the case only "in principle." This may not be the case in practice; efficient quantum computation to-date has not yet been experimentally realized and may never be. Although quantum computers have a vast Hilbert space, individually controlling all the amplitudes in this Hilbert space, which requires substantially mitigating an equally vast array of uncontrolled sources of decoherences, may prove to be experimentally impractical after all is said and done.

Yet, this review of the quantum lattice gas method is not meant to cover the experimental details of implementing quantum computers or the experimental difficulty of achieving viable quantum error correction. My goal is merely to explain the method in the simplest terms I know of. I use well-known notions such as those regarding numerical finite-difference schemes, the statistical behavior of many-body kinetic systems, and the Feynman path integral representation of quantum mechanics.

3.3 The historical development of type I quantum lattice-gas algorithms

The inventor the quantum logic gate was the famous American physicist Richard Feynman [Feynman, 1982, Feynman, 1985, Hey and Allen, 1996], who won the Nobel prize in 1965 for his elegant quantum theory of light and matter called *quantum electrodynamics*.

The path integral representation of non-relativistic quantum particle dynamics was introduced by Feynman in the mid 1940's. In 1958, Riazanov extended the Feynman path integral formulation to handle the relativistic quantum particle dynamics described by the Dirac equation [Riazanov, 1958]. Although he did not state it in these terms, Riazanov was the first to discover a quantum algorithm to represent quantum particle dynamics on a discrete space-time grid, which is a crucial step in the formulation of a methodology suited for our numerical implementation. As it turns out, the efficiency of the numerical implementation depends on the existence of a type I analog quantum computer, not proposed until 1982 by Feynman himself, when Feynman conceived of the idea of using a many-body quantum mechanical spin system, a new type of computer which he called a quantum computer, to efficiently simulate general quantum mechanical many-body dynamics [Feynman, 1982, Feynman, 1985, Hey and Allen, 1996].

For quite some time Feynman had been aware of Riazanov's result, a form of which Feynman published in 1965, although at that time he did not refer to it as a quantum algorithm as such. It appears in the second chapter of his book on path integrals published with Hibbs [Feynman and Hibbs, 1965], where the problem is given to prove that the one-dimensional (1D) Dirac equation can be modeled by summing over all the possible zigzag paths of a single-speed particle traveling at the speed of light in a discrete two-dimensional space-time hopping from lattice site to lattice site, turning left or right. The amplitude a particular path contributes to the kernel is proportional to the number of its turns or bends, where each bend contributes a multiplicative factor of $i\varepsilon m$ to the probability amplitude associated with the path, where ε is the grid size of the space-time lattice and m the mass of the modeled quantum particle. In this way, the time evolution of the 2-spinor field of a single quantum particle is modeled by a summation over paths on a discrete space-time. A continuous effective field theory, the 1D Dirac equation, emerges in the limit of the infinite lattice resolution. A solution to Feynman's relativistic 1D problem was published in 1984 by Jacobson and Schulman [Jacobson and Schulman, 1984] which shows a remarkable correspondence between the formulation of the discrete path integral representation and the statistical mechanics formulation of an Ising spin system. Jacobson and Schulman were close to discovering the connection between the discrete path integral and the type of quantum

lattice-gas spin systems we use today to numerically implement quantum particle dynamics on a type I analog quantum computer.

In the quantum lattice-gas formulation, instead of summing over paths, one uses a "gas" of particles to numerically and simultaneously compute all paths in a time-explicit fashion. The bends in the paths as understood by Riazanov, Feynman, Jacobson, and Schulman are caused by spin-spin "collisions" at the local sub-space level. The speed of light movement of the modeled quantum particle is handled by local spin exchanges between neighboring sites, which we refer to as "streaming" at the sub-space level.

3.3.1 Review of type-I quantum algorithms

In 1994 Bialynicki-Birula presented a general quantum algorithmic approach of this kind for modeling the Weyl, Dirac, and Maxwell equations on a body-centered cubic lattice in three-dimensions [Bialynicki-Birula, 1994]. This model is 1st-order convergent (doubling the grid resolution merely doubles the numerical accuracy), but convergence is problematic when modeling particle dynamics in an external potential. Although the model is unitary, it is specified using non-unitary matrices and requires ad hoc lattice partitioning if implemented in parallel. Furthermore, Bialynicki-Birula addresses only the one-body problem.

In a series of papers on simulating the one-dimensional Dirac equation [Meyer, 1996a, Meyer, 1997c, Meyer, 1997b], Meyer presented a quantum algorithm similar to that of Bialynicki-Birula with a variety of numerical simulations including the effects of boundary conditions, inhomogeneities, and an external scalar potential. Meyer set the quantum algorithm for the discretized path integral in the context of the quantum lattice gas method and his algorithm is equivalent to the one-dimensional version of the Bialynicki-Birula quantum algorithm for the Dirac equation.

Meyer contributed 1D one-body numerical simulations and addressed the non-interacting lattice or checker-board problem using an additional rest particle. Yet he too did not address the many-body case nor the low-order numerical convergence issue.

The approach taken by Succi and Benzi is a classically-oriented computational approach that begins with a "kinetic" lattice Boltzmann equation of motion [2] (effectively the one-dimensional Dirac equation in the Majorana representation) and shows that the Schroedinger wave equation emerges as the governing equation of motion for the slow mode in the long wavelength "hydrodynamic" limit. That is, Succi and Benzi observed that the "super-scale" Schroedinger wave equation arises from the "middle scale" Dirac equation in a manner quite analogous to how the macroscopic Navier-Stokes hydrodynamic fluid equation arises from

[2] (The classical lattice Boltzmann equation was popularized with its application to computational fluid dynamics [Succi et al., 1991, Qian et al., 1992a, Chen et al., 1992].)

the mesoscopic kinetic Boltzmann equation through the Chapman-Enskog expansion.

Succi published a series of papers on this subject emphasing the analogy between quantum mechanics and fluid mechanics: the connection between the Dirac equation and the Schroedinger equation to that between the kinetic Boltzmann equation and the Navier-Stokes equation of hydrodynamics [Succi and Benzi, 1993, Succi, 1996, Succi, 1998]. Succi's quantum lattice gas model on a cubic lattice for the 3D Dirac equation has, at the "kinetic" level, the particles undergoing mixing during free propagation and is again similar to Bialynicki-Birula's model. Succi discusses the many-body case, but his algorithm runs into an "exponential complexity wall" [Succi, 2002] because it is implemented as a one-body system at the middle-scale.

Boghosian and Taylor followed an approach along the lines of Meyer's approach in that their model is developed as a generalization of the classical lattice gas method. A quantum spin system, now formuated directly at the "sub-scale," again leds to the Schroedinger wave equation at the "super-scale" in the continuum limit. The Boghosian and Taylor quantum lattice gas model focuses on solving the many-body Schroedinger wave equation with an arbitrary scalar potential in an arbitrary number of spatial dimensions. They argue that an exponential numerical speedup arises from simulation in the many-body sector of the full Hilbert space carried out simultaneously using quantum superposition of states. The Boghosian and Taylor version of the quantum algorithm is cast explicitly for direct implementation using an array of quantum bits [Boghosian and IV, 1998b].

Polley has presented an argument for inserting both an external scalar and vector potential into a quantum lattice-gas model by analytically demonstrating the discrete model's invariance with respect to a general local gauge transformation [Polley, 2000].

Zalka proposed an efficient quantum algorithm to model the Schroedinger wave equation with an external scalar potential [Zalka, 1996]. A periodic wave function is mapped onto the numbered basis states of the full Hilbert space of the quantum computer. The numerous Hilbert space dimensions are mapped onto the many coordinates of a quantum system of one spatial dimension. A deficiency of Zalka's approach is that it does not offer a way to measure the time-dependent behavior of the modeled quantum system, because upon observation of the l-bit quantum register, the 2^l number of amplitudes associated with the modeled wave function's values at each spatial coordinate collapse into only l classical bits.

The quantum algorithm in Section 4.4 for the relativistic Dirac equation is suited to direct implementation on a quantum computer using only two-qubit quantum gates and efficiently handles the many-body problem. To encode the relativistic wave function, which is a spinor field, four qubits per spatial coordinate are required. For pedagoical purposes, one can consider the simplest quantum lattice-gas algorithm on a cubic lattice. There exists an improved

version that remedies two difficiencies: the checkerboard problem of non-interacting sublattices and the low-order convergence. The non-relativistic case for modeling the Schroedinger equation is presented in Section 5.

The quantum algorithm can handle the many-body case in a second-quantized representation without any additional computational overhead. Therefore, this is an efficient quantum algorithm for the many-body three-dimensional Dirac equation. Its computational complexity is dominantly linear in the number of qubits used to spatially resolve the 4-spinor wave function. With Q-number of qubits, the number of quantum gate operations needed to model a one-body quantum system is $\sim \alpha Q$, where α is a fixed constant. The efficiency of type I analog computing derives from the fact that exactly same the number of quantum gate operations are needed to model a many-body quantum system, for up to $2Q$ particles.

We can "upgrade" the quantum lattice-gas algorithm for the Schroedinger equation using the external scalar potential as a modeling device: one considers the scalar potential to be a time-dependent dynamical quantity where the spatial dependence of this scalar potential is determined by the value of the modeled wave function. With this scheme, the resulting effective field theory accurately approximates the *nonlinear Schroedinger equation* [Vahala et al., 2003b]. The "external" scalar potential is an intrinsically determined spacetime-dependent quantity, proportional to the probability of particle occupation, the modulus squared of the wave function. The numerical solution to the nonlinear Schroedinger equation has the form of a hyperbolic secant function, which agrees with the analytical solution of the integrable equation of motion.

It is possible to go further and model soliton behavior governed by the Kortweg de Vries equation [Vahala et al., 2003b]. Here the "convective" term $\psi \partial_x \psi$ is modeled using a scalar potential that depends on the spatial gradient of the wave function, which causes the governing effective field theory be a nonlinear one yet again. In the Kortweg de Vies, there is no second-order spatial derivative; instead, there is a third-order spatial derivative. This allows for time-reversibility and is therefore amenable to modeling with a unitary quantum algorithm. By cleverly modifying the particle streaming protocol, it is possible to model a cubic spatial term instead of the usual quadratic term.

We have generalized the quantum algorithm approach to handle vector solitons. We can accurately model the collisional dynamics of the solitons, where the effective field theory of the system is a coupled set of nonlinear Schroedinger equations, known as the *Manakov equations* and is in general nonintegrable [Vahala et al., 2003a]. Two Schroedinger equations can be straightforwardly coupled in a nonlinear way by having the scalar potential of one wave equation depend not only on the value of its own wave function but also on the value of the wave function of the other wave equation, and vice versa. This coupling scheme can

accurately capture the behavior and interaction of two distinct optical pulses, orthogonally polarized to one and another for example, traveling in a birefringent optical fiber. This approach allows us to handle the case of the Manakov system with inelastic soliton collisions [Vahala et al., 2004a].

Chapter 4

The Dirac equation

4.1 Introduction

Finding a simple rule to represent the spacetime quantum mechanical dynamics of a system of Dirac particles in 1+1 dimensions as a discrete path integral, or more accurately as a path summation, is known as the *Feynman chessboard problem* [Feynman and Hibbs, 1965]. In Feynman's notes we see that he first solved this problem in 1946 [Feynman, 1946]. A proof by Jacobson and Schulman of Feynman's solution to this chessboard problem relies on a deep isomorphism between the discrete path integral and the partition function in statistical mechanics of an Ising spin system with nearest-neighbor spin-spin interaction [Jacobson and Schulman, 1984]. The 1+1 dimensional chessboard is a square spacetime lattice with grid sizes Δz and Δt. Feynman's solution is the following: the probability amplitude for a free massive Dirac particle to go from one lattice site to another is represented by summing over all the possible zigzag pathways a particle may travel with velocity $\pm\Delta z/\Delta t$, hopping $\pm\Delta z$ from lattice site to lattice site, continuing forward or reversing direction at each time step Δt. The probability amplitude a particular path contributes to the kernel depends on the number of reversals, or bends, where each bend contributes a multiplicative factor of $i\frac{mc^2\Delta t}{\hbar}$ to the overall probability amplitude associated with the path and where m is the particle mass.

Employing just this rule, the relativistic quantum mechanical evolution is correctly emulated. The Dirac Hamiltonian in 1+1 dimensions is recovered in the continuum limit as the grid resolution becomes infinite: $\Delta z \to 0$ and $\Delta t \to 0$ where the limit is taken such that the ratio $\Delta z/\Delta t$ remains constant, which is interpreted as the speed of light c. The Dirac equation of motion in 1+1 dimensions for a 2-spinor field emerges as the effective field theory in the long wavelength limit. A solution to the chessboard problem is given in Section 4.2, employing the isomorphism between the path summation and the partition function, but also employing the *stream* and *collide* paradigm used in quantum lattice gases to further

simplify matters.

Feynman attempted to find a simple solution to the chessboard problem in 3+1 dimensions, but had no success. Jacobson presented a solution, but his model is unsettling, if not unphysical, because the Dirac particle locally moves faster than the speed of light [Jacobson, 1984]. Furthermore, Jacobson's solution is complicated because it is implemented on a kind of random spacetime lattice and, hence, is neither useful for numerical simulation purposes nor quantum computation. Here we consider a simple solution for 3+1 dimensions where the Dirac particle locally moves at the speed of light and where the solution is directly suited for numerical simulation and quantum computation.

The full problem, checkered in four dimensions instead of on the plane, is the following: Using a spatial body-centered cubic Bravais lattice, show that the probability amplitude for a free massive Dirac particle to go from one lattice site to another, by moving independently and simultaneously along the orthogonal cubic lattice directions with velocity $\pm\Delta x/\Delta t$, $\pm\Delta y/\Delta t$, and $\pm\Delta z/\Delta t$, is equal to the sum of all possible pathways between those sites, where the probability amplitude a particular path contributes to the kernel depends on the number of reversals of motion, or bends, counted by projecting along the orthogonal $\hat{x}$, $\hat{y}$, and $\hat{z}$ axes, where each bend contributes a multiplicative factor of $i\frac{mc^2\Delta t}{D\hbar}$ to the overall probability amplitude associated with the path, and where m is the particle mass and $D = 3$ is the number of spatial dimensions.

Presented in Section 4.3 is a solution that is a straightforward generalization of the 1+1 dimensional solution given in Section 4.2. The key is to designate the quantum mechanical velocity vector of the Dirac particle in terms of the spin components $s_x = \pm 1$, $s_y = \pm 1$, and $s_z = \pm 1$ as follows:

$$\frac{c}{\sqrt{3}}(s_x\hat{x} + s_y\hat{y} + s_z\hat{z}). \tag{4.1}$$

Locally there are only eight possible spin combinations, hence the choice of the body-centered cubic lattice. All the spacetime translational degrees of freedom are specified in terms of the spin variables. The relativistically invariant Dirac system is recovered in the continuum limit as the grid resolution becomes infinite: $\Delta r \to 0$ and $\Delta t \to 0$ where $\Delta r = \Delta x = \Delta y = \Delta z$ and where the limit is taken such that the ratio $\Delta r/\Delta t$ remains constant, which is interpreted as the speed of light c. The Dirac Hamiltonian generating the unitary evolution for the 4-spinor field of a relativistic particle emerges as the effective field theory in the long wavelength.

4.1.1 Relativistic path integral as a type-I quantum algorithm

The basic approach is to use an externally controlled array of qubits to encode the quantum wave function of the modeled quantum system of Dirac particles and to use an engineered

local Hamiltonian to emulate the Dirac Hamiltonian so as to approximate the subsequent time-dependent behavior of the wave function on a spacetime lattice. Two qubits are used per lattice node to model the Dirac equation in 1+1 and 2+1 dimensions and four qubits are used per lattice node to model the Dirac equation in 3+1 dimensions. The 3 dimensional spatial lattice is a body-centered cubic (bcc) lattice. The 3+1 dimensional spacetime lattice is a hyper-bcc lattice.

The final result of the computation is obtained by measuring all Q qubits. To recover the moduli squared of the modeled wave function, an ensemble measurement or repeated measurement is required. The frequency of occurrence is associated with the moduli squared of the wave function. Upon measurement, the probability of finding a "particle" at time t at a lattice node at location $\vec{x}$ is equals the sum of the moduli squared of the excited-energy eigenstate probability amplitudes of the qubits at that quantum node. This probability is called an *occupation probability*.

The local Hamiltonian that emulates the Dirac Hamiltonian has a kinetic energy part related to the motion of qubits and an on-site qubit-qubit interaction part. Both generate the time-dependent dynamics of a discrete amplitude field. The local Hamiltonian is spatially homogeneously applied to the lattice-based amplitude field independently on all the lattice nodes. Each part of the Hamiltonian generates unitary evolution operators:

1. The on-site interaction, represented by a unitary operator $\mathscr{C}$ called the *collision operator*, emulates particle-particle "collisions."

2. Site-to-site exchange, represented by a unitary operator $\mathscr{S}$ called the *stream operator*, emulates local "translation" of particles between neighboring lattice sites.

The quantum mechanical local evolution equation is:

$$|\psi(\vec{x}, t + \Delta t)\rangle = \mathscr{C}\mathscr{S}|\psi(\vec{x}, t)\rangle, \tag{4.2}$$

where $|\psi\rangle$ is local value of the probability amplitude field and where $\mathscr{S}$ causes quantum mechanical streaming. (4.2) is called a *quantum lattice gas equation of motion* and is derived in Section 4.2.4 for the 1+1 dimensional case and in Section 4.3.4 for the 3+1 dimensional case.

In the one particle case, (4.2) can rewritten as follows:

$$|\psi(\vec{x}, t + \Delta t)\rangle = \mathscr{C} \sum_{\vec{c} \in \text{bcc}} M_S |\psi(\vec{x} - \vec{c}, t)\rangle, \tag{4.3}$$

where M_S is a matrix that represents $\mathscr{S}$ on a local stencil of the body-centered cubic (bcc) lattice and the sum is over the eight diagonal neighbors. Then with $\mathscr{C}$ represented by a unitary matrix, (4.3) becomes a finite-difference representation of the Dirac equation.

The first-order numerically convergent version of the quantum algorithm can be expressed as a quantum lattice-gas evolution equation (4.2). In 3+1 dimensions, $\mathscr{S}$ moves each quantum particle located at the lattice site $\vec{x}$ to 8 neighboring sites on the body-centered cubic lattice, which on R.H.S. of (4.3) is notated $\vec{x} - \vec{c}$ [1]. $\mathscr{S}$ is quantum mechanical because a particle moves to multiple locations at each time unit Δt.

In Section 4.4, the unitary matrix representation of the stream and collide quantum mechanical operators are given to specify quantum algorithms for numerically modeling a system of relativistic Dirac particles. The quantum algorithms are distinguished by whether they may handle one or many particles and by their numerical convergence properties. Several quantum algorithms are presented in Section 4.4: one particle algorithms in Section 4.4.1 in the form of (4.3) and many particle algorithms in Section 4.4.2 in the form of (4.2) in the second quantized representation using ladder operators. The structure of $\mathscr{S}$ depends on the number of spatial dimensions of the modeled quantum mechanical system and it can be altered to improve the numerical convergence properties of the quantum algorithm.

The quantum mechanical stream operator is rewritten in terms of a classical stream operator, denoted $S = S_x S_y S_z$ (not to be confused with the action). Each product component operator of S moves a particle along an orthogonal cubic lattice direction. The following identity relating the quantum stream operator to the classical stream operator is proved in Section 4.4.1:

$$\mathscr{S} = e^{i\frac{\pi}{4}\sigma_y^{(2)}} S_x e^{-i\frac{\pi}{4}(\sigma_y^{(2)}+\sigma_x^{(2)})} S_y e^{i\frac{\pi}{4}\sigma_x^{(2)}} S_z. \tag{4.4}$$

As a starting point, in Section 4.4.1, the simplest quantum lattice-gas algorithm on a bcc lattice is treated. This quantum algorithm is a direct transcription of the path summation in Section 4.3. However, this algorithm suffers two difficiencies: the checkboard problem of non-interacting sublattices and only first-order numerical convergence. Therefore, next in Section 4.4.1, an improved version of the quantum algorithm that remedies these deficiencies is presented.

The simulation of many Dirac particles is treated in Section 4.4.2. This quantum algorithm is naturally suited to implementation on a quantum computer using conservative quantum gates. If implemented on this hypothethical quantum computer, it efficiently predicts time-dependendent solutions of the four spinor Dirac field associated with the many-body relativistic system in 3+1 dimensions.

As already mentioned in the overview Chapter 3, the quantum algorithm can handle the many-body Dirac system in a second-quantized representation without any additional computational overhead. The efficiency of the quantum algorithm for the many-body system

[1] Say the net motion is along $\hat{z}$-axis. Then a positive energy particle starting at $(0,0,0)$ moves to the 4 sites $(\pm\Delta x, \pm\Delta y, \Delta z)$ whereas a negative energy particle moves to $(\pm\Delta x, \pm\Delta y, -\Delta z)$.

of Dirac particles in 3+1 dimensions is discussed again in Section 4.1. The kind of exponential speedup is just like that previously shown to occur in quantum lattice-gas algorithms for modeling a many-body system of non-relativistic particles [Boghosian and IV, 1998a].

4.2 1+1 dimensions

4.2.1 Feynman path integral representation of non-relativistic quantum mechanics

The probability amplitude that a quantum particle at position z_a at time t_a will transfer to a new position z_b and time t_b is given by the following path integral:

$$K(z_a t_a; z_b t_b) = \int \mathcal{D}[z(t)] e^{i\frac{S[z(t)]}{\hbar}}, \tag{4.5}$$

where $\int \mathcal{D}[z(t)]$ denotes integration over all trajectories $z(t)$ for which $z(t_a) = z_a$ and $z(t_b) = z_b$, and where the increase of the action

$$S = \int_{t_a}^{t_b} dt L[\dot{z}(t), z(t)], \tag{4.6}$$

along a trajectory $z(t)$ is determined using the classical Lagrangian L.

4.2.2 Path summation representation of relativistic quantum mechanics

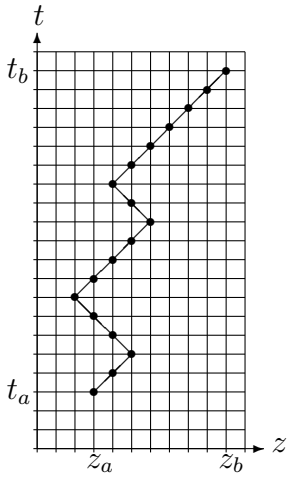

Figure 4.1: Example trajectory of a massive relativistic particle starting at location z_a at time t_a and ending at z_b at time t_b. The total number of steps is $N = 17$, so the elapsed time is $t = 17\Delta t$. The number of steps to the right minus the number to the left is $M = 7$, so the net distance traversed is $z = 7\Delta z$. The relativistic particle moves at the speed of light $c \equiv \Delta z/\Delta t$. The number of bends is $R = 4$.

Feynman [Feynman and Hibbs, 1965] found a discrete representation of the Feynman path integral principle on a square spacetime lattice to compute (4.5) for a relativistic quantum particle:

$$K_{\alpha\beta}(z_a t_a; z_b t_b) = \lim_{N\to\infty} \sum_{R\geq 0} \Phi_{\alpha\beta}(R) \left(i\Delta t \, \frac{mc^2}{\hbar} \right)^R , \tag{4.7}$$

where $\Delta t \equiv \frac{t_b - t_a}{N}$, where α and β are the $\pm$ components of the spinor amplitude field (spin-up or spin-down), $\Phi_{\alpha\beta}(R)$ is the number of paths with N steps and R bends, where the length of each step is $\Delta z \equiv \frac{z_b - z_a}{M} \equiv c\,\Delta t$, where c is the speed of light, and where m is the mass of the quantum particle. An example relativistic trajectory with 4 bends along $\hat{z}$ is depicted in Figure 4.1.

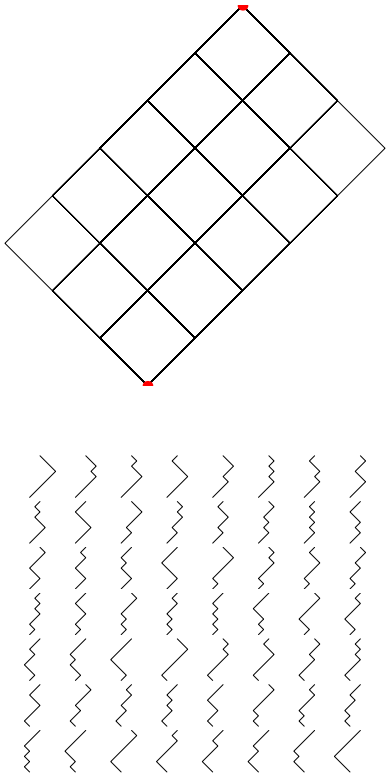

Figure 4.2: Example problem in 1+1 dimensions with $N = 8$ and $M = 2$. (Top) Allowable rectangular region of the square lattice within the light cone, with sides of length $Q = \lceil \frac{N+M}{2} \rceil = 5$ and $P = \lfloor \frac{N-M}{2} \rfloor = 3$. (Bottom) Enumeration of all possible paths, the 56 permutations of the set $(1, 1, 1, 1, 1, -1, -1, -1)$.

The allowable region of the lattice is bounded by the intersection of two light cones, with boundaries $z = \pm c(t - t_a) + z_a$ and $z = \pm c(t - t_b) + z_b$ for $t_a \leq t \leq t_b$ and $z_a \leq z \leq z_b$. One light cone originates at the spacetime point (z_a, t_a) and an inverted light zone terminates at (z_b, t_b), see Figure 4.2. With $z_b - z_a = M\Delta z$ and $t_b - t_a = N\Delta t$, the edges of the allowable rectangular region are given by $P \equiv \lfloor \frac{N-M}{2} \rfloor$ and $Q \equiv \lceil \frac{N+M}{2} \rceil$, for $N \geq M \geq 0$. Hence, the

paths are the permutations of the set with $N = P + Q$ members ± 1:

$$(\underbrace{1, 1, \ldots, 1}_{Q \text{ number of 1's}} \underbrace{-1, -1, \cdots, -1}_{P \text{ number of -1's}}). \tag{4.8}$$

The number of permutations is the binomial coefficient:

$$\text{number of paths} = \binom{P+Q}{P} = \binom{P+Q}{Q}. \tag{4.9}$$

4.2.3 Spin system representation

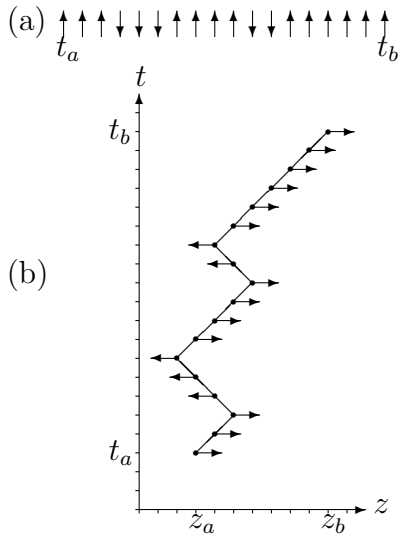

Figure 4.3: (a) Spin representation of the trajectory of a massive relativistic particle starting at time t_a and ending at time t_b for $N = 7$ and $M = 17$. (b) Quantum lattice-gas representation of the same trajectory where the particle is stream-plus (or "spin-up") as it moves to the right and stream-minus (or "spin-down") as it moves to the left. Pre-collision spin orientations are shown.

Because the summation (4.7) occurs on a discrete spacetime lattice, in 1+1 dimensions it is possible to enumerate all the paths originating at point a and ending at point b using $N+1$ spin variables s_i, for $i = 0, 1, 2, \ldots, N$. This is depicted in Figure 4.3a for the example relativistic trajectory. Identifying α with s_0 and β with s_N, the summation (4.7) is equivalent to:

$$K_{s_0 s_N}(z_a t_a; z_b t_b) = \sum_{\{s_1, \ldots, s_{N-1}\}|\mathrm{M}} \left(i \Delta t \, \frac{mc^2}{\hbar} \right)^R, \tag{4.10}$$

where the set $\{s_0, \ldots, s_N\}$ specifies a discrete trajectory with a path length constrained by the condition

$$\sum_{i=0}^{N} s_i = \frac{z_b - z_a}{\Delta z}. \tag{4.11}$$

Since the starting and ending points s_0 ands_N are fixed, they do not appear in the sum on the R.H.S. of (4.10), and the condition (4.11) is equivalent to fixing the spin magnetization $M = \sum_i s_i$ of a system of $N+1$ spins.

At the ith step, the particle continues to move straight when $s_i = s_{i+1}$, and it changes direction when $s_i = -s_{i+1}$. As the particle moves (or *streams*) to the right its spin orientation is "spin-up" and as it moves to the left it is "spin-down," as shown in Figure 4.3b. Therefore, the following binary value counts the occurrence of a bend at the ith step:

$$\frac{1}{2}(1 - s_i s_{i+1}) = \begin{cases} 0, & \text{no bend} \\ 1, & \text{bend.} \end{cases} \tag{4.12}$$

Hence, the following sum counts the total number of bends in a path:

$$R = \frac{1}{2}\sum_{i=0}^{N-1}(1 - s_i s_{i+1}). \tag{4.13}$$

With a change of variables

$$\nu \equiv -\frac{1}{2}\log\left(i\Delta t\,\frac{mc^2}{\hbar}\right), \tag{4.14}$$

(4.10) can be written as the partition function of an ensemble of spins with nearest neighbor coupling and with fixed total magnetization

$$K_{s_0 s_N} = \sum_{\{s_1,\ldots,s_{N-1}\}} \delta\left(M, \sum_i s_i\right)\; e^{-\nu\sum_{i=0}^{N-1}(1-s_i s_{i+1})}, \tag{4.15}$$

where the Kronecker delta $\delta(a,b) = 1$ for $a = b$ and $\delta(a,b) = 0$ for $a \neq b$. We may write the Kronecker delta as follows:

$$\delta\left(M, \sum_{i=0}^{N} s_i\right) = \frac{1}{2N}\sum_{n=-N}^{N-1} e^{i\frac{2\pi n}{N}\left(M - \sum_i s_i\right)}, \tag{4.16}$$

since M and $\sum_{i=0}^{N} s_i$ are integers. Then inserting (4.16) into (4.15) gives

$$K_{s_0 s_N} = \frac{1}{2N}\sum_{n=-N}^{N-1} e^{i\left(\frac{2\pi n}{N}\right)M} \sum_{\{s_1,\ldots,s_{N-1}\}} e^{-i\left(\frac{2\pi n}{N}\right)\sum_{i=0}^{N} s_i - \nu\sum_{i=0}^{N-1}(1-s_i s_{i+1})}. \tag{4.17}$$

Now since $\sum_{i=0}^{N} s_i = \frac{1}{2}(s_0 + s_N) + \frac{1}{2}\sum_{i=0}^{N-1}(s_i + s_{i+1})$, we pull down the summation in the argument of the exponential to form the following product:

$$K_{s_0 s_N} = \frac{1}{2N}\sum_{n=-N}^{N-1} e^{i\left(\frac{2\pi n}{N}\right)M} e^{-i\pi\left(\frac{n}{N}\right)(s_0+s_N)} \sum_{\{s_1,\ldots,s_{N-1}\}} \prod_{i=0}^{N-1} e^{-i\pi\left(\frac{n}{N}\right)(s_i+s_{i+1}) - \nu(1-s_i s_{i+1})}. \tag{4.18}$$

The components of a unitary transfer matrix $\mathscr{U}$ are defined as

$$\mathscr{U}_{s_i,s_{i+1}} \equiv e^{-\nu(1-s_i s_{i+1})-i\pi\left(\frac{n}{N}\right)(s_i+s_{i+1})}, \tag{4.19}$$

so that (4.18) becomes

$$K_{s_0 s_N} = \frac{1}{2N}\sum_{n=-N}^{N-1} e^{i\left(\frac{2\pi n}{N}\right)M} e^{-i\pi\left(\frac{n}{N}\right)(s_0+s_N)}\,\mathscr{Z}_{s_0 s_N}, \tag{4.20}$$

where we have defined

$$\mathscr{Z}_{s_0 s_N} \equiv \sum_{s_1=\pm 1}\cdots\sum_{s_{N-1}=\pm 1}\mathscr{U}_{s_0,s_1}\mathscr{U}_{s_1,s_2}\cdots\mathscr{U}_{s_{N-1},s_N}. \tag{4.21}$$

The matrix form of (4.19) is

$$\mathscr{U} = \begin{pmatrix}\mathscr{U}_{1,1} & \mathscr{U}_{-1,1}\\ \mathscr{U}_{1,-1} & \mathscr{U}_{-1,-1}\end{pmatrix} = \begin{pmatrix}e^{-i2\pi n/N} & e^{-2\nu}\\ e^{-2\nu} & e^{i2\pi n/N}\end{pmatrix} \tag{4.22}$$

and so (4.21) becomes simply an $N-1$ fold matrix multiplication of $\mathscr{U}$:

$$\mathscr{Z} = \begin{pmatrix}\mathscr{Z}_{1,1} & \mathscr{Z}_{-1,1}\\ \mathscr{Z}_{1,-1} & \mathscr{Z}_{-1,-1}\end{pmatrix} = \begin{pmatrix}e^{-i2\pi n/N} & e^{-2\nu}\\ e^{-2\nu} & e^{i2\pi n/N}\end{pmatrix}^N. \tag{4.23}$$

4.2.4 Quantum lattice gas representation

To simplify (4.20), we acknowledge the discrete nature of the spacetime lattice by using the following variable transformations:

$$\frac{2\pi n}{N} = \frac{p_n \Delta z}{\hbar} \qquad z = z_b - z_a = \Delta z M \qquad t = t_b - t_a = \Delta t N, \tag{4.24}$$

where p_n is the discrete momentum. From (4.14), the off-diagonal components of (4.22) are $e^{-2\nu} = i\Delta t\,\frac{mc^2}{\hbar}$, and the transfer matrix (4.22) becomes

$$\mathscr{U} = \begin{pmatrix}1 - i\frac{p_n\Delta z}{\hbar} + \mathcal{O}(\Delta z^2) & i\Delta t\,\frac{mc^2}{\hbar}\\ i\Delta t\,\frac{mc^2}{\hbar} & 1 + i\frac{p_n\Delta z}{\hbar} + \mathcal{O}(\Delta z^2)\end{pmatrix}. \tag{4.25}$$

Our basic approach to formulate the space-time translation degrees of freedom in terms of the spin variables is to partition (4.25) into a product of a temporal matrix and a spatial matrix

$$\mathscr{U} = \mathscr{C}\mathscr{S}, \tag{4.26}$$

where the temporal matrix is called the *collision matrix*

$$\begin{aligned}
\mathscr{C} &= e^{i\sigma_x \frac{mc^2\Delta t}{\hbar}} && (4.27a)\\
&= \begin{pmatrix} \cos\left(\frac{mc^2\Delta t}{\hbar}\right) & i\sin\left(\frac{mc^2\Delta t}{\hbar}\right) \\ i\sin\left(\frac{mc^2\Delta t}{\hbar}\right) & \cos\left(\frac{mc^2\Delta t}{\hbar}\right) \end{pmatrix} && (4.27b)\\
&= \begin{pmatrix} 1 & i\Delta t\,\frac{mc^2}{\hbar} \\ i\Delta t\,\frac{mc^2}{\hbar} & 1 \end{pmatrix} + \mathcal{O}(\Delta t^2) && (4.27c)
\end{aligned}$$

and the spatial matrix is called the *stream matrix*

$$\begin{aligned}
\mathscr{S} &= e^{-i\sigma_z \frac{p_n\Delta z}{\hbar}} && (4.28a)\\
&= \begin{pmatrix} e^{-i\frac{p_n\Delta z}{\hbar}} & 0 \\ 0 & e^{i\frac{p_n\Delta z}{\hbar}} \end{pmatrix} && (4.28b)\\
&= \begin{pmatrix} 1-i\frac{p_n\Delta z}{\hbar} & 0 \\ 0 & 1+i\frac{p_n\Delta z}{\hbar} \end{pmatrix} + \mathcal{O}(\Delta z^2). && (4.28c)
\end{aligned}$$

The decomposition of $\mathscr{U}$ given in (4.26) is a *quantum lattice gas representation* of the transfer matrix. In this construction with $\Delta z = c\Delta t$ where the particles stream through space at a fixed unit velocity equal to the speed of light, (4.23) becomes

$$\begin{aligned}
\mathscr{Z} &= (\mathscr{C}\mathscr{S})^N && (4.29a)\\
&= e^{i(\sigma_x mc^2 - \sigma_z p_n c)N\Delta t/\hbar} + \mathcal{O}(\Delta t^2). && (4.29b)
\end{aligned}$$

Inserting (4.29b) into (4.20), the quantum lattice-gas kernel becomes

$$K_{s_0 s_N} = \frac{1}{2N}\sum_{n=-N}^{N-1} e^{i\frac{p_n z}{\hbar}} e^{-\frac{ip_n\Delta z}{2\hbar}(s_0+s_N)} \left[e^{i(\sigma_x mc^2-\sigma_z p_n c)N\Delta t/\hbar}\right]_{s_0 s_N}. \qquad (4.30)$$

As N approaches infinity in the continuum limit, we can neglect $\Delta z = c\Delta t$ compared with $t = N\Delta t$ (that is, $N \gg c$), so we have

$$K_{s_0 s_N} = \frac{1}{2N}\sum_{n=-N}^{N-1} e^{i\frac{p_n z}{\hbar}} \left[e^{i(\sigma_x mc^2-\sigma_z p_n c)N\Delta t/\hbar}\right]_{s_0 s_N}. \qquad (4.31)$$

In the continuum limit, the summation goes over to an integral ($\frac{1}{N}\sum_n \to \frac{dz}{\hbar}\int dp$) and so we have

$$\begin{aligned}
K_{\alpha\beta}(z,t) &\equiv \lim_{N\to\infty} K_{s_0 s_N} && (4.32a)\\
&= \frac{dz}{2h}\int_{-\infty}^{\infty} dp\, e^{i\frac{pz}{\hbar}} \left[e^{i(\sigma_x mc^2-\sigma_z pc)t/\hbar}\right]_{\alpha\beta}. && (4.32b)
\end{aligned}$$

Our result (4.32) is equivalent to the result found by Jacobson and Schulman [Jacobson and Schulman, 1984] which is rederived in Appendix Section E. Our derivation, based on the quantum lattice gas representation (4.26), is simpler. Furthermore, the quantum lattice gas representation allows us to generalize the derivation to obtain the Dirac equation in 3+1 dimensions.

4.3 3+1 dimensions

4.3.1 Feynman path integral representation of non-relativistic quantum mechanics

The probability amplitude that a quantum particle at position $\vec{r}_a = (x_a, y_a, z_a)$ at time t_a will transfer to a new position $\vec{r}_b = (x_b, y_b, z_b)$ at time t_b is given by the following path integral:

$$K(\vec{r}_a t_a; \vec{r}_b t_b) = \int \mathcal{D}[\vec{r}(t)] e^{i\frac{S[\vec{r}(t)]}{\hbar}} \tag{4.33}$$

where $\int \mathcal{D}[\vec{r}(t)]$ denotes integration over all trajectories $\vec{r}(t)$ for which $\vec{r}(t_a) = \vec{r}_a$ and $\vec{r}(t_b) = \vec{r}_b$, and where the increase of the action

$$S = \int_{t_a}^{t_b} dt\, L[\dot{\vec{r}}(t), \vec{r}(t)], \tag{4.34}$$

along a trajectory $\vec{r}(t)$ is determined using the classical Lagrangian L. Equation (4.33) is a solution of the quantum mechanical wave equation [Feynman, 1948].

4.3.2 Path summation representation of relativistic quantum mechanics

We introduce a discrete representation of the Feynman path integral principle on a body-centered cubic spatial lattice with discrete time steps to compute (4.33) for a relativistic quantum particle:

$$K_{\vec{\alpha}\vec{\beta}}(\vec{r}_a t_a; \vec{r}_b t_b) = \lim_{N\to\infty} \prod_{w=1}^{D} \sum_{R_w \geq 0} \Phi_{\vec{\alpha}\vec{\beta}}(R_w) \left(i\frac{mc^2 \Delta t}{D\hbar} \right)^{R_w}, \tag{4.35}$$

where $\Delta t \equiv \frac{t_b - t_a}{N}$, where $\vec{\alpha}$ and $\vec{\beta}$ represented by initial and final spin vectors of the form (s_x, s_y, s_z) =$(\pm 1, \pm 1, \pm 1)$, where $K_{\vec{\alpha}\vec{\beta}}$ is the kernel of a 4-spinor amplitude field, where the length of each step is $\Delta r \equiv c\,\Delta t$, where c is the speed of light, where m is the mass of the quantum particle, where R_w is the number of bends in a path counted by projecting the path along the $\hat{w}$ axis, and where $\Phi_{\vec{\alpha}\vec{\beta}}(R_w)$ is the number of allowable paths with R_w bends and N steps along the $\hat{w}$ axis, and where D is the number of spatial dimensions. The separation distance between the starting and ending points is:

$$\vec{r}_b - \vec{r}_a = \hat{r}\sqrt{(x_b - x_a)^2 + (y_b - y_a)^2 + (z_b - z_a)^2}. \tag{4.36}$$

An example three dimensional relativistic trajectory with 3 bends along $\hat{x}$ and $\hat{y}$, and 2 bends along $\hat{z}$ is depicted in Figure 4.4 where a bend occurs when the particle changes its direction of motion along any axis. Equation (4.35) reduces to the Feynman chessboard formula (4.7) when $D = 1$.

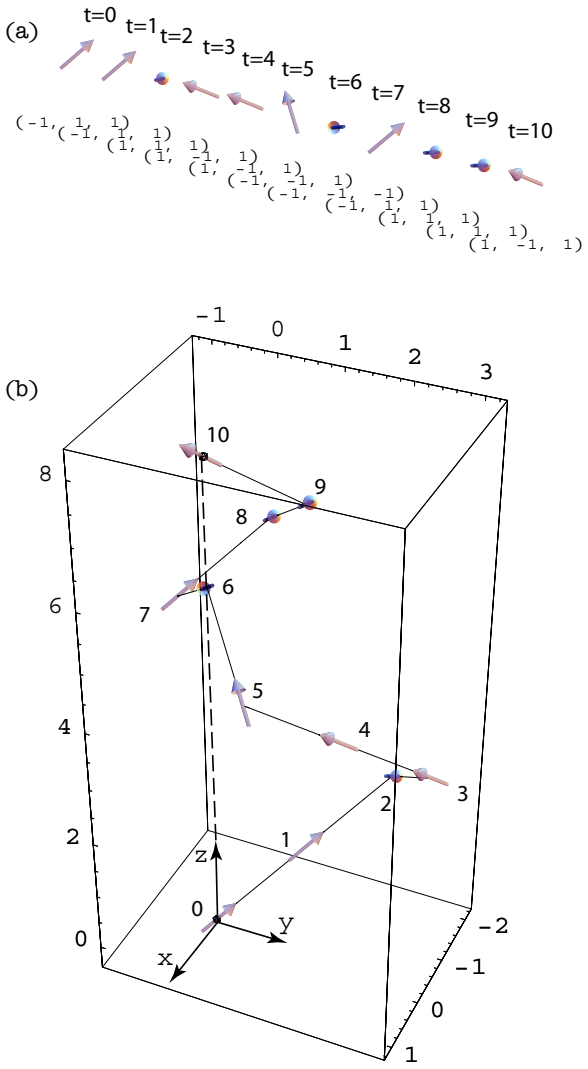

Figure 4.4: (a) Spin representation of the trajectory of a massive relativistic particle. The components of each spin vector are shown. (b) Quantum lattice-gas representation of an example trajectory of a relativistic particle (solid lines). The coordinate system is chosen so that the final displacement (dashed line) is along the $\hat{z}$-axis direction: the particle starts at location $\vec{r}_a = \vec{0}$ at time $t_a = 0$ (labeled "0") and ends at $\vec{r}_b = (8\Delta z)\hat{z}$ at time $t_b = 10\Delta t$ (labeled "10"). The total number of steps is $N = 10$. There are 3 bends along $\hat{x}$ at $t = 2$, $t = 5$, and $t = 8$; 3 bends along $\hat{y}$ at $t = 3$, $t = 7$, and $t = 10$; and 2 bends along $\hat{z}$ at $t = 6\Delta t$ and $t = 7\Delta t$. The particle moves at the speed of light $c = \Delta r/\Delta t$ along three cubic lattice directions simultaneously. The spin at each step specifies the direction of motion for that step. Post-collision spin orientations are shown.

4.3.3 Spin system representation

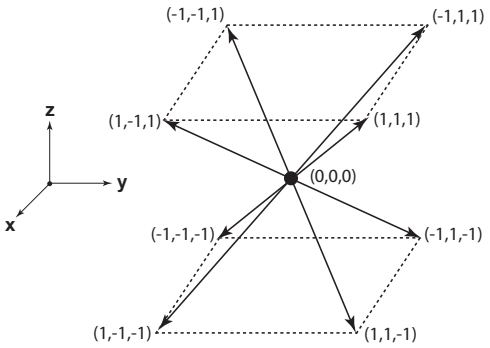

Figure 4.5: Lattice diagonal directions for a body-centered cubic spatial lattice for a quantum particle starting at the origin $\vec{r}_a = (0, 0, 0)$.

With three spatial dimensions, it is possible to enumerate all the paths originating at point $\vec{a}$ and ending at point $\vec{b}$ using $N+1$ spin variables $\vec{s}_n = (s_{xn}, s_{yn}, s_{zn})$, for $n = 0, 1, 2, \ldots, N$, and where $s_{wn} = \pm 1$ for $w = x, y, z$. There are eight distinct spin vectors, one for each direction along a diagonal of the body centered cubic (bcc) lattice $\vec{s}_n = (\pm 1, \pm 1, \pm 1)$. This is depicted in Figure 4.5. Note that $\vec{s}_n$ is a discrete 3-vector whereas the spin vector $\vec{\sigma} = (\sigma_x, \sigma_y, \sigma_z)$ is a 3-vector of 2×2 Pauli matrices. We shall see in the following exactly how and why $\vec{s}$ and $\vec{\sigma}$ are related. The result is that a Dirac particle quantum mechanically moves along a diagonal of the bcc lattice with its spin vector $\vec{\sigma}$ "parallel" to its direction of motion $c\vec{s}$, where D is the spatial dimension.

Identifying $\vec{\alpha}$ with $\vec{s}_0$ and $\vec{\beta}$ with $\vec{s}_N$, the summation (4.35) is equivalent to:

$$K_{\vec{s}_0\vec{s}_N}(\vec{r}_a t_a; \vec{r}_b t_b) = \sum_{\{\vec{s}_1,\ldots,\vec{s}_{N-1}\}|\vec{M}} \left(i\frac{mc^2\Delta t}{D\hbar} \right)^R , \tag{4.37}$$

where $R = \sum_{w=1}^{D} R_w$, where R_w is a bend along the $\hat{w}$ direction, and where the set $\{\vec{s}_0, \ldots, \vec{s}_N\}$ specifies a discrete trajectory with a path length constrained by the condition

$$\sum_{n=0}^{N} \vec{s}_n = \left(\frac{x_b - x_a}{\Delta x}, \frac{y_b - y_a}{\Delta y}, \frac{z_b - z_a}{\Delta z} \right). \tag{4.38}$$

Since the starting and ending points $\vec{s}_0$ and$\vec{s}_N$ are fixed, they do not appear in the sum on the R.H.S. of (4.37), and the condition (4.38) is equivalent to fixing the spin magnetization $\vec{M} = \sum_n \vec{s}_n$ of a system of $N+1$ spins.

At the nth step, the particle continues to move straight when $\vec{s}_n \cdot \vec{s}_{n+1} = D$, reverses direction along on orthogonal axis when $\vec{s}_n \cdot \vec{s}_{n+1} = 1$, reverses directions along two orthogonal

axes when $\vec{s}_n \cdot \vec{s}_{n+1} = -1$, and completely reverses (flips) direction when $\vec{s}_n \cdot \vec{s}_{n+1} = -D$. The following sum counts the occurrence of a bend along the $\hat{w}$ axis at the nth step:

$$\frac{1}{2}[1 - s_{wn}s_{w(n+1)}] = \begin{cases} 0, & \text{no bend along } \hat{w} \\ 1, & \text{bend along } \hat{w}. \end{cases} \tag{4.39}$$

In turn, the following sum counts the total number of bends in a path between $\vec{r}_a$ and $\vec{r}_b$:

$$R = \frac{1}{2}\sum_{w=1}^{D}\sum_{n=0}^{N-1}[1 - s_{wn}s_{w(n+1)}]. \tag{4.40}$$

With a simple generalizational of the change of variables (4.14) used in the one-dimensional case

$$\nu \equiv -\frac{1}{2}\log\left(i\frac{mc^2\Delta t}{D\hbar}\right), \tag{4.41}$$

(4.37) can be written as the partition function of an ensemble of spins with nearest neighbor coupling and with fixed total magnetization $\vec{M} = (M_x, M_y, M_z)$:

$$K_{\vec{s}_0\vec{s}_N} = \sum_{\{\vec{s}_1,\ldots,\vec{s}_{N-1}\}} \delta\left(\vec{M}, \sum_n \vec{s}_n\right) e^{-\nu\sum_{n=0}^{N-1}[D - \vec{s}_n\cdot\vec{s}_{n+1}]}, \tag{4.42}$$

where the Kronecker delta is:

$$\delta\left(\vec{M}, \sum_{n=0}^{N}\vec{s}_n\right) = \prod_{w=1}^{D}\delta\left(M_w, \sum_n s_{wn}\right) = \delta\left(M_x, \sum_n s_{xn}\right)\delta\left(M_y, \sum_n s_{yn}\right)\delta\left(M_z, \sum_n s_{zn}\right), \tag{4.43}$$

where

$$\delta\left(M_x, \sum_n s_{xn}\right) = \frac{1}{2N}\sum_{n_x=-N}^{N-1} e^{i\frac{2\pi n_x}{N}\left(M_x - \sum_n s_{xn}\right)} \tag{4.44a}$$

$$\delta\left(M_y, \sum_i s_{yn}\right) = \frac{1}{2N}\sum_{n_y=-N}^{N-1} e^{i\frac{2\pi n_y}{N}\left(M_y - \sum_n s_{yn}\right)} \tag{4.44b}$$

$$\delta\left(M_z, \sum_i s_{zn}\right) = \frac{1}{2N}\sum_{n_z=-N}^{N-1} e^{i\frac{2\pi n_z}{N}\left(M_z - \sum_n s_{zn}\right)}. \tag{4.44c}$$

The total magnetization is related to the total displacement vector as follows:

$$\vec{x} \equiv (M_x\Delta x, M_y\Delta y, M_z\Delta z). \tag{4.45}$$

Furthermore, the wave number is defined as follows:

$$\vec{k}_{\vec{n}} \equiv \frac{2\pi}{N}\left(\frac{n_x}{\Delta x}, \frac{n_y}{\Delta y}, \frac{n_z}{\Delta z}\right). \tag{4.46}$$

Using (4.45) and (4.46), the Kronecker delta (4.43) becomes

$$\delta\left(\vec{M},\sum_{n=0}^{N}\vec{s}_n\right)=\frac{1}{(2N)^3}\sum_{\vec{n}=(n_x,n_y,n_z)}e^{i\vec{k}_{\vec{n}}\cdot\vec{x}-i\Delta r\sum_n\vec{k}_{\vec{n}}\cdot\vec{s}_n}. \tag{4.47}$$

Then inserting (4.47) into (4.42) gives

$$K_{\vec{s}_0\vec{s}_N}=\frac{1}{(2N)^3}\sum_{\vec{n}}e^{i\vec{k}_{\vec{n}}\cdot\vec{x}}\sum_{\{\vec{s}_1,\ldots,\vec{s}_{N-1}\}}e^{-i\Delta r\sum_{n=0}^{N}\vec{k}_{\vec{n}}\cdot\vec{s}_n-\nu\sum_{n=0}^{N-1}[D-\vec{s}_n\cdot\vec{s}_{n+1}]}. \tag{4.48}$$

We can proceed from (4.48) using the identity $\sum_{n=0}^{N}\vec{s}_n=\frac{1}{2}(\vec{s}_0+\vec{s}_N)+\frac{1}{2}\sum_{n=0}^{N-1}(\vec{s}_n+\vec{s}_{n+1})$, which allows us to pull down the summation in the argument of the exponential to form the following product:

$$K_{\vec{s}_0\vec{s}_N} = \frac{1}{(2N)^3}\sum_{\vec{n}}e^{i\vec{k}_{\vec{n}}\cdot\vec{x}}e^{-\frac{i}{2}\Delta r\vec{k}_{\vec{n}}\cdot(\vec{s}_0+\vec{s}_N)}\sum_{\{\vec{s}_1,\ldots,\vec{s}_{N-1}\}}\prod_{n=0}^{N-1}e^{-\frac{i}{2}\Delta r\vec{k}_{\vec{n}}\cdot(\vec{s}_n+\vec{s}_{n+1})-\nu[D-\vec{s}_n\cdot\vec{s}_{n+1}]} \tag{4.49a}$$

$$= \frac{1}{(2N)^3}\sum_{\vec{n}}e^{i\vec{k}_{\vec{n}}\cdot\vec{x}}e^{-\frac{i}{2}\Delta r\vec{k}_{\vec{n}}\cdot(\vec{s}_0+\vec{s}_N)}\prod_{w=1}^{D}\sum_{\{s_{w1},\ldots,s_{w(N-1)}\}}\prod_{n=0}^{N-1}e^{-\frac{i}{2}\Delta rk_{nw}(s_{wn}+s_{w(n+1)})-\nu(1-s_{wn}s_{w(n+1)})}. \tag{4.49b}$$

As in the one-dimensional case, here again we use a unitary transfer matrix. The components of the transfer matrix $\mathscr{U}$ for the cartesian axis $\hat{w}$ are defined as

$$\mathscr{U}_{s_{wn},s_{w(n+1)}}\equiv e^{-\frac{i}{2}\Delta rk_{nw}(s_{wn}+s_{w(n+1)})-\nu(1-s_{wn}s_{w(n+1)})}, \tag{4.50}$$

then (4.49b) becomes

$$K_{\vec{s}_0\vec{s}_N}=\frac{1}{(2N)^3}\sum_{\vec{n}}e^{i\vec{k}_{\vec{n}}\cdot\vec{x}}e^{-\frac{i}{2}\Delta r\vec{k}_{\vec{n}}\cdot(\vec{s}_0+\vec{s}_N)}\mathscr{Z}_{\vec{s}_0\vec{s}_N}, \tag{4.51}$$

where we have defined

$$\mathscr{Z}_{\vec{s}_0\vec{s}_N}\equiv\prod_{w=1}^{D}\sum_{\{s_{w1},\ldots,s_{w(N-1)}\}}\mathscr{U}_{s_{w0},s_{w1}}\mathscr{U}_{s_{w1},s_{w2}}\cdots\mathscr{U}_{s_{w(N-1)},s_{wN}}. \tag{4.52}$$

The generic sum over all possible spin components in (4.52) can be rewritten explicitly as $N-1$ binary sums:

$$\mathscr{Z}_{\vec{s}_0\vec{s}_N}=\prod_{w=1}^{D}\sum_{s_{w1}=\pm1}\cdots\sum_{s_{w(N-1)}=\pm1}\mathscr{U}_{s_{w0},s_{w1}}\mathscr{U}_{s_{w1},s_{w2}}\cdots\mathscr{U}_{s_{w(N-1)},s_{wN}}. \tag{4.53}$$

The form of (4.53) suggests that we can write the transfer matrix (4.50) for the $\hat{w}$ direction as a 2×2 matrix where the binary sums represent matrix multiplication, just as in the 1+1

dimensional case. However, in accordance with the product $\prod_w$ in (4.53), the sums over the orthogonal cartesian axes $\hat{w}$ directions must be kept independent. The only alternative when enumerating the four spin components, $s_{wn} = \pm 1$ and $s_{w(n+1)} = \pm 1$, is to introduce D number of new token variables, say μ_w, to keep the directional sums independent of each other. The kinetic term $e^{\frac{i}{2}\Delta r k_{nw}(s_{wn}+s_{w(n+1)})}$ in (4.50) contributes to only the diagonal (non-reversal) components in (4.55) when $s_{wn} = s_{w(n+1)}$, and contributes 0 to the non-diagonal (reversal) components when $s_{wn} = -s_{w(n+1)}$. For its diagonal contribution, we take the local translation operator

$$e^{-\frac{i}{2}\Delta r k_{wn}(s_{wn}+s_{w(n+1)})} \rightarrow \begin{cases} e^{-i\Delta r k_{wn}\mu_w} & s_{wn} = 1 \\ & s_{w(n+1)} = 1, \\ e^{i\Delta r k_{wn}\mu_w} & s_{wn} = -1 \\ & s_{w(n+1)} = -1. \end{cases} \tag{4.54}$$

The mass term $e^{-\nu(1-s_{wn}s_{w(n+1)})}$ in (4.50) contributes 0 to the diagonal (non-reversal) components in (4.55) when $s_{wn} = s_{w(n+1)}$ and contributes $e^{-2\nu}$ to the non-diagonal (reversal) components when $s_{wn} = -s_{w(n+1)}$. Hence, (4.50) is written in 2×2 matrix form as follows:

$$\mathscr{U}_w = \begin{pmatrix} \mathscr{U}_{1,1} & \mathscr{U}_{-1,1} \\ \mathscr{U}_{1,-1} & \mathscr{U}_{-1,-1} \end{pmatrix} = \begin{pmatrix} e^{-i\Delta r k_{wn}\mu_w} & e^{-2\nu} \\ e^{-2\nu} & e^{i\Delta r k_{wn}\mu_w} \end{pmatrix}. \tag{4.55}$$

Notice we have no need to employ a token variable that depends on w for the off-diagonal components of (4.55) since the term $e^{-2\nu}$ for each $\hat{w}$ direction contributes equally to the mass of the Dirac particle. That is, since bends in the $\hat{x}$, $\hat{y}$, or $\hat{z}$ directions equally contribute to the particle's mass, all the $e^{-2\nu}$ components in (4.51) may add together. So we can omit using another token variable for the off-diagonal terms.

With (4.55), we see that (4.53) is simply an $N-1$ fold matrix multiplication of $\mathscr{U}$:

$$\mathscr{Z} = \begin{pmatrix} \mathscr{Z}_{1,1} & \mathscr{Z}_{-1,1} \\ \mathscr{Z}_{1,-1} & \mathscr{Z}_{-1,-1} \end{pmatrix} = \prod_{w=1}^{D} \begin{pmatrix} e^{-i\Delta r k_{wn}\mu_w} & e^{-2\nu} \\ e^{-2\nu} & e^{i\Delta r k_{wn}\mu_w} \end{pmatrix}^N. \tag{4.56}$$

At this point, we have not yet determined a specific form of the object μ_w. This will be determined in the next section.

4.3.4 Fourier transform of the Dirac propagator

Just as we had previously in the one-dimensional case, we can rewrite (4.51) using momentum variables. Along with (4.45) and (4.46), we have the following variable transformations:

$$p_{wn} \equiv \hbar k_{wn} \qquad t = t_b - t_a = \Delta t N. \tag{4.57}$$

From our change of variables (4.14), the off-diagonal components of (4.55) are $e^{-2\nu} = i\Delta t\,\frac{mc^2}{D\hbar}$, and the transfer matrix (4.55) becomes

$$\mathscr{U}_w = \begin{pmatrix} e^{-i\Delta r\frac{p_{wn}\mu_w}{\hbar}} & i\Delta t\,\frac{mc^2}{D\hbar} \\ i\Delta t\,\frac{mc^2}{D\hbar} & e^{i\Delta r\frac{p_{wn}\mu_w}{\hbar}} \end{pmatrix} \tag{4.58a}$$

$$= e^{-i\sigma_z\mu_w p_{wn}\Delta r/\hbar} + i\sigma_x\frac{mc^2}{D\hbar}\Delta t, \tag{4.58b}$$

where σ_x and σ_z are Pauli matrices.

As in the 1+1 dimensional case, our basic approach here is to represent the spacetime translation degrees of freedom in terms of the spin variables by writing (4.58b) as a product of a collision matrix and a stream matrix

$$\mathscr{U}_w = e^{-i\sigma_z\mu_w p_{wn}\Delta r/\hbar}e^{i\sigma_x\frac{mc^2}{D\hbar}\Delta t} \tag{4.59a}$$

$$= \mathscr{C}\mathscr{S}_w, \tag{4.59b}$$

where in the 3+1 dimensional case we now have

$$\mathscr{C} \equiv e^{i\sigma_x\frac{mc^2}{D\hbar}\Delta t} \tag{4.60}$$

and

$$\mathscr{S}_w \equiv e^{-i\sigma_z\mu_w p_{wn}\Delta r/\hbar}. \tag{4.61}$$

Inserting (4.59) into (4.56), we have

$$\mathscr{Z} = \prod_{w=1}^{D}(\mathscr{C}\mathscr{S}_w)^N \tag{4.62a}$$

$$= \prod_{w=1}^{D} e^{-\frac{i}{\hbar}\left(\sigma_z\mu_w p_{wn}c - \sigma_x\frac{mc^2}{D}\right)N\Delta t}. \tag{4.62b}$$

Now with (4.57), we have

$$\mathscr{Z}(t) = \prod_{w=1}^{D} e^{-\frac{i}{\hbar}\left(\sigma_z\mu_w p_{wn}c - \sigma_x\frac{mc^2}{D}\right)t}. \tag{4.63}$$

We impose a physical constraint on $\mathscr{Z}(t)$ in (4.63) that the quantum mechanical propagation of a Dirac particle be factorable in time as follows:

$$\mathscr{Z}(t_1 + t_2) = \mathscr{Z}(t_2)\mathscr{Z}(t_1). \tag{4.64}$$

Let us square the propagator by choosing $t_1 = t$ and $t_2 = t$ so by inserting (4.63) into (4.64) we have

$$\begin{aligned}\prod_{w=1}^{D} e^{-\frac{i}{\hbar}\left(\sigma_z \mu_w p_{wn} c - \sigma_x \frac{mc^2}{D}\right) 2t} &= \left(\prod_{w=1}^{D} e^{-\frac{i}{\hbar}\left(\sigma_z \mu_w p_{wn} c - \sigma_x \frac{mc^2}{D}\right) t}\right)\left(\prod_{w=1}^{D} e^{-\frac{i}{\hbar}\left(\sigma_z \mu_w p_{wn} c - \sigma_x \frac{mc^2}{D}\right) t}\right) \quad (4.65)\\ &= \left(1 - \sum_{w=1}^{D} \frac{i}{\hbar}\left(\sigma_z \mu_w p_{wn} c - \frac{\sigma_x mc^2}{D}\right) t + \cdots\right)\\ &\quad \times \left(1 - \sum_{w'=1}^{D} \frac{i}{\hbar}\left(\sigma_z \mu_{w'} p_{w'n} c - \frac{\sigma_x mc^2}{D}\right) t + \cdots\right),\end{aligned}$$

where in the Taylor expansions on the R.H.S we must keep all high order terms since, in the continuum limit, $t = \lim_{N\to\infty} N\Delta t$ is not a small parameter. The only way for the L.H.S. to equal the R.H.S. is for the all the cross-terms to vanish. Now, all the cross-terms between the momentum and time components automatically vanish because of the anti-commutation of the Pauli matrices σ_z and σ_x. However, for all the cross-terms between the momentum components to vanish requires our token variables μ_w be anti-commuting Grassman variables:

$$\mu_i \mu_j + \mu_j \mu_i = 0, \tag{4.66}$$

for $1 \leq i \leq D$ and $1 \leq j \leq D$. We are free to represent the μ_w variables in terms of Pauli matrices by choosing

$$\mu_w \to \sigma_w. \tag{4.67}$$

In this representation, $\mathscr{C}$ and $\mathscr{S}$ become 4×4 matrices. The collision operator is

$$\begin{aligned}\mathscr{C} &= \prod_{w=1}^{D} e^{i\sigma_x \otimes \mathbf{1} \frac{mc^2 \Delta t}{D\hbar}} = e^{i\sigma_x \otimes \mathbf{1} \frac{mc^2 \Delta t}{\hbar}} && (4.68a)\\ &= \begin{pmatrix} \cos\left(\Delta t \frac{mc^2}{\hbar}\right) & i\sin\left(\Delta t \frac{mc^2}{\hbar}\right) \\ i\sin\left(\Delta t \frac{mc^2}{\hbar}\right) & \cos\left(\Delta t \frac{mc^2}{\hbar}\right) \end{pmatrix} \otimes \mathbf{1} && (4.68b)\\ &= \begin{pmatrix} \mathbf{1} & i\Delta t \frac{mc^2}{\hbar}\mathbf{1} \\ i\Delta t \frac{mc^2}{\hbar}\mathbf{1} & \mathbf{1} \end{pmatrix} + \mathcal{O}(\Delta t^2) && (4.68c)\\ &= \begin{pmatrix} 1 & 0 & i\Delta t \frac{mc^2}{\hbar} & 0 \\ 0 & 1 & 0 & i\Delta t \frac{mc^2}{\hbar} \\ i\Delta t \frac{mc^2}{\hbar} & 0 & 1 & 0 \\ 0 & i\Delta t \frac{mc^2}{\hbar} & 0 & 1 \end{pmatrix}, && (4.68d)\end{aligned}$$

and the stream operator is

$$\mathscr{S} = \prod_{w=1}^{D} e^{-\frac{i}{\hbar}\sigma_z\otimes\sigma_w p_{wn}c\Delta t} = e^{-\frac{i}{\hbar}\sigma_z\otimes\vec{\sigma}\cdot\vec{p}_{\vec{n}}c\Delta t} = \begin{pmatrix} e^{-\frac{i}{\hbar}\sigma\cdot\vec{p}_{\vec{n}}c\Delta t} & 0 \\ 0 & e^{\frac{i}{\hbar}\vec{\sigma}\cdot\vec{p}_{\vec{n}}c\Delta t} \end{pmatrix} \tag{4.69a}$$

$$= \begin{pmatrix} \mathbf{1} - \frac{i\Delta r}{\hbar}\vec{\sigma}\cdot\vec{p}_{\vec{n}} & 0 \\ 0 & \mathbf{1} + \frac{i\Delta r}{\hbar}\vec{\sigma}\cdot\vec{p}_{\vec{n}} \end{pmatrix} + \mathcal{O}(\Delta r^2) \tag{4.69b}$$

$$= \begin{pmatrix} 1 - \frac{i\Delta r p_{zn}}{\hbar} & -\frac{i\Delta r(p_{xn}-ip_{yn})}{\hbar} & 0 & 0 \\ -\frac{i\Delta r(p_{xn}+ip_{yn})}{\hbar} & 1 + \frac{i\Delta r p_{zn}}{\hbar} & 0 & 0 \\ 0 & 0 & 1 + \frac{i\Delta r p_{zn}}{\hbar} & \frac{i\Delta r(p_{xn}-ip_{yn})}{\hbar} \\ 0 & 0 & \frac{i\Delta r(p_{xn}+ip_{yn})}{\hbar} & 1 - \frac{i\Delta r p_{zn}}{\hbar} \end{pmatrix}. \tag{4.69c}$$

Equation (4.69) is not diagonal and therefore it is a quantum mechanical stream operator; a single particle moves from one place to multiple places in one time Δt. Even a wave function of a massless particle will undergo dispersion. So a quantum particle does not have a single trajectory since its position continually spreads out as it moves. This is compatible with the Heisenberg uncertainty principle [2].

Finally, using (4.68a) and (4.69a), and neglecting terms proportional to $\frac{\Delta r}{N} \ll \Delta t$, the kernal (4.62b) becomes the following three dimensional discrete Fourier transform:

$$K_{\vec{\sigma}_0\vec{\sigma}_N} = \frac{1}{(2N)^3}\sum_{\vec{n}} e^{i\frac{\vec{p}_{\vec{n}}\cdot\vec{x}}{\hbar}}\left[e^{-\frac{i}{\hbar}\left(\sigma_z\otimes\sigma\cdot\vec{p}_{\vec{n}}c-\sigma_x\otimes\mathbf{1}mc^2\right)t}\right]_{\vec{\sigma}_0\vec{\sigma}_N}. \tag{4.70}$$

In the continuum limit, we recover the kernel

$$K_{\vec{\alpha}\vec{\beta}} = \frac{dx^3}{(2h)^3}\int dp^3 e^{i\frac{\vec{p}\cdot\vec{x}}{\hbar}}\left[e^{-\frac{i}{\hbar}H_{\text{Dirac}}t}\right]_{\vec{\alpha}\vec{\beta}}, \tag{4.71}$$

where the Dirac Hamiltonian is

$$H_{\text{Dirac}} = \sigma_z\otimes\vec{\sigma}\cdot pc - \sigma_x\otimes 1mc^2. \tag{4.72}$$

[2] Niels Bohr objected to Feynman's talk at the 1948 Pocono conference for the reason that the classical paths Feynman was enumerating were not consistent with the Heisenberg uncertainty principle [Schweber, 1986]. With our 3+1 dimensional solution, we see from (4.69) that Bohr's objective could have been resolved by answering that the path integral formalism *does* accommodate the notion of path spreading, consistent with the Heisenberg uncertainty principle. However, Feynman used the viewpoint referred to as "calculate and shut-up" in response to Bohr (the quote now attributed to David Mermin). By that time although Feynman had worked out relativistic QED in 3+1 dimensions, he had only worked out discrete spacetime pictures of the particle motion for the 1+1 dimensional square lattice, where the translation is classical.

4.4 Quantum algorithms

4.4.1 One particle quantum simulations

Finite-difference equation in 1+1 dimensions

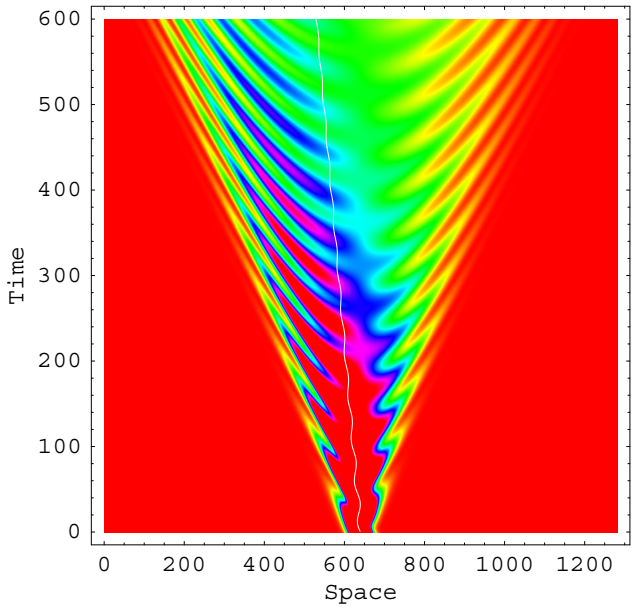

Figure 4.6: Simulation of one relativistic quantum particle with $m = 1$, $\hbar = 1$, $\Delta z = 1$ and $\Delta t = 1$. Plotted is the sum of the moduli squared of the spinor components, $|\alpha|^2 + |\beta|^2$, using (4.77). The average location of the quantum particle oscillates in time (white curve).

According to (4.26), a single time step of the evolution of the relativistic spinor field $\psi = \begin{pmatrix} \alpha \\ \beta \end{pmatrix}$ is accomplished as follows:

$$\psi(t + \Delta t) = \mathscr{C}\mathscr{S}\psi(t). \tag{4.73}$$

The first step is to analyze the streaming part of (4.73). To do this, we write (4.28) as

$$\mathscr{S}\psi(z,t) = e^{-i\sigma_z \frac{p_n \Delta z}{\hbar}} \psi(z,t), \tag{4.74}$$

which in matrix form is

$$\mathscr{S} \begin{pmatrix} \alpha(z,t) \\ \beta(z,t) \end{pmatrix} \simeq \begin{pmatrix} 1 - \Delta z \partial_z & 0 \\ 0 & 1 + \Delta z \partial_z \end{pmatrix} \begin{pmatrix} \alpha(z,t) \\ \beta(z,t) \end{pmatrix}, \tag{4.75}$$

where the momentum operator is taken to be $p_n \to -i\hbar\partial_z$. (4.75) as written is exact only in the continuum limit. It follows that a consistent definition of the streaming operator for the discrete lattice is:

$$\mathscr{S} \begin{pmatrix} \alpha(z,t) \\ \beta(z,t) \end{pmatrix} \equiv \begin{pmatrix} \alpha(z - \Delta z, t) \\ \beta(z + \Delta z, t) \end{pmatrix}. \tag{4.76}$$

Taylor expanding the R.H.S. of (4.76) about z and keeping only the first-order terms, we recover (4.75). There is a geometric interpretation of (4.76) where the α component of the spinor field at node z streams (or hops) to the neighboring node on the "right" at node $z-\Delta z$ and the β component streams to node $z+\Delta z$ on the "left," as depicted in Figure 4.3b.

The second step is to analyze the collision part of (4.73). Substituting (4.27) and (4.76) into (4.73), we have

$$\begin{pmatrix}\alpha(z,t+\Delta t)\\ \beta(z,t+\Delta t)\end{pmatrix} = \begin{pmatrix}\cos\left(\frac{mc^2\Delta t}{\hbar}\right) & i\sin\left(\frac{mc^2\Delta t}{\hbar}\right)\\ i\sin\left(\frac{mc^2\Delta t}{\hbar}\right) & \cos\left(\frac{mc^2\Delta t}{\hbar}\right)\end{pmatrix}\begin{pmatrix}\alpha(z-\Delta z,t)\\ \beta(z+\Delta z,t)\end{pmatrix}. \tag{4.77}$$

An example simulation using (4.77) is shown in Figure 4.6. Simulations of this sort have been carried out by Thaller [Thaller, 2004]. Taylor expanding the collision operator to first-order in Δt, we have

$$\begin{pmatrix}\alpha(z,t+\Delta t)\\ \beta(z,t+\Delta t)\end{pmatrix} = \begin{pmatrix}1 & i\Delta t\,\frac{mc^2}{\hbar}\\ i\Delta t\,\frac{mc^2}{\hbar} & 1\end{pmatrix}\begin{pmatrix}\alpha(z-\Delta z,t)\\ \beta(z+\Delta z,t)\end{pmatrix}. \tag{4.78}$$

Upon multiplying out the R.H.S. and Taylor expanding about z and t, to first-order, we have

$$\Delta t\partial_t\begin{pmatrix}\alpha(z,t)\\ \beta(z,t)\end{pmatrix} = -\sigma_z\Delta z\partial_z\begin{pmatrix}\alpha(z,t)\\ \beta(z,t)\end{pmatrix} + i\Delta t\frac{mc^2}{\hbar}\sigma_x\begin{pmatrix}\alpha(z,t)\\ \beta(z,t)\end{pmatrix}, \tag{4.79}$$

which is the Dirac equation in one spatial dimension

$$i\hbar\partial_t\psi(z,t) = \left(\sigma_z pc - mc^2\sigma_x\right)\psi(z,t). \tag{4.80}$$

We can write (4.80) in propagator form

$$\psi(t) = e^{-i\hat{H}t/\hbar}\psi(0), \tag{4.81}$$

where the Hamiltonian is

$$\hat{H} = \sigma_z pc - mc^2\sigma_x, \tag{4.82}$$

This derivation of the Dirac Hamiltonian by the quantum lattice-gas method is consistent with (4.32) where the Feynman path integral expressed as the following Fourier transformation:

$$K(z,t) = \frac{dz}{2\hbar}\int_{-\infty}^{\infty} dp\; e^{i\frac{pz}{\hbar}}\; e^{-i\hat{H}t/\hbar}. \tag{4.83}$$

Finite-difference equation in higher dimensions

The wave function is specified on a spacetime lattice with grid spacing

$$Dc^2\Delta t^2 - \Delta x^2 - \Delta y^2 - \Delta z^2 = 0. \tag{4.84}$$

The local evolution equation of motion is

$$\psi' = \mathscr{S}\mathscr{C}\psi \tag{4.85a}$$

$$= \mathscr{S}_x\mathscr{S}_y\mathscr{S}_z\mathscr{C}\psi \tag{4.85b}$$

$$= e^{\sum_{i=1}^{3}\sigma_z\otimes\sigma_i\Delta r\partial_i}e^{i\frac{mc^2}{\hbar}\Delta t\sigma_x\otimes\mathbf{1}}\psi, \tag{4.85c}$$

which approximates the Dirac equation in the continuum limit and in the relativistic limit where $\hbar\omega \sim mc^2$ and $\hbar k \sim mc$.

The 4×4 matrix

$$\sigma_z\otimes\sigma_z = \begin{pmatrix} 1 & 0 & 0 & 0 \\ 0 & -1 & 0 & 0 \\ 0 & 0 & -1 & 0 \\ 0 & 0 & 0 & 1 \end{pmatrix}, \tag{4.86}$$

operating with the z spatial derivative in (4.85c) is diagonal whereas the matrices $\sigma_z\otimes\sigma_x$ and $\sigma_z\otimes\sigma_y$ for the x and y partial derivatives, respectively, are not diagonal.

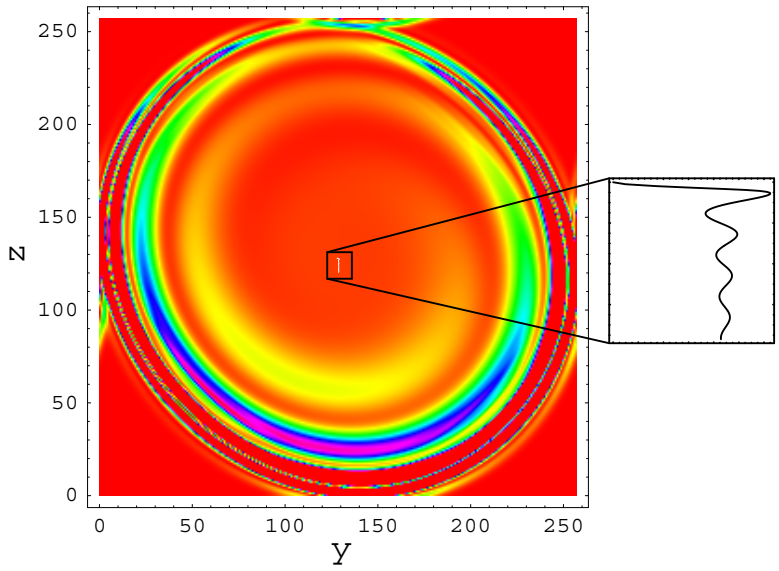

Figure 4.7: Simulation of one relativistic quantum particle with $m = 1$, $\hbar = 1$ in 2+1 dimensions ($\Delta y = 1$, $\Delta z = 1$ and $\Delta t = 1$). Plotted is the sum of the moduli squared of the spinor components, $|\alpha|^2 + |\beta|^2$, at time $t = 128\Delta t$. The mean value of the position of the quantum particle oscillates in time (white curve in center and black curve in the expanded view on the right).

We would like to transform $\mathscr{S}$ in (4.85) in such a way that all the matrices operating with the spatial partial derivatives are diagonal (and hence correspond to shifting qubits along the orthogonal lattice directions). To do this, we need the two identities:

$$e^{-i\frac{\pi}{4}\sigma_x}e^{\varepsilon\sigma_z}e^{i\frac{\pi}{4}\sigma_x} = e^{\varepsilon\sigma_y} \qquad e^{i\frac{\pi}{4}\sigma_y}e^{\varepsilon\sigma_z}e^{-i\frac{\pi}{4}\sigma_y} = e^{\varepsilon\sigma_x}, \tag{4.87}$$

that follow from $e^{i\frac{\pi}{4}\sigma_i} = \frac{1}{\sqrt{2}}(1 + i\sigma_i)$. Then, using the identity $\mathbf{1} \otimes e^{i\theta a} = e^{i\theta \mathbf{1}\otimes a}$, the 2-spinor similarity transformations (4.87) can be generalized to 4-spinor transformatons

$$\left(\mathbf{1} \otimes e^{-i\frac{\pi}{4}\sigma_x}\right) e^{\varepsilon\sigma_z\otimes\sigma_z} \left(\mathbf{1} \otimes e^{i\frac{\pi}{4}\sigma_x}\right) = e^{\varepsilon\sigma_z\otimes\sigma_y} \tag{4.88a}$$

$$\left(\mathbf{1} \otimes e^{i\frac{\pi}{4}\sigma_y}\right) e^{\varepsilon\sigma_z\otimes\sigma_z} \left(\mathbf{1} \otimes e^{-i\frac{\pi}{4}\sigma_y}\right) = e^{\varepsilon\sigma_z\otimes\sigma_x}, \tag{4.88b}$$

which we will use to diagonalize the x and y components of $\mathscr{S}$. Using (4.88) and defining

$$\mathscr{X}_\theta^{(1)} \equiv e^{i\theta\sigma_x} \otimes \mathbf{1} = \begin{pmatrix} \cos\theta & 0 & i\sin\theta & 0 \\ 0 & \cos\theta & 0 & i\sin\theta \\ i\sin\theta & 0 & \cos\theta & 0 \\ 0 & i\sin\theta & 0 & \cos\theta \end{pmatrix}, \tag{4.89a}$$

$$\mathscr{X}_\theta^{(2)} \equiv \mathbf{1} \otimes e^{i\theta\sigma_x} = \begin{pmatrix} \cos\theta & i\sin\theta & 0 & 0 \\ i\sin\theta & \cos\theta & 0 & 0 \\ 0 & 0 & \cos\theta & i\sin\theta \\ 0 & 0 & i\sin\theta & \cos\theta \end{pmatrix}, \tag{4.89b}$$

and

$$\mathscr{Y}_\theta^{(2)} \equiv \mathbf{1} \otimes e^{i\theta\sigma_y} = \begin{pmatrix} \cos\theta & \sin\theta & 0 & 0 \\ -\sin\theta & \cos\theta & 0 & 0 \\ 0 & 0 & \cos\theta & \sin\theta \\ 0 & 0 & -\sin\theta & \cos\theta \end{pmatrix}, \tag{4.89c}$$

and

$$S = S_x S_y S_z \equiv e^{\sigma_z\otimes\sigma_z \Delta r \nabla}, \tag{4.90}$$

where $S_w \equiv e^{\sigma_z\otimes\sigma_z\Delta r\partial_w}$, the product components of $\mathscr{S} = \mathscr{S}_x\mathscr{S}_y\mathscr{S}_z$ can be written

$$\mathscr{S}_x = e^{\sigma_z\otimes\sigma_x\Delta r\partial_x} = \mathscr{Y}_{\frac{\pi}{4}}^{(2)} S_x \mathscr{Y}_{\frac{\pi}{4}}^{(2)\dagger} \tag{4.91a}$$

$$\mathscr{S}_y = e^{\sigma_z\otimes\sigma_y\Delta r\partial_y} = \mathscr{X}_{\frac{\pi}{4}}^{(2)\dagger} S_y \mathscr{X}_{\frac{\pi}{4}}^{(2)} \tag{4.91b}$$

$$\mathscr{S}_z = e^{\sigma_z\otimes\sigma_z\Delta r\partial_x} = S_z, \tag{4.91c}$$

so (4.85) can be rewritten as the following quantum algorithm:

$$\psi' = \mathscr{Y}_{\frac{\pi}{4}}^{(2)} S_x \mathscr{Y}_{\frac{\pi}{4}}^{(2)\dagger} \mathscr{X}_{\frac{\pi}{4}}^{(2)\dagger} S_y \mathscr{X}_{\frac{\pi}{4}}^{(2)} S_z \mathscr{X}_{\frac{mc^2\Delta t}{\hbar}}^{(1)} \psi. \tag{4.92}$$

The quantum algorithm (4.92) has local qubit-qubit interaction operators $\mathscr{X}_{\frac{\pi}{4}}^{(2)}$, $\mathscr{Y}_{\frac{\pi}{4}}^{(2)}$ and $\mathscr{C} = \mathscr{X}_{\frac{mc^2\Delta t}{\hbar}}^{(1)}$ (quantum collision operators), as well as cubic lattice translation operators S_x, S_y, and S_z (classical stream operators). It is demonstrated in 2+1 dimensions for a single massive Dirac particle, see Figure 4.7.

For numerical purposes in the one particle case, the discrete amplitude field is:

$$\psi(\vec{x}, t) = \begin{pmatrix} \alpha(\vec{x}, t) \\ \beta(\vec{x}, t) \\ \mu(\vec{x}, t) \\ \nu(\vec{x}, t) \end{pmatrix}, \tag{4.93}$$

where the spacetime point $(\vec{x}, t)$ coincides with the nodes of a hypercubic lattice with grid size Δr. The operators S_w induce a finite displacement

$$S_w\psi(\vec{x}) = \psi\left(\vec{x} + \Delta r(\sigma_z \otimes \sigma_z)_{ww}\hat{w}\right) \tag{4.94}$$

of the components of the 4-spinor only along lattice directions:

$$S_x\psi(x,y,z) = \begin{pmatrix} \alpha(x+\Delta r, y, z) \\ \beta(x-\Delta r, y, z) \\ \mu(x-\Delta r, y, z) \\ \nu(x+\Delta r, y, z) \end{pmatrix}, \tag{4.95a}$$

$$S_y\psi(x,y,z) = \begin{pmatrix} \alpha(x, y+\Delta r, z) \\ \beta(x, y-\Delta r, z) \\ \mu(x, y-\Delta r, z) \\ \nu(x, y+\Delta r, z) \end{pmatrix}, \tag{4.95b}$$

and

$$S_z\psi(x,y,z) = \begin{pmatrix} \alpha(x, y, z+\Delta r) \\ \beta(x, y, z-\Delta r) \\ \mu(x, y, z-\Delta r) \\ \nu(x, y, z+\Delta r) \end{pmatrix}. \tag{4.95c}$$

These streaming operators are data shifting operators causing permutations of the components of the 4-spinor wave function across the lattice. The collision operators act independently on each node of the lattice and cause local quantum entanglement between component pairs of the 4-spinor. The streaming operators in turn propagate this local on-site entanglement to next nearest neighbors so that eventually quantum entanglement covers the entire lattice.

It is possible to rewrite (4.92) as a finite difference equation on a body-centered cubical lattice. The resulting set of coupled finite difference equations are similar to the finite difference representation of the 3D Dirac equation given by Bialynicki-Birula in 1994 [Bialynicki-Birula, 1994]. A drawback of expressing the algorithm as a finite-difference equation is its unsuitability for a quantum computer implementation using two-qubit quantum gates whereas our manifestly unitary expression (4.92) is suitable.

A continuous effective field theory for $\psi = (\alpha, \beta, \mu, \nu)$ follows in the continuum limit of the emergent finite-difference equations by Taylor expanding in the small grid sizes. We

obtain

$$\partial_t \begin{pmatrix} \alpha \\ \beta \\ \mu \\ \nu \end{pmatrix} = \frac{\Delta r}{\Delta t}\partial_x \begin{pmatrix} -\beta \\ -\alpha \\ \nu \\ \mu \end{pmatrix} + i\frac{\Delta r}{\Delta t}\partial_y \begin{pmatrix} \beta \\ -\alpha \\ -\nu \\ \mu \end{pmatrix} + \frac{\Delta r}{\Delta t}\partial_z \begin{pmatrix} \alpha \\ -\beta \\ -\mu \\ \nu \end{pmatrix} - i\frac{mc^2}{\hbar} \begin{pmatrix} \mu \\ \nu \\ \alpha \\ \beta \end{pmatrix} + \mathcal{O}(c\Delta r, \Delta t), \tag{4.96}$$

which is exactly the Dirac equation

$$\partial_t \psi = c \sum_i \sigma_z \otimes \sigma_i \partial_i \psi - i\sigma_x \otimes 1 \frac{mc^2}{\hbar}\psi, \tag{4.97}$$

when $\Delta t \sim \Delta r \sim \varepsilon$ are infinitesimal and when the partial derivative with respect to time is defined as $\partial_t \psi \equiv \lim_{\Delta t \to 0} \frac{\psi' - \psi}{\Delta t}$. Equation (4.92) gives rise to perfectly unitary evolution of the discrete wave function and, therefore, is an unconditionally stable numerical algorithm. The quantum algorithm (4.92) for modeling (4.96) is less than first-order convergent; see Fig. 5.2. For practical numerical purposes, we will need to modify (4.92) to improve the algorithm's convergence properties.

Improved finite-difference equation in 3+1 dimensions

Our basic approach to improving the accuracy of the quantum algorithm is to set the grid size Δr to be smaller than the Compton wavelength $\lambda = \frac{h}{mc}$ of the modeled particle

$$\Delta r \sim \varepsilon \frac{h}{mc}, \tag{4.98}$$

and to introduce a small temporal scale that is much smaller than $\frac{\lambda}{c}$

$$\Delta t \sim \varepsilon^2 \frac{h}{mc^2}. \tag{4.99}$$

The diffusive ordering condition of spatial and temporal fluctuations typical of random walk processes, $\Delta r^2 = \nu \Delta t$, provides a context to understand the scaling behavior of the small parameter ε. According to (4.98) and (4.99), the diffusive transport coefficient is $\nu = \frac{h}{\varepsilon m}$ and the unit lattice velocity is $\frac{\Delta r}{\Delta t} = \frac{c}{\varepsilon}$, which approaches infinity as $\varepsilon \to 0$. In this limit, the mean velocity of the modeled quantum particle is relatively small, compared to $\Delta r / \Delta t$, hence the resulting effective field theory corresponds to the non-relativistic limit of the Dirac equation as $\varepsilon \to 0$.

To diagonalize the stream operators in (4.91), we used a fixed and finite rotation angle $\frac{\pi}{4}$ independent of the grid resolution. We will now diagonalize the stream operators using

a small rotation angle proportional to Δt. By (4.99), the rotation angle is $\theta = \frac{mc^2\Delta t}{h} = \varepsilon^2$, which is dependent on the grid resolution. The displacement operators in the Dirac equation can be represented by interleaving stream and collision operators on a cubical lattice as follows:

$$\mathscr{S}_x = e^{\sigma_z \otimes \sigma_x \Delta r \partial_x} \rightarrow S^{2,4}_{-x} \mathscr{Y}^{(2)}_{\frac{\varepsilon}{2}} S^{2,4}_{x} \mathscr{Y}^{(2)\dagger}_{\frac{\varepsilon}{2}} S^{1,3}_{x} \mathscr{Y}^{(2)}_{\frac{\varepsilon}{2}} S^{1,3}_{-x} \mathscr{Y}^{(2)\dagger}_{\frac{\varepsilon}{2}} \tag{4.100}$$

and

$$\mathscr{S}_y = e^{\sigma_z \otimes \sigma_y \Delta r \partial_y} \rightarrow S^{2,4}_{-y} \mathscr{X}^{(2)\dagger}_{\frac{\varepsilon}{2}} S^{2,4}_{y} \mathscr{X}^{(2)}_{\frac{\varepsilon}{2}} S^{1,3}_{y} \mathscr{X}^{(2)\dagger}_{\frac{\varepsilon}{2}} S^{1,3}_{-y} \mathscr{X}^{(2)}_{\frac{\varepsilon}{2}}, \tag{4.101}$$

where the superscripts on the streaming operators refer to individual components of the 4-spinor. For example, the classical streaming operators in (4.95) are $S_w = S^{2,3}_{-w} S^{1,4}_{w}$. The quantum stream operators (4.91a) and (4.91b) are now redefined in terms of the respective component-wise classical stream operators separated by collision operators according to (4.100) and (4.101). This kind of interleaving of streaming and collision operators removes the spurious checkerboard effect of independent sublattice dynamics that otherwise occurs [Yepez, 2001b, Yepez and Boghosian, 2002]. So far we treated the non-diagonal quantum stream operators $e^{\sigma_z \otimes \sigma_x \Delta r \partial_x}$ and $e^{\sigma_z \otimes \sigma_y \Delta r \partial_y}$, but not the classical operator $e^{\sigma_z \otimes \sigma_z \Delta r \partial_z}$ because no such improvement exists since it is diagonal. However, if instead of using the Dirac matrix $\sigma_z \otimes \sigma_z$, we use an alternative non-diagonal representation for the z-direction partial derivative, then we can again employ interleaving. Therefore, we consider the following alternate form of the Dirac equation:

$$\partial_t \psi = c\sigma_z \otimes \sigma_x \partial_x \psi + c\sigma_z \otimes \sigma_y \partial_y \psi + c\sigma_y \otimes \mathbf{1} \partial_z \psi - i\sigma_x \otimes 1 \frac{mc^2}{\hbar} \psi. \tag{4.102}$$

Now the quantum stream operator in (4.102) for the z-direction can be re-expressed in a fashion similar to (4.100) and (4.101) as

$$\mathscr{S}_z \equiv e^{\sigma_y \otimes \mathbf{1} \Delta r \partial_z} \rightarrow S^{2,3}_{z} \mathscr{X}^{(1)}_{\frac{\varepsilon}{2}} S^{2,3}_{-z} \mathscr{X}^{(1)\dagger}_{\frac{\varepsilon}{2}} S^{1,4}_{z} \mathscr{X}^{(1)}_{\frac{\varepsilon}{2}} S^{1,4}_{-z} \mathscr{X}^{(1)\dagger}_{\frac{\varepsilon}{2}}. \tag{4.103}$$

Then instead of (4.91), we use (4.100), (4.101), and (4.103) for an improved quantum algorithm

$$\psi(t + \Delta t) = \mathscr{S}_x \mathscr{S}_y \mathscr{S}_z \psi(t). \tag{4.104}$$

In the interleaved algorithm (4.104), the mass term in the Dirac equation is automatically produced at order ε^2.

It is possible to derive a finite-difference equation representation of the quantum lattice-gas algorithm (4.104) by carrying out all the collision and streaming operations symbolically. The result expressed as a finite-difference equation is no longer expressible using a stencil including only the nearest neighbors of the body-centered cubic lattice. Nevertheless, once

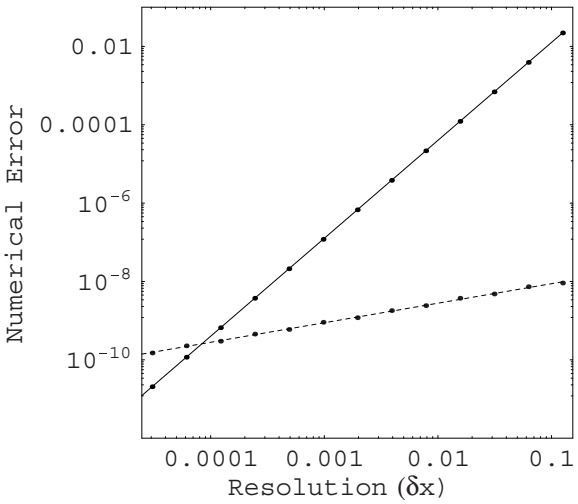

Figure 4.8: L2 norm error $\sqrt{\frac{1}{L}\sum_{i=1}^{L}[|\psi(x_i)|^2 - |\psi_{\text{ex}}(x_i)|^2]}$ plotted versus grid resolution $\Delta x = \frac{1}{L}$ for numerical simulations of the 1D Weyl equation (Dirac equation with $m = 0$) with lattice sizes from $L = 8$ to $L = 32768$. The error curve's slope is 0.5 for the original algorithm (dashed line) and 2.5 for the improved algorithm (solid line). This demonstrates the high numerical accuracy of the improved (symmetrized and interleaved) quantum algorithm.

again, a continuous effective field theory, in the one-particle sector of the Hilbert space, for $\psi = (\alpha, \beta, \mu, \nu)$ follows in the continuum limit as we Taylor expand in Δr and in Δt:

$$\begin{aligned} \partial_t \begin{pmatrix} \alpha \\ \beta \\ \mu \\ \nu \end{pmatrix} &= \frac{\Delta r}{\Delta t}\partial_x \begin{pmatrix} -\beta \\ -\alpha \\ \nu \\ \mu \end{pmatrix} + i\frac{\Delta r}{\Delta t}\partial_y \begin{pmatrix} \beta \\ -\alpha \\ -\nu \\ \mu \end{pmatrix} \\ &+ i\frac{\Delta r}{\Delta t}\partial_z \begin{pmatrix} -\mu \\ -\nu \\ \alpha \\ \beta \end{pmatrix} + i\frac{mc^2}{\hbar} \begin{pmatrix} \mu \\ \nu \\ \alpha \\ \beta \end{pmatrix} + \mathcal{O}(\Delta r^4, \Delta t^2), \end{aligned} \tag{4.105}$$

which approximates the Dirac equation (4.102) when Δt is small. In (4.105), according to symbolic mathematics, the mass term arises at order ε^2, the spatial terms arise at order ε^3, and the error terms arise at order ε^4. Yet, according to numerical simulations, the effective field theory (4.105) is first-order convergent. With the quantum stream operator $\mathscr{S} = \mathscr{S}_x\mathscr{S}_y\mathscr{S}_z$, we define the dual operator $\tilde{\mathscr{S}} \equiv \mathscr{S}_{-x}^\dagger\mathscr{S}_{-y}^\dagger\mathscr{S}_{-z}^\dagger$, by taking the adjoint of the quantum stream operators and reversing the displacement directions. Then, it is possible use a symmetrized evolution operator [Yepez and Boghosian, 2002]

$$\psi(t + \Delta t) = \tilde{\mathscr{S}}\mathscr{S}e^{-\zeta\Delta t^2}\psi(t), \tag{4.106}$$

where ζ is a constant parameter. According to numerical simulation, the interleaved and

symmetrized algorithm (4.106) is better than second-order convergent, as demonstrated in Fig. 5.2 for the 1+1 dimensional case.

4.4.2 Many particle quantum simulations

A useful characteristic of the quantum algorithm to model a many-body system of Dirac particles is that it uses the same protocol for local collisions and local translations used to model the dynamical behavior of the one-body problem governed by the Dirac equation. Therefore, the computational overhead associated with the action of the unitary operators is fixed for both the one-body and many-body cases. What differs is the number of quantum states (configurations of qubits) that must be dealt with in the numerical simulation.

To model all the dynamics of many Dirac particles, we use an interfering set of probability amplitudes defined on the lattice. All these probability amplitudes, considered as an ordered finite set of complex numbers, constitutes a discrete amplitude field with 2^Q complex components for a quantum computer with Q qubits. With 4 qubits per node on a body-centered cubic lattice with $V = L^3$ nodes, the quantum state of the system is the following tensor product:

$$|\Psi(t)\rangle = \bigotimes_{q=1}^{4} \bigotimes_{x=1}^{L} \bigotimes_{y=1}^{L} \bigotimes_{z=1}^{L} |q(x,y,z,t)\rangle. \tag{4.107}$$

The quantum algorithm amounts to unfolding a quantum mechanical evolution operator into an ordered sequence on 2-qubit quantum gate operations. We have analytically determined an accurate approximation of the local Hamiltonian, say $\mathscr{H}_n$ for the nth lattice site, finding it to be the Dirac Hamiltonian $\sigma_z \otimes \vec{\sigma} \cdot \vec{p}c + \sigma_x \otimes \mathbf{1}mc^2$ with momentum $\vec{p} = (p_x, p_y, p_z)$ and the Pauli spin matrices $\vec{\sigma} = (\sigma_x, \sigma_y, \sigma_z)$. The Dirac Hamiltonian is an effective local Hamiltonian. The total system Hamiltonian $\mathcal{H}$ formally generates the quantum mechanical evolution:

$$\mathcal{U} = e^{-i\mathcal{H}\Delta t/\hbar} = \bigotimes_{n=0}^{N} e^{-i\mathscr{H}_n \Delta t/\hbar}, \tag{4.108}$$

represented by a $2^Q \times 2^Q$ matrix. An analytical expression of $\mathcal{H}$ could have an infinite number of terms due to the Campbell-Baker-Hausdorff theorem and the noncommutability of the quantum gates ($[\mathscr{H}_n, \mathscr{H}_m] \neq 0$). Nevertheless, this is a crucial feature of the quantum algorithm: it is possible to numerically compute an accurate approximation of $\mathcal{H}$, a *many-body Dirac Hamiltonian*, as a total system generator of the spacetime evolution. It is in this sense that the quantum algorithm is isomorphic to a Feynman path summation.

In general, the quantum mechanical evolution is expressed as a Schrödinger propagation equation as follows:

$$|\Psi(t+\tau)\rangle = \mathcal{U}|\Psi(t)\rangle. \tag{4.109}$$

Equation (4.109) has an implied operator ordering that must be retained in the quantum algorithmic representation. $\mathcal{U}$ depends on the local unitary operator $\mathscr{U} = \mathscr{C}\mathscr{S}$, which changes the probability amplitudes on each node independently. So the L^3-fold tensor product over the lattice nodes is the total quantum system evolution operator:

$$\mathcal{U} = \bigotimes_{\ell=1}^{L^3} \mathscr{C}\mathscr{S}. \tag{4.110}$$

Therefore, the specifying the many-particle form of the quantum algorithms (4.92) and (4.106) entails representing $\mathscr{S}$ and $\mathscr{C}$ in (4.110) in terms of conservative and local 2-qubit quantum gates. This is accomplished using fermionic ladder operators in a second quantized representation.

With $\hat{a}_\alpha^\dagger$, $\hat{a}_\alpha$, and $\hat{n} = \hat{a}_\alpha^\dagger \hat{a}_\alpha$ denoting the fermionic creation, annihilation, and number operator, respectively, of the αth qubit ($1 \leq \alpha \leq 4L^3$), the collision operators (4.89) are the following:

$$\begin{aligned} \mathscr{X}_{\alpha\beta}(\theta) &= \mathbf{1} - i\sin\theta(\hat{a}_\alpha^\dagger \hat{a}_\beta + \hat{a}_\beta^\dagger \hat{a}_\alpha) + (\cos\theta - 1)(\hat{n}_\alpha + \hat{n}_\beta) \\ &\quad -2\cos\theta \hat{n}_\alpha \hat{n}_\beta \qquad (4.111a) \\ \mathscr{Y}_{\alpha\beta}(\theta) &= \mathbf{1} + \sin\theta(\hat{a}_\alpha^\dagger \hat{a}_\beta - \hat{a}_\beta^\dagger \hat{a}_\alpha) + (\cos\theta - 1)(\hat{n}_\alpha + \hat{n}_\beta) \\ &\quad -2\cos\theta \hat{n}_\alpha \hat{n}_\beta, \qquad (4.111b) \end{aligned}$$

where α and β index different qubits at the same site [Yepez, 2001a]. Then (4.89) are rewritten as

$$\begin{aligned} \mathscr{X}_\theta^{(1)} &\to \mathscr{X}_{13}(\theta)\mathscr{X}_{24}(\theta) \qquad (4.112a) \\ \mathscr{X}_\theta^{(2)} &\to \mathscr{X}_{12}(\theta)\mathscr{X}_{34}(\theta) \qquad (4.112b) \\ \mathscr{Y}_\theta^{(2)} &\to \mathscr{Y}_{12}(\theta)\mathscr{Y}_{34}(\theta). \qquad (4.112c) \end{aligned}$$

$2L^3$ applications of either $\mathscr{X}_{\alpha\beta}$ or $\mathscr{Y}_{\alpha\beta}$ are required for a single collision step.

Streaming occurs by successive application of the interchange operator [Yepez, 2001a]

$$\hat{S}_{\mu\nu} = \mathbf{1} + \hat{a}_\mu^\dagger \hat{a}_\nu + \hat{a}_\nu^\dagger \hat{a}_\mu - \hat{n}_\mu + \hat{n}_\nu. \tag{4.113}$$

$(L-1)^3$ number of applications of $\hat{S}_{\mu\nu}$ (μ refers to one qubit-component at some site and ν to the same component at its neighboring site) are required to stream each qubit along a cubic lattice direction.

The total evolution operator $\hat{E}$ is the product of collision operators $\mathscr{X}$ and $\mathscr{Y}$ and streaming operator S corresponding to algorithm (4.92) or some variant of (4.104) depending on the desired degree of numerical accuracy.

With the new ket $|\Psi'(t+\Delta t)\rangle = \hat{E}|\Psi(t)\rangle$, the resulting probability of finding a particle at site $\vec{x}$ is

$$P(\vec{x}) = \sum_{i=1}^{4} \langle \Psi' | \hat{n}_{\alpha+i} | \Psi' \rangle, \tag{4.114}$$

where α is the index of the first qubit at $\vec{x}$.

With 4 qubits per node, the local propagator $\mathscr{U}$ is represented by a 16×16 size matrix. This appears to be larger than necessary, because there are only 4 component to a Dirac spinor. However, for the purpose of being able to model a many-body quantum system, we require one qubit for each component of the Dirac spinor.

One may strive to execute the maximum possible number of quantum gates in parallel to save physical time in the actual implementation because of the experimental limitations due to de-phasing related to spin-spin decoherence and spin relaxation. The issue of operator ordering is handled intrinsically by the quantum algorithm in the case when quantum gates are applied in parallel to different and non-overlapping pairs of qubits.

Algorithmic complexity

Algorithmic variant	Eq. No.	$2\rho_c$	ρ_s	Total Ops.
Standard	(4.92)	10	12	22
Interleaved	(4.104)	24	24	48
Symmetrized interleaved	(4.106)	49	48	97

Table 4.1: Summary of the number of local quantum gate operation per node.

To quantify the algorithmic complicity associated with evolving the modeled quantum wave function by one unit time Δt, we count the total number of required basic quantum logic operations. We count each conservative collide operator, $\mathscr{X}$ and $\mathscr{Y}$ defined in (4.111), as one basic quantum logic operation. So according to (4.112), the quantum mechanical collide operators each take 2 basic quantum logic operations. Furthermore, we count the operation (4.113) of streaming a single qubit between neighboring nodes as one basic quantum logic operation. That is, streaming a single component of the Dirac spinor along one orthogonal lattice direction (cubic lattice vector) counts as one quantum logic operation.

The algorithmic complexity for numerical simulations a system of Dirac particles in 3+1 dimensions for one time step scales as $C = 2\rho_c L^3 + \rho_s (L-1)^3$, where ρ_c and ρ_s are the number of operations per node for collisions and streaming, respectively. This measure of the algorithmic complexity counts the total number of quantum gate operations required to updated the modeled wave function, whether or not those operations are performed in a serial or parallel fashion. For the simplest algorithm (4.92), $\rho_c = 5$ and $\rho_s = 12$, and for the

improved algorithm (4.104), $\rho_c = 12$ and $\rho_s = 24$. Both ρ_c and ρ_s double when we use a symmetrized rule like (4.106) but are a fixed-cost overhead. With $Q = 4L^3$ qubits, the size of the Hilbert space is exponential 2^Q, whereas the complexity $C = \frac{\rho_c}{2}Q + \rho_s[Q - \frac{3}{4}(2Q)^{\frac{2}{3}} + \frac{3}{2}(2Q)^{\frac{1}{3}} - 1]$ for all the variants of our quantum algorithm is dominantly linear in Q.

4.5 Summary

A solution of Feynman's chessboard problem in 3+1 dimensions was presented. With this result, we have shown how to design a quantum algorithm suitable for implementation on a quantum computer to accurately model one or more Dirac particles. In the one-body case, the mechanical wave equation is the Dirac equation (or Weyl equation in the case when $m = 0$). We say the quantum computer performs analog computation because it relies on one physical quantum mechanical system (a system of qubits with only local qubit-qubit interaction) to model another physical quantum mechanical system, a relativistic Dirac system. Each qubit contained within the quantum computer is embodied by a two-level quantum system, such as a spin-$\frac{1}{2}$ nucleus. Every quantum logic gate operation between local qubit pairs may be embodied by a local interaction Hamiltonian, say a secular dipolar Hamiltonian for the spin-spin coupling.

The initial state of a quantum node is an unequally weighted superposition of states over the Hilbert space of that node, generated by tipping, or rotating, each qubit of the quantum node independently. The quantum algorithm approximates a spatially continuous wave function using a numerical grid with finite resolution, and that provides a natural cut-off. From the point-of-view of the modeler, there exists a small numerical grid-level scale below the physical microscopic scale of the modeled quantum mechanical system.

Through the combined actions of the unitary collision and translation operators, all the quantum mechanical pathways of the possible motions of the modeled quantum particles are numerically treated. The numerical model can be viewed as a kind of kinetic system of locally interacting spins on the small grid-level scale. There also exists a large scale, which corresponds to the long wavelength limit of the dynamical modes in the discrete spin system. This numerical large scale is equivalent to the physical microscopic scale where the many-body wave function of the modeled quantum mechanical system in question is well defined. A continuous wave function is accurately approximated as one approaches the continuum limit where the grid resolution of the spatial lattice become infinite (the lattice cell size approaches zero). In the long wave length limit, the dynamical amplitude field is both continuous and differentiable in space and time. An emergent effective field theory, such as (4.96) or (4.105), is analytically determined by Taylor expanding a finite-difference equation representation of

the dynamics. What is physical in the model is the finite-difference equation. That is, it is this finite-difference equation that governs the dynamical amplitude field. The effective field theory, such as (4.96) or (4.105), is actually a partial differential equation of infinite order. Only the low-order time and space partial derivatives are numerically relevant during the early stage of evolution of the wave function and all the higher order partial derivatives are considered error terms during this early stage.

4.5.1 Final remarks

The method can be used to analytically derive the relativistic Hamiltonian for a small number of Dirac particles. For example, the few-body Hamiltonians, and the associated coupled set of partial differential equations of motion, will be presented in a subsequent paper. In any case, to be a practical and useful algorithm, it must have at least second-order convergence which means that decreasing the grid cell size by a factor of two causes the numerical error inherent in the algorithm to decrease by a factor of four. We have demonstrated it is possible to improve the numerical convergence of the quantum algorithmic method to meet this requirement.

All the qubits in the quantum computer must remain phase-coherent, *i.e.* globally entangled, over the entire course of the quantum computation. In any practical experimental implementation, this quantum algorithm may therefore require the use of extra qubits to correct for bit-flip and phase errors [Shor, 1995, Knill et al., 1998], significantly increasing the number of required qubits per node.

Quantum logical operations are embodied in the spin-spin coupling mechanism, or some other mathematically equivalent two-qubit coupling mechanism appropriate to the particular experimental realization. The form of a naturally occurring interaction Hamiltonian can be effectively altered by applying appropriately timed spin rotations using externally applied electromagnetic pulses, whose frequency, strength, polarization, and pulse duration depends on the particular experimental realization, so that the natural coupling along with the program of externally applied pulses together cause the desired quantum lattice-gas collision operation [Pravia et al., 2002, Pravia et al., 2003, Chen et al., 2006a] [3].

In relativistic formuatlions one typically sees space and time as intrinsically coupled, yet the quantum algorithm presented here based on local stream and collide operators rigidly seems to enforce a Galilean-like separation between space and time–space and time are geometrically coupled in a regular lattice structure. Yet since the fundamental stream and

[3] A subsequent paper will address how to use nuclear magnetic resonance spectroscopy of a solid-state crystal with a secular dipolar Hamiltonian for two spin-$\frac{1}{2}$ nuclei to emulate both the quantum lattice-gas collision and stream operators for numerically predicting space-time dependent solutions for the wave function of a system of Dirac particles.

collide operators do not commute, the continuous Lorentz transformations of special relativity emerge in the long-wave length limit. Furthermore, the dynamical equation of motion governing the continuous four spinor field modeled by this method remains invariant under the Lorentz transformation, but only in the continuum limit. The four spinor field may be treated as a continuous Dirac field in the case when the lattice has infinite resolution (this is, when the lattice cell size is infinitesimal). So any Galilean-like separation can occur only at a very small scale. If the operative relativistic quantum mechanical evolution is generated by the Dirac Hamiltonian, leading to an effective field theory perfectly first order in its space and time derivatives, then the small scale (lattice cell size) must be infinitesimal, and hence it would always be beyond experimental detectably. However, if a discrete sub-lattice were a physical property of spacetime, and it had a finite cell size (perhaps on the order of the Planck scale), then there may be physical significance to the hyper bcc spacetime lattice. It remains an outstanding open problem to determine whether or not it is possible experimentally to measure any lattice property of spacetime, such as a fundamental grid size.

Chapter 5

The Schroedinger equation

5.1 Introduction

In quantum lattice-gas algorithms, the quantum wave function, whether for a single quantum particle or a many-body system of quantum particles, is resolved on a computational grid (a Bravais lattice). The finite grid size of the lattice provides a cut-off regulation to the modeled quantum theory, stabilizing the model by removing high k-modes. The evolution operator governing the time-dependent behavior of the wave function is cast in terms of three unitary operators locally applied in time-step fashion: (1) a homogeneous stream operator for the site-to-site hopping of the particles, (2) a homogeneous collision operator for the on-site particle-particle interactions, and (3) an inhomogeneous gauge operator for particle-field interactions.

With the first two spatially independent (homogeneously applied) stream and collide operators alone, we recover free linear quantum wave equations. With the third spatially dependent (inhomogeneously applied) gauge operation, we go much further to model nonlinear quantum systems: many-body dynamics in an external potential and an internally generated potential. Hence, we find the quantum lattice gas algorithm is well suited to modeling soliton dynamics. The external spatially varying scalar potential is modeled as a gauge rotation fixed over time at each lattice site and where the phase angle of rotation is site dependent. The internal nonlinear mean-field scalar potential is modeled as a gauge rotation dependent on the local value of the ground state wave function, a mean-field treatment. That is, the gauge rotation varies over time and space in a nonlinear way.

We introduce the type-I quantum lattice-gas algorithm for modeling the Schroedinger wave equation by starting in Section 5.2 with the simplest case of a single free particle in a one-dimensional space [Yepez and Boghosian, 2002]. This is the limiting case of the Dirac equation considered in Chapter 4. Here the kinetic energy of the modeled quantum particle is much much less than its rest energy. In this nonrelativistic case, the wave function $\psi(x,t)$

obeys the following partial differential equation in the position representation

$$i\hbar\frac{\partial\psi(x,t)}{\partial t} = -\frac{\hbar^2}{2m}\frac{\partial^2\psi(x,t)}{\partial x^2}, \tag{5.1}$$

where $\hbar$ is Planck's constant and m is the mass of the quantum particle. Here $\psi(x,t)$ is a continuous probability amplitude field (e.g. a complex scalar field).

The nonlinear Schroedinger (NLS) equation is one of the most basic equations of nonlinear physics. Its salient feature is that it emits soliton solutions by exact integration. Hence, it plays a vital role in weakly nonlinear systems with the dispersion relation dependent on the wave amplitude. The NLS equation is pivotal in nonlinear optics [Kivshar and Agrawal, 2003], plasma physics [Infeld and Rowlands, 2000] as well as in ideas for information transfer in optical computers [Jakubowski et al., 1998, Jakubowski et al., 2001]. In 1+1 dimensions, both the focusing and defocusing NLS equations are exactly integrable and exhibit soliton solutions. Tests of the 1+1 dimensional quantum lattice gas algorithm for the NLS equation [Vahala et al., 2003b] and the vector Manakov system [Vahala et al., 2004a] have been published. In Section 5.3, we present the quantum lattice representation of the (focusing) NLS equation in 2+1 dimensions

$$i\hbar\frac{\partial\psi(x,y,t)}{\partial t} + \frac{\partial^2\psi(x,y,t)}{\partial x^2} + \frac{\partial^2\psi(x,y,t)}{\partial y^2} + 2|\psi|^2\psi = 0. \tag{5.2}$$

as a generalization of the quantum lattice representations in 1+1 dimensions. In particular, we shall consider the transverse modulational instability of the one-dimensional soliton wave train solution $\psi_\circ(x,t)$ of (5.2).

In the quantum lattice algorithm for the Schrödinger equation, at each spatial node, the wave function is represented by the interference sum of probability amplitudes of the upper excited state of each qubit. In the quantum algorithm for the NLS equation in 1+1 dimensions, 2 qubits per node are used, and collisional interaction is induced by the unitary $\sqrt{SWAP}$ quantum logic gate. The $\sqrt{SWAP}$ quantum gate has been implemented experimentally using two qubits per computational node in a quantum lattice gas model of the diffusion equation [Pravia et al., 2002, Pravia et al., 2003, Siskind et al., 2005]. This entanglement is then spread throughout the lattice by the unitary streaming operator, which is real. In extending the algorithm to 2+1 dimensions, still only 2 qubits per node are required and the $\sqrt{SWAP}$ still represents local qubit-qubit interactions. If implemented on a platform using future quantum information processing device technology, the quantum algorithm presented here is suited for a type-I quantum computer architecture, as described in this Quantum Computation for Physical Modeling (QCPM) special issue in §IA of [Yepez, 2005], but with local nonlinear interactions inherent in the quantum device.

Finally, as a straightforward generalization of the quantum algorithm in 2+1 dimensions, in this Section 5.4 we present the quantum algorithm for the Schroedinger equation in 3+1 dimensions:

$$i\hbar\frac{\partial\psi(\vec{x},t)}{\partial t} = -\frac{\hbar^2}{2m}\nabla^2\psi(\vec{x},t) + V(\vec{x},t)\psi(\vec{x},t). \tag{5.3}$$

5.2 1+1 dimensions

5.2.1 Qubit representation for a single free particle

Encoding the wave function

To "program" a quantum computer to simulate (5.3), it is necessary to first formulate an encoding scheme where a collection of qubits is used to store the value of the wave function. Since the number of qubits in any quantum computer is necessarily a finite number, the wave function will have to be approximated in the usual way by representing a physically continuous amplitude field as an artificially discrete and finite set of complex numbers. To do this, let us begin with a one-dimensional spatial lattice with L number of nodes. With each node of the lattice we associate a position basis ket denoted by $|x_l\rangle$, where $0 \geq l \geq L-1$. The discrete system ket in the position basis is

$$|\psi\rangle = \sum_{l=0}^{L-1} c_l|x_l\rangle, \tag{5.4}$$

where $c_l = \langle x_l|\psi\rangle$ is a complex number. In other words, the basic approach to model the single particle wave function governed by (5.3) is to express $|\psi\rangle$ as a sum of all the possible ways the particle can be situated on the lattice with a probability amplitude c_l associated with each possible location $|x_l\rangle$.

In our model, we assign two qubits to each node of the lattice, for a total of $2L$ qubits in the whole quantum computer. The qubits that reside at the lth node of the lattice are denoted by $|q_0^l\rangle$ and $|q_1^l\rangle$ and they are used to encode the coefficient c_l of (5.4) of the position ket for that node. Each qubit is a two-level quantum system $|q_a^l\rangle = \alpha_a^l|0\rangle + \beta_a^l|1\rangle$, where $|\alpha_a^l|^2 + |\beta_a^l|^2 = 1$ for $a = 0$ or 1 and $0 \geq l \geq L-1$. We consider each qubit to be a container that may or may not be occupied by the quantum particle. The quantum particle is said to *occupy* the ath local state at position x_l when $\beta_a^l = 1$. Similarly, the ath local state at position x_l is said to be *empty* when $\beta_a^1 = 0$.

To see how the qubit encoding works, we write $|\psi\rangle$ in the number representation. In the number representation, each basis state is expressible as the ket $|n_0^0 n_1^0 n_0^1 n_1^1 n_0^2 n_1^2 \cdots n_0^L n_1^L\rangle$, where $n_a^l = 0$ or 1 for all l and a. The Boolean variables n_a^l are called the *number variables* and they correspond to a binary indexing of the basis states in the number representation.

Since we are concerned with modeling the one-particle wave equation, we need consider only a subset of all the basis states where only one of the number variables is 1 and all the rest are 0. This subset of all the basis states is called the *one-particle sector*. There are $2L$ such combinations and we shall label these with the binary encoding formula $|2^{2l+a}\rangle$, for $a = 0, 1$ and $0 \geq l \geq L-1$. Therefore, the system ket in the number representation can be written as

$$|\psi\rangle = \sum_{l=0}^{L-1} \sum_{a=0}^{1} \xi_{2l+a} |2^{2l+a}\rangle, \tag{5.5}$$

where each ξ_{2l+a} is a probability amplitude (e.g. complex number).

Now for each position ket $|x_l\rangle$ there are two corresponding basis states in the number representation $|2^{2l}\rangle$ and $|2^{2l+1}\rangle$. There are two *interfering possibilities* for a particle to occupy the lth position on the lattice. Therefore, the occupancy probability of the lth node is computed by first summing the probability amplitudes of these corresponding basis states and then computing the square of the absolute value thereof. In other words, the coefficient c_l in (5.4) is set equal to the sum of the on-site coefficients in (5.5)

$$c_l \equiv \xi_{2l} + \xi_{2l+1}. \tag{5.6}$$

The definition (5.6) is an essential part of the quantum lattice-gas model presented in this chapter. In the section below, where we analytically predict an effective field theory for our artificially discrete model, we explain why we need to make this assignment. We will find that (5.6) is needed for the predicted effective field theory to accurately approximate the Schroedinger wave equation in the long-wavelength limit, which is also defined below.

Formulating a suitable gate sequence

We shall require that the algorithmic scheme be at least second order convergent in space, so that double the grid resolution (e.g. double the number of qubits) will give us one fourth of the numerical error due to the field discretization. With this type of convergence characteristic, we are assured that we can simulate a wave function governed by the Schroedinger wave equation (5.3) to any arbitrary degree of accuracy. After we formulate our algorithmic scheme, we will then a posteriori verify by direct numerical simulation that it is indeed at least a second-order convergent numerical scheme. In fact, in Section 5.2.3 we will find that our numerical scheme is fourth-order convergent with an error that goes as $(\delta x)^4$.

To simulate the quantum behavior of the wave function, we seek to develop a sequence of 2-qubit gate operations that will act on a large collection of qubits in the simplest way. We impose the following four simplifying constraints:

1. All quantum gate operations are homogeneous and independent of space and time.

2. Only a single quantum gate is used to evolve the wave function and this gate is applied to each lattice node independently (locality).

3. To provide communication channels between lattice nodes, only the simplest gate is used (e.g. a swap gate).

4. Because the final value of the computed wave function depends on summing interfering possibilities according to (5.6), we shall use the Hadamard gate at the very end of the simulation prior to making a measurement of the wave function so that a single qubit at each node will encode the probability amplitude $c_l = \langle x_l|\psi\rangle$ in (5.4).

With two qubits per node, there are four on-site basis kets, $|0\rangle \otimes |0\rangle \equiv (1,0,0,0)$, $|0\rangle \otimes |1\rangle \equiv (0,1,0,0)$, $|1\rangle \otimes |0\rangle \equiv (0,0,1,0)$, and $|1\rangle \otimes |1\rangle \equiv (0,0,0,1)$. In the context of a quantum lattice-gas model, the unitary matrix $\hat{U}$ is called the *local collision operator* and the on-site ket $|\nu\rangle \equiv |0\rangle \otimes |1\rangle + |1\rangle \otimes |0\rangle = (0,1,1,0)$ is called the *number density ket*. To have a well behaved local equilibrium associated with the collision process, the local collision operator must have the number density ket as an eigenvector with unity eigenvalue.

Quantum algorithm

The quantum gate that we use to evolve the wave function, which is applied independently on a site-by-site basis, is the $\sqrt{\text{SWAP}}$-gate given in (2.82). The two nontrivial eigenvalues of (2.82) are $\lambda_1 = 1$ and $\lambda_2 = -i$, with eigenvectors $|\nu_1\rangle = (0,1,1,0)$ and $|\nu_2\rangle = (0,-1,1,0)$, respectively. Also, since $\sqrt{\text{SWAP}}$, which we may denote by $\sqrt{\hat{\chi}}$, causes mixing only between the single-particle basis kets $|0\rangle \otimes |1\rangle$ and $|1\rangle \otimes |0\rangle$, it conserves particle number. So (2.82) is an appropriate choice for the local collision operator. The full collision operator is $\hat{C} = \bigotimes_{l=0}^{L-1} \sqrt{\hat{\chi}}$. The streaming operator, denoted $\hat{S}_1$, causes a global shift to the right of the first qubit on all the lattice nodes. Therefore, $\hat{S}_1$ can be represented by a sequence of interchangers (2.37) acting on nearest neighbors

$$\hat{S}_1 = \prod_{l=0}^{\frac{L-1}{2}} \hat{\chi}_{2l,2l+2}. \tag{5.7}$$

The algorithm we use to model the Schroedinger wave equation involves multiple applications of the collision operator interleaved with streaming operations as follows:

$$|\psi(t+\tau/2)\rangle = \hat{E}_1^{\frac{1}{2}} |\psi(t)\rangle, \tag{5.8}$$

where the square root of the evolution operator is

$$\hat{E}_1^{\frac{1}{2}} = \hat{S}_1^{\mathrm{T}} \hat{C} \hat{S}_1 \hat{C}. \tag{5.9}$$

Here $\hat{S}_1^{\mathrm{T}}$ denotes the transpose of $\hat{S}_1$ and is the inverse of $\hat{S}_1$. Application of $\hat{S}_1^{\mathrm{T}}$ causes a global shift to the left of the first qubit on all the lattice nodes. One full time step of the evolution is

$$|\psi(t+\tau)\rangle = \hat{E}_1|\psi(t)\rangle. \tag{5.10}$$

We use four applications of the collision operator in $\hat{E}_1$ because $\hat{C}^4$ is the identity operation. Note that $\hat{S}_1$ and $\hat{C}$ do not commute, otherwise (5.10) would be a trivial evolution equation.

Note that in (5.10), our choice of streaming the first qubit was arbitrary. A more balanced algorithmic approach would treat both qubits identically. Therefore, we could alternatively define one full time step as

$$|\psi(t+\tau)\rangle \equiv \hat{E}_2\hat{E}_1|\psi(t)\rangle, \tag{5.11}$$

where

$$\hat{E}_2^{\frac{1}{2}} = \hat{S}_2^{\mathrm{T}}\hat{C}\hat{S}_2\hat{C}, \tag{5.12}$$

and where the streaming operator $\hat{S}_2$ causes a global shift to the right of the second qubit on all the lattice nodes. The advantage of using the balanced algorithm (5.11) is that its error is fourth-order in space whereas for the unbalanced algorithm (5.10) it is only third-order.

Finite difference formulation

It is possible to specify the quantum algorithm to model the Schroedinger equation without the use of matrices. Instead we can write down a set of finite difference equations, which are equivalent to (5.8), but perhaps simpler to comprehend at first glance. To do this, let us introduce a new notation for the $2L$ probability amplitudes ξ_{2l+a} in (5.5). We will denote the two complex numbers per lattice node by $\varphi_0(x_l, t_n)$ and $\varphi_1(x_l, t_n)$. That is, we have L-pairs of complex numbers. Then, the quantum algorithmic operations (5.12) can be expressed as

follows:

$$\begin{aligned}
&\text{if } \mathrm{mod}(n,4)=0 && (5.13)\\
&\qquad \varphi_0(x_l,t_n) &&= A^*\varphi_0(x_l,t_{n-1}) + A\varphi_1(x_l,t_{n-1})\\
&\qquad \varphi_1(x_l,t_n) &&= A\varphi_0(x_l,t_{n-1}) + A^*\varphi_1(x_l,t_{n-1}),\\
&\text{if } \mathrm{mod}(n,4)=1 && (5.14)\\
&\qquad \varphi_0(x_l,t_n) &&= \varphi_0(x_{l-1},t_{n-1})\\
&\qquad \varphi_1(x_l,t_n) &&= \varphi_1(x_l,t_{n-1}),\\
&\text{if } \mathrm{mod}(n,4)=2 && (5.15)\\
&\qquad \varphi_0(x_l,t_n) &&= A^*\varphi_0(x_l,t_{n-1}) + A\varphi_1(x_l,t_{n-1})\\
&\qquad \varphi_1(x_l,t_n) &&= A\varphi_0(x_l,t_{n-1}) + A^*\varphi_1(x_l,t_{n-1}),\\
&\text{and if } \mathrm{mod}(n,4)=3 && (5.16)\\
&\qquad \varphi_0(x_l,t_n) &&= \varphi_0(x_{l+1},t_{n-1})\\
&\qquad \varphi_1(x_l,t_n) &&= \varphi_1(x_l,t_{n-1}),
\end{aligned}$$

where $A = \frac{1}{2} + \frac{i}{2}$. The finite-difference equation pair (5.13) is equivalent to the local collision operation $\hat{C}$, as is the pair (5.15). The equation pairs (5.14) and (5.16) are equivalent to the streaming operations $\hat{S}$ and $\hat{S}^{\mathrm{T}}$, respectively.

(Noting that $A + A^* = 1$, this set of finite difference equations can be expressed in a more compact way

$$\begin{aligned}
\varphi_0(x_{l+\epsilon},t_{n+1}) &= \varphi_0(x_l,t_n) + \Omega_0\\
\varphi_1(x_l,t_{n+1}) &= \varphi_1(x_l,t_n) + \Omega_1
\end{aligned}$$

where $\epsilon = (-1)^n$ and $\Omega_0 = A(\varphi_1 - \varphi_0)$ and $\Omega_1 = -\Omega_0$, which has the standard form of a lattice-gas transport equation.)

This finite-difference representation of the algorithm is nearly identical to that presented by Boghosian and Taylor in 1997 [Boghosian and IV, 1998a] where the two on-site qubits are simultaneously streamed to the left and right after collision operation

$$\begin{aligned}
\varphi_0(x_{l+1},t_n) &= A^*\varphi_0(x_l,t_{n-1}) - A\varphi_1(x_l,t_{n-1})\\
\varphi_1(x_{l-1},t_n) &= -A\varphi_0(x_l,t_{n-1}) + A^*\varphi_1(x_l,t_{n-1}).
\end{aligned} \qquad (5.17)$$

They noted that after four time steps, the total amplitude $\psi(x_l,t_n) = \phi_0(x_l,t_n) + \phi_1(x_l,t_n)$ satisfies a finite-difference equation which approximates the Schroedinger equation in the

continuum limit. The two essential differences between the improved algorithm (5.13) through (5.16) presented in this chapter and the quantum algorithm (5.17) appearing in [Boghosian and IV, 1997] is that we have alleviated the problem of the occurrence of two non-interpenetrating lattice-gas systems independently evolving on different checker-board sub-lattices and we have doubled the numerical accuracy. This is a problem that occurs when both on-site qubits are simultaneously streamed because streaming only a single qubit at a time, as was done for the quantum lattice-gas model of the diffusion equation [Yepez, 2001b], causes interactions between all the qubits at each time step.

5.2.2 Effective field theory

It is straightforward using a symbolic mathematics program, and tedious by hand, to use the update rules (5.13) through (5.16) to algebraically determine the value of φ_0 and φ_1 at a later time. With the initial wave function set at t_0, one complete cycle of the algorithm is completed at t_8 (that is, $t_8 - t_0 \equiv \delta\tau$). With the wave function defined as $\psi(x_l, t_n) \equiv \varphi_0(x_l, t_n) + \varphi_1(x_l, t_n)$, the result after one cycle is[1]

$$\begin{aligned} \psi(x_l, t_8) &= -\frac{1+i}{2}\psi(x_l, t_0) + \psi(x_{l+1}, t_0) + \psi(x_{l-1}, t_0) \\ &\quad -\frac{1-i}{4}\left[\psi(x_{l+2}, t_0) + \psi(x_{l-2}, t_0)\right], \end{aligned} \tag{5.18}$$

Note that (5.18) is the simplified form of the finite-difference equation at the macroscopic scale when the system is very close to local equilibrium throughout the course of the evolution as $\varphi_0(x,t) = \varphi_1(x,t) \simeq \frac{1}{2}\psi(x,t)$ for all x. The full finite-difference equation is too long to present here, but is given in Appendix F. This result is a finite-difference equation for the following partial differential equation governing the continuous amplitude field $\psi(x,t)$

$$\frac{\partial\psi(x,t)}{\partial t} + \mathcal{O}(\delta t^2) = \frac{i}{2}\frac{\delta x^2}{\delta\tau}\frac{\partial^2\psi(x,t)}{\partial x^2} + \mathcal{O}(\delta x^4), \tag{5.19}$$

which is an approximation of (5.3) where the diffusion constant is $\hbar/m = \delta x^2/\delta\tau$ and where δx is the lattice cell size.

If one adds a phase angle ζ to the off-diagonal components of the collision operator (2.82) to obtain a more general collision operator according to (2.48a) (conservative quantum logic

[1] (Note that the result (5.18) is accurate up to fourth order in δx only in the situation where the initial system is in local equilibrium defined by $\varphi_0(x_l, t_n) = \varphi_1(x_l, t_n)$. In the more general situation when the system is not in local equilibrium where $\varphi_0(x_l, t_n) \neq \varphi_1(x_l, t_n)$, the result (5.18) is accurate only up to third order in δx.)

gate) with $z = -i\pi$ and $\delta = 1$, then

$$\sqrt{\hat{\chi}} = \begin{pmatrix} 1 & 0 & 0 & 0 \\ 0 & \frac{1}{2} - \frac{i}{2} & \left(\frac{1}{2} + \frac{i}{2}\right) e^{i\zeta} & 0 \\ 0 & \left(\frac{1}{2} + \frac{i}{2}\right) e^{-i\zeta} & \frac{1}{2} - \frac{i}{2} & 0 \\ 0 & 0 & 0 & -i \end{pmatrix}, \tag{5.20}$$

and the resulting governing partial differential equation will have its transport coefficient dependent on this phase angle as follows:

$$\frac{\partial \psi(x,t)}{\partial t} + \mathcal{O}(\delta t^2) = \frac{i}{2\sec\zeta} \frac{\delta x^2}{\delta \tau} \frac{\partial^2 \psi(x,t)}{\partial x^2} + \mathcal{O}(\delta x^4). \tag{5.21}$$

This allows us to simulate a quantum system where a particle's mass can be arbitrarily large $m = \sec\zeta$, but has a minimum of one. Note that in this case the error is cubic and is proportional to $\sin\zeta$. So for very large masses, the accuracy of the model is reduced to third-order in space. Note that (5.21) is a valid effective field theory at the macroscopic scale when the system is very close to local equilibrium where $\varphi_0(x,t) = \varphi_1(x,t) \simeq \frac{1}{2}\psi(x,t)$ for all x.

5.2.3 Dispersion of a Gaussian packet

To numerically test that the quantum algorithm (5.10) is indeed equivalent to the finite-difference equation (5.18) and to see just how good an approximation of the single-particle Schroedinger equation it is, we have performed two simulations.

In the first simulation, we test the numerical time evolution of a Gaussian packet

$$\psi(x,0) = \frac{1}{\sigma^{\frac{1}{2}} \pi^{\frac{1}{4}}} e^{-\frac{x^2}{2\sigma^2}}, \tag{5.22}$$

where $\ell \geq x \geq L$ for a lattice of size $L = 64\ell$ and where the packet width is $\sigma = L/10$ as shown in Figure 5.1.

The exact anaytical solution of (5.19) is obtained by computing the Fourier components of the energy basis functions

$$a_\circ = \frac{1}{L} \int_{-L/2}^{L/2} \psi(x,0) dx \tag{5.23}$$

$$a_n = \frac{2}{L} \int_{-L/2}^{L/2} \psi(x,0) \cos\left(2n\pi \frac{x}{L}\right) dx. \tag{5.24}$$

With $\hbar = 1$ and $m = 1$, the energy eigenvalues are

$$E_n = \frac{2n^2\pi^2\delta x^2}{L^2 \delta t}, \tag{5.25}$$

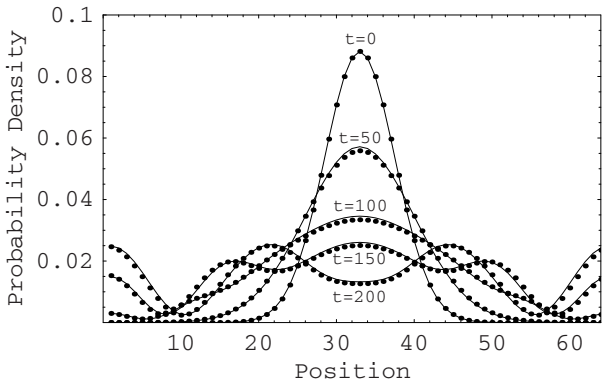

Figure 5.1: Dispersion of a Gaussian packet: Time evolution of a Gaussian packet for a single quantum particle overplotted in succession where the x-axis is the position on a 64-node lattice in units of the lattice spacing ℓ and the y-axis is the probability density $|\psi(x,t)|^2$. The solid curves are the exact analytical solution and the circles are the data from the quantum lattice-gas simulation (the initial wave function was normalized, therefore the area under each curve is one). The lattice size is $L = 64\ell$. The initial Gaussian packet of with $\sigma = L/10$ at $t = 0$ is centered at $x = 32\ell$ and the dispersion is evident by observing the wave function at the subsequent times $t = 50\tau, 100\tau, 150\tau$, and 200τ. Periodic boundary conditions were used and $n_{\max} = 20$ energy eigenmodes were used to generate the exact solutions. A time scale factor $t_s = 1.04$ was used to improve the agreement between the numerical and analytical solutions.

and the time-dependent solution to (5.19) plotted in Figure 5.1 is

$$\psi_{\text{exact}}(x,t) = a_\circ + \sum_{n=1}^{n_{\max}} a_n \cos\left(2n\pi\frac{x}{L}\right) e^{-iE_n t/t_s}. \tag{5.26}$$

Note that in (5.26), time is scaled by a factor t_s to account for kinetic corrections to the time step. As the number of lattice nodes becomes large, this scaling factor approaches one.

The second test of the quantum lattice-gas algorithm as a model of the Schroedinger wave equation is the measurement of its numerical convergence. Multiple simulations (10 in total) were carried out for lattice sizes ranging from $L = 8\ell, 16\ell, 32\ell, \ldots$ up to $L = 8192\ell$. In each case the initial state of the simulation was the ground state (a sinusoidal energy eigenstate)

$$\psi(x,0) = \psi^{\text{exact}}(x) = \frac{\cos(2\pi x/L)}{\sqrt{L/2}}. \tag{5.27}$$

Each simulation was run for one time step $T = \tau$ and the numerical error, denoted ϵ, from the exact solution was then measured using the following formula

$$\epsilon(L) = \frac{1}{L}\sqrt{\sum_{x=1}^{L}\left\{|\psi(x,T)|^2 - |\psi^{\text{exact}}(x)|^2\right\}^2}. \tag{5.28}$$

We define the grid resolution as the inverse of the total number of lattice points. That is, for a box of size 1, the *resolving cell size* is defined as $\delta x \equiv \frac{1}{L}$. A plot of the error versus

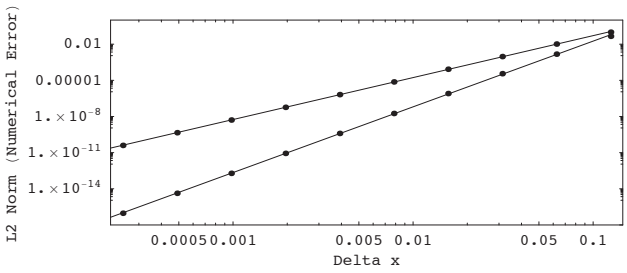

Figure 5.2: L2 norm error for the Schroedinger equation: Log-log plot of the numerical error versus resolving grid cell size, δx, indicating the convergence property of the quantum lattice-gas algorithm (5.10) and (5.11) for the Schroedinger equation. The data (black circles) are taken from numerical simulations with grid sizes from $L = 8\ell$ up to 8192ℓ after a single time step $T = \tau$. The solid curves are best-fit linear regression with a slope of 3.48 and 5.45 for the models defined by (5.10) and (5.11), respectively. These results demonstrate third-order and fourth-order convergence in space for the two models, respectively.

the resolution is given in Figure 5.2. As the resolution is increased, the error drops off as $\epsilon(L) \sim L^{-5.45}$.

5.2.4 Adding an external scalar potential

It is possible to model an external potential by applying a local phase change to the system wave function [Boghosian and IV, 1998b, Boghosian and IV, 1998a]

$$\psi(x,t) \to e^{-iV(x)\delta t}\psi(x,t). \tag{5.29}$$

The effect of this phase change is to alter the finite difference equation (5.18) as follows

$$\begin{aligned}
\psi(x_l,t_8) &= -\frac{1+i}{2}e^{-iV(x_l)\delta t}\psi(x_l,t_0) \\
&+ e^{-iV(x_{l+1})\delta t}\psi(x_{l+1},t_0) \\
&+ e^{-iV(x_{l-1})\delta t}\psi(x_{l-1},t_0) \\
&- \frac{1-i}{4}\left[e^{-iV(x_{l+2})\delta t}\psi(x_{l+2},t_0)\right. \\
&\quad \left. + e^{-iV(x_{l-2})\delta t}\psi(x_{l-2},t_0)\right].
\end{aligned} \tag{5.30}$$

If we expand the potential terms in the arguments of the exponentials

$$V(x_{l+1})\delta t = V(x_l)\delta t + \delta t\delta x \left.\frac{dV(x)}{dx}\right|_{x=x_l} + \mathcal{O}(\delta t\delta x^2) \tag{5.31}$$

we see that we can neglect the second term on the RHS because of diffusive ordering $\delta t\delta x \sim \delta x^3$ since we need to keep terms only to order δx^2. Therefore, in the continuum limit (5.30)

is well approximated by

$$\begin{aligned}\psi(x_l,t_8) &= -\frac{1+i}{2}e^{-iV(x_l)\delta t}\psi(x_l,t_0) \\ &+ e^{-iV(x_l)\delta t}\left[\psi(x_{l+1},t_0)+\psi(x_{l-1},t_0)\right] \\ &- \frac{1-i}{4}e^{-iV(x_l)\delta t}\left[\psi(x_{l+2},t_0)+\psi(x_{l-2},t_0)\right].\end{aligned} \tag{5.32}$$

Now multiplying through by $e^{iV(x_l)\delta t}$ and expanding the LHS to order δt^2 we have the following finite-difference equation:

$$\begin{aligned}\left[1+iV(x_l)\delta t\right]\psi(x_l,t_8) &= -\frac{1+i}{2}\psi(x_l,t_0) \\ &+ \psi(x_{l+1},t_0)+\psi(x_{l-1},t_0) \\ &- \frac{1-i}{4}\left[\psi(x_{l+2},t_0)+\psi(x_{l-2},t_0)\right].\end{aligned} \tag{5.33}$$

In the continuum limit, this finite-difference equation represents the Schroedinger wave equation with an external potential term

$$\frac{\partial\psi(x,t)}{\partial t}+\mathcal{O}(\delta t^2)=\frac{i}{2}\frac{\delta x^2}{\delta\tau}\frac{\partial^2\psi(x,t)}{\partial x^2}-iV(x)\psi(x,t)+\mathcal{O}(\delta x^4). \tag{5.34}$$

To confirm the validity of (5.34) we perform the following numerical simulations that yield results that can be checked against analytical predictions:

1. Harmonic oscillation of a displaced Gaussian wave packet in a parabolic potential.
2. Quantum tunneling through a potential barrier.

Harmonic oscillator

The first numerical test presented here is the simulation of the behavior of a wave packet in an external parabolic potential. This is the well-known problem of the linear harmonic oscillator. Schroedinger analytically calculated the exact time-dependent solution for the evolution of a Gaussian packet that is displaced by a distance a from its central ground state in a parabolic potential well of the form $V(x)=\frac{1}{2}Kx^2$. The initial wave function is

$$\psi(x,0)=\frac{\alpha^{\frac{1}{2}}}{\pi^{\frac{1}{2}}}e^{-\frac{1}{2}\alpha^2(x-a)^2}, \tag{5.35}$$

where $\alpha=\left(mK/\hbar^2\right)^{\frac{1}{4}}$ is the width of the packet and $\omega_c=(K/m)^{\frac{1}{2}}$ is the angular frequency of the classical harmonic oscillator [Schrodinger, 1926]. The exact time-dependent solution for the probability density is the following:

$$|\psi(x,t)|^2=\frac{\alpha}{\pi^{\frac{1}{2}}}e^{-\frac{1}{2}\alpha^2(x-a\cos\omega_c t)^2}. \tag{5.36}$$

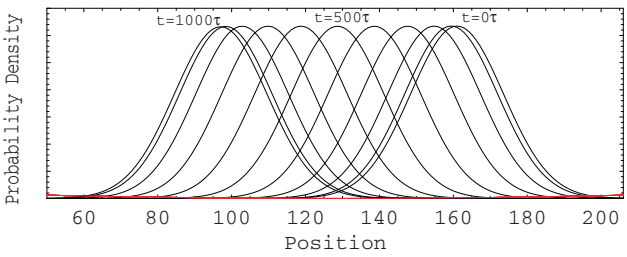

Figure 5.3: Harmonically oscillating wave packet: Time evolution of a Gaussian packet initially displaced by $a = 32\ell$ lattice sites from the center of a parabolic potential well with $K = 10^{-5}$. The width of the packet is $\alpha = 14.4\ell$. The time development of the Gaussian packets over plotted in succession where the x-axis is the position on a $L = 256\ell$ node lattice and the y-axis is the probability density $|\psi(x,t)|^2$. The red curve is the parabolic potential. The $\hbar = 1$ and $m = 1$, the time period of the oscillation is $T_c = \frac{2\pi}{\omega_c} = 1986.92\tau$. A total of ten profiles are over plotted corresponding to time $t = 0, 100\tau, 200\tau, ..., 1000\tau$, which is approximately half of the oscillation time period, so the packet is seen to "swing" to the other side of the potential well while maintaining a fixed shape as analytically predicted.

A derivation of the result (5.36) is also presented by Schiff [Schiff, 1968].

To test the quantum lattice gas algorithm against (5.36) we used a periodic lattice with $L = 256\ell$ nodes. The initial Gaussian packet is displaced to the right of the center of the grid by 32 lattice nodes and so is initially located at $x_\circ = 160\ell$ as shown in Fig 5.3. With $\hbar = 1$ and $m = 1$, the classical time period is $T_c = 2\pi/\omega_c = 1987\tau$. So letting the simulation run for 1000 iterations allows the packet to move to the other side of the potential well near position $x = 96\ell$ as demonstrated in Fig 5.3.

The simulation was rum for a total of 6000 time steps and the location of the peak of the Gaussian wave packet was recorded every 100τ time steps. These data are plotted in Fig 5.4. The location of the peak oscillates in time as expected. Overplotted on these numerical data is the exact solution for the oscillation $a\cos\omega_c t + x_\circ$ and the agreement between the analytical solution and the numerical data is excellent.

Scattering off a potential barrier

The next numerical test of the quantum lattice gas is to simulate the well-known case of quantum tunneling through a constant potential barrier of width a. That is, $V(x) = V_\circ$ for $0 \le x \le a$ and $V(x) = 0$ otherwise. The initial wave function is a Gaussian packet with net momentum to the right

$$\psi(x,0) = \frac{1}{\pi^{\frac{1}{4}}\sigma^{\frac{1}{4}}} e^{-\frac{1}{2}\left(\frac{x-x_\circ}{\sigma}\right)^2 + ipx}, \tag{5.37}$$

where p is the momentum parameter. We choose the mean kinetic energy of the packet to be equal to the constant energy level of the potential barrier $\frac{1}{2}p^2 = V_\circ$. In this case, the packet tunnels through the barrier but the sum of the transmission and reflection probabilities are

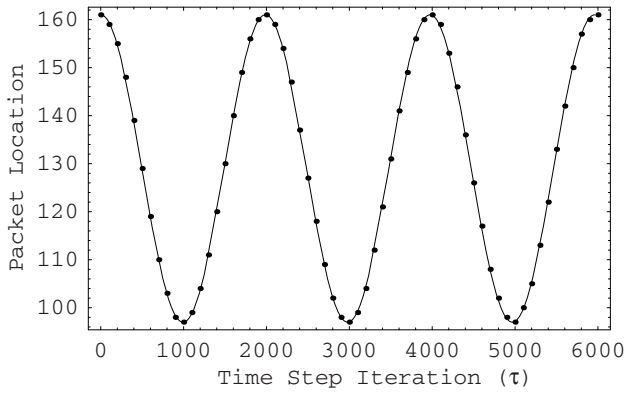

Figure 5.4: A comparison between the analytical and numerical predictions of the location of an oscillating Gaussian packet in a harmonic parabolic potential well. The solid curve is the analytical prediction and the black circles are the numerical data taken from the quantum lattice gas simulation presented in Figure 5.3. In the simulation, the packet is initially displaced 32 lattice units from the center of the grid at lattice node 128 for a periodic system with a total of $L = 256\ell$ nodes. The numerical predictions are in excellent agreement with the exact analytical solution.

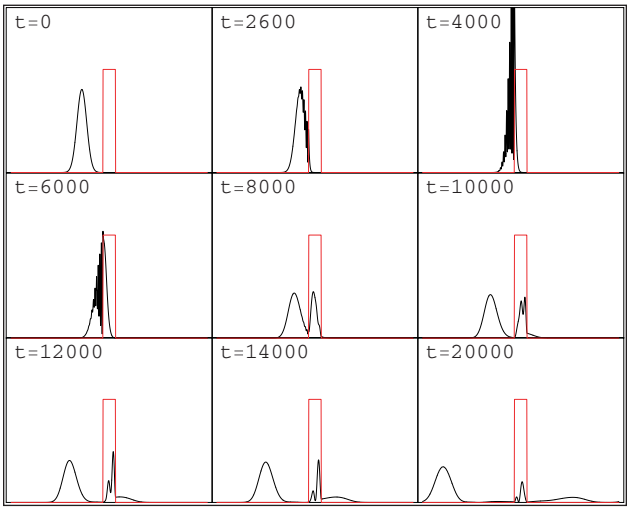

Figure 5.5: Resonance tunneling through a square potential barrier: A sequence of snapshots of the time evolution of a packet that is incident from the left onto a potential barrier where the mean kinetic energy of the packet equals the energy of the barrier. The x-axis is the lattice position and the y-axis is the probability density. The iteration time step for each frame of the sequence is labeled in the upper left corners. The simulation was run on a periodic grid of size $L = 4000\ell$ for a total of 20000 time steps. The width of the incident packet was set to $\sigma = .035L = 140\ell$ and the initial momentum parameter was set to $p = 0.1$ in units where $\ell = 1$, $\tau = 1$ and $m = 1$. The width of the barrier was set to $a = 0.064L = 256\ell$. As expected the numerical simulation clearly demonstrates the resonance effect where there is a non-zero probability of the particle to be trapped within the barrier itself.

less than one because there is a resonance effect where the particle is also trapped inside of the barrier. This effect is observed in the numerical simulation shown in Figure 5.5.

5.2.5 Two fermionic particles

The efficiency of the quantum algorithm (5.10) becomes evident when it is used to simulate the dynamics of multiple quantum particles. The case of multiple quantum particles is still handled by the same evolution operator $\hat{E}$ that we tested for the single particle case. The particular sequence and number of quantum gate operations remains fixed, independent of the number of particles to be simulated. The only difference is how the system wave function is initialized.

In this section, for pedagogical reasons, we will consider the case of simulating two free quantum particles. The approach we use in this case can be directly generalized to the many-particle case.

To begin with we write the Schroedinger wave equation for two free quantum particles

$$i\hbar\frac{\partial\psi(x,y,t)}{\partial t} = -\frac{\hbar^2}{2m}\frac{\partial^2\psi(x,y,t)}{\partial x^2} - \frac{\hbar^2}{2m}\frac{\partial^2\psi(x,y,t)}{\partial y^2}, \tag{5.38}$$

where x and y are the spatial coordinates of the first and second particle, respectively. Since the wave function is spatially separable as $\psi(x,y,t) = \varphi(x,t)\varphi(y,t)$, the analytical solution to (5.38) is obtained in a similar fashion to the one-body case by computing the Fourier components of the energy basis functions

$$a_\circ = \frac{1}{L}\int_{-L/2}^{L/2}\varphi(x,0)dx \tag{5.39}$$

$$a_n = \frac{2}{L}\int_{-L/2}^{L/2}\varphi(x,0)\cos\left(2n\pi\frac{x}{L}\right)dx \tag{5.40}$$

$$b_n = \frac{2}{L}\int_{-L/2}^{L/2}\varphi(x,0)\sin\left(2n\pi\frac{x}{L}\right)dx. \tag{5.41}$$

The energy eigenvalues are still given by (5.25) and the time-dependent single-particle solution is

$$\begin{aligned}\varphi(x,t) &= a_\circ + \sum_{n=1}^{n_{\max}}\left[a_n\cos\left(2n\pi\frac{x}{L}\right)\right. \\ &+ \left. b_n\sin\left(2n\pi\frac{x}{L}\right)\right]e^{-iE_nt/t_s},\end{aligned} \tag{5.42}$$

which is basically the same as (5.26) except that we had to add the sine term because with two particles the wavefunction is not even, as is (5.22) for example. We shall test the time

evolution of two Gaussian packets. The initial wave function in our test is the odd function

$$\begin{aligned}\psi_{\text{exact}}(x,y,t) &= \frac{1}{\sqrt{2}}[\varphi_{\alpha_1,\sigma_1}(x,t)\varphi_{\alpha_2,\sigma_2}(y,t) \\ &- \varphi_{\alpha_1,\sigma_1}(y,t)\varphi_{\alpha_2,\sigma_2}(x,t)],\end{aligned} \tag{5.43}$$

where

$$\varphi_{\alpha,\sigma}(x,0) = \frac{1}{\sigma^{\frac{1}{2}}\pi^{\frac{1}{4}}} e^{-\frac{(x-\alpha)^2}{2\sigma^2}}. \tag{5.44}$$

The subscripts on the function $\varphi_{\alpha,\sigma}$ denote its dependence on the position and width of the individual Gaussian packet. This functional dependence is actually contained within the form of the coefficients $a_\circ$, a_n, and b_n that depend on the position and width of the Gaussian packet in accordance with (5.39) through (5.41). Note that given the form of (5.43), $\psi_{\text{exact}}(x,x,t) = 0$, which satisfies the Pauli exclusion principle.

Numerical confirmation

To numerically simulate the evolution of the two-particle wave function governed by (5.38) using quantum algorithm (5.10) we must use a new computational formulation to implement our algorithm. The finite-difference equation implementation that we used in Section 5.2.1, in the single-particle case, cannot be directly applied in the two-particle case to each particle individually because it does not allow for the possibility that the particles can be quantum mechanically entangled. In general, this will be the case when there is an interaction between the particles. Therefore, we shall use an implementation that can handle the most general situations involving correlated particles and one that naturally scales to handle an arbitrarily large number of particles in the system, the second quantized representation given above in Section 2.6.

The $\sqrt{\text{SWAP}}$ gate (2.82) acting on the on-site qubits indexed by α and $\alpha+1$ can be expressed in terms of the creation and annihilation operators as

$$\begin{aligned}\sqrt{\hat{\chi}}_{\alpha,\alpha+1} &= A^*\hat{n}_\alpha(\mathbf{1}-\hat{n}_{\alpha+1}) - A\hat{a}^\dagger_\alpha\hat{a}_{\alpha+1} - A\hat{a}^\dagger_{\alpha+1}\hat{a}_\alpha \\ &+ A^*(\mathbf{1}-\hat{n}_\alpha)\hat{n}_{\alpha+1} + \mathbf{1} - \hat{n}_\alpha - \hat{n}_{\alpha+1},\end{aligned} \tag{5.45}$$

where $A = \frac{1}{2} + \frac{i}{2}$. The swap operator (2.28) acting between the first qubits indexed by α and β at neighboring nodes is

$$\hat{\chi}_{\alpha\beta} = \mathbf{1} + \hat{a}^\dagger_\alpha\hat{a}_\beta + \hat{a}^\dagger_\beta\hat{a}_\alpha - \hat{n}_\alpha - \hat{n}_\beta. \tag{5.46}$$

The quantum gates (5.45) and (5.46) are used to implement the quantum lattice gas collision and streaming operations, respectively [Yepez, 2001a].

The basis state in the two-particle sector can be labeled with the binary encoding formula $|2^{\alpha-1}+2^{\beta-1}\rangle$ where the integers α and β are in the ranges $1 \leq \alpha \leq Q$ and $\alpha+1 \leq \beta \leq Q$. The number of basis states in this case is the binomial coefficient $\binom{Q}{2}$. The system ket can then be expressed in the two-particle sector as

$$|\psi\rangle = \sum_{\alpha=1}^{Q} \sum_{\beta=\alpha+1}^{Q} \xi_{\alpha,\beta} |2^{\alpha-1}+2^{\beta-1}\rangle. \tag{5.47}$$

Since there are two qubits per site, we initialize the wave function using (5.43) as follows:

$$\xi_{\alpha,\beta} \equiv \psi_{\text{exact}} \left(\lfloor \frac{\alpha+1}{2} \rfloor - \frac{L+1}{2}, \lfloor \frac{\beta+1}{2} \rfloor - \frac{L+1}{2}, 0 \right), \tag{5.48}$$

where the notation $\lfloor x \rfloor$ means the floor of x and where $Q \equiv 2L$. The floor operation is used so that the initial value of the wave function at each node is divided evenly between each pair of on-site qubits. This is needed because definition (5.6) allowed us to have interfering possibilities for a single particle to occupy a single position on the lattice. Moreover in the two particle case, a single particle can still occupy only a single position because of the form of the wave function (5.43) which is consistent with the anti-commutation relations (2.21). However, particle one can interfere on-site with itself or with particle two, or vice versa since the particles are indistinguishable.

At this point we have described how we implement the two quantum gates used in our algorithm, how we enumerate the basis states, and how we initialize the two-body wave function in this basis. The only remaining issue left to describe is how we project the two-coordinate wave function $\psi(x,y,t)$ on to a single-coordinate wave function $\psi(x,t)$ that can be plotted on a single physical axis. Because of the underlying lattice in our system this is straightforward to do by summing out one of the coordinates as follows:

$$\psi(x_l, t_n) \equiv \sum_{m=0}^{L-1} \psi(x_l, y_m, t_n). \tag{5.49}$$

If $\psi(x_l, y_m, t_n)$ is normalized then so is $\psi(x_l, t_n)$ according to (5.49). A comparison of the time evolution of the analytical solution (5.43) and the numerical solution (5.49) for a lattice with 30 nodes is shown in Figure 5.6. Even with this small lattice, throughout the time evolution of the model run the numerical predictions are in good agreement with the predictions of the exact solution.

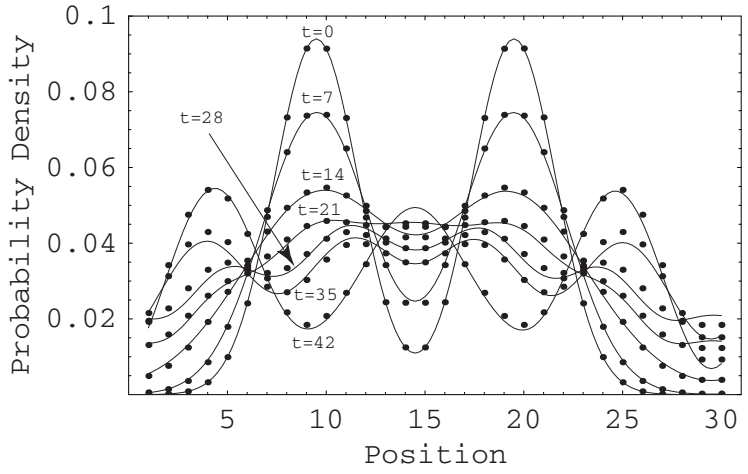

Figure 5.6: Simulation of two fermions: Time evolution of two fermionic particles initialized as Gaussian packets is overplotted in succession where the x-axis is the position on a 30-node lattice in units of the lattice spacing ℓ and the y-axis is the probability density $|\psi(x_1, x_2, t)|^2$ projected onto the x_1-axis. The solid curves are the exact analytical solution and the circles are the data from the quantum lattice-gas simulation (the initial wave function was normalized, therefore the area under each curve is one). The initial Gaussian packets of width $\sigma = 3\ell$ at $t = 0$ of the first and second particle are centered at $x = 10\ell$ and $x = 20\ell$, respectively. The dispersion of both packets is evident by observing the wave function at the subsequent times $t = 7\tau, 21\tau, 28\tau, 35\tau$ and 42τ. Periodic boundary conditions were used and $n_{\max} = 40$ energy eigenmodes were used to generate the exact solutions at four times the resolution of the numerical solution. No time scale factor was used and there is good agreement between the analytical and numerical predictions at all later times of the numerical simulation as demonstated by the graphs.

5.3 2+1 dimensions

5.3.1 Qubit representation for the NLS wave function

We discretize the single-particle wave function over a two dimensional square Bravais lattice (the wave function is defined only on a spacetime lattice) where two qubits are used at each lattice node to encode the local value of the wave function at that node. Let L denote the number of lattice nodes along an orthogonal direction and let i and j be integer valued spatial indices ranging from 1 up to L. Then, at lattice node (i, j) one defines a position basis ket $|x_{ij}\rangle$. The discrete single-particle wave function ket $|\psi\rangle$ is modeled by a sum over all possible ways the particle can be located on the lattice sites:

$$|\psi\rangle = \sum_{i,j=0}^{L-1} \gamma^{ij} |x_{ij}\rangle, \tag{5.50}$$

where the (complex) probability amplitude for each possibility is $\gamma^{ij} \equiv \langle x^{ij}|\psi\rangle$.

The two qubit kets for each lattice node are denoted by $|q_0^{ij}\rangle$ and $|q_1^{ij}\rangle$ with each qubit having the standard two-level representation

$$|q_a^{ij}\rangle = \alpha_a^{ij}|0\rangle + \beta_a^{ij}|1\rangle, \tag{5.51}$$

with normalization $|\alpha_a^{ij}|^2 + |\beta_a^{ij}|^2 = 1$ for $a = 0, 1$ at spatial site (i, j). In particular, the quantum particle is said to occupy the ath local state at position x_{ij} when $\beta_a^{ij} = 1$, while the ath local state at x_{ij} is empty when $\beta_a^{ij} = 0$. For each position ket there are four basis states in the number representation:

$$\begin{aligned}
&|q_0^{11}q_1^{11}\rangle \ldots \underbrace{|11\rangle}_{x_{ij}} \ldots |q_0^{LL}q_1^{LL}\rangle && \text{doubly occupied at } x_{ij} \\
&|q_0^{11}q_1^{11}\rangle \ldots \underbrace{|10\rangle}_{x_{ij}} \ldots |q_0^{LL}q_1^{LL}\rangle && \text{spin-up at } x_{ij} \\
&|q_0^{11}q_1^{11}\rangle \ldots \underbrace{|01\rangle}_{x_{ij}} \ldots |q_0^{LL}q_1^{LL}\rangle && \text{spin-down at } x_{ij} \\
&|q_0^{11}q_1^{11}\rangle \ldots \underbrace{|00\rangle}_{x_{ij}} \ldots |q_0^{LL}q_1^{LL}\rangle && \text{empty at } x_{ij},
\end{aligned}$$

where we use conventional terminology letting $|q_0^{ij}\rangle$ encode *spin-up* and $|q_1^{ij}\rangle$ encode *spin-down*, say.

In the number representation of the one-particle wave function ket $|\psi\rangle$, we need consider that subset of basis states in which only one amplitude $\beta_a^{ij} = 1$ is non-zero (all other β amplitudes are zero). This subset of basis states is called the *one-particle sector*. There are

$(2L)^2$ such states. So in the one-particle sector, there are two ways (interfering possibilities) for a particle to occupy the ij^{th} lattice position

$$\beta_0^{ij}\alpha_1^{ij}|00\ldots\underbrace{10}_{x_{ij}}\ldots 00\rangle + \alpha_0^{ij}\beta_1^{ij}|00\ldots\underbrace{01}_{x_{ij}}\ldots 00\rangle. \tag{5.52}$$

Hence the occupancy probability of the ij^{th} node is determined by first summing up the probability amplitudes of the spin-up and spin-down basis states in the one-particle sector and then computing the resulting square of this absolute value. Letting $\gamma_\uparrow^{ij} \equiv \beta_0^{ij}\alpha_1^{ij}$ and $\gamma_\downarrow^{ij} \equiv \alpha_0^{ij}\beta_1^{ij}$, the complex probability amplitude in (5.50) is set equal to the sum of the two on-site probability amplitudes

$$\gamma_{ij} = \gamma_\uparrow^{ij} + \gamma_\downarrow^{ij}. \tag{5.53}$$

5.3.2 Quantum algorithm

To recover a macroscopic scale effective theory that approximates the Schrödinger wave equation in the long wave length limit, our quantum lattice representation of the dynamics uses the unitary $\sqrt{\text{SWAP}}$ quantum logic gate as the collision operator that couples the on-site probability amplitudes:

$$\mathscr{C}\begin{pmatrix}\gamma_\uparrow^{ij}\\ \gamma_\downarrow^{ij}\end{pmatrix} = \frac{1}{2}\begin{pmatrix}1-i & 1+i\\ 1+i & 1-i\end{pmatrix}\begin{pmatrix}\gamma_\uparrow^{ij}\\ \gamma_\downarrow^{ij}\end{pmatrix}, \tag{5.54}$$

and eight stream operators which independently shift the $\uparrow$ and $\downarrow$ components of the discrete spinor wave function in the $\pm\hat{x}$ and $\pm\hat{y}$ directions. The stream operator and its transpose (which is its adjoint and inverse) in the $\hat{x}$ direction for the first (spin-up) component are:

$$S_{x\uparrow}\begin{pmatrix}\gamma_\uparrow^{ij}\\ \gamma_\downarrow^{ij}\end{pmatrix} = \begin{pmatrix}\gamma_\uparrow^{i+1,j}\\ \gamma_\downarrow^{ij}\end{pmatrix} \qquad S_{x\uparrow}^{\mathrm{T}}\begin{pmatrix}\gamma_\uparrow^{ij}\\ \gamma_\downarrow^{ij}\end{pmatrix} = \begin{pmatrix}\gamma_\uparrow^{i-1,j}\\ \gamma_\downarrow^{ij}\end{pmatrix}, \tag{5.55}$$

and the stream operators in the $\hat{x}$ direction for the second (spin-down) component of the discrete spinor wave function:

$$S_{x\downarrow}\begin{pmatrix}\gamma_\uparrow^{ij}\\ \gamma_\downarrow^{ij}\end{pmatrix} = \begin{pmatrix}\gamma_\uparrow^{i,j}\\ \gamma_\downarrow^{i+1,j}\end{pmatrix} \qquad S_{x\downarrow}^{\mathrm{T}}\begin{pmatrix}\gamma_\uparrow^{ij}\\ \gamma_\downarrow^{ij}\end{pmatrix} = \begin{pmatrix}\gamma_\uparrow^{i,j}\\ \gamma_\downarrow^{i-1,j}\end{pmatrix}. \tag{5.56}$$

Similarly. we define the four stream operators in the $\hat{y}$ direction:

$$S_{y\uparrow}\begin{pmatrix}\gamma_\uparrow^{ij}\\ \gamma_\downarrow^{ij}\end{pmatrix} = \begin{pmatrix}\gamma_\uparrow^{i,j+1}\\ \gamma_\downarrow^{ij}\end{pmatrix} \qquad S_{y\uparrow}^{\mathrm{T}}\begin{pmatrix}\gamma_\uparrow^{ij}\\ \gamma_\downarrow^{ij}\end{pmatrix} = \begin{pmatrix}\gamma_\uparrow^{i,j-1}\\ \gamma_\downarrow^{ij}\end{pmatrix}. \tag{5.57}$$

$$S_{y\downarrow}\begin{pmatrix}\gamma_\uparrow^{ij}\\ \gamma_\downarrow^{ij}\end{pmatrix} = \begin{pmatrix}\gamma_\uparrow^{ij}\\ \gamma_\downarrow^{i,j+1}\end{pmatrix} \qquad S_{y\downarrow}^{\mathrm{T}}\begin{pmatrix}\gamma_\uparrow^{ij}\\ \gamma_\downarrow^{ij}\end{pmatrix} = \begin{pmatrix}\gamma_\uparrow^{ij}\\ \gamma_\downarrow^{i,j-1}\end{pmatrix}. \tag{5.58}$$

We define the fundamental evolution operator for direction $\hat{w} = \hat{x}$ or $\hat{y}$ and spin $\sigma = \uparrow$ or $\downarrow$ as follows:

$$\mathscr{U}_{w\sigma} = S_{w\sigma}\mathscr{C}. \tag{5.59}$$

Now we define the *interleaved evolution operator* (which would be identity if the stream and collide operators commuted) as follows:

$$\begin{aligned}
\mathscr{I}_{w\sigma} &\equiv S^{\dagger}_{w\sigma}\mathscr{U}^{\dagger}_{w\sigma}S_{w\sigma}\mathscr{U}_{w\sigma} && \text{(5.60a)}\\
&= S^{\dagger}_{w\sigma}\mathscr{C}^{\dagger}S_{w\sigma}\mathscr{C} && \text{(5.60b)}\\
&= S^{\mathrm{T}}_{w\sigma}\mathscr{C}S_{w\sigma}\mathscr{C} && \text{(5.60c)}\\
&= S_{-w,\sigma}\mathscr{C}S_{w\sigma}\mathscr{C}, && \text{(5.60d)}
\end{aligned}$$

since the adjoint of the fundamental evolution operator is $\mathscr{U}^{\dagger}_{w\sigma} = \mathscr{C}^{\dagger}S^{\dagger}_{w\sigma}$, the stream operator is real $S^{\dagger}_{w\sigma} = S^{\mathrm{T}}_{w\sigma}$, and the collide operator is self-adjoint $\mathscr{C}^{\dagger} = \mathscr{C}$. Because of the spacetime interpretation of spin [Yepez, 2005], where if spin-up moves along $\hat{w}$ say then spin-down moves along $-\hat{w}$, then the interleaved evolution operator is invariant under the following simultaneous spin flip and spatial inversion:

$$\mathscr{I}_{-w,-\sigma} = \mathscr{I}_{w\sigma}. \tag{5.61}$$

For example, $\mathscr{I}_{-x,\uparrow} = \mathscr{I}_{x\downarrow}$.

Now we let E denote the local quantum evolution operator that advances the discrete spinor wave function one unit in time. Then the evolution equation is the following:

$$\begin{pmatrix}\gamma^{i,j}_{\uparrow}(t+\Delta t)\\ \gamma^{ij}_{\downarrow}(t+\Delta t)\end{pmatrix} = E\begin{pmatrix}\gamma^{i,j}_{\uparrow}(t)\\ \gamma^{ij}_{\downarrow}(t)\end{pmatrix} \tag{5.62}$$

The evolution operator can be partitioned in space using an operator splitting method. A third-order accurate quantum algorithm for the local evolution operator has the form

$$E = \mathscr{I}_{-y\downarrow}\mathscr{I}_{y\uparrow}\mathscr{I}_{-x\uparrow}\mathscr{I}_{x\downarrow} \tag{5.63}$$

where the macroscopic effective field theory for the spinor field $\psi = \begin{pmatrix}\gamma_{\uparrow}\\ \gamma_{\downarrow}\end{pmatrix}$ is

$$\partial_t\psi = \frac{i}{2}\frac{\Delta x^2}{\Delta t}\sigma_x\left(\partial_{xx} + \partial_{yy}\right)\psi + \mathcal{O}(\epsilon^3), \tag{5.64}$$

where $\sigma_x = \begin{pmatrix}0 & 1\\ 1 & 0\end{pmatrix}$ and where $\epsilon \sim \Delta x \sim \sqrt{\Delta t}$. So if we trace over the spin components of ψ and form the scalar $\Psi \equiv \gamma_{\uparrow} + \gamma_{\downarrow}$, we obtain the following non-relativistic wave equation for a free quantum particle:

$$\partial_t\Psi = i\frac{\hbar}{2m}\left(\partial_{xx} + \partial_{yy}\right)\Psi + \mathcal{O}(\epsilon^3), \tag{5.65}$$

where the diffusion constant associated with the particle mass is $\frac{\hbar}{m} = \frac{\Delta x^2}{\Delta t}$ in lattice units. Quadratic products of the interleaved evolution operator (5.60) are invariant to order ϵ^3 under the following double spin flip and spatial interchange operation:

$$\mathscr{I}_{w,\sigma}\mathscr{I}_{w',\sigma'} = \mathscr{I}_{w',-\sigma'}\mathscr{I}_{w,-\sigma} + \mathcal{O}(\epsilon^3). \tag{5.66}$$

For example, $\mathscr{I}_{x\uparrow}\mathscr{I}_{y\downarrow} = \mathscr{I}_{y\uparrow}\mathscr{I}_{x\downarrow}$ and $\mathscr{I}_{x\uparrow}\mathscr{I}_{y\uparrow} = \mathscr{I}_{y\downarrow}\mathscr{I}_{x\downarrow}$. Hence using (5.66), there are $\binom{4}{2} = 6$ ways to re-order the spatial indices of the evolution operator (5.63). Then, using (5.61), for each configuration of the spatial indices there are 16 ways to re-order the spin indices of (5.63). Hence, there are a total of 96 ways to rewrite the quantum algorithm (5.63). For example, we can rewrite (5.63):

$$E \overset{(5.61)}{=} \mathscr{I}_{y\uparrow}\mathscr{I}_{y\uparrow}\mathscr{I}_{x\downarrow}\mathscr{I}_{x\downarrow} \tag{5.67a}$$

$$\overset{(5.66)}{=} \mathscr{I}_{y\uparrow}\mathscr{I}_{x\uparrow}\mathscr{I}_{y\downarrow}\mathscr{I}_{x\downarrow} \tag{5.67b}$$

$$\overset{(5.66)}{=} \mathscr{I}_{x\uparrow}\mathscr{I}_{x\uparrow}\mathscr{I}_{y\downarrow}\mathscr{I}_{y\downarrow}. \tag{5.67c}$$

Every version has the same algorithmic complexity and the error terms are always order ϵ^3. Furthermore, there are versions of the quantum algorithm where the error terms differ only by an overall sign change. We exploit this feature to judiciously cause a cancellation of all ϵ^3 error terms by using twice as many operators. This doubles the algorithmic complexity, but the error is then pushed out to 4th order. Although the algorithmic complexity increases by a factor of 2, the numerical accuracy of the algorithm increases by a factor of 4 because of the diffusive ordering of the space and time fluctuations (because (5.65) is parabolic). Therefore, it is advantageous to employ this numerical schema.

As a case in point, the error terms in (5.67a) and in (5.67c) differ only by an overall sign. Hence, choosing our evolution operator to be

$$E = \mathscr{I}^2_{x\uparrow}\mathscr{I}^2_{y\downarrow}\mathscr{I}^2_{y\uparrow}\mathscr{I}^2_{x\downarrow}, \tag{5.68}$$

we recover the following macroscopic effective field theory for the spinor field

$$\partial_t\psi = i\frac{\Delta x^2}{\Delta t}\sigma_x\left(\partial_{xx} + \partial_{yy}\right)\psi + \mathcal{O}(\epsilon^4). \tag{5.69}$$

Again, tracing over the spin degrees of freedom, we obtain the Schrödinger wave equation as our effective field theory, but now with diffusion constant

$$\frac{\hbar}{m} = 2\frac{\Delta x^2}{\Delta t}. \tag{5.70}$$

We add a potential V by rotating the overall phase of the spinor field following each application of (5.68)

$$\psi(t+\Delta t) = E\, e^{-i\Delta t V/\hbar}\psi(t) \tag{5.71}$$

$$\overset{(5.70)}{=} E\, e^{-i\Delta x^2(2m/\hbar^2)V}\psi(t). \tag{5.72}$$

The resulting equation of motion is

$$\partial_t\psi = i\frac{\Delta x^2}{\Delta t}\sigma_x\left(\partial_{xx}+\partial_{yy}\right)\psi - \frac{i}{\hbar}V\psi + \mathcal{O}(\epsilon^4), \tag{5.73}$$

or in terms of the scalar wave function

$$i\hbar\partial_t\Psi = -\hbar\frac{\Delta x^2}{\Delta t}\left(\partial_{xx}+\partial_{yy}\right)\Psi + V\Psi + \mathcal{O}(\epsilon^4). \tag{5.74}$$

The addition of the potential does not introduce any greater error nor diminishes the numerical accuracy of the scheme. Using (5.61), there are 2^8 ways to rewrite (5.68). Furthermore, (5.68) must be invariant under an interchange of the spatial labels x and y and the spin labels $\uparrow$ and $\downarrow$. Hence, there are at least 256 ways of writing a quantum algorithm that is forth order accurate.

5.3.3 Transverse instability

For convenience, we briefly review some properties of a 1D soliton wave train solution of (5.2) [Kivshar and Agrawal, 2003]. A planar 1D bright soliton solution of (5.2) is

$$\psi_0(x,t) = \phi(x-x_0-2\nu t;\beta)e^{i(\nu x-\nu^2 t+\beta t+\theta)}, \tag{5.75}$$

where the standard soliton shape is given by

$$\phi(x;\beta) = \beta^{1/2}\mathrm{sech}(\beta^{1/2}x) \tag{5.76}$$

The location of the soliton wave train is x_0, 2ν is the (transverse) soliton wave train speed, β controls its amplitude and θ its phase. For a linear stability analysis of this 1D soliton wave train, one considers perturbations of the form

$$\delta\psi(x,y,t) = [u(x)+iw(x)]e^{i\beta t+\Gamma t+ipy}, \tag{5.77}$$

where p is the transverse perturbation wavenumber in the y-direction, and $\Gamma(p)$ is the linear growth rate of the perturbation. An analytic solution to this linear perturbation problem does not exist, and one must resort to asymptotic theory–either about the long wavelength limit ($p=0$) or about the maximum growth rate wavenumber p_c where $\Gamma(p_c)=0$. Here, we

shall consider the linear instability in the long wavelength limit, $p << 1$. In this limit, it can be shown [Kivshar and Agrawal, 2003] that the resulting eigenvalue problem has

$$u(x) = 0 \qquad w(x) = \phi(x). \tag{5.78}$$

In the long wavelength limit, the transverse modulation will break up the 1D soliton wave train into N filaments, where

$$N = \frac{pL_y}{2\pi}. \tag{5.79}$$

5.3.4 Predictions for NLS equation

We apply our quantum lattice algorithm to the solution of the NLS equation in 2+1 dimensions, using a 1024×1024 spatial grid with a soliton wave train speed $\nu = 0.05$ and amplitude $\beta^{1/2} = 0.085$ for three cases presented below: an unperturbed soliton wave train, a solition wave train with an additional transverse modulation, and the interaction of two perpendicularly directed solition wave trains.

Unperturbed 1D Soliton Wave Train

To test whether (classical) floating-point roundoff will trigger the transverse instability in the quantum lattice algorithm we examine the propagation of the planar 1D bright soliton solution in the NLS equation in 2+1 dimensions. We find even after 10,000 lattice time steps there is no triggering of the transverse modulation instability, and the 1D soliton train propagates undistorted through the lattice, see Fig. 5.7. The quantum algorithm is numerically stable. This is verified in the simulations for $t = 0\Delta t$, $t = 5\mathrm{K}\Delta t$, $t = 10\mathrm{K}\Delta t$. The simulation error in soliton speed after 10K iterations is only 0.5% (about 5 lattice grid points on the 1024 grid).

Transverse Modulation Instability of the 1D Soliton Wave Train

A transverse perturbation of the form of (5.77) with wavenumber $p = 2\pi N/L_y, N = 8$ with an amplitude that is a factor of 10^-7 below the initial wave train amplitude. The asymptotic linear stability predicts that the 1D soliton train should break up into 8 filamentary structures, an unstable phase, as shown in Fig. 5.8. This is indeed found in our simulations, with the filamentary structures becoming so isolated and peaked that the steep gradient of the wave function cannot be resolved on the grid after about $t = 2100\Delta t$ iterations, even on using a 1024×1024 lattice.

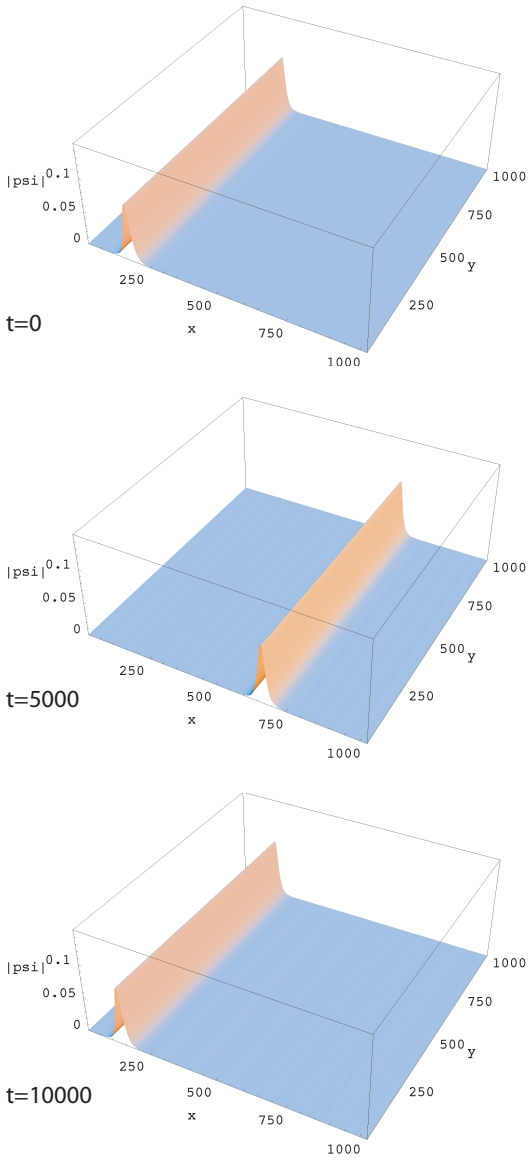

Figure 5.7: Evolution of a 1D soliton wave train for the NLS equation in 2+1 dimensions on a 1024^2 grid with periodic boundary conditions. No transverse modulation instabilities are triggered, even after 10,000 iterations. By $t = 10,1000\Delta t$ (bottom), the wave train has wrapped around the grid.

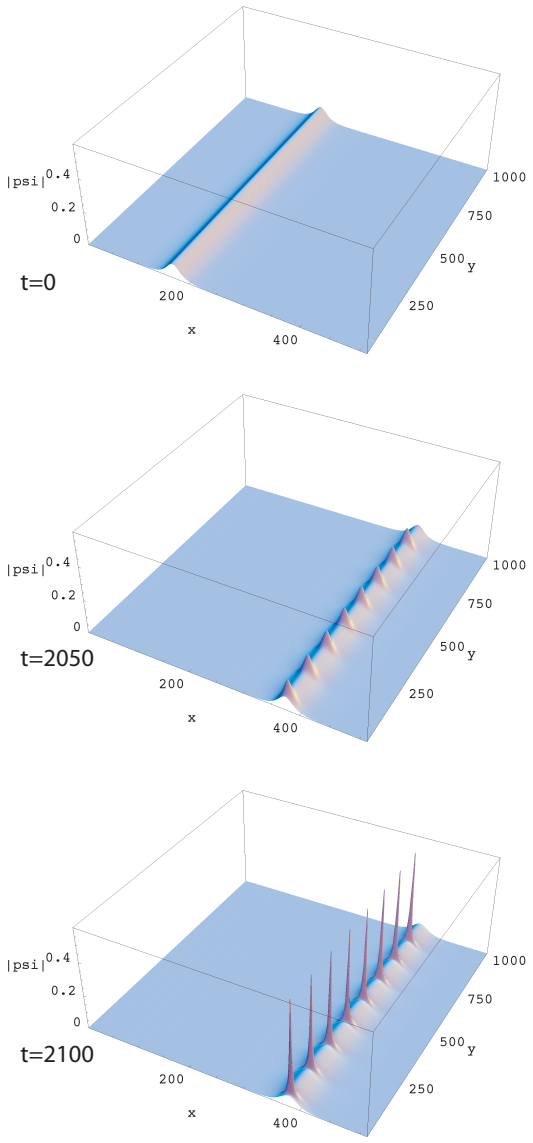

Figure 5.8: Evolution of a 1D soliton wave train for the NLS equation in 2+1 dimensions on a 1024^2 grid (only half the grid is shown) with a transverse perturbation with amplitude 10^{-7} lower than the initial peak amplitude of the soliton wave train. A transverse modulation instability is triggered, clearly observable after $t = 2000\Delta t$ time steps.

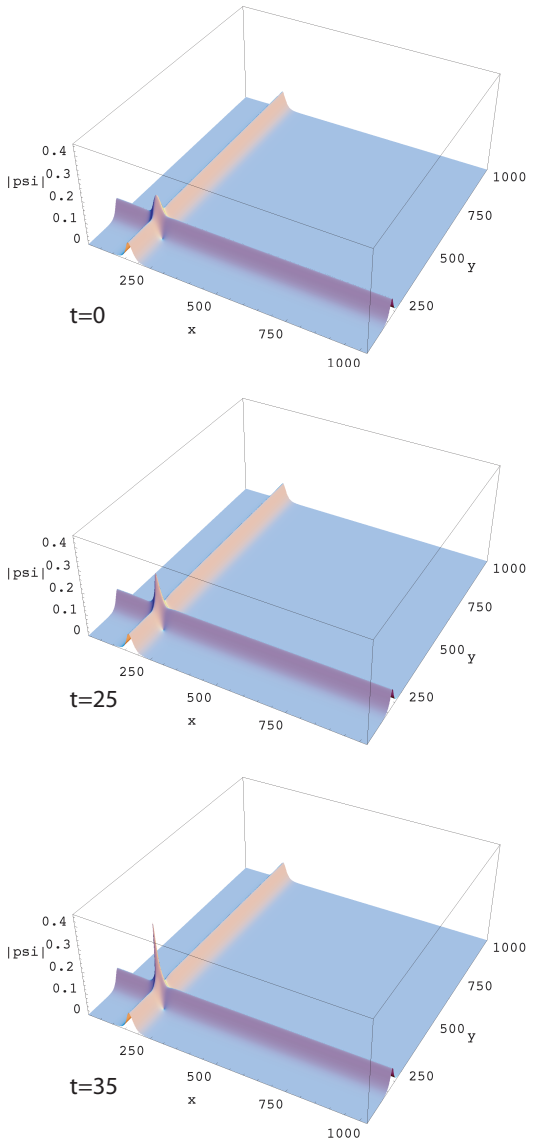

Figure 5.9: Evolution of a two orthogonally directed 1D soliton wave trains for the NLS equation in 2+1 dimensions on a 1024^2 grid. An rapid instability is immediately triggered, creating a rising peak at the intersection point of the solitons that reached the grid resolution after $t = 35\Delta t$ time steps.

Interaction of Two Perpendicular Soliton Wave Trains

Finally, we consider the interaction of two perpendicularly directed soliton wave trains. No initial perturbations are needed due to the "overlap" region of the two wave trains. A very rapid instability is immediately triggered at the intersection region of the two wave trains, and its localization and peak are so rapid that the gradient of the wave function cannot be further resolved on the grid after just 35 time steps. The instability occurs only at the point of intersection of the two soliton trains and the unaffected regions of both soliton trains propagate in normal fashion. This expected behavior is observed in the simulation shown in Fig. 5.9.

5.4 3+1 dimensions

5.4.1 Quantum algorithm

We model a scalar wave function $\psi(\vec{x},t)$ governed by the one-body Schroedinger equation in 3+1 dimensions by using a 2-spinor field with component amplitudes

$$\begin{pmatrix}\alpha(\vec{x},t)\\ \beta(\vec{x},t)\end{pmatrix}, \tag{5.80}$$

where α and β complex numbers, and the scalar wave function is the "density" of the 2-spinor field

$$\Psi(\vec{x},t) = (1,1)\cdot\begin{pmatrix}\alpha(\vec{x},t)\\ \beta(\vec{x},t)\end{pmatrix} = \alpha(\vec{x},t)+\beta(\vec{x},t). \tag{5.81}$$

The streaming operators act independently on the components of the 2-spinor

$$\hat{S}_{\Delta\vec{x},0}\psi = \begin{pmatrix}\alpha(\vec{x}+\Delta\vec{x},t)\\ \beta(\vec{x},t)\end{pmatrix} \tag{5.82a}$$

$$\hat{S}_{\Delta\vec{x},1}\psi = \begin{pmatrix}\alpha(\vec{x},t)\\ \beta(\vec{x}+\Delta\vec{x},t).\end{pmatrix} \tag{5.82b}$$

With the 2-spinor field defined on a lattice with periodic boundary conditions, (5.82) are simply permutation operators, representing classical operations on the quantum state.

The collision operator causes local quantum entanglement of the spinor amplitudes

$$\hat{C}\,\psi(\vec{x},t) = \frac{1}{2}\begin{pmatrix}1-i & 1+i\\ 1+i & 1-i\end{pmatrix}\begin{pmatrix}\alpha(\vec{x},t)\\ \beta(\vec{x},t)\end{pmatrix}. \tag{5.83}$$

In a many-body setting, where α and β are the amplitudes of two on-site particles, then from a quantum information viewpoint $\hat{C}$ is the $\sqrt{\text{SWAP}}$ quantum logic gate. Yet, here we

need only consider the one-body sector to explain the essence of the quantum algorithm. It is convenient to define the interleaved operator

$$\mathscr{I}_{\vec{x}\sigma} = \hat{S}_{-\Delta\vec{x},\sigma}\hat{C}\hat{S}_{\Delta\vec{x},\sigma}\hat{C}, \tag{5.84}$$

in terms of which the full evolution operator is defined

$$\hat{U}(\vec{x}) = \mathscr{I}^2_{x0}\mathscr{I}^2_{y1}\mathscr{I}^2_{z0}e^{-i\varepsilon^2\Omega(\vec{x})/2}\mathscr{I}^2_{z1}\mathscr{I}^2_{y0}\mathscr{I}^2_{x1}e^{-i\varepsilon^2\Omega(\vec{x})/2}, \tag{5.85}$$

where $\varepsilon \sim \frac{1}{N}$, where N is the grid resolution (*i.e.* N is the number of grid points along one edge of the simulation volume). In dimensionless units (hopping speed $c = 1$), note that $\varepsilon^2 \sim \Delta x^2 \sim \Delta t$.

The evolution operator is spatially dependent only through the gauge term and it is strictly local

$$\psi(\vec{x}, t + \Delta t) = \hat{U}(\vec{x})\psi(\vec{x}, t). \tag{5.86}$$

5.4.2 Effective field theory

The R.H.S. of (5.86) is a finite-difference of ψ, which is too long to write out here. If we Taylor expand the R.H.S. in ε, we obtain the following quantum lattice gas equation

$$\begin{pmatrix}\alpha'\\ \beta'\end{pmatrix} = \begin{pmatrix}\beta\\ \alpha\end{pmatrix} + i\frac{\varepsilon^2}{2}\nabla^2\begin{pmatrix}\beta\\ \alpha\end{pmatrix} - i\varepsilon^2\Omega\begin{pmatrix}\alpha\\ \beta\end{pmatrix} + \frac{\varepsilon^3}{4}\nabla^3\begin{pmatrix}\alpha - i\beta\\ -\beta + i\alpha\end{pmatrix} + \mathcal{O}(\varepsilon^4). \tag{5.87}$$

where $\begin{pmatrix}\alpha'\\ \beta'\end{pmatrix} = \psi(\vec{x}, t + \Delta t)$. (5.89) is considered a valid dynamical equation of motion only in the situation where the 2-spinor field is everywhere near local equilibrium. We remark that this statement about local equilibrium is equivalent to requiring that all the relevant dynamics is modeled by long wavelength and low frequency modes of (5.86) in the continuum limit approximation. Therefore, we first consider the local equilibrium configuration with respect to the collision operator, defined as follows:

$$\begin{pmatrix}\alpha^{\text{leq}}\\ \beta^{\text{leq}}\end{pmatrix} \equiv \hat{C}\begin{pmatrix}\alpha^{\text{leq}}\\ \beta^{\text{leq}}\end{pmatrix}. \tag{5.88}$$

Since the ket $\begin{pmatrix}1\\ 1\end{pmatrix}$ is an eigenvector of $\hat{C}$, we require $\alpha^{\text{leq}} = \beta^{\text{leq}}$ as our principal condition for local equilibrium. Then, the locally equilibrated quantum lattice gas equation (with equal spinor components $\frac{\Psi}{2}$) is the following:

$$\begin{pmatrix}\frac{\Psi}{2}'\\ \frac{\Psi}{2}'\end{pmatrix} = \begin{pmatrix}\frac{\Psi}{2}\\ \frac{\Psi}{2}\end{pmatrix} - i\frac{\varepsilon^2}{2}\nabla^2\begin{pmatrix}\frac{\Psi}{2}\\ \frac{\Psi}{2}\end{pmatrix} + i\varepsilon^2\Omega\begin{pmatrix}\frac{\Psi}{2}\\ \frac{\Psi}{2}\end{pmatrix} + \frac{\varepsilon^3}{4}\nabla^3\begin{pmatrix}\frac{\Psi}{2}\\ -\frac{\Psi}{2}\end{pmatrix} + i\frac{\varepsilon^3}{4}\nabla^3\begin{pmatrix}\frac{\Psi}{2}\\ -\frac{\Psi}{2}\end{pmatrix} + \mathcal{O}(\varepsilon^4). \tag{5.89}$$

So the equation of motion for the scalar density (5.81) becomes a finite-difference of the Schroedinger wave equation

$$\Psi' = \Psi - i\frac{\varepsilon^2}{2}\nabla^2\Psi + i\varepsilon^2\Omega\,\Psi + \mathcal{O}(\varepsilon^4), \tag{5.90}$$

where the real and imaginary parts of the cubic terms cancel out, separately. Defining the partial time derivative as $\partial_t\Psi \equiv \lim_{\varepsilon\to 0}\frac{\Psi'-\Psi}{\varepsilon^2}$, in the continuum limit the effective field theory becomes

$$i\partial_t\Psi = -\frac{1}{2}\frac{\Delta x^2}{\Delta t}\nabla^2\Psi + \Omega\Psi. \tag{5.91}$$

The Hamiltonian operator that generates the evolution, $\hat{U} = e^{i\Delta t\hat{H}/\hbar}$, is the following

$$\hat{H} = -\frac{\hbar^2}{2m}\nabla^2 + \hbar\Omega(\vec{x}) + \mathcal{O}(\hbar\Delta t^2, \hbar\Delta x^4), \tag{5.92}$$

where we have written the "diffusion" coefficient as $\frac{\Delta x^2}{\Delta t} = \frac{\hbar}{m}$. We promote (5.91) to the nonlinear Schroedinger equation by writing the local gauge term with an external part and a nonlinear internal part

$$\hbar\,\Omega(\vec{x}) = V(\vec{x}) + U|\Psi(\vec{x})|^2, \tag{5.93}$$

where U is the on-site two-body interaction energy (not to be confused with the unitary evolution operator $\hat{U}$). Finally, we obtain the Gross-Pitaevskii equation for the special case when the external trapping potential is parabolic, $V(\vec{x}) = k\,r^2$, where $r = \sqrt{x^2+y^2+z^2}$.

5.5 Summary

Presented was a lattice-based quantum algorithmic method to numerically model time-dependent solutions of the Schrödinger wave equation in an arbitrary number of spatial dimensions using a fourth-order accurate operator splitting method. Here we tested the method in 1+1, 2+1, and 3+1 dimensions, including modeling a quantum system with a nonlinear potential. These were the first numerical test of the quantum lattice gas algorithm in multiple spatial dimensions–all previous simulation results that have appeared in the literature have been for 1+1 dimensional cases. Furthermore, we probed to determine if the quantum algorithm was cable of accurately modeling the expected physical behavior of the nonlinear quantum system by triggering the onset of strong and rapid nonlinear instabilities in solitary wave trains. This was a stringent test of the method.

In all the cases, the quantum algorithm performed excellently with the numerical results in perfect agreement with the theoretical predictions. Ultimately, in tracking the late time developed of the growth of the instabilities, we were limited by our fixed grid resolution. To follow the quantum evolution for significantly longer periods of time following the onset

of a nonlinear instability, one could introduce adaptive mesh refinements into our quantum algorithmic scheme.

Chapter 6

Introduction to Type II analog quantum computing

There exists a class of quantum algorithms that also requires many qubits (at least millions), but which only requires that the qubits be entangled over short ranges (the width of a single molecule) and for only short times (less than the natural T_2 spin-spin decoherence time) [Yepez, 1998, Yepez, 1999]. Such quantum algorithms are suited for implementation on large parallel arrays of small quantum computers, with each quantum-computing node embodying only a few qubits, and where a classical communication network connects the nodes together. Such a hybrid quantum computing architecture is a second type of analog quantum computer I have that termed a *type II quantum computer* [Yepez, 2001c].

Type II quantum computers offer a practical solution for general purpose computing for several reasons. Here are three primary ones:

1. Only a limited degree (in both space and time) of quantum phase-coherence is required and therefore type II quantum computers can be built today.

2. Its computational power grows exponentially in the number of phase-coherent qubits per node. (I discuss "computational power" in terms of algorithm complexity in Section 11.6.)

3. The number of quantum bits per unit volume is naturally commensurate with the density of matter in the liquid or solid state (that is, on the scale of Avagadro's number of qubits per cubic centimeter) over arbitrarily large volumes. Therefore, the achievable computational power is not limited by technological difficulties but is mainly limited by the cost of the technological implemenation, as is characteristic of massively parallel classical computing architectures.

With the one exception of a measurement step, the type II quantum computing architecture is identical to the type I architecture discussed in Section 3. The measurement step is continually and spatially homogeneously applied to all lattice nodes causing repeated wave function collapse to mitigate against uncontrolled decoherence. Hence, a type II quantum computer is characterized by both classical parallelism (there being effectively many small quantum computer nodes) and quantum parallelism (there being, quantum entanglement within each node for some short time span). Therefore, a type II quantum algorithm is a hybrid algorithm that is part quantum mechanical and part classical. The quantum part of the algorithm requires quantum state preparation, application of two-qubit quantum gates [DeVincenzo, 1995, Barenco et al., 1995, Barenco, 1995], and a measurement protocol. The classical part of the algorithm involves transferring information between qubit (spin) pairs. This is done by preparing the state of some qubit in the quantum computer to be equal to the state of some other qubit that was previously measured in the quantum computer. Hence, its computational power is related to the product of the number of nodes in the array times the number of quantum states per node that can be entangled.

6.1 Three spatial scales

There are three spatial scales used to describe the behavior of a type II quantum computer: the sub-scale, the middle scale, and the super-scale. In Section 3.1 we have already discussed the sub-scale and the super-scale. These descriptive regimes also apply to type II quantum computing. That is, at the sub-scale, all the quantum dynamics of the type II quantum computer occurs on a discrete spatial lattice, just as in the type I case. Again, the Hamiltonian of the sub-scale quantum system is an engineered one, produced by a program of externally applied controls as discussed in Section 3. In effect, one quantum spin system, on a discrete lattice with a Hamiltonian of our choosing, is engineered to act like another quantum system.

The middle scale is a regime between the sub-scale and super-scale where the probability of finding a spin in a spin-up state is a real-valued quantity. This is called an *occupancy probability*, which is well-defined only at the mesoscopic scale. The mesoscopic spin dynamics are still spatially and temporally discrete.

One can then describe the dynamical behavior of the "programmed" quantum spin system at a middle scale by a finite-difference quantum Boltzmann equation. The sub-scale spin system at the middle scale is isomorphic to a mesoscopic many-body particle system, whose kinetic behavior is described by a quantum Boltzmann equation with a highly nonlinear collision function. The quantum Boltzmann equation models the dynamical behavior

of the occupation probabilities of the the kinetic particle's positional state encoded in a qubit's excited energy state. To estimate an occupation probability experimentally, one may employ an ensemble or repeated measurement over identical sub-scale realizations, or a coarse-grained or block measurement of a single sub-scale realizations, to determine the occupancy of the two-level energy eigenstates of each qubit in the system. In this way a discrete field of probabilities is obtained, one probability per qubit. At this middle scale, the occupancy probabilities are defined only on the lattice points, so these probabilities constitute a discrete field of real-valued quantities. The quantum lattice Boltzmann equation for kinetic transport exactly governs the dynamical evolution of this spatially discrete probability field.

Finally, to bridge the gap to the super-scale, the number of lattice points is increased towards infinite spatial resolution, the continuum limit, and the resulting effective field becomes both a continuous and differentiable field. However, the effective field is not a modeled wave function as in the type I quantum computing case. Instead, it represents a dynamical classical field at the physical macroscopic scale. The middle-scale occupancy probabilities at each site of the lattice are summed together to determine what is called a *number density field*. In turn, this number density field may be mapped onto a temperature field, mass density field, or a flow field. These continuous field quantities are well defined only when the cell size of the lattice approaches zero. So, this different approach involving state reduction or measurement, allows us to use a type II quantum computer to model very different super-scale effective fields, in particular classical physical field quantities governed by dissipative dynamical equations of motion.

Its dynamical evolution is approximately described, to any order of desired precision, by a dissipative parabolic partial differential equation of motion. To be clear, the origin of the dissipation terms in the effective equation of motion is the continual wave function collapse that is induced at the sub-scale of the type II quantum computer. This is in stark contrast to the effective equation of motion of a type I quantum computer model which in principle have no dissipative terms.

The effective equation of motion of a type II quantum computer is chosen by construction, for example it may be a fluid-like equation, but it is not possible to arbitrarily select a priori any equation of motion one may want to model. There is a well defined procedure for deriving the operative effective field theory, which may turn out to be the heat equation, Burgers equation, the wave equation, magnetohydrodynamic equations, or the Navier-Stokes equation, for example, depending on the quantum gate protocol employed and the number of qubit per lattice node.

I know of no procedure to go in the opposite direction. If one chooses any dissipative partial differential equation of motion a priori, it may not be possible to find the appropri-

ate quantum gate and quantum circuit topology needed to reproduce this particular partial differential equation as the operative effective field theory of the type II quantum computer. Obtaining a particular equation of motion specified a priori requires intuition and a great deal of experience dealing with the quantum Boltzmann equation formulation. As a "programmed" aid, it is convenient to use symbolic software to predict the emergent effective field theory for a particular quantum gate protocol. Perhaps in the future, quantum gate protocols for a specified effective field theory could be automatically generated by an intelligent computer program, perhaps using the genetic algorithms approach.

In any case, we consider the type II quantum computer to be a model of the physical system described by that equation of motion so long as the super-scale effective field theory of the type II quantum computer approximates the physical equation of motion to within an acceptable level of numerical error. In this sense, the sub-scale quantum mechanical system is programmed to act, at its super-scale, like a physical macroscopic-scale classical system.

In contrast to the type I quantum algorithms discussed in Section 3, the middle scale behavior of the type II quantum lattice gas presented here is classical in nature, even though the microscopic scale dynamics is quantum mechanical, and even though the quantum collision function has nonlinearities with no classical interpretation. As already mentioned, this is due to the collapse of each qubit of the quantum computer after each and every application of a local quantum mechanical collision operator independently applied on each site or node of the system. Therefore, unlike the type I quantum computing case, a mean-field approximation of the quantum Boltzmann equation associated with a type II quantum computer that neglects high-order particle-particle (spin-spin) correlations can be readily implemented on a classical computer. This is very much in analogy with the implementation of a mean-field lattice Boltzmann equation to represent the mesoscopic dynamics of a classical lattice gas system [McNamara and Zanetti, 1988].

6.2 Efficiency of type II quantum computing

A speedup due to quantum parallelism is a salient characteristic of a type II quantum computer with the periodic measurement process. There are three advantages of nano-scale quantum computing technology that significantly reduce the algorithmic complexity of computational physics applications.

1. The dissipation in the modeled physical system, such as the viscosity of a fluid system, can be made arbitrarily small without numerical instabilities or any added computational overhead. Our basic approach is to set the transport coefficient, such as the shear viscosity, to a sufficiently low value that the number of time steps needed to advance

the numerical simulation forward one physical unit of time is order unity regardless of the grid size.

2. By using the nano-scale device technology to store and process information with short logic gate times, it is practical to physically build ensemble averaging directly into the "hardware" of the quantum computer [Pravia et al., 2002, Pravia et al., 2003]. Hence, we can make the computational overhead associated with ensemble averaging be order unity.

3. Exploiting quantum entanglement within each node, the amount of required local resources needed to compute the nonlinear collision function is logarithmically less than the required resources of the classical lattice-gas algorithm.

Speedup occurs even though the quantum mechanical superposition of states is restricted to only a sub-manifold of the full Hilbert space. In principle, it is possible to gain a speedup because the computational work required to implement the collision process is order unity in certain cases. This is possible because the Hamiltonian (say a molecular spin system of a hydrogen and carbon 13 nuclei of Section 2.12) governing the evolution of a node conserves certain quantities, such as the total magnetization along an external applied uniform magnetic field which can be mapped to a conserved quantity such as the mass density of the modeled classical physical system.

In the quantum lattice-gas model of Section 9, the total magnetization is mapped on to a field quantity that is governed by the Burgers equation in the continuum limit. Therefore, once the appropriate quantum state preparation is completed on each node of the type II quantum computer, only one unitary transformation step is needed before the quantum state of each qubit is measured. By refocusing two-spin interactions in a nuclear magnetic resonance quantum computer [Jones and Knill, 1999], the collision process can therefore be computed. Other conserved quantities of the on-site Hamiltonian may be mapped to recover the macroscopic-scale evolution of additional field quantities. For example, the square of the total spin may be mapped onto a conserved local momentum vector to recover nonlinear hydrodynamic flow.

Therefore, with the three advantages of tunable viscosity, inherent ensemble averaging, and localized quantum entanglement, in Section 11.6 we give an argument for a speedup that goes as the reciprocal of the Reynolds number, $\frac{1}{\mathrm{Re}}$, for computational Navier-Stokes fluid dynamics simulation carried out with a quantum lattice gas versus the classical lattice gas model. The quantum speedup therefore improves with the modeled fluid's nonlinearity.

The usefulness of the type-II quantum computing approach is that practical and efficient computation can be carried out at the mesoscopic scale by an emergent finite-difference

quantum Boltzmann transport equation to model a broad class of classical effective field theories in an unconditionally stable manner. The controlled state reduction process in effect "factorizes" the collision function in the quantum Boltzmann equation so that quantum superpositions and entanglement cannot spread throughout the quantum computer. This keeps quantum entanglement localized within the lattice nodes for a short duration of time, less than the spin-spin decoherence time of the physical system in question [1]. In this way, the controlled state reduction process mitigates against any uncontrolled decoherence mechanisms that would otherwise destroy the phase coherence of the quantum computer's wavefunction.

6.3 Controlled state reduction

The state reduction of a phase-coherent quantum system may be induced by either measurement or be intrinsic to the quantum system's unitary evolution. The subject of the measurement apparatus as an open quantum mechanical system has been studied as a means for understanding the reduction of a quantum state following observation of the system [Zurek, 1981, Zurek, 1982, Walls et al., 1985]. Alternatively, there have been proposals [Ghirardi et al., 1986, Milburn, 1987, Pearle, 1989, Diósi, 1989, Ghirardi et al., 1990, Milburn, 1991] that modify the fundamental quantum theory to include microscopic processes that inherently cause the reduction of the quantum state as a way to naturally give rise to macroscopic scale dissipative behavior. One approach due to Milburn for modifying the Schrödinger equation is to introduce a minimum time step for the quantum mechanical evolution where at each time step there is a randomization of the unitary phase generated by the system Hamiltonian [Milburn, 1987, Milburn, 1991]. The resulting evolution is a sequence of unitary transformations instead of being continuous and this evolution sufficiently describes decoherence in open quantum systems [Buzek and Konôpka, 1998]. At "laboratory" time scales much larger than this minimum time step, the evolution appears continuous; the Schrödinger equation is recovered at zeroth order and the decay of coherence in the energy eigenstate basis is recovered at first order. Caves *et al.* have developed models of continual quantum measurements distributed in time [Caves, 1986, Caves and Milburn, 1987] and has developed a path-integral formulation of a one-dimensional quantum system governed by two rules: (1) between measurements unitary evolution and (2) at each measurement collapse of

[1] Nuclear spins precess at a frequency of $\omega = \frac{geB}{mc}$ about the externally applied magnetic field B. They can precess in phase with each other only for a characteristic time called the *spin-spin decoherence time*, usually denoted by T_2. Moreover, the *relaxation time* usually denoted T_1, which is greater than T_2, is the characteristic time required for the spins to relax back to the energy eigenstates of the two-level spin-system, where these two eigenstates are populated according to the Boltzmann equilibrium occupancy probabilities.

the wave function.

6.4 The historical development

For the purpose of testing quantum lattice-gas dynamics on a *type II quantum computer* (a massively parallel array of small quantum computers) [Yepez, 2001b], it is prudent to use the simplest of models so that results from prototype experimental implementations can most readily and easily be compared to results obtained by numerical simulations on conventional computers.

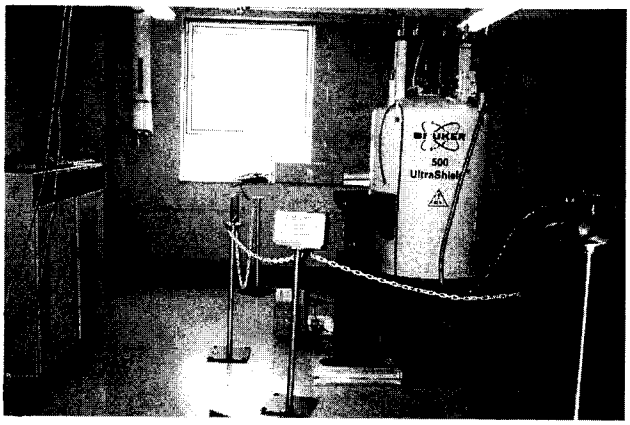

Figure 6.1: NMR quantum computer: Quantum computing facility at the Air Force Research Laboratory, Hanscom AFB. Bruker Ultrashield 500MHz NMR Spectrometer.

A type II quantum computer prototype is presently under joint development by the Air Force Research Laboratory and the department of Nuclear Engineering at MIT using a spatial nuclear magnetic resonance spectroscopic technique, see Figure 6.1. The quantum lattice gas algorithm for the diffusion equation presented in Section 8 and the Burgers equation presented in Section 9 both served as baseline numerical test cases for the type-II quantum computing experiment.

The reason we chose these test cases is that the prediction of solutions obtained with the quantum algorithm can be compared against exact solutions obtained by analytical means. The simplest lattice-gas models are one-dimensional [Boghosian and Levermore, 1987, Qian et al., 1992b] and have only a single conserved quantity, the particle number. The macroscopic field, well defined in the continuum limit and which corresponds to microscopic particle conservation, is the mass-density field. The simplest particle conserving dynamics is diffusion. Therefore, a quantum lattice-gas model can be used to simmulate the behavior of a macroscopic mass-density field governed by a parabolic diffusion equation in the long-wavelength limit.

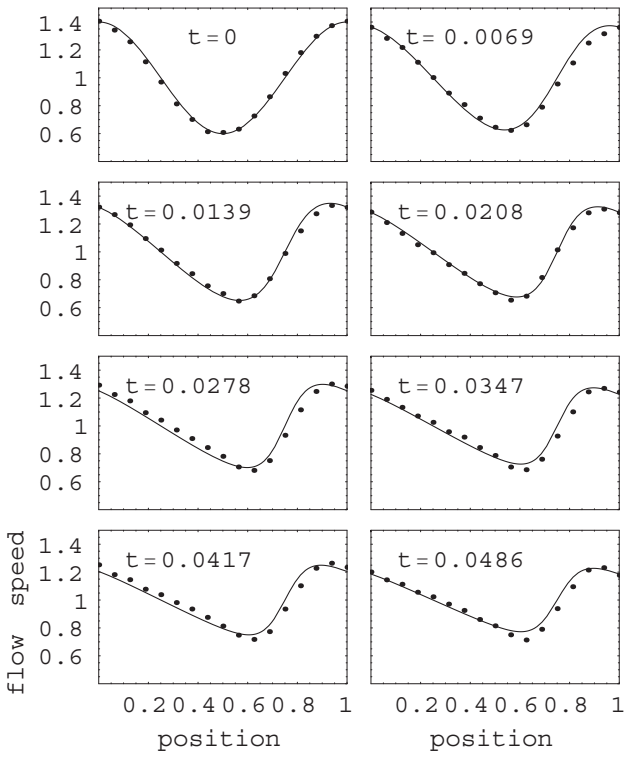

Figure 6.2: Inviscid flow governed by the Burgers equation: Type-II NMR quantum computer solution of the Burgers equation, a simple mode of turbulence and shock formation. Experimental NMR data (dots) versus analytical solution (curves). Lattice size: 16 nodes. Viscosity: $\nu = \frac{1}{4}\frac{\Delta x^2}{\Delta t}$. In collaboration with the MIT Nuclear Engineering Department [Chen et al., 2006a].

The quantum algorithm presented in Section 9 for modeling the nonlinear Burgers equation represents a stronger numerical test of the modeling utility of quantum computers because the Burgers equation is a difficult nonlinear partial differential equation to accurately model without numerical instabilities, as demonstrated in Figure 6.2. Its applications to turbulence, intermittency, structures in a self-gravitating medium [Shandarin and Zeldovich, 1989] and shock formation in inelastic gases [Ben-Naim et al., 1999] gives the Burgers equation unique importance in the field of computational physics.

Only two qubits are needed at each node of the type II quantum computer and a single quantum gate is simultaneously and independently applied to all the nodes. In general, to solve nonlinear partial differential equations in two and three dimensions, more than two qubits per node is required. The minimum number of qubits required for various nonlinear systems, including the Burgers equation, in two and three dimensions is presently unknown.

A quantum algorithm presented in Section 10 for the nonintegrable magnetohydrodynamic equations in one dimension has been developed and tested [Vahala et al., 2003c]. This quantum algorithm is a generalization of the quantum algorithm for Burgers equations. In this case, two nonlinear Burgers equations are modeled using the basis quantum algorithmic approach, but then modified so as to couple the Burgers equations. The resulting coupled system of equations, transformed using the Elsasser variables, accurately approximate the magnetohydrodynamic equations for a velocity field and a magnetic field.

Finally, in Section 11 we present the quantum algorithm for modeling the Navier-Stokes equation. We derive the effective field theory using a Chapman-Enskog perturbation expansion procedure. However, this quantum algorithm requiring six qubits per node has not yet been experimentally tested on the prototype NMR quantum computer.

6.5 State preparation using real-valued amplitudes

Each qubit embodied in a quantum spin of a type-II quantum computer is initialized using a single real-valued number in the range of zero to one, which we will denote as a_α. Since digital binary values are not used, but continuous amplitudes for the qubit state, the type II quantum computer may also be considered an analog quantum computer. With $|1\rangle$ and $|0\rangle$ denoting the true and false states of a qubit, then to start out, each qubit is placed into internal superposition according to the following prescription:

$$|q_\alpha\rangle = \sqrt{a_\alpha}\,|1\rangle + \sqrt{1-a_\alpha}\,|0\rangle,$$

for $\alpha = 1, 2, \ldots, Q$. This is a simple way of encoding the probability that the qubit is true using the value $a_\alpha = \cos^2\varphi_\alpha$, and the probability it is false using the value $1 - a_\alpha = \sin^2\varphi_\alpha$.

6.6 Conservative quantum gates

For two qubits, there are two numbers, a and b say, that are needed to specify the tipping angles, and in turn the amplitudes of the four possible numbered states: $|11\rangle$, $|10\rangle$, $|01\rangle$, and $|00\rangle$. Each of the qubits is set independently:

$$|q_1\rangle = \sqrt{a}\,|1\rangle + \sqrt{1-a}\,|0\rangle$$

and

$$|q_2\rangle = \sqrt{b}\,|1\rangle + \sqrt{1-b}\,|0\rangle.$$

We can see how analog quantum logic works by considering our initial two-qubit state as the input to the various gates of interest and writing down the respective outputs.

We begin with the logical swap gate, which is the most basic two-qubit gate. It simply exchanges the amplitudes corresponding to the basis states $|10\rangle$ and $|01\rangle$ and it has no affect on the amplitudes corresponding to the basis states $|11\rangle$ and $|00\rangle$, where the first qubit has value b and the second has value a. So by exchanging the amplitudes, the swap gate exchanges the probabilities as depicted in Figure 6.3A.

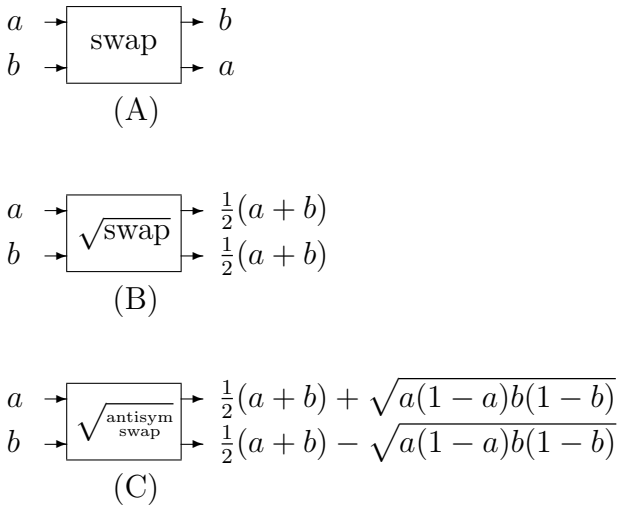

Figure 6.3: Analog quantum logic gates: (A) swap gate, (B) $\sqrt{\text{swap}}$ gate, and (C) antisymmetric $\sqrt{\text{swap}}$ gate.

The actions of the symmetric and antisymmetric $\sqrt{\text{swap}}$ gates entangle their two input qubits. Hence, for these analog quantum gates, the output values for each qubit following a measurement will depend on the values a and b of both input qubits. These analog quantum gates are depicted in Figures 6.3B and 6.3C, respectively. Both of these gates are said to be *conservative* because the sum of their input values equals the sum of their output values: $a + b$.

6.7 Nonlinear scattering

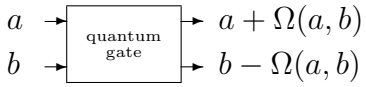

Figure 6.4: General conservative quantum logic gate: $\Omega(a, b)$ is a nonlinear *collision function* of the inputs a and b specifying the operation of the gate.

In Figure 6.4, we express the output values of a conservative quantum logic gate as a nonlinear function of the inputs a and b. This function called the *collision function* and is denoted here by $\Omega(a, b)$. The general form of the collision function is

$$\Omega(a, b) = \sin^2 \theta(b - a) + \sin 2\theta \cos \xi \sqrt{a(1 - a)b(1 - b)}. \tag{6.1}$$

We can think of a quantum logic gate as causing a scattering event where the input quantum particles entering the gate "collide" with each other and subsequently exit the gate with altered probability amplitudes. For $\theta = \frac{\pi}{2}$, the collision function causes a swap operation. For $\theta = \frac{\pi}{4}$ and $\xi = \frac{\pi}{2}$, it causes a $\sqrt{\text{swap}}$ operation. For $\theta = \frac{\pi}{4}$ and $\xi = \frac{\pi}{4}$, it causes an antisymmetric $\sqrt{\text{swap}}$ operation.

A simple version of a general result from Section 7: At the mesoscopic scale, the collision function is determined by the matrix element

$$\langle q_\alpha q_\beta | e^{z^* \hat{H}} \hat{n}_\gamma e^{z \hat{H}} - \hat{n}_\gamma | q_\alpha q_\beta \rangle,$$

where α is an index referring to one qubit and β refers to another qubit, where $\gamma = \alpha$ or β, and where $\hat{n}_\gamma$ is a qubit number operator.

If the scattering process shown in Figure 6.4, which includes the evaluation of a nonlinear collision function, were to be computed in the traditional way using a conventional floating-point coprocessor, it would entail 6 additions and subtractions, 8 multiplies, 3 trignometric functions, and 1 square root operation, all of which would be floating-point operations. Using an iterative Newton-Raphson algorithm, the square root operation takes 13 floating-point operations for the newest Intel Itanium 64-bit architecture (IA-64). The floating-point operations required for a sinusoid computation is about two to three times that required for the square root operation. Using the coordinate rotation digital computer algorithm for the

sinusoids, the worst case is 50 multiplies. Hence, the quantum gate operation takes 6 + 8 + 3 (50) + 13 =177 equivalent floating-point operations.

The trigonometric factors $A \equiv \sin^2\theta$ and $B \equiv \sin 2\theta \cos\xi$ are actually fixed by the Euler angles chosen for the quantum gate, and for physical modeling applications, these factors can be considered pre-computed quantities. The number of equivalent floating-point operations is reduced to 6 additions and subtractions, 5 multiplies, and 1 square root operation:

$$\begin{aligned} a' &= a + A*(b-a) + B*\sqrt{a*(1-a)*b*(1-b)} \\ b' &= b - A*(b-a) - B*\sqrt{a*(1-a)*b*(1-b)}, \end{aligned}$$

where the evaluation of the collision function $\Omega(a,b)$ is counted only once. Hence, the quantum gate operation takes 6 + 5 + 13 =24 equivalent floating-point operations.

6.8 Quantum analog circuits

As an alternative to the formal description of (2.96) applied to quantum spin systems, we can think of quantum algorithms represented graphically. We image an abstract quantum circuit through which quantum particles move or "flow." Throughout this review, we will switch between the two different, but isomorphic, pictures. Circuits can be made out of

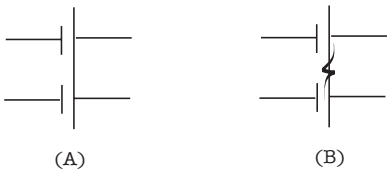

Figure 6.5: Logic symbols for quantum $\sqrt{\text{swap}}$ gates : (A) symmetric and (B) antisymmetric.

these two-input and two-output quantum gates by connecting the output "lines" of one gate to the "input" lines of some other gate in various topological configurations. To help make the task of drawing quantum circuits more simple, we follow the convention used to draw classical electrical circuits by assigning logic symbols to each fundamental element in the circuit. Quantum logic symbols for our $\sqrt{\text{swap}}$ gates are given in Figure 6.5. The inputs and outputs are connected by "wires," which are not necessarily electrical wires; these quantum wires carry quantum particles and these wires are not necessarily made out of conductive metals, such as aluminum. At the moment we will think of these circuits and their interconnecting wires in an abstract way.

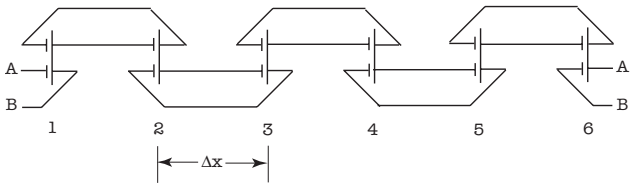

Figure 6.6: An analog quantum circuit for modeling diffusion: Point A connects to point A, and point B connects to point B in periodic fashion.

6.9 The diffusion equation

Figure 6.6 shows a simple quantum circuit with six nodes connected together to form a periodic one-dimensional lattice. This circuit is periodic because the end points on the left side of the circuit labeled A and B are connected to the end points on the right side and so the starting point for numerically labeling the nodes is arbitrary. The circuit shown in Figure 6.6 is symmetrical in two ways. First of all, the connections between each node and its neighbors are identical for all the nodes. So if the circuit is periodically shifted from left to right by a distance Δx, or any multiple thereof, the circuit remains the same. Second of all, the circuit looks the same whether viewed from the top or from the bottom. If it is flipped over and shifted by Δx, it looks exactly the same as before. There are a large number of ways we could connect together a linear array of gates, but it is only the symmetric circuits that are useful for our purposes of physical modeling. It is possible to write down

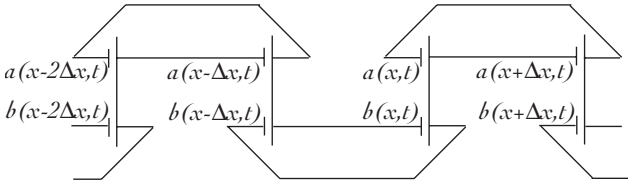

Figure 6.7: Circuit fragment with labeled input values.

a simple discrete equation, called a *finite-difference equation*, that describes the behavior of this circuit. We shall consider the inputs a and b to depend on a position variable x and time variable t, so all the inputs taken together as an ordered set constitute a time-dependent field that is a function of x and t. That is, the field of inputs is denoted $a(x,t)$ and $b(x,t)$, and the subsequent field of outputs is denoted $a(x,t+\Delta t)$ and $b(x,t+\Delta t)$, where Δt is the small amount of time it takes for the analog quantum gate to convert its inputs to outputs. As a simplification, we imagine that all the gate operations occur in lock-step fashion, so the circuit can be said to be *clocked*.

The finite-difference equation is said to be a *mesoscopic* description of the quantum

circuit. The mesoscopic scale is a middle scale between the smallest microscopic scale, where we can see the motions of individual quantum particles, and the macroscopic scale, which is so large a spatial scale where we cannot even distinguish the individual gates, let alone the individual quantum particles. At the mesoscopic scale, we can still clearly distinguish the individual gates, but there are so many quantum particles that we talk about their population density or frequency of occurrence using language from the subject of probability and statistics. At this medium scale, the inputs to the quantum gates a and b are continuous numbers, or analog quantities, which are the kind of numbers accurately and deterministically predicted by the theory of quantum mechanics.

6.9.1 A microscopic scale argument for diffusive behavior

It is possible to understand the behavior of the analog quantum circuit shown in Figure 6.6 by taking a purely microscopic viewpoint. Imagine that a single quantum particle is "placed" on one of the wires of the circuit. When this particle subsequently enters one of the input leads of a $\sqrt{\text{swap}}$ gate, the particle will simultaneously exit this quantum gate on both output leads, which is allowed by quantum superposition. The final measurement stage of the quantum gate then causes the collapse of the quantum particle's wave function. Consequently, the quantum particle will have an equal likelihood of ending up in a classical state on either one of the gate's output leads, but not on both. If it lands on the forward output lead, the particle can then "hop" a distance Δx to the next quantum gate up the chain, and if it lands on the backward output lead, it can hop a distance $-\Delta x$ to the previous quantum gate down the chain. Effectively, the quantum particle hops either forward or backward with equal likelihood, randomly making its way up and down the chain of quantum gates. Therefore, the action of the $\sqrt{\text{swap}}$ gates causes the quantum particle to undergo a random walk. Given a fixed number of time steps T, it is well known that random walkers on average move a distance $\sqrt{T}$. And this microscopic random-walk property is crucial to correctly understand the behavior of our quantum circuit from a macroscopic viewpoint. The diffusion equation constitutes an effective field theory that describes the behavior of a quantum spin system constrained by the topology of our simple quantum circuit. It relates the time rate of change of the number density field at some point x to the curvature of the field at that point. The greater the curvature, the faster the field changes, and this process causes the field to smooth out over time, as shown in Figure 6.8.

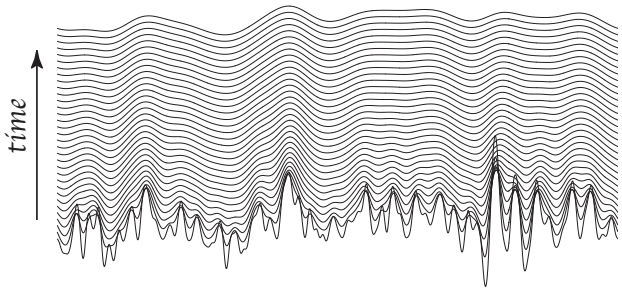

Figure 6.8: Diffusion equation: Diffusion on a linear quantum circuit of 2048 $\sqrt{\text{swap}}$ gates. Successive time profiles, sampled every 128 time steps, are over-plotted in the vertical.

6.9.2 A mesoscopic scale derivation of the macroscopic effective field theory

A result from Section 8: If we define a number density field as the sum of the qubit probabilities $\rho(x,t) = a(x,t) + b(x,t)$, then this field satisfies the diffusion equation

$$\frac{\partial \rho}{\partial t} = \frac{1}{2}\frac{\Delta x^2}{\Delta t}\frac{\partial^2 \rho}{\partial x^2},$$

if we neglect terms of order Δx^4 and Δt^2 or smaller.

As a quick derivation of this result, in this subsection we develop a set of finite-difference equations by expressing $a(x, t+\Delta t)$ and $b(x, t+\Delta t)$ in terms of the qubit probabilities at one time step earlier at time t, and then Taylor expand these equations. In Figure 6.6, each gate located at an even numbered node gets its input from the output of gates at neighboring odd numbered nodes, and vice versa. The spatial interval Δx shown in Figure 6.6 is called the *cell size* of the lattice. We can express the "new" input values $a(x, t+\Delta t)$ and $b(x, t+\Delta t)$ going to an odd-numbered node, located at position x say, in terms of the outputs of the $\sqrt{\text{swap}}$ operations that occurred at the neighboring nodes at positions $x+\Delta x$ and $x-\Delta x$ one time step earlier at time t. Thus we obtain the following finite-difference equations for all odd-numbered nodes:

$$\begin{aligned} a(x, t+\Delta t) &= \frac{1}{2}\left[a(x+\Delta x, t) + b(x+\Delta x, t)\right] \\ b(x, t+\Delta t) &= \frac{1}{2}\left[a(x-\Delta x, t) + b(x-\Delta x, t)\right]. \end{aligned}$$

A useful quantity to consider is the sum of the quantities a and b. This is called the *number density* and is denoted by $\rho = a+b$. The number density field $\rho(x,t)$ is a discrete field of real-valued quantities. If we add together the above two equations, we get a single finite-difference

equation for the number density:

$$\rho(x, t + \Delta t) = \frac{1}{2} \left[\rho(x + \Delta x, t) + \rho(x - \Delta x, t) \right]. \tag{6.2}$$

Similarly, the outputs for the even-numbered nodes are

$$\begin{aligned} a(x, t + \Delta t) &= \frac{1}{2} \left[a(x - \Delta x, t) + b(x - \Delta x, t) \right] \\ b(x, t + \Delta t) &= \frac{1}{2} \left[a(x + \Delta x, t) + b(x + \Delta x, t) \right], \end{aligned}$$

and when we add these two equations together we get the same result as before, so the finite-difference equation (6.2) applies to all nodes of the lattice and therefore is the operative equation describing the behavior of the analog quantum circuit shown in Figure 6.6.

For a one-dimensional array with L nodes (where in this case each node constitutes a single $\sqrt{\text{swap}}$ gate), the total size of the system is $L = N\Delta x$. Keeping L fixed, I would like to discuss how this circuit behaves when L becomes very large and Δx becomes very small. At the macroscopic scale, the cell size Δx and the gate time Δt both approach zero and are infinitesimally small quantities so the number density field $\rho(x, t)$ becomes a continuous field of real-valued quantities. Hence we can express the number density in (6.2) in differential point form using the Taylor expansion:

$$\rho(x, t + \Delta t) = \rho(x) + \Delta t \frac{\partial \rho}{\partial t} + \mathcal{O}(\Delta t^2).$$

This is possible because Δt is an infinitesimally small quantity at the macroscopic scale, yet we must remember that it is not actually zero, and so keep the error term of order Δt^2, which is denoted $\mathcal{O}(\Delta t^2)$, on the right hand side of the equation to account for this fact. We can also Taylor expand the number density about x but we have to make sure the error term in the x-expansion that we keep is of a comparable size to the error in the t-expansion so as to maintain consistency and balance in our approach. Because of the random walk nature of quantum particles in this circuit, we must expand ρ to fourth-order in the spatial terms:

$$\rho(x \pm \Delta x, t) = \rho(x) \pm \Delta x \frac{\partial \rho}{\partial x} + \frac{1}{2} \Delta x^2 \frac{\partial^2 \rho}{\partial x^2} \pm \frac{1}{6} \frac{\partial^3 \rho}{\partial x^3} + \mathcal{O}(\Delta x^4).$$

If we insert these Taylor expansions into the finite-difference equation (6.2), after some cancellation, we get the following partial differential equation:

$$\frac{\partial \rho}{\partial t} = \frac{1}{2} \frac{\Delta x^2}{\Delta t} \frac{\partial^2 \rho}{\partial x^2} + \mathcal{O}(\Delta t^2, \Delta x^4), \tag{6.3}$$

which the *diffusion equation*. The diffusive transport coefficient is $\nu = \frac{1}{2} \frac{\Delta x^2}{\Delta t}$. This partial differential equation constitutes an effective field theory that describes the behavior of a quantum spin system constrained by the topology of our simple quantum circuit.

6.9.3 Numerical accuracy

To test the accuracy and convergence of the quantum algorithm, we can compare the predicted numerical solution to the exact solution after a fixed number of time steps. To obtain the most statistically accurate results, we choose to initialize the circuit using the largest possible sinusoid with a wave length equal to the total size of the lattice. This test is repeated over a range of small to large lattices, and the numerical error is then calculated as the "distance" between the numerical and exact predictions. The total numerical error obtained from each test was plotted versus *inverse resolution* of the numerical simulation. The result, shown in Figure 6.9, is that the error accurately follows a power law $\Delta x^{4.471}$, which demonstrates that the actual numerical error is close to fourth order convergence in space as we had analytically predicted, and in fact the circuit behaves better than expected because it has a slightly higher rate of convergence.

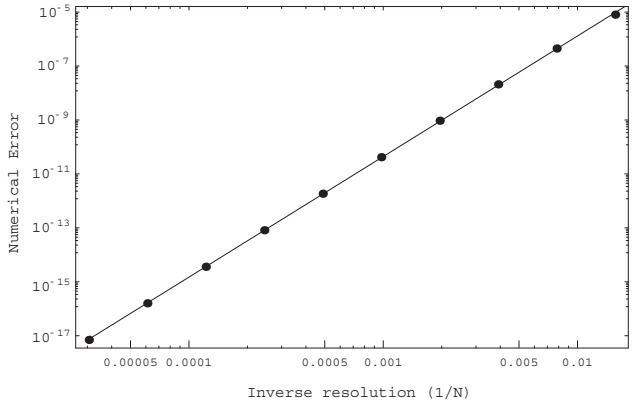

Figure 6.9: Diffusion equation: Numerical error as a function of the inverse of the grid resolution, $\frac{1}{N}$, graphed on a log-log plot for the quantum algorithm for the diffusion equation as described in Section 8.2. The data (black circles) are taken from numerical simulations with the number of nodes from $N = 64$ up to $N = 32768$. The slope of the best-fit regression line is 4.471.

6.10 Burgers equation

At the macroscopic scale, we can talk about the flux density of particles and the flow speed. For a conservative system with no source terms, the change per unit time of the number of particles within the interval x and $x + \Delta x$ can be related to the flux density entering and exiting that interval. Particles are driven "down-slope" by gradients in the number density field. This dynamics is linear. In fluids, such as air and water, the dynamics driving the motion of particles is a nonlinear one called *convection*, and we are able to model this process as well. If we replace all the gates in the strictly diffusive circuit of Figure 6.6, with

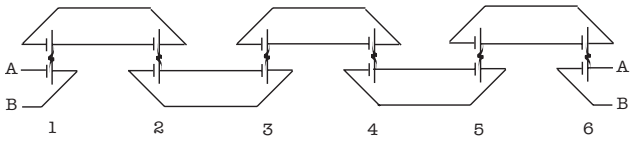

Figure 6.10: An analog quantum circuit for modeling shock formation. The quantum gates have alternating polarity from node to node. Point A connects to point A, and point B connects to point B in periodic fashion.

antisymmetric $\sqrt{\text{swap}}$ gates, the circuit becomes a nonlinear one in the sense that there is a new nonlinear term that appears in the effective field theory governing the quantum spin system within the circuit. Since an antisymmetric $\sqrt{\text{swap}}$ gate has a definite polarity, to retain the required symmetry of the circuit as we discussed above, we need to orient the gates in alternating fashion from node to node as shown in Figure 6.10.

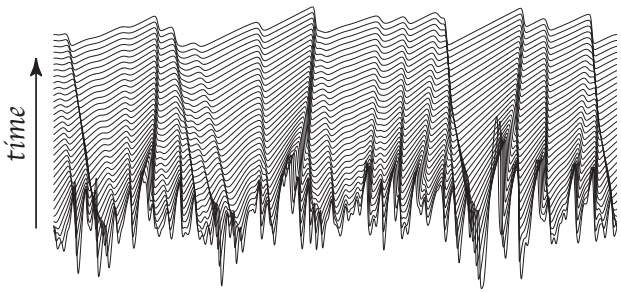

Figure 6.11: Dynamical evolution governed by the Burgers equation: Diffusion and shock formation on a linear quantum circuit of 2048 antisymmetric $\sqrt{\text{swap}}$ gates. Successive time profiles, sampled every 128 time steps, are over-plotted in the vertical.

A result from Section 9: The spacetime-dependent macroscopic behavior of the quantum circuit shown in Figure 6.12 is governed by the nonlinear partial differential equation

$$\partial_t u + u\partial_x u = \nu \partial_{xx} u.$$

where we have defined the flow velocity as $u = \frac{\Delta x}{\Delta t}\left[\rho(x,t) - 1\right]$*, and where the number density field is the sum of the qubit probabilities* $\rho(x,t) = a(x,t) + b(x,t)$*.*

6.10.1 A microscopic scale argument for shock wave formation

The macroscopic scale dynamical behavior of the circuit shown in Figure 6.12 is also described by the nonlinear Burgers equation. Although this circuit is less accurate than the one shown in Figure 6.10 in that its spatial discretization error is of order Δx^3, its simplicity nevertheless

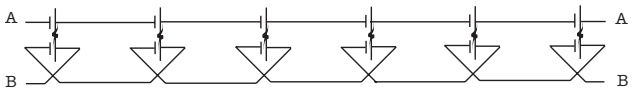

Figure 6.12: A simple analog quantum circuit in one dimension: Point A connects to point A, and point B connects to point B in periodic fashion.

makes it useful for us to intuitively see why the Burgers equation is indeed the appropriate effective field theory.

The microscopic scale argument that we made in Section 6.9.1 still basically applies to the circuit in Figure 6.12 because the first term of the collision function for the antisymmetric $\sqrt{\text{swap}}$ gate still equally splits the input probabilities, so a particle entering a quantum gate at one of the lattice nodes is equally influenced to exit in the forward or backward direction. However, there exists a second second-order polynomial term in the collision function for the antisymmetric $\sqrt{\text{swap}}$ gate that biases the outcome. So if Circuit 6.12 is initialized with a quantum particle on the top rail, that particle will more likely be fed forward to the next adjacent node. Vice versa, if a quantum particle were initially placed on the bottom rail, it would more likely be fed backward to the previous adjacent node in the chain. This directional bias has the affect of giving rise to a convective term in the governing equation of motion, which is the nonlinear term in the Burgers equation. That is, the total time derivative of the right hand side of the equation of motion can be expressed as the sum of two basic parts: the partial time derivative $\frac{\partial u}{\partial t}$ and the convective spatial derivative $\frac{\partial x}{\partial t}\frac{\partial u}{\partial x}$.

Chapter 7

The quantum Boltzmann equation

7.1 Preliminaries

I will use the following convention for indices

1. Small roman letters (a, b, c) for the momentum directions on the lattice, $a \in \{0, \ldots, B-1\}$.
2. Greek letters (α, β, γ) for specifying qubits, $\alpha \in \{0, \ldots, N-1\}$.
3. Italic letters (i, j, k) for the spatial dimensions, $i \in \{1, \ldots, D\}$.

7.2 Overview

Here we present a quantum lattice gas algorithm to numerically predict the time-dependent solutions of a classical equations which are moments of a Fokker-Planck equation:

$$\text{dissipative classical equation of motion,} \tag{7.1}$$

for example dynamical equations for fluid turbulence. At this point, we purposefully are not specifying any details about (7.1) since these depend on the quantum algorithm in question

Table 7.1: Ket symbols

Symbol	Size of Manifold	Description
$\|\Psi\rangle$	2^Q	Total system ket
$\|\psi\rangle$	2^B	On-site ket
$\|q\rangle$	2	Qubit, local state ket

for the computational physics application at hand. We shall derive (7.1) as the effective field theory for the macroscopic behavior of a system of quantum particles governed at the mesoscopic scale by a discrete quantum Boltzmann equation:

$$\left[\partial_t + \vec{c}_a \cdot \nabla + \frac{1}{2}\delta t\ \vec{c}_a\vec{c}_a : \nabla\nabla\right] f_a(\vec{x},t) = \frac{1}{\delta t}\Omega_a(f_*). \tag{7.2}$$

$f_a(\vec{x},t)$ are probability fields for the occupation at position coordinate $\vec{x}$ and at time t of a particle moving along lattice direction $\vec{c}_a$, where $a = 1, 2, \ldots, B$. $\Omega_a(f_*)$ is a nonlinear collision function for local particle interaction that satisfies the isotropic condition $\sum_a \Omega_a(f_*) = 0$. δr and δt are the cell sizes of the space-time lattice.

(7.2) is a statistical description of the kinetic transport dynamics of a microscopic system of quantum particles. We shall derive (7.2) as the effective field theory for the mesoscopic behavior of the microscopic quantum system where the motion of the particles and their quantum mechanical interactions are represented by two unitary operators, a streaming operator $\hat{\mathscr{S}}$ and a collision operator $\hat{\mathscr{C}}$, respectively, according to the quantum lattice gas paradigm. The parabolic partial differential operator on the L.H.S. of (7.2) derives from $\hat{\mathscr{S}}$. The form of $\Omega(f_*)$ on the R.H.S. of (7.2) derives from $\hat{\mathscr{C}}$. Denoting the microscopic quantum state of the system at time t by $|\Psi(t)\rangle$, the microscopic quantum mechanical evolution equation is written as follows:

$$|\Psi(t+\delta t)\rangle = \hat{\mathscr{S}}\hat{\mathscr{G}}\hat{\mathscr{C}}|\Psi(t)\rangle. \tag{7.3}$$

(7.3) is the fundamental equation that specifies the quantum algorithm. Furthermore, (7.3) reduces to the Schroedinger wave equation when the operator $\hat{\mathscr{G}}$ is the identity operator. Here, the Hamiltonian $\mathscr{H}$ that generates the quantum evolution is formally expressed as $e^{i\hat{\mathscr{H}}\delta t/\hbar} \equiv \hat{\mathscr{S}}\hat{\mathscr{C}}$ (type-I case). However, for (7.3) to give rise to fluid equations of motion with viscous dissipation proportional to the curvature of the flow field, $\hat{\mathscr{G}}$ must be chosen to be a projection operator that commutes with the particle number operator (type-II case).

(7.3) comprises a four-step quantum algorithm: initialization step (state preparation of $|\Psi(t)\rangle$), collision step (entanglement of quantum state by $\hat{\mathscr{C}}$), measurement step (collapse of quantum state by $\hat{\mathscr{G}}$), and streaming step (interchange of amplitudes by $\hat{\mathscr{S}}$).

7.3 Occupancy probability and the mass and momentum densities

The probability of occupancy at time t of the αth local state is denoted $f_\alpha(t)$. Let the αth local state be associated with a displacement vector $\hat{e}_a$ at position $\vec{x}$. Also, let $\hat{n}_\alpha$ denote the

number operator for the αth local state. That is, $\hat{n}_\alpha|\Psi(t)\rangle$ has eigenvalue 1 or 0 corresponding to the αth local state being occupied or empty at time t. A fundamental construct of the quantum lattice-gas formalism is that the probability of occupancy, $f_\alpha(t)$, is expressed in terms the quantum mechanical density matrix $\varrho(t) = |\Psi(t)\rangle\langle\Psi(t)|$ as the following trace

$$f_\alpha(t) = f_a(\vec{x}, t) \equiv \mathrm{Tr}[\varrho(t)\hat{n}_\alpha]. \tag{7.4}$$

In the literature on classical lattice gases and the lattice-Boltzmann equation, $f_a(\vec{x}, t)$ is referred to as the *single-particle distribution function*, and it is defined at the mesoscopic scale.

Let $\alpha_\circ$ denote the first local state within the group of local states at position $\vec{x}$ of the Bravais lattice. In addition, let $\alpha_\circ$ correspond to the displacement vector $\hat{e}_0$. Next, suppose the local states are numbered in a systematic and well ordered fashion so that each local state $\alpha = \alpha_\circ + a$, for all $a \in \{0, 1, \ldots, B-1\}$, resides at position $\vec{x}$. Note that with this numbering scheme, the directional index a, associated with the αth local state, is found by the modulus operation $a = (\alpha \bmod B)$. Then, the local mass density and the momentum density at $\vec{x}$ and t can be expressed in terms of the occupancy probability, $f_a(\vec{x}, t)$, following the convention used to define the mass and momentum densities in a classical lattice gas

$$\begin{aligned} \rho(\vec{x}, t) &= \lim_{\ell_s \to 0} \sum_{a=1}^{B} m\ f_a(\vec{x}, t) \qquad (7.5) \\ &= \lim_{\ell \to 0} \sum_{\alpha=\alpha_\circ}^{\alpha_\circ + B} m \mathrm{Tr}[\varrho(t)\hat{n}_\alpha] \\ \rho(\vec{x}, t) v_i(\vec{x}, t) &= \lim_{\ell_s \to 0} \sum_{a=1}^{B} mc^2 e_{ai}\ f_a(\vec{x}, t) \qquad (7.6) \\ &= \lim_{\ell \to 0} \sum_{\alpha=\alpha_\circ}^{\alpha_\circ + B} mc^2 e_{(\alpha \bmod B)i} \mathrm{Tr}[\varrho(t)\hat{n}_\alpha]. \end{aligned}$$

The mass and momentum densities are considered "macroscopic" field quantities. They are only well defined in the *continuum limit*, where the primitive cell size of the lattice approaches zero. However, for practical considerations, they are approximated by high resolution grids with small but finite cell size.

7.4 Mesoscopic transport equation

Let us consider two qubits $|q\rangle$ and $|q'\rangle$, which are located at neighboring sites $\vec{x}$ and $\vec{x}' = \vec{x} + \ell\hat{e}_a$, respectively. I shall refer to the local states encoded by these two neighboring qubits

Table 7.2: Two neighboring qubits

Qubits	$\|q\rangle$	$\|q'\rangle$
Local State	α	α'
Position	$\vec{x}$	$\vec{x}' = \vec{x} + \ell\hat{e}_a$
Momentum	$\vec{p} = mc\hat{e}_a$	$\vec{p}' = \vec{p}$

by their numerical labels α and α', respectively. Next, suppose these local states may be occupied by particles with momentum $mc\hat{e}_a$. Following this construction, the action of the streaming operator $\hat{S}$ causes a particle to move from site $\vec{x}$ to the neighboring site $\vec{x}'$, hopping from local state α with momentum $\vec{p} = mc\hat{e}_a$ to local state α' with the same momentum $\vec{p}' = \vec{p}$. This labelling convention is summarized in Table 7.2. With this understanding, we can write the identity

$$\langle\Psi|\hat{n}_\alpha|\Psi\rangle = \langle\Psi|\hat{S}^\dagger\hat{n}_{\alpha'}\hat{S}|\Psi\rangle. \tag{7.7}$$

This is a simple mathematical way of stating the following: If you make a measurement of the occupancy of local state α before streaming, the result you get must be the same as when you make a measurement of α' after streaming.

The first step toward deriving a mesoscopic transport equation for the quantum lattice gas is to rewrite the basic evolution equation $|\Psi(t+\tau)\rangle = \hat{S}\hat{C}|\Psi(t)$ in (2.99) as

$$\langle\Psi(t)|\hat{C}^\dagger\hat{n}_\alpha\hat{S}^\dagger \mid \Psi(t+\tau)\rangle = \langle\Psi(t)|\hat{C}^\dagger\hat{n}_\alpha\hat{C} \mid \Psi(t)\rangle, \tag{7.8}$$

which is done by multiplying through from the left by $\langle\Psi(t)|\hat{C}^\dagger\hat{n}_\alpha\hat{S}^\dagger$, and then using the identity $\hat{S}^\dagger\hat{S} = \mathbf{1}$. From the identity (7.7), we know that $\hat{n}_\alpha\hat{S}^\dagger = \hat{S}^\dagger\hat{n}_{\alpha'}$. Using this fact in the above equation allows us to write it as follows

$$\langle\Psi(t)|\hat{C}^\dagger\hat{S}^\dagger\hat{n}_{\alpha'} \mid \Psi(t+\tau)\rangle = \langle\Psi(t)|\hat{C}^\dagger\hat{n}_\alpha\hat{C} \mid \Psi(t)\rangle. \tag{7.9}$$

The "bra" vector on the LHS of this equation can be simplified using the adjoint of (2.99), which is $\langle\Psi(t+\tau)| = \langle\Psi(t)|\hat{C}^\dagger\hat{S}^\dagger$, so that we obtain the following result

$$\langle\Psi(t+\tau)|\hat{n}_{\alpha'}|\Psi(t+\tau)\rangle = \langle\Psi(t)|\hat{C}^\dagger\hat{n}_\alpha\hat{C}|\Psi(t)\rangle. \tag{7.10}$$

Using (7.4) and referring to Table 7.2, (7.10) expresses the probability of occupancy of local state α' at site $\vec{x}+\ell_s\hat{e}_a$ at time $t+\tau$ in terms of a matrix element evaluated at the neighboring site $\vec{x}$ and at the earlier time t. That is,

$$f_a(\vec{x} + \ell_s\hat{e}_a, t+\tau) = \langle\Psi(t)|\hat{C}^\dagger\hat{n}_\alpha\hat{C}|\Psi(t)\rangle. \tag{7.11}$$

We may add $f_a(\vec{x},t) - \langle\Psi(t)|\hat{n}_\alpha|\Psi(t)\rangle$, which vanishes by definition, to the right hand side (RHS) of (7.11). Then, we recognize (7.11) as a transport equation for the particle occupancies. The result is a *quantum Boltzmann equation*, in finite-difference form, for the quantum lattice-gas system

$$f_a(\vec{x}+\ell_s\hat{e}_a, t+\tau) = f_a(\vec{x},t) + \Omega_a^{\text{meso}}(\Psi), \tag{7.12}$$

where the collision term is expressed as the following matrix element:

$$\Omega_a^{\text{meso}}(\Psi) \equiv \langle\Psi(t)|\hat{C}^\dagger\hat{n}_\alpha\hat{C} - \hat{n}_\alpha|\Psi(t)\rangle. \tag{7.13}$$

7.5 Continuum limit derivation of the quantum Boltzmann equation

I would like to rederive the transport equation (7.12) for the quantum lattice-gas system. The derivation given here is carried out in the continuum limit (imagine a space-time lattice with infinite resolution as the cell size vanishes). All the usual restrictions arising from the discretization of the microscopic quantities are temporarily removed. A particle can exist at any point in space and time, and it can also have any momentum $\vec{p} = m\vec{v}$. The only assumption I make here is that I can still decompose the space-time into an ordered set of local states, which in this case is infinite but denumerable. That is, I imagine there are an infinite number of local states at each point in space ($B = \infty$), one corresponding to every possible particle momentum. Since the number of points in the space is also infinite ($V = \infty$), the total number of local states is doubly infinite ($N = BV = \infty^2$). Nevertheless, I assume the local states are well ordered and denumerable.

The probability of finding a particle with momentum $\vec{p}$ in the α^{th}-local state located at position $\vec{x}$ given by (7.4) is the following matrix element:

$$f(\vec{x},\vec{p},t) \equiv \langle\Psi(t)|\hat{n}_\alpha|\Psi(t)\rangle. \tag{7.14}$$

I assume $f(\vec{x},\vec{p},t)$ is a continuous and differentiable mesoscopic field quantity. For the moment, suppose the α is the local state of an "incoming" particle, preceding a possible collision event. I still want to imagine the particle dynamics divided into mutually exclusive events (collision followed by streaming) repeated in stepwise fashion ad infinitum. Next, the probability of finding a particle in the local state, α', corresponding to momentum $\vec{p}'$ at position $\vec{x}' = \vec{x} + \frac{\tau}{m}\vec{p}'$, is expressed by the matrix element

$$f(\vec{x}+\frac{\tau}{m}\vec{p}', \vec{p}', t+\tau) \equiv \langle\Psi(t+\tau)|\hat{n}_{\alpha'}|\Psi(t+\tau)\rangle. \tag{7.15}$$

Suppose α' is the local state of the "outgoing" particle. Then, a basic definition of the total time derivative of $f(\vec{x},\vec{p},t)$ is the following ratio

$$\frac{df(\vec{x},\vec{p},t)}{dt} \equiv \lim_{\tau\to 0} \frac{f(\vec{x}+\frac{\tau}{m}\vec{p}',\vec{p}',t)-f(\vec{x},\vec{p},t)}{\tau}, \tag{7.16}$$

or, in terms of the matrix elements, it is

$$\frac{df(\vec{x},\vec{p},t)}{dt} = \lim_{\tau\to 0} \frac{\langle\Psi(t+\tau)|\hat{n}_{\alpha'}|\Psi(t+\tau)\rangle - \langle\Psi(t)|\hat{n}_{\alpha}|\Psi(t)\rangle}{\tau}. \tag{7.17}$$

This is the seed of a Boltzmann equation for particle transport and the RHS of this equation constitutes the collision term, although this may not appear quite obvious at this point in the development. In the following development, I shall interpret the collision term and rewrite it so that it explicitly depends only on $\hat{n}_\alpha$ at position $\vec{x}$ and $|\Psi(t)\rangle$. In so doing, we shall see how the collision dynamics is inherently encoded in this expression.

First, we add zero to the RHS of the above equation to write the collision term in two parts, explicitly separating the total change into "temporal-change" and "spatial-change" parts, as follows:

$$\frac{df(\vec{x},\vec{p},t)}{dt} = \lim_{\tau\to 0} \frac{\langle\Psi(t+\tau)|\hat{n}_{\alpha'}|\Psi(t+\tau)\rangle - \langle\Psi(t)|\hat{n}_{\alpha'}|\Psi(t)\rangle}{\tau} + \lim_{\tau\to 0} \frac{\langle\Psi(t)|\hat{n}_{\alpha'}|\Psi(t)\rangle - \langle\Psi(t)|\hat{n}_{\alpha}|\Psi(t)\rangle}{\tau}. \tag{7.18}$$

From the time-displacement operation, $e^{\tau\frac{\partial}{\partial t}}f(\vec{x},\vec{p},t) = f(\vec{x},\vec{p},t+\tau)$, we see that the first term on the RHS of the above equation is a partial derivative with respect to time

$$\frac{\partial f(\vec{x}+\frac{\tau}{m}\vec{p},\vec{p},t)}{\partial t} + \mathcal{O}(\mathrm{Sh}^2) = \lim_{\tau\to 0} \frac{\langle\Psi(t+\tau)|\hat{n}_{\alpha'}|\Psi(t+\tau)\rangle - \langle\Psi(t)|\hat{n}_{\alpha'}|\Psi(t)\rangle}{\tau}. \tag{7.19}$$

The Strouhal number, Sh, is defined as the ratio of the mean-free time to the characteristic time scale ($\mathrm{Sh} \equiv \frac{\tau}{T}$). Similarly, from the space-displacement operation, $e^{\tau\vec{v}\cdot\nabla}f(\vec{x},\vec{p},t) = f(\vec{x}+\tau\vec{v},\vec{p},t)$, we see that the second term is a partial derivative with respect to position

$$\vec{v}\cdot\nabla f(\vec{x},\vec{p},t) + \frac{1}{2}(\vec{v}\cdot\nabla)^2 f(\vec{x},\vec{p},t) + \mathcal{O}(\mathrm{Kn}^3) = \lim_{\tau\to 0} \frac{\langle\Psi(t)|\hat{n}_{\alpha'}|\Psi(t)\rangle - \langle\Psi(t)|\hat{n}_{\alpha}|\Psi(t)\rangle}{\tau}. \tag{7.20}$$

The Knudsen number, Kn, is defined as the ratio of the mean-free path to the characteristic length scale ($\mathrm{Kn} \equiv \frac{\ell}{L}$). Therefore, we have the convective derivative

$$\frac{df(\vec{x},\vec{p},t)}{dt} = \frac{\partial f(\vec{x}+\frac{\tau}{m}\vec{p},\vec{p},t)}{\partial t} + \vec{v}\cdot\nabla f(\vec{x},\vec{p},t) + \frac{1}{2}(\vec{v}\cdot\nabla)^2 f(\vec{x},\vec{p},t) + \mathcal{O}(\mathrm{Sh}^2,\mathrm{Kn}^3), \tag{7.21}$$

composed of a local term and a nonlocal advection term. In the local term, it is technically correct (albeit unconventional) to explicitly write the partial time derivative's dependence on τ, even though $\tau \to 0$. This is done to stress an equivalence with the matrix element formulation given by (7.18).

Second, we rewrite the "local change" term. Since $|\Psi(t+\tau)\rangle = e^{i\hat{H}\tau/\hbar}|\Psi(t)\rangle$ and $e^{i\hat{H}\tau/\hbar} = 1 + i\hat{H}\tau/\hbar + \mathcal{O}(\tau^2)$, we have

$$\langle\Psi(t+\tau)|\hat{n}_{\alpha'}|\Psi(t+\tau)\rangle = \langle\Psi(t)|\hat{n}_{\alpha'}|\Psi(t)\rangle + \frac{i\tau}{\hbar}\langle\Psi(t)|[\hat{n}_{\alpha'}, \hat{H}]|\Psi(t)\rangle + \mathcal{O}(\tau^2). \tag{7.22}$$

Using this equation in conjuction with (7.19), we have

$$\hbar\frac{\partial f(\vec{x} + \frac{\tau}{m}\vec{p}, \vec{p}, t)}{\partial t} = i\langle\Psi(t)|[\hat{n}_{\alpha'}, \hat{H}]|\Psi(t)\rangle. \tag{7.23}$$

This result is expected, since in quantum mechanics, the partial time derivative of an operator is found by calculating the commutator of that operator with the Hamiltonian. Using this result, the Boltzmann equation (7.18) becomes

$$\frac{df(\vec{x}, \vec{p}, t)}{dt} = \frac{i}{\hbar}\langle\Psi(t)|[\hat{n}_{\alpha'}, \hat{H}]|\Psi(t)\rangle + \lim_{\tau\to 0}\langle\Psi(t)|\frac{n_{\alpha'} - n_{\alpha}}{\tau}|\Psi(t)\rangle. \tag{7.24}$$

Now the RHS no longer depends on $|\Psi(t+\tau)\rangle$ (so it is local in time), but it is still nonlocal in space because it depends on $\hat{n}_{\alpha'}$ as well. That is, if the RHS of the above equation were to depend only on $\hat{n}_{\alpha}$, then it would have "strictly local" form.

Third, using the fact that $e^{i\hat{H}\tau/\hbar} \equiv \hat{S}\hat{C}$, we can rewrite the commutator as

$$\frac{i}{\hbar}[\hat{n}_{\alpha'}, \hat{H}] = \lim_{\tau\to 0}\frac{e^{-i\hat{H}\tau/\hbar}\hat{n}_{\alpha'}e^{i\hat{H}\tau/\hbar} - \hat{n}_{\alpha'}}{\tau} = \lim_{\tau\to 0}\frac{\hat{C}^\dagger\hat{S}^\dagger\hat{n}_{\alpha'}\hat{S}\hat{C} - \hat{n}_{\alpha'}}{\tau}. \tag{7.25}$$

Now, $\hat{n}_{\alpha}$ and $\hat{n}_{\alpha'}$ are related by the similarity transformation (7.7), $\hat{n}_{\alpha} = \hat{S}^\dagger\hat{n}_{\alpha'}\hat{S}$, so the commutator reduces to

$$\frac{i}{\hbar}[\hat{n}_{\alpha'}, \hat{H}] = \lim_{\tau\to 0}\frac{\hat{C}^\dagger\hat{n}_{\alpha}\hat{C} - \hat{n}_{\alpha'}}{\tau}. \tag{7.26}$$

Inserting this into (7.24) gives the final local form of the *quantum Boltzmann equation* for $f(\vec{x}, \vec{p}, t)$, which is

$$\frac{df(\vec{x}, \vec{p}, t)}{dt} = \lim_{\tau\to 0}\frac{1}{\tau}\langle\Psi(t)|\hat{C}^\dagger\hat{n}_{\alpha}\hat{C} - \hat{n}_{\alpha}|\Psi(t)\rangle. \tag{7.27}$$

Notice that the collision term depends only on the wave function evaluated at time t and the occupancy of the α^{th} local state located at position $\vec{x}$. However, if there exists quantum entanglement between particles at different points in space, then $|\Psi(t)\rangle$ cannot be written in separable tensor product form over the spatial points. So in this case, the collision term is "nonlocal." When we say the quantum Boltzmann equation is local in form, we refer to a special case barring nonlocal quantum entanglements. The quantum Boltzmann equation accounts for global entanglement through the collision process and is an exact reformulation of the many-body Schrödinger equation.

There is one more point to make in this section. From the basic definition (7.16) for the total time rate of change of $f(\vec{x},\vec{p},t)$, we see that (7.27) can be written as the following "finite-difference" equation

$$f(\vec{x}+\frac{\tau}{m}\vec{p}',\vec{p}',t) = f(\vec{x},\vec{p},t) + \langle\Psi(t)|\hat{C}^\dagger\hat{n}_\alpha\hat{C} - \hat{n}_\alpha|\Psi(t)\rangle. \tag{7.28}$$

This is the quantum Boltzmann equation [see (7.12) in Section 7.4]. It is important to note that the quantum Boltzmann equation is still an exact representation of the particle dynamics, even when expressed in finite-difference form. This is immediately obvious when the identity $\hat{n}_\alpha = \hat{S}^\dagger\hat{n}_{\alpha'}\hat{S}$ is inserted into the collision term, $\langle\Psi(t)|\hat{C}^\dagger S^\dagger\hat{n}_{\alpha'}\hat{S}\hat{C} - \hat{n}_\alpha|\Psi(t)\rangle$. Then, the quantum Boltzmann equation becomes a simple identity

$$f(\vec{x}+\frac{\tau}{m}\vec{p}',\vec{p}',t) = f(\vec{x},\vec{p},t) + \langle\Psi(t+\tau)|\hat{n}_{\alpha'}|\Psi(t+\tau)\rangle - \langle\Psi(t)|\hat{n}_\alpha|\Psi(t)\rangle. \tag{7.29}$$

For a finite resolution lattice (used in a computational simulation of the quantum lattice-gas system), the quantum Boltzmann equation is the appropriate formulation of the particle dynamics. However, the quantum Boltzmann equation (7.27), in differentiable point-form, becomes the appropriate formulation of the particle dynamics for the system in the continuum limit.

7.6 Derivation of the type-II collision function

In practice, we will not be able to analytically evaluate (7.13) for a large quantum lattice-gas system with global entanglement because of the exponential size of the $|\Psi\rangle$ ket. However, it is possible to formally express the collision term Ω_a^{meso} when $|\Psi\rangle$ is represented as the linear combination. This is done as follows:

$$\Omega_a^{\text{meso}} = \sum_{\{\psi_{1'},\ldots,\psi_{V'}\}}\sum_{\{\psi_1,\ldots,\psi_L\}}\mathcal{A}^*(\psi_{1'},\ldots,\psi_{V'})\mathcal{A}(\psi_1,\ldots,\psi_L)\langle\psi_{1'}|\otimes\cdots\otimes\langle\psi_{V'}|\hat{C}^\dagger\hat{n}_\alpha\hat{C}-\hat{n}_\alpha|\psi_1\rangle\otimes\cdots\otimes|\psi_L\rangle. \tag{7.30}$$

Moreover, it is possible to express Ω_a^{meso} in terms of the on-site number operator $\hat{n}_a$, which is represented by a $2^B \times 2^B$ matrix. That is, $\hat{n}_a$ acts only in the submanifold $\mathcal{B}$ on the qubits at a single site. We write the Q-qubit number operator $\hat{n}_\alpha$ as an L-fold tensor product that has a single B-qubit number operator $\hat{n}_a$ located at the nth site index corresponding to the position vector $\vec{x}_n$ as

$$\hat{n}_\alpha = \mathbf{1}\otimes\mathbf{1}\otimes\cdots\otimes\hat{n}_a\otimes\cdots\otimes\mathbf{1}, \tag{7.31}$$

where $\mathbf{1}$ denotes the $2^B \times 2^B$ identity matrix. The collision operator $\hat{C}^\dagger\hat{n}_\alpha\hat{C} - \hat{n}_\alpha$ can then be written

$$\mathbf{1}\otimes\mathbf{1}\otimes\cdots\otimes\left(\hat{U}^\dagger\hat{n}_a\hat{U}-\hat{n}_a\right)\otimes\cdots\otimes\mathbf{1} = \bigotimes_{x=1}^{L}\hat{\Omega}_a, \tag{7.32}$$

where

$$\hat{\Omega}_a \equiv \begin{cases} \hat{U}^\dagger \hat{n}_a \hat{U} - \hat{n}_a, & x = x_n \\ \mathbf{1}, & \text{otherwise.} \end{cases} \tag{7.33}$$

Using Equations (7.33), (7.31), and the orthonormality of the on-site kets $\langle \psi_{n'} | \psi_n \rangle = \delta_{n'n}$, (7.30) reduces to a local matrix element evaluated at a single site $\vec{x}_{n'} = \vec{x}_n = \vec{x}$ as

$$\Omega_a^{\text{meso}} = \sum_{\psi_{n'}} \sum_{\{\psi_1,\ldots,\psi_L\}} \mathcal{A}^*(\psi_1,\ldots,\psi_{n-1},\psi_{n'},\psi_{n+1},\ldots,\psi_V)\mathcal{A}(\psi_1,\ldots,\psi_n,\ldots,\psi_L)\langle \psi_{n'}|\hat{U}^\dagger \hat{n}_a \hat{U} - \hat{n}_a|\psi_n\rangle. \tag{7.34}$$

Let us make the following definition:

$$\mathcal{R}(\psi_{n'},\psi_n) \equiv \sum_{\{\psi_1,\ldots,\psi_{n-1},\psi_{n+1},\ldots,\psi_L\}} \mathcal{A}^*(\psi_1,\ldots,\psi_{n-1},\psi_{n'},\psi_{n+1},\ldots,\psi_V)\mathcal{A}(\psi_1,\ldots,\psi_n,\ldots,\psi_L). \tag{7.35}$$

The quantity $\mathcal{R}(\psi_{n'},\psi_n)$ represents the superposition of the on-site basis states at site $\vec{x}$ with all the other on-site basis states in the system at the other sites. With this definition, (7.34) can be written in a simpler way,

$$\Omega_a^{\text{meso}} = \sum_{\psi_{n'}} \sum_{\psi_n} \mathcal{R}(\psi_{n'},\psi_n)\langle \psi_{n'}|\hat{U}^\dagger \hat{n}_a \hat{U} - \hat{n}_a|\psi_n\rangle. \tag{7.36}$$

If each on-site state is not entangled or superposed with any other on-site state, then $\mathcal{R}$ can be written in factorized form, $\mathcal{R}(\psi_{n'},\psi_n) = \mathcal{C}(\psi_{n'})\mathcal{C}(\psi_n)$. In this case, (7.36) is simplified

$$\Omega_a^{\text{meso}} = \langle \psi|\hat{U}^\dagger \hat{n}_a \hat{U} - \hat{n}_a|\psi\rangle, \tag{7.37}$$

where the coefficients $\mathcal{C}(\psi_n)$ specify any local superposition and entanglement

$$|\psi\rangle \equiv \sum_{\psi_n} \mathcal{C}(\psi_n)|\psi_n\rangle. \tag{7.38}$$

Then using (7.37), the quantum Boltzmann equation for the quantum lattice-gas system becomes a local finite-difference equation that can be simulated on a classical computer so long as the number of qubits per quantum node is small [Yepez, 1998, Yepez, 1999].

Chapter 8

The diffusion equation

8.1 Model formulation

Consider the quantum computer with L number of nodes depicted in Figure 8.1. There are two qubits per node that may remain phase coherent for a short duration in time. Initially, the state of each qubit

$$|q_a(x,t)\rangle = \alpha_a|0\rangle + \beta_a|1\rangle \tag{8.1}$$

is independently set so that the on-site ket, $|\psi(x,t)\rangle$, is a tensor product over the qubit residing at site x

$$|\psi(x,t)\rangle = |q_1(x,t)\rangle \otimes |q_2(x,t)\rangle, \tag{8.2}$$

for all x. The occupancy probability of the a^{th} qubit at site x at time t is

$$f_a(x,t) \equiv \langle\psi(x,t)|\hat{n}_a|\psi(x,t)\rangle, \tag{8.3}$$

for $a = 1, 2$. We define the "*mass density*" field as the sum of the occupancy probabilities[1]

$$\rho(x,t) \equiv f_1(x,t) + f_2(x,t). \tag{8.4}$$

In the continuum limit, where the lattice resolution becomes infinite, the mass density field is considered to be a continuous and differentiable field. Given an appropriate sequence of quantum gate operations applied to the quantum computer array depicted in Figure 8.1, the ρ field will evolve in time in a diffusive fashion. The dynamics is governed, in the long-wavelength limit, a parabolic partial differential equation of motion of the form

$$\frac{\partial\rho}{\partial t} = D\frac{\partial^2\rho}{\partial x^2}. \tag{8.5}$$

The value of the diffusion constant, D, is determined by the choice of the quantum gate used to compute *outgoing configurations* and is also determined by the discrete particle movement on the one dimensional lattice used in this model.

[1]Here we have taken the mass of a particle to be unity, $m = 1$.

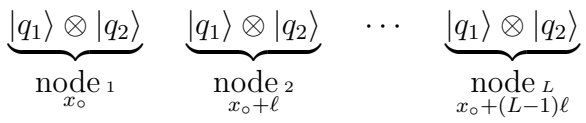

Figure 8.1: Depiction of a type II quantum computer with L nodes and 2 qubits per node. The array is one dimensional with periodic boundary conditions. The coordinate $x_\circ$ refers to the location of the first node. The symbol $\otimes$ represents the tensor (or outer) product operation.

Let use a particle-conserving dynamics and therefore use a conservative two-qubit quantum gate of the form (2.40).

8.2 Factorized quantum lattice-gas algorithm

The factorized quantum lattice-gas algorithm for the one-dimensional diffusion equation can be implemented in the following three steps.

STEP 1: We assume the initial state of the quantum computer is set as specified in Figure 8.1, where $|q_a(x,t)\rangle = \sqrt{f_a(x,t)}|1\rangle + \sqrt{1-f_a(x,t)}|0\rangle$.

STEP 2: Apply the collision operator simultaneously to all sites

$$|\psi'(x,t)\rangle = \hat{U}|\psi(x,t)\rangle.$$

This step accounts for all the quantum computation that is accomplished in a classically parallel fashion across all nodes of the array.

STEP 3: Measure ("read") all the occupancy probabilities using the following matrix element

$$\begin{aligned} f_1'(x,t) &= \langle\psi'(x,t)|\hat{n}_1|\psi'(x,t)\rangle \\ f_2'(x,t) &= \langle\psi'(x,t)|\hat{n}_2|\psi'(x,t)\rangle \end{aligned}$$

on all sites. In practice, f_1 and f_2 must be determined by either repeated measurement of a single realization of the system or by a single measurement over a statistical ensemble of systems.

STEP 4: Reinitialize ("write") the state of the quantum computer as a separable state

where each qubit is set as follows

$$\begin{aligned} |q_1(x,t+\tau)\rangle &= \sqrt{f_1'(x-\ell,t)}|1\rangle + \sqrt{1-f_1'(x-\ell,t)}|0\rangle \\ |q_2(x,t+\tau)\rangle &= \sqrt{f_2'(x+\ell,t)}|1\rangle + \sqrt{1-f_2'(x+\ell,t)}|0\rangle \end{aligned}$$

for all x. Note that qubit $|q_1\rangle$ is shifted to its neighboring node at the left and $|q_2\rangle$ is shifted to its neighboring node at the right. This step requires nearest-neighbor classical communication between all lattice nodes.

ONE TIME-STEP UPDATE COMPLETED.

8.3 Model analysis

To model the diffusion equation, we use the following symmetric collision operator

$$\hat{U} = \sqrt{\hat{\chi}} = \begin{pmatrix} 1 & 0 & 0 & 0 \\ 0 & \frac{1}{2}-\frac{i}{2} & \frac{1}{2}+\frac{i}{2} & 0 \\ 0 & \frac{1}{2}+\frac{i}{2} & \frac{1}{2}-\frac{i}{2} & 0 \\ 0 & 0 & 0 & 1 \end{pmatrix}. \tag{8.6}$$

which is obtained from the Heisenberg Hamiltonian (2.76). With this collision operator, the outgoing occupancy probabilities f_1' and f_2' are computed from the incoming occupancy probabilities f_1 and f_2 according to step 2 of the algorithm specified in the previous section

$$\begin{aligned} f_1' &= \langle\psi|\hat{U}^\dagger \hat{n}_1 \hat{U}|\psi\rangle \\ f_2' &= \langle\psi|\hat{U}^\dagger \hat{n}_2 \hat{U}|\psi\rangle, \end{aligned} \tag{8.7}$$

where $|\psi\rangle = (\sqrt{f_1}|1\rangle + \sqrt{1-f_1}|0\rangle) \otimes (\sqrt{f_2}|1\rangle + \sqrt{1-f_2}|0\rangle)$, as stated in Section 8.2. These functional relations between the outgoing and incoming probabilities reduce to the following equations

$$\begin{aligned} f_1' &= f_1 f_2 + \frac{1}{2}\left|\sqrt{f_1(1-f_2)} + i\sqrt{(1-f_1)f_2}\right|^2 = \frac{1}{2}(f_1+f_2) \\ f_2' &= f_1 f_2 + \frac{1}{2}\left|i\sqrt{f_1(1-f_2)} + \sqrt{(1-f_1)f_2}\right|^2 = \frac{1}{2}(f_1+f_2). \end{aligned} \tag{8.8}$$

According to this prescription, Equation (8.8) is guaranteed to keep the mass at a site conserved

$$f_1' + f_2' = f_1 + f_2. \tag{8.9}$$

We can express the collision Equation (8.7) along with the streaming operation as a single finite-difference quantum Boltzmann equation

$$f_a(x + e_a\ell, t+\tau) = f_a(x,t) + \Omega_a, \tag{8.10}$$

where the collision term is

$$\Omega_a \equiv \langle\psi|\hat{U}^\dagger \hat{n}_a \hat{U} - \hat{n}_a|\psi\rangle = \frac{1}{2}\left[f_{a+1}(1-f_a) - f_a(1-f_{a+1})\right], \tag{8.11}$$

for $a = 1, 2$ and where $e_1 = 1$ and $e_2 = -1$. The lattice Boltzmann equation (8.10) can be linearized by expanding the collision term to first order in the fluctuation [Das et al., 1993, Bussemaker et al., 1995], $\Omega_a \simeq \sum_b J_{ab}\delta f_b$, where the Jacobian matrix is

$$J = \begin{pmatrix} \frac{\partial\Omega_1}{\partial f_1} & \frac{\partial\Omega_1}{\partial f_2} \\ \frac{\partial\Omega_2}{\partial f_1} & \frac{\partial\Omega_2}{\partial f_2} \end{pmatrix} = \frac{1}{2}\begin{pmatrix} -1 & 1 \\ 1 & -1 \end{pmatrix}. \tag{8.12}$$

The eigenvalues and eigenvectors of J characterize the behavior of a lattice-gas system in the long-wavelength and low frequency limit. The eigenvalues of J are $\lambda_1 = 0$ and $\lambda_2 = -1$, with eigenvectors $\vec{\xi_1} = (1, 1)$ and $\vec{\xi_2} = (-1, 1)$, respectively. The conserved macroscopic field corresponding to the zero eigenvalue is the mass-density field

$$\rho = \vec{\xi_1} \cdot (f_1, f_2) = f_1 + f_2 \tag{8.13}$$

as expected.

Local equilibrium of the mass-density field, $\rho^{\rm eq} \equiv d$, occurs when the on-site particle distribution causes the collision term to vanish, $\Omega_a|_{f=f^{\rm eq}} = 0$, for all a. In the present case, this occurs when the occupancy probability of the left and right channels are equal

$$f_1^{\rm eq} = f_2^{\rm eq} = \frac{d}{2}, \tag{8.14}$$

which is evident from Equation (8.11). Local equilibrium of the system can also be defined in terms of the collision operator $\hat{U}$ by the following constraint

$$\hat{U}|\psi^{\rm eq}\rangle = |\psi^{\rm eq}\rangle, \tag{8.15}$$

which is also evident from Equation (8.11) since in this situation $\Omega_a|_{\psi=\psi^{\rm eq}} = 0$. Now if we explicitly write out Equation (8.15) in matrix form

$$\begin{pmatrix} 1 & 0 & 0 & 0 \\ 0 & \frac{1}{2}-\frac{i}{2} & \frac{1}{2}+\frac{i}{2} & 0 \\ 0 & \frac{1}{2}+\frac{i}{2} & \frac{1}{2}-\frac{i}{2} & 0 \\ 0 & 0 & 0 & 1 \end{pmatrix} \begin{pmatrix} \sqrt{f_1^{\rm eq}}\sqrt{f_2^{\rm eq}} \\ \sqrt{f_1^{\rm eq}}\sqrt{1-f_2^{\rm eq}} \\ \sqrt{1-f_1^{\rm eq}}\sqrt{f_2^{\rm eq}} \\ \sqrt{1-f_1^{\rm eq}}\sqrt{1-f_2^{\rm eq}} \end{pmatrix} = \begin{pmatrix} \sqrt{f_1^{\rm eq}}\sqrt{f_2^{\rm eq}} \\ \sqrt{f_1^{\rm eq}}\sqrt{1-f_2^{\rm eq}} \\ \sqrt{1-f_1^{\rm eq}}\sqrt{f_2^{\rm eq}} \\ \sqrt{1-f_1^{\rm eq}}\sqrt{1-f_2^{\rm eq}} \end{pmatrix} \tag{8.16}$$

we see that the following two equations must be satisfied

$$\begin{aligned} \frac{e^{-i\frac{\pi}{4}}}{\sqrt{2}}\left(\sqrt{f_1^{\rm eq}}\sqrt{1-f_2^{\rm eq}} + i\sqrt{1-f_1^{\rm eq}}\sqrt{f_2^{\rm eq}}\right) &= \sqrt{f_1^{\rm eq}}\sqrt{1-f_2^{\rm eq}} \\ \frac{e^{-i\frac{\pi}{4}}}{\sqrt{2}}\left(i\sqrt{f_1^{\rm eq}}\sqrt{1-f_2^{\rm eq}} + \sqrt{1-f_1^{\rm eq}}\sqrt{f_2^{\rm eq}}\right) &= \sqrt{1-f_1^{\rm eq}}\sqrt{f_2^{\rm eq}}. \end{aligned} \tag{8.17}$$

If $f_1^{\rm eq} = f_2^{\rm eq} \equiv \frac{d}{2}$, these local equilibrium conditions reduce to the single identity

$$\frac{e^{-i\frac{\pi}{4}}}{\sqrt{2}}(1+i) = 1. \tag{8.18}$$

Therefore, we now see why it is necessary to include the phase factor $e^{-i\frac{\pi}{4}}$ in the definition of the collision operator so that $\hat{U}$ has an eigenvalue of unity value with an eigenvector corresponding to a local equilibrium configuration.

8.4 Numerical confirmations

In this section we show several results from one-dimensional numerical simulations of the factorized quantum lattice gas. All the numerical simulations were carried out using Mathematica.

8.4.1 Delta function initial condition

The algorithm described in Section 8.2 for the factorized quantum lattice gas, with two qubits per site, for the diffusion equation has the property that it simulates two non-interpenetrating lattice-gas systems simultaneously. That is, there are two independent "checker-board" sub-lattices. For illustration purposes, let all even numbered cells of the lattice be color-coded white and all the odd numbered cells of the lattice be color-coded black. This defines the two "checker-board" partitions of the lattice. Any particles initially on the black partition collide and stream to the white partition and vice versa. This is because each of the qubits per site move to their nearest neighboring sites which are on the alternate partition. After a second application of the local update rule, the particles return to the original partition. For this reason, particles on the white sub-lattice never interact with those on the black one. This dual-lattice behavior is shown on the left column of Figure 8.2 which shows snapshots of the time evolution at every other time step for a small lattice of size $L = 32\ell$. Initially all the particles are located at the center cell of the lattice. There is a delta function peak in the mass-density field

$$\rho(x, 0) = \delta(x - \frac{L}{2}), \tag{8.19}$$

where $\delta(x) = 1$ for $x = 0$ and $\delta(x) = 0$ otherwise. After two time-steps, particles diffuse two lattice cells away from the center point and there are no particles occupying the lattice cells immediately neighboring the center one. The double lattice effect is seen in the subsequent snapshots of the mass-density field.

It is possible to repair this deficiency in the algorithm by allowing only the state of one of the qubits of a cell to be transferred to the neighboring cell. The state of the other qubit

in the cell remains fixed. The improved version of the algorithm is described in a step-by-step fashion in Appendix H. With the improved version of the algorithm, the resulting mass-density field is smoothly varying across the lattice cell even in this case with the most discrete initial condition. This is depicted on the right column of Figure 8.2.

8.4.2 Broadening of a Gaussian packet

The next numerical test of the factorized quantum lattice gas demonstrates that the dynamical evolution of its mass-density field is indeed governed by the diffusion equation. The mass-density field is initialized with a Gaussian waveform

$$\rho(x,0) = \frac{1}{4} e^{\frac{(x-\frac{L}{2})^2}{\sigma_\circ^2}} + \frac{1}{2}, \tag{8.20}$$

where the initial packet width is $\sigma_\circ = \frac{L}{10}\ell$. The Gaussian packet will undergo diffusive broadening as its width, $\sigma(t) = \sqrt{\sigma_\circ^2 + 4Dt}$, increases over time while its peak amplitude decreases at a rate of $\frac{1}{\sigma(t)}$, as shown in Figure 8.3. The exact analytical solution for the mass-density field at some later time, t, is given by the following expression

$$\rho^{\text{exact}}(x,t) = \frac{1}{4} \frac{\sigma_\circ}{\sqrt{\sigma_\circ^2 + 4Dt}} e^{\frac{(x-\frac{L}{2})^2}{\sigma_\circ^2+4Dt}} + \frac{1}{2}, \tag{8.21}$$

where the diffusion constant is $D = \frac{1}{2}\frac{\ell^2}{\tau}$.

The dispersion rate of the packet can be directly determined by measuring the decay rate of the peak, since the peak amplitude is proportional to the inverse of the packet width. The numerical data extracted from the simulation is plotted along with the exact analytical solution in Figure 8.4. The agreement between the numerical simulation and the exact analytical solution is excellent, which confirms that the dynamical space-time evolution of the mass-density field is governed by the parabolic diffusion equation.

8.4.3 Exponential decay of a sinusoidal perturbation

As another test of the factorized quantum lattice-gas model, let us consider an example problem to illustrate diffusive damping in the continuum limit. We begin with a lattice with $L = 128\ell$ sites (or nodes). The mass density field is initially set to be a sine wave

$$\rho(x,0) = \frac{1}{4} \sin\frac{2\pi x}{L} + \frac{1}{2}. \tag{8.22}$$

The boundary conditions are periodic and remain fixed at all time

$$\rho(0,t) = \rho(L,t) = \frac{1}{2}. \tag{8.23}$$

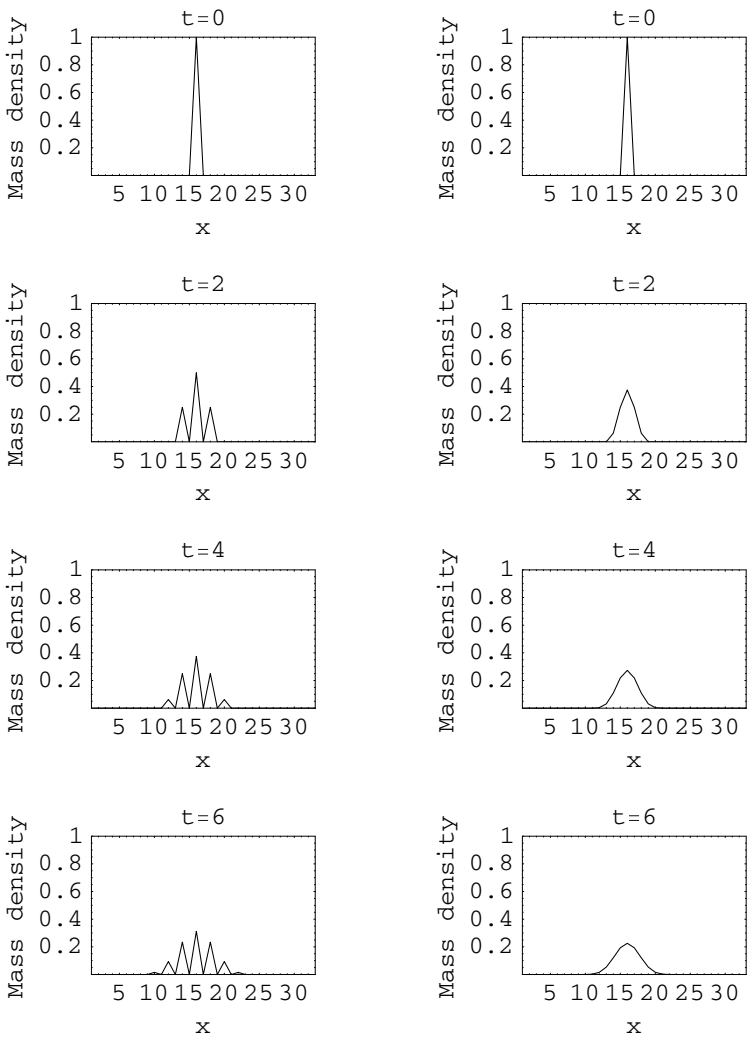

Figure 8.2: Mass-density field with an initial delta function: The initial condition of the mass-density field is set to a delta function in the middle of a lattice of size $L = 32\ell$. Snapshots of the time evolution of the mass-density field is shown for the case where both qubits are streamed (left column plots) as described in Section 8.2 and also for the case where a single qubits are streamed alternatively in both directions (right column plots) as described in Appendix H. A double lattice effect is observed in the first case and does not occur in the second case with the improved version of the algorithm.

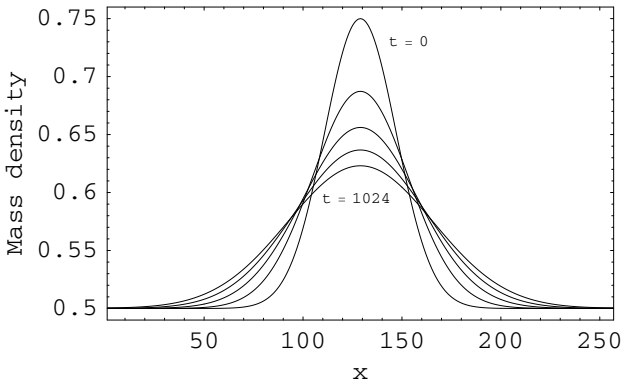

Figure 8.3: The time evolution of a Gaussian packet of a lattice of size $L = 256\ell$ for $t = 0, 256, 512, 768, 1024\tau$. The packet width is initially $\sigma = 0.1\ell$ and broadens over time as shown in the figure by over plotting.

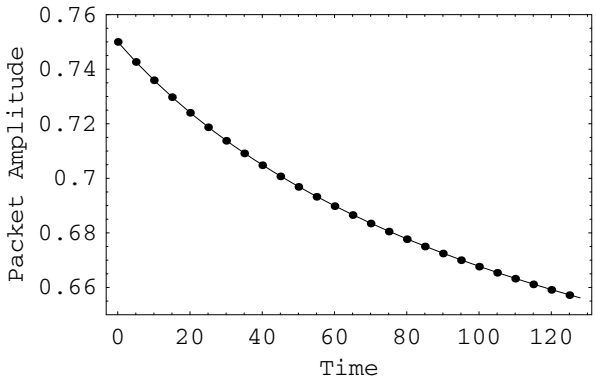

Figure 8.4: Time series plot of the temporal decay of a Gaussian packet of a lattice of size $L = 128\ell$ for $t = 0$ up to $t = 128\tau$. The packet width is initially $\sigma = \frac{L}{10}\ell$ and broadens in time as $\sigma = \sqrt{\sigma_\circ + 4Dt}$ where the initial width is $\sigma_\circ = 0.1\ell$ and the diffusion constant is $D = \frac{1}{2}\frac{\ell^2}{\tau}$. The packet's amplitude decays at a rate of $\frac{1}{\sigma}$, which is the exact solution plotted as the solid curve. The plotted data (black circles) taken from the numerical simulation of the factorized quantum lattice gas are in excellent agreement with the exact analytical solution.

After repeated application of the collision and streaming operators of the factorized quantum lattice gas, the amplitude of the mass-density wave is observed to decay in time. To be a solution of the diffusion equation (8.5), the mass-density field must have the form

$$\rho^{\text{exact}}(x,t) = \frac{1}{4}e^{-\Gamma t}\sin\frac{2\pi x}{L} + \frac{1}{2}, \tag{8.24}$$

where the damping constant is $\Gamma = Dk^2$, the wave number is $k = \frac{2\pi}{L}$, and the diffusion constant is $D = \frac{1}{2}\frac{\ell^2}{\tau}$. This is in fact observed in the numerical simulation which indicates

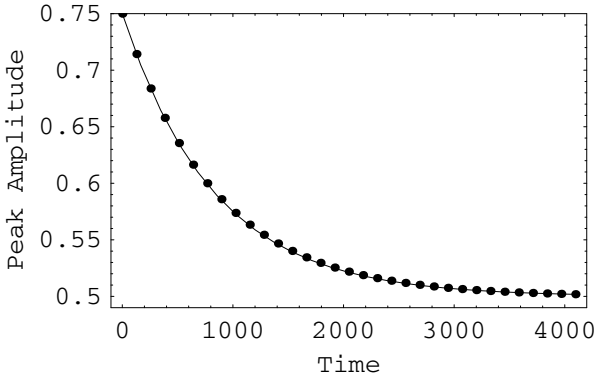

Figure 8.5: Exponential damping of a sinusoidal profile by action of mass diffusion. The solid curve is the predicted envelope $\frac{1}{4}e^{-\frac{1}{2}(\frac{2\pi}{128})^2} + \frac{1}{2}$. The plotted data (black circles) taken from the numerical simulation of the factorized quantum lattice gas are in excellent agreement with the theoretical envelope.

exponential decay of the mass-density profile, as shown in Figure 8.5.

A final test of the factorized quantum lattice-gas algorithm as a model of the diffusion equation is the measurement of its numerical convergence. Multiple simulations (10 in total) were carried out for lattice sizes ranging from $L = 64\ell, 128\ell, 256\ell, \ldots$ up to $L = 32768\ell$. In each case the initial state of the simulation was a sinusoidal perturbation of the mass-density field about half-filling according to Equation (8.22). Each simulation was run for $T = 64\tau$ time-step iterations and the numerical error, denoted ϵ, from the exact solution was then measured using the following formula

$$\epsilon(L) = \frac{1}{L}\sqrt{\sum_{x=1}^{L}\left[\rho(x) - \rho^{\text{exact}}(x)\right]^2}, \tag{8.25}$$

where the exact solution for the mass-density field is

$$\rho^{\text{exact}}(x) = \frac{1}{4}e^{-\frac{1}{2}(\frac{2\pi}{L})^2 T}\sin\frac{2\pi x}{L} + \frac{1}{2}. \tag{8.26}$$

We define the grid resolution as the inverse of the total number of lattice points. That is, for a box of size 1, the *resolving cell size* is defined as $\delta x \equiv \frac{1}{L}$. A plot of the error versus

the resolution is given in Figure 6.9. As the resolution is increased, the error drops off as $\epsilon(L) \sim L^{4.471}$. The factorized quantum lattice-gas algorithm has numerical convergence that is at least second-order accurate in space and first-order accurate in time.

Chapter 9

The Burgers equation

9.1 Introduction

The purpose of this chapter is to theoretically and numerically analyze the dynamical behavior of a quantum model of the classical nonlinear Burgers equation in one spatial dimension. The quantum model is a particular construction or example of an open quantum system with a minimum time step allowing for interleaved non-unitary measurment and unitary evolution. The measurement steps are dispersed periodically in time and across all the elements of the quantum system. At the microscopic scale, the equation of motion is a quantum mechanical wave equation with localization. That is, the Schrödinger equation is modified in such a way that long-range quantum coherence is destroyed whereby the physical behavior of the system at the macroscopic scale effectively becomes a nonlinear classical field theory with dissipation, the Burgers equation for shock formation.

We begin in Section 9.1.1 by summarizing the dynamical equations of motion of the open quantum system and we do this for three spatial scales. The microscopic scale equation is a Schrödinger wave equation modified to allow for localization. The open quantum system comprises a set of two-level qubits (*e.g.* spin-$\frac{1}{2}$ nuclei). The Hamiltonian that generates the phase-coherent part of the evolution is engineered in such as way that the quantum system effectively models a kinetic many-particle system. The open quantum system acts as a kind of analog simulator.

Each qubit in the system is assigned a unique position and momentum-space coordinate pair. The moduli squared of the probability amplitude of a qubit's logical $|1\rangle$ state (*e.g* expectation value of its excited state) is equated to an element of a "single-particle" distribution associated with the position and momentum-space coordinate of a modeled particle in a many-body system. There can be as many particles in the emulated kinetic system as there are qubits in the quantum system. Let us denote a qubit's quantum state as $|q\rangle = \alpha|0\rangle + \beta|1\rangle$, where $|\alpha|^2 + |\beta|^2 = 1$. We shall refer to the state the $|0\rangle$ as the qubit's *ground state* and the

state $|1\rangle$ as the qubit's *excited state*. If $|\alpha| = 0$ and $|\beta| = 1$, we say that the qubit encodes the presence of a "*particle*" of unit mass. If $|\alpha| = 1$ and $|\beta| = 0$, we say that the qubit encodes a "*hole*," or the absence of a particle. Hence, we shall sometimes refer to $|\beta|^2$ as an *occupation probability*. The quantum system dynamics comprises both qubit-qubit interaction and motion of the qubits. Sometimes the terms *qubit* and *particle* are used interchangeably.

Further details about the qubit encoding are given in Section 9.2.1. For reasons of reducing computational expense when simulating the quantum model, the mesoscopic scale single-particle distribution is highly resolved in position-space but minimally resolved in momentum-space. The mesoscopic scale equation of motion of the effective kinetic many-particle system is a quantum Boltzmann equation that governs the time-dependent behavior of the single-particle distribution function. A derivation of the quantum Boltzmann equation from the modified Schrödinger equation is given in Section 9.2.2. The quantum Boltzmann equation has an unconventional collision function with a unique analytical form that is derived from the microscopic Hamiltonian that generates the locally coherent quantum mechanical evolution.

A derivation of the collision function is given in Section 9.3.1. Since the underlying quantum mechanical system is locally phase-coherent, one can ask if there exists an eigenstate of the unitary evolution operator that has a unity eigenvalue. The quantum evolution is stationary with respect to this particular eigenstate: the probability of occurrence of this eigenstate must be identical before and after the local unitary quantum mechanical evolution. Equating the analytical expressions for these probabilities allows us to uniquely determine the mesoscopic local equilibria associated with the single-particle probability distribution. This calculation is carried out in Section 9.3.2 and the result is that the equilibrium values of the single-particle probability distribution are parameterized by Fermi-Dirac functions. This is consistent with the fact that two-level qubits, or spin-$\frac{1}{2}$ quantum objects, are used to encode these mesoscopic occupation probabilities. The energy eigenvalue of each qubit within a localized region of space is accordingly shifted. That is, the energy eigenvalues of local qubits are non-degenerate.

In Section 9.3.3, we linearize the quantum Boltzmann equation about its local equilibria and then use a Chapman-Enskog perturbative expansion to derive the nonlinear macroscopic scale equation of motion as the zeroth-order moment of the single-particle distribution function. The macroscopic equation of motion is effectively a diffusive and convective nonlinear Burgers equation. The consequence of this perturbative expansion is an analytically predictable macroscopic scale transport coefficient, which in this case is the shear viscosity of the modeled fluid. The freedom we have in choosing our local quantum mechanical evolution translates into our ability to choose any desired shear viscosity in the model, from inviscid

flow all the way up to highly viscous flow. In other words, the rate of dissipation is arbitrarily tunable in the model.

Next, Section 9.4 we analyze the non-equilibrium mesoscopic dynamics from the perspective of entropy considerations. This is a way of understanding the numerical stability of the quantum algorithm. The quantum mechanical entropy function is introduced in Section 9.4.1. By extremizing this entropy function, using a Lagrange multiplier to fix energy conservation, we again obtain the Fermi-Dirac function as the local equilibria for the qubit excited state's occupation probabilities. In Section 9.4.2, we calculate an effective transition matrix, defined at the mesoscopic scale, of the quantum system. The transition matrix recasts the quantum evolution as a Markov process at the mesoscopic scale. In Section 9.4.2 and Section 9.4.2, we demonstrate that the transition matrix of the modeled kinetic system obeys the principle of detailed-balance in its qubit-qubit interactions.

Finally, in Section 9.5 we present several numerical results obtained from simulating the quantum model on a standard classical computer. Shock front development is readily observed. In Section 9.5.1, the consistency of the entropy function description of the mesoscopic dynamics is compared with the quantum Boltzmann equation description of the dynamics. The entropy function and quantum Boltzmann equation descriptions are found to be in perfect agreement. The quantum collision function maps incoming local qubit configurations into outgoing qubit configurations with higher entropy in such a way that the trajectory of configurations always follows contours on the entropy surface. The quantum model manifests behavior that at the mesoscopic scale emulates the second law of thermodynamics. An entropic lattice Boltzmann model of the Burgers equation has also been developed [Boghosian et al., 2004a], but its numerical stability is not as good as stability we find for the quantum lattice gas model.

9.1.1 Multiscale dynamics descriptions

The open quantum system model numerically predicts the time-dependent solutions of the one-dimensional Burgers equation

$$\partial_t u(x,t) + u\partial_x u(x,t) = \nu \partial_{xx} u(x,t), \tag{9.1}$$

which is a simplified model of shock formation with flow field $u(x,t)$ and kinematic viscosity ν. From a kinetic theory perspective, (9.1) is the effective field theory for the macroscopic behavior of a system of qubits governed at the mesoscopic scale by a quantum lattice Boltzmann equation:

$$f_{\pm}(x \pm c\delta t, t + \delta t) = f_{\pm}(x,t) \pm \Omega(f_+, f_-). \tag{9.2}$$

$f_\pm(x,t)$ are probability fields for the occupation at position x and at time t of a right moving qubit (+ direction) and a left moving qubit (− direction). $\Omega(f_+, f_-)$ is a nonlinear collision function for local qubit-qubit interaction. A qubit's local speed is $c \equiv \frac{\delta x}{\delta t}$, where δx and δt are the cell sizes of the space-time lattice.

(9.2) is a statistical description of the kinetic transport dynamics of the system of qubits on a lattice. (9.2) is the effective finite-difference equation for the mesoscopic behavior of the microscopic quantum system where the motion of the qubits and their quantum mechanical interactions are represented by two unitary operators, a streaming operator $\hat{\mathscr{S}}$ and a collision operator $\hat{\mathscr{C}}$, respectively, according to the quantum lattice gas paradigm [Yepez, 2001a]. The spatial displacement of $f_\pm$ appearing on the L.H.S. of (9.2) derives from the unitary streaming operator $\hat{\mathscr{S}}$. Taylor expanding $f_\pm(x \pm c\delta t, t + \delta t)$ about the spacetime point (x,t) gives rise to a parabolic partial differential equation. Hence, (9.2) can be written in differential point form as $\partial_t f_\pm(x,t) = \hat{\mathscr{L}}_\pm f_\pm(x,t) \pm \frac{1}{\delta t}\Omega(f_+, f_-)$, where $\hat{\mathscr{L}}_\pm = \partial_x\left(\mp c - \mathscr{D}_\circ \partial_x\right)$ is a Fokker-Planck operator, c is a constant drift coefficient, and $\mathscr{D}_\circ = \frac{1}{2}\frac{\delta x^2}{\delta t}$ is the diffusion coefficient. Here, the reason the spatial derivatives occur at second order while the temporal derivative occurs at first order is that the diffusive ordering of the fluctuations $\varepsilon \sim \delta x \sim \sqrt{\delta t}$ arises because of the microscopic random walk motion of the qubits. The form of the nonlinear collision function $\Omega(f_+, f_-)$ on the R.H.S. of (9.2) is derived from the unitary collision operator $\hat{\mathscr{C}}$ in Section 9.3.1. In Section 9.3.2 the nonlinear collision function is linearized about the equilibrium occupation probabilities $f_\pm^{\text{eq}}$. Then using a perturbative technique in Section 9.5.3, corrections to the drift and diffusion coefficients arise from the quantum mechanical qubit-qubit interactions, particularly nonlinearities appearing in the drift. The result is a nonlinear parabolic partial differential equation for the sum of the occupation probabilities $f_+ + f_-$.

Denoting the microscopic quantum state of the system at time t by $|\Psi(t)\rangle$, the microscopic quantum mechanical evolution equation is written as follows:

$$|\Psi(t+\delta t)\rangle = \hat{\mathscr{S}}\hat{\mathscr{G}}\hat{\mathscr{C}}|\Psi(t)\rangle. \tag{9.3}$$

(9.3) reduces to the Schrödinger wave equation when the operator $\hat{\mathscr{G}}$ is the identity operator. Quantum mechanical evolution, such as governed by the Schrödinger wave equation, is both linear and non-dissipative. The reason for employing the unconventional operator $\hat{\mathscr{G}}$ is to induce both non-linearity and dissipation into the effective dynamics. There are various alternatives for the operational form of $\hat{\mathscr{G}}$. As mentioned above, one representational choice for $\hat{\mathscr{G}}$ is the non-unitary process of quantum measurement that effectively erases local phase information contained in the wave function upon its collapse. Another representational choice for $\hat{\mathscr{G}}$ is as a unitary operator that randomly alters the local phase of the wave function.

In either case, the result is similar and local in its effect at the spacetime point where $\hat{\mathscr{G}}$ is applied: coherent phase information, and entanglement, is lost. It is this essential projective property of the $\hat{\mathscr{G}}$ operator to which we ascribe the nonlinearity and dissipation of the model and to which we refer by using the terms *wave function localization* or *open quantum system*.

9.1.2 Application to quantum computing

The type of open quantum model treated in this paper may be viewed as a parallel quantum algorithm designed for implementation on a quantum computer with periodic state reduction. (9.3) comprises a four-step quantum algorithm:

1. initialization step (state preparation of $|\Psi(t)\rangle$),
2. collision step (entanglement of the quantum state by $\hat{\mathscr{C}}$),
3. localization step (long-range decoherence or reduction of the quantum state by $\hat{\mathscr{G}}$),
4. and streaming step (interchange of amplitudes by $\hat{\mathscr{S}}$).

The Hamiltonian $\mathscr{H}$ that generates the unitary quantum evolution in (9.3), when formally expressed as $e^{i\hat{\mathscr{H}}\delta t/\hbar} \equiv \hat{\mathscr{S}}\hat{\mathscr{C}}$, may be called a *quantum lattice-gas Hamiltonian* (type I case). Quantum models of the form given by (9.3), when $\hat{\mathscr{G}}$ is identity, are known as quantum lattice gas algorithms and include models by Riazanov [Riazanov, 1958], Feyman and Hibbs [Feynman and Hibbs, 1965], Jacobson and Schulman [Jacobson and Schulman, 1984], Bialynicki-Birula [Bialynicki-Birula, 1994], Succi *et al.* [Succi and Benzi, 1993, Succi, 1996, Succi, 1998, Succi, 2002], Meyer [Meyer, 1996a, Meyer, 1996b, Meyer, 1997c, Meyer, 1997a, Meyer, 1998], Boghosian *et al.* [Boghosian and IV, 1997, Boghosian and IV, 1998b, Boghosian and IV, 199 Yepez and Boghosian [Yepez and Boghosian, 2002], and Vahala *et al.* [Vahala et al., 2003b, Vahala et al., 2004b, Vahala et al., 2003a, Vahala et al., 2004a]. However, for (9.3) to give rise to a macroscopic dissipative effective field theory, such as (9.1) with viscous dissipation proportional to the curvature of the flow field, $\hat{\mathscr{G}}$ can be chosen to be a projection operator that commutes with the number operator (type II case).

Parallel quantum algorithms of this sort for computational physics have been developed to numerically predict time-dependent field solutions of the classical wave equation [Yepez, 1998, Yepez, 2001a], the diffusion equation [Yepez, 2001b, Berman et al., 2002], the Navier-Stokes equation [Yepez, 1999, Yepez, 2001a], the nonlinear Burgers equation [Yepez, 2002c, Yepez, 2002a], and the one dimensional equations for magnetohydrodynamic shocks [Vahala et al., 2003c]. Such parallel quantum algorithms do not fully exploit the computational complexity of the underlying quantum computer because of the imposed state reduction. Hence, any quantum mechanical complexity that provides an algorithmic speedup can only be harnessed

locally over a relatively limited spatial region. So long as the spatial localization limits phase-coherence to less than a few dozen qubits, implementation of the parallel quantum algorithms is straightforward using present day classical computers, otherwise these parallel quantum algorithms could only be implemented on type-II quantum computers that may be built someday [Yepez, 2002b]. The first parallel quantum algorithms for the diffusion and Burgers equations have with success been experimentally tested on quantum information processing prototypes of parallel quantum computers, or type-II quantum computers [Yepez, 2001c], using spatial nuclear magnetic resonance (NMR) spectroscopy on a linear array (in both position-space and momentum-space) of segmented ensembles of two-qubit labeled chloroform molecules [Pravia et al., 2002, Pravia et al., 2003, Chen et al., 2006a]. The experimental implementation details and results from a recent NMR-based quantum information processing experiment of the open quantum model presented in this paper are discussed in our companion paper [Chen et al., 2006a].

9.2 Model construction

9.2.1 Qubit encoding

$$\begin{array}{rccccl} \text{macro:} & (\rho,u) & (\rho,u) & \cdots & (\rho,u) & \text{Burgers} \\ \text{meso:} & (f_+,f_-) & (f_+,f_-) & \cdots & (f_+,f_-) & \text{Boltzmann} \\ \text{micro:} & \underbrace{|q_+\rangle\otimes|q_-\rangle}_{\substack{\text{node }1\\ x_\circ}} & \underbrace{|q_+\rangle\otimes|q_-\rangle}_{\substack{\text{node }2\\ x_\circ+\delta x}} & \cdots & \underbrace{|q_+\rangle\otimes|q_-\rangle}_{\substack{\text{node }L\\ x_\circ+(L-1)\delta x}} & \text{Schrödinger} \end{array}$$

Figure 9.1: A type II quantum lattice gas with L nodes and 2 qubits per node depicted at three spatial scales. The array is one dimensional with periodic boundary conditions. The coordinate $x_\circ$ refers to the location of the first node. The symbol $\otimes$ represents the tensor (or outer) product operation. At the lowest level are microscopic field quantities (*i.e.* amplitudes of qubit states) governed by the modified Schrödinger equation (9.3) with an "programmed" Hamiltonian. At the middle level are mesoscopic field quantities (*i.e.* occupation probabilities $f_\pm$) governed by the quantum Boltzmann equation (9.2). Finally, at the highest level are macroscopic field quantitites (*i.e.* ρ or u) governed by the nonlinear Burgers equation (9.1).

We consider a quantum system with Q number of qubits used to encode (9.3). A quantum lattice gas system with $L = \frac{Q}{2}$ number of nodes is depicted in Figure 9.1 where, at the microscopic scale, two qubits $|q_+\rangle$ and $|q_-\rangle$ per node are used to encode the mesoscopic probabilities f_+ and f_- of the qubit excited state occupations at that node:

$$|q_\pm(x,t)\rangle = \sqrt{1-f_\pm(x,t)}|0\rangle + \sqrt{f_\pm(x,t)}|1\rangle, \tag{9.4}$$

for $0 \leq f_\pm \leq 1$, and where $|0\rangle$ and $|1\rangle$ denote the ground state and excited state, respectively, of a qubit. Each qubit in the system is independently set; the on-site ket, $|\psi(x,t)\rangle$, is a tensor

product over the qubits residing at site x

$$|\psi(x,t)\rangle = |q_+(x,t)\rangle \otimes |q_-(x,t)\rangle, \tag{9.5}$$

for all x. At time t, the quantum state of the entire microscopic quantum lattice gas system in (9.3) is the tensor product of all the on-site kets:

$$|\Psi(t)\rangle = \bigotimes_{j=0}^{L-1} |\psi(x+j\delta x,t)\rangle. \tag{9.6}$$

Since the qubits can be thought of as containers for encoding the quantum particle occupation probabilities according to (9.4), the particle number operator is equivalent to the qubit number operator. Let $\hat{n}_\alpha$, where $\alpha = 1,\ldots,Q$, denote the qubit number operator for the α^{th} qubit at site x. The occupancy probability of a particle located at the α^{th} qubit at time t is the matrix element

$$f_\alpha(x,t) \equiv \langle \Psi(t)|\hat{n}_\alpha|\Psi(t)\rangle. \tag{9.7}$$

Because the quantum state (9.6) is separable over the nodes of the lattice, (9.7) can be rewritten using the on-site ket at node x:

$$f_\pm(x,t) \equiv \langle \psi(x,t)|\hat{n}_\pm|\psi(x,t)\rangle, \tag{9.8}$$

where we have assumed the on-site kets are normalized $\langle\psi(x,t)|\psi(x,t)\rangle = 1$ for all x, and where $\hat{n}_+ \equiv \hat{n}\otimes\mathbf{1}$ and $\hat{n}_- \equiv \mathbf{1}\otimes\hat{n}$ are defined in terms of the singleton number operator $\hat{n}$.

9.2.2 Quantum Boltzmann equation

Here we shall derive (9.2) from (9.3). The application of $\hat{\mathscr{S}}$ causes the amplitudes associated with the $|q_+\rangle$ qubits to move to the right by δx and the amplitudes of the $|q_-\rangle$ qubits to the left. In particular, say $|\Psi'\rangle = \hat{\mathscr{S}}|\Psi\rangle$ causes the amplitudes of the α-th qubit to be transferred to the α'-th qubit. Then, by streaming, the occupation probabilities shift so that we must have the equality $f_{\alpha'} = f_\alpha$. By (9.7), this equality is expressible directly in terms of the operators:

$$\hat{\mathscr{S}}^\dagger \hat{n}_{\alpha'} \hat{\mathscr{S}} = \hat{n}_\alpha. \tag{9.9}$$

The identity (9.9) will allow us to derive (9.2) from (9.3). We include collisional scattering and write:

$$f_{\alpha'} \overset{(9.7)}{=} \langle \Psi(t+\delta t)|\hat{n}_{\alpha'}|\Psi(t+\delta t)\rangle \tag{9.10}$$

$$\overset{(9.3)}{=} \langle \Psi(t)|\hat{\mathscr{C}}^\dagger\hat{\mathscr{G}}^\dagger\hat{\mathscr{S}}^\dagger\hat{n}_{\alpha'}\hat{\mathscr{S}}\hat{\mathscr{G}}\hat{\mathscr{C}}|\Psi(t)\rangle \tag{9.11}$$

$$\overset{(9.9)}{=} \langle \Psi(t)|\hat{\mathscr{C}}^\dagger\hat{\mathscr{G}}^\dagger\hat{n}_\alpha\hat{\mathscr{G}}\hat{\mathscr{C}}|\Psi(t)\rangle. \tag{9.12}$$

Since $\hat{\mathscr{G}}$ commutes with $\hat{n}_\alpha$, for all α, and $\hat{\mathscr{G}}^\dagger\hat{\mathscr{G}} = 1$, we have

$$f_{\alpha'} - f_\alpha = \langle\Psi(t)|\hat{\mathscr{C}}^\dagger\hat{n}_\alpha\hat{\mathscr{C}} - \hat{n}_\alpha|\Psi(t)\rangle, \tag{9.13}$$

where we have subtracted $f_\alpha = \langle\Psi(t)|\hat{n}_\alpha|\Psi(t)\rangle$ from the both sides of (9.13). In the continuum limit, as the lattice resolution becomes infinite ($\delta x \to 0$ and $\delta t \to 0$), the occupation probabilities form a continuous and differentiable field in position space. Defining its total time derivative as $\frac{f_{\alpha'}-f_\alpha}{\delta t}$, we obtain the general form of (9.2):

$$\frac{df_\alpha}{dt} = \frac{1}{\delta t}\langle\Psi(t)|\hat{\mathscr{C}}^\dagger\hat{n}_\alpha\hat{\mathscr{C}} - \hat{n}_\alpha|\Psi(t)\rangle. \tag{9.14}$$

Because of the diffusive ordering of the temporal and spatial fluctuations of f_α, we expand the L.H.S. to first order in time and second order in space. Furthermore, since the collisions are separable over the nodes of the lattice, $\hat{\mathscr{C}} = \bigotimes_{j=0}^{L-1}\hat{U}$, where $\hat{U}$ is the on-site collision operator, we recover (9.2) where the type-II collision function is

$$\Omega[\psi(x,t)] = \langle\psi(x,t)|\hat{U}^\dagger\hat{n}_\pm\hat{U} - \hat{n}_\pm|\psi(x,t)\rangle. \tag{9.15}$$

9.2.3 Macroscopic field assignment

The mesoscopic probabilities $f_\pm$ in turn are used to calculate the macroscopic variables using the Chapman-Enskog perturbative expansion given in Section 9.3.3. The number density field $\rho(x,t)$ is

$$\rho(x,t) \equiv f_+(x,t) + f_-(x,t), \tag{9.16}$$

and the flow field $u(x,t)$ in (9.1) is

$$u(x,t) \equiv c\left[f_+(x,t) + f_-(x,t) - 1\right], \tag{9.17}$$

where the propagation speed of the qubits is the ratio of the lattice cell size to the time step interval, $c = \frac{\delta x}{\delta t}$, as is characteristic of lattice gas models [1].

9.2.4 Summary of the four-step quantum algorithm

(9.3) is encapsulated in the following four steps:

1. Initialization step: The state of the quantum lattice gas is set as specified in Figure 9.1, where $|q_\pm(x,t)\rangle = \sqrt{f_\pm(x,t)}|1\rangle + \sqrt{1-f_\pm(x,t)}|0\rangle$.

[1] Here we have taken the mass of a particle encoded in a qubit to be unity, $m = 1$.

2. Collsion step: Apply the collision operator simultaneously to all sites

$$|\psi'(x,t)\rangle = \hat{U}|\psi(x,t)\rangle.$$

3. Localization step: This step may be implemented in a non-unitary or unitary way. In the non-unitary way, the outgoing occupancy probability distribution is represented by the following matrix element

$$f'_{\pm}(x,t) = \langle\psi'(x,t)|\hat{n}_{\pm}|\psi'(x,t)\rangle. \tag{9.18}$$

To recover the Burgers' equation, $f_{\pm}$ can be determined by observation of a single system repeated enough times to recover the distribution (9.18) by equating to the frequency-of-occurrence of outcomes ("non-unitary read"). Alternatively, the phase of each qubit in the system can be periodically randomized by application of a unitary rotation of the qubits.

4. Streaming step: Reinitialize ("write") the state of the quantum lattice gas as a separable state where each qubit is set as follows

$$|q_{\pm}(x,t+\tau)\rangle = \sqrt{f'_{\pm}(x \mp \delta x,t)}|1\rangle + \sqrt{1-f'_{\pm}(x \mp \delta x,t)}|0\rangle \tag{9.19}$$

for all x. Note that qubit $|q_+\rangle$ is shifted to its neighboring node at the left while $|q_-\rangle$ is shifted to its neighboring node at the right. This step requires nearest-neighbor communication between all lattice nodes. At this point, one time-step update is completed.

9.3 Analytical treatment

9.3.1 Quantum collision function

Here we shall derive (9.1) from (9.2). We begin with the outgoing occupation probabilities

$$f'_{\pm} = \langle\psi'|\hat{n}_{\pm}|\psi'\rangle = \langle\psi|\hat{U}^{\dagger}\hat{n}_{\pm}\hat{U}|\psi\rangle. \tag{9.20}$$

The initial on-site ket $|q_+\rangle \otimes |q_-\rangle$ is

$$\begin{aligned} |\psi\rangle &= \sqrt{f_+f_-}|11\rangle + \sqrt{f_+(1-f_-)}|10\rangle \\ &\quad +\sqrt{(1-f_+)f_-}|01\rangle + \sqrt{(1-f_+)(1-f_-)}|00\rangle \end{aligned} \tag{9.21}$$

$$= \begin{pmatrix} \sqrt{(1-f_+)(1-f_-)} \\ \sqrt{(1-f_+)f_-} \\ \sqrt{f_+(1-f_-)} \\ \sqrt{f_+f_-} \end{pmatrix}. \tag{9.22}$$

We use a conservative quantum logic gate to represent the collision operator:

$$\hat{U} = \begin{pmatrix} 1 & 0 & 0 & 0 \\ 0 & e^{-i\xi}\cos\theta & -e^{-i\zeta}\sin\theta & 0 \\ 0 & e^{i\zeta}\sin\theta & e^{i\xi}\cos\theta & 0 \\ 0 & 0 & 0 & 1 \end{pmatrix}. \tag{9.23}$$

The qubit number operators are:

$$\hat{n}_+ = \begin{pmatrix} 0 & 0 & 0 & 0 \\ 0 & 0 & 0 & 0 \\ 0 & 0 & 1 & 0 \\ 0 & 0 & 0 & 1 \end{pmatrix} \qquad \hat{n}_- = \begin{pmatrix} 0 & 0 & 0 & 0 \\ 0 & 1 & 0 & 0 \\ 0 & 0 & 0 & 0 \\ 0 & 0 & 0 & 1 \end{pmatrix} \tag{9.24}$$

Substituting (9.22-9.24) into (9.20) gives us explicit update rules for the probability occupancies

$$f'_+ = f_+ f_- + \left\| e^{i\xi}\cos\theta\sqrt{f_+(1-f_-)} + e^{i\zeta}\sin\theta\sqrt{(1-f_+)f_-} \right\|^2 \tag{9.25a}$$

$$f'_- = f_+ f_- + \left\| -e^{-i\zeta}\sin\theta\sqrt{f_+(1-f_-)} + e^{-i\xi}\cos\theta\sqrt{(1-f_+)f_-} \right\|^2, \tag{9.25b}$$

where the double vertical bars denote the norm or absolute value of the enclosed quantity. After some algebraic manipulation, this pair of equations can be reduced to the standard form

$$f'_\pm \equiv \langle\psi'|\hat{n}_\pm|\psi'\rangle = f_\pm \pm \Omega(f_+, f_-). \tag{9.26}$$

On the R.H.S. of (9.26), the quantum collision function, $\Omega(f_+, f_-)$, is

$$\begin{aligned} \Omega(f_+, f_-) = & -\sin^2\theta[f_+(1-f_-) - (1-f_+)f_-] \\ & + \sin 2\theta\cos(\zeta-\xi)\sqrt{f_+(1-f_+)f_-(1-f_-)}, \end{aligned} \tag{9.27}$$

where θ, ζ, and ξ are Euler angles. In addition to the dependence of the Euler angles, there appears an unusual dependence on the square root of the occupation probabilities. This type of additional term is a consequence of the microscopic scale quantum nature of the model that remains evident at the mesoscopic scale. This term gives rise to non-linearity in the macroscopic equation of motion. The reason the square root term arises in (9.27) has its origin in the fundamental qubit encoding, described in Section 9.2.4, where the square root of the occupation probabilities is employed to generate the initial probability amplitudes of a qubit's two-level states. In turn, the local on-site ket appearing in (9.21) and (9.22) depends on the square root of the occupation probabilities. Inserting (9.22) into (9.20), and after working through some algebraic manipulations, we see that the mesoscopic collision operator too must depend explicitly on the value of a probability amplitude, and not just

on classical probabilities. The fact that the square root of probabilities are employed in the algorithm is a characteristic feature of its quantum mechanical nature.

(9.27) can be expressed a bit more simply:

$$\begin{aligned}\Omega(f_+, f_-) &= \sin^2\theta(f_- - f_+) \\ &+ \sin 2\theta\cos(\zeta-\xi)\sqrt{f_+(1-f_+)f_-(1-f_-)}.\end{aligned} \tag{9.28}$$

9.3.2 Local equilibria

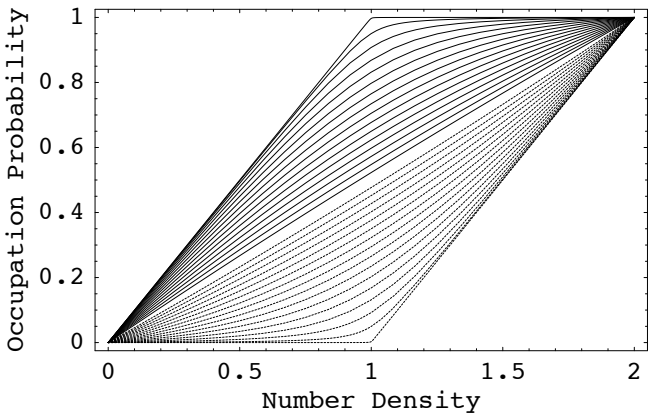

Figure 9.2: A plot of the equilibrium occupancy probabilities $d_\pm$ versus the number density at that site. The upper solid curves are $d_+(\theta,\xi,\zeta)$ and the lower dotted curves are $d_-(\theta)$ as specified by (9.34) for $\theta = \frac{\pi}{512}, ..., \frac{\pi}{2} - \frac{\pi}{512}$ in steps of $\Delta\theta = \frac{\pi}{32}$ for $\xi = \zeta$. The abscissa and ordinate are both non-dimensional probability values. As $\theta = \frac{\pi}{2}$ is the diffusive case where $d_\pm = \frac{\rho}{2}$.

Let $d_\pm$ denote the local equilibrium values of the occupation probabilities. The equilibrium condition $\Omega(f_+, f_-)|_{f_\pm = d_\pm} = 0$ becomes:

$$\frac{d_+}{1-d_+} - \frac{d_-}{1-d_-} = 2\cot\theta\cos(\zeta-\xi)\sqrt{\frac{d_+}{1-d_+}\frac{d_-}{1-d_-}}, \tag{9.29}$$

which is a statement of detailed-balance of collisions at the mesoscopic scale and which we analyze in Section 9.4.2.

We take the equilibrium occupation probabilities to have the following form:

$$d_+ = \frac{1}{\gamma z + 1} \qquad \text{and} \qquad d_- = \frac{1}{\frac{z}{\gamma} + 1}. \tag{9.30}$$

Substituting (9.30) into (9.29) gives a quadratic equation in γ that has the solution

$$\gamma = \sqrt{\alpha^2+1} + \alpha \tag{9.31a}$$

$$\frac{1}{\gamma} = \sqrt{\alpha^2+1} - \alpha, \tag{9.31b}$$

where $\alpha \equiv \cot\theta\cos(\zeta - \xi)$. Next, substituting (9.30) into the total number density, $\rho = d_+ + d_-$, we obtain a quadratic equation in z

$$\rho z^2 + \left(\gamma + \frac{1}{\gamma}\right)(\rho - 1)z + \rho - 2 = 0. \tag{9.32}$$

Substituting the positive root solution of (9.32) into (9.30), we find after much algebraic manipulation

$$d_+ = \frac{1 + \gamma^2 + (1 - \gamma^2)\rho - \gamma\sqrt{\left(\frac{1}{\gamma} + \gamma\right)^2(\rho - 1)^2 + 4(\rho - 2)\rho}}{2(1 - \gamma^2)}. \tag{9.33}$$

Then substituting $\gamma = \sqrt{\alpha^2 + 1} + \alpha$ into (9.33) gives the result

$$d_\pm = \frac{\rho}{2} \mp \frac{1}{2\alpha}\left(\sqrt{1 + \alpha^2} - \sqrt{1 + \alpha^2(\rho - 1)^2}\right). \tag{9.34}$$

The local equilibria $d_\pm$ are plotted in Figure 9.2 for a range of angles.

9.3.3 Chapman-Enskog expansion for the Burgers equation

It is convenient to treat the occupation probabilities as a two-component field

$$\mathbf{f} = \begin{pmatrix} f_+ \\ f_- \end{pmatrix}. \tag{9.35}$$

We expand $\mathbf{f}$ about its equilibrium value denoted $\mathbf{d}$ so that $\mathbf{f} = \mathbf{d} + \delta\mathbf{f} + \mathcal{O}(\varepsilon^2)$, where $\varepsilon \sim \delta x$ is analogous to what in the literature on fluid dynamics is called the *Knudsen number* [2]. The equilibrium condition $\Omega|_{\mathbf{f}=\mathbf{d}} = 0$ leads to a tractable polynomial equation for the components of $\mathbf{d}$. The linearized finite-difference quantum Boltzmann equation is

$$\mathbf{f}(x \pm \delta x, t + \delta t) - \mathbf{f}(x, t) = J\delta\mathbf{f}(x, t), \tag{9.36}$$

where the Jacobian of the collision term is

$$\mathbf{J} \equiv \begin{pmatrix} \frac{\partial\Omega}{\partial a} & \frac{\partial\Omega}{\partial b} \\ -\frac{\partial\Omega}{\partial a} & -\frac{\partial\Omega}{\partial b} \end{pmatrix}\Bigg|_{\mathbf{f}=\mathbf{d}} = \begin{pmatrix} J_+ & J_- \\ -J_+ & -J_- \end{pmatrix}. \tag{9.37}$$

The left and right eigenvectors of J are

$$\xi^1 = \begin{pmatrix} 1 & 1 \end{pmatrix} \qquad \xi_1 = \frac{1}{J_- - J_+}\begin{pmatrix} J_- \\ -J_+ \end{pmatrix} \tag{9.38}$$

$$\xi^2 = \frac{1}{J_+ - J_-}\begin{pmatrix} J_+ & J_- \end{pmatrix} \qquad \xi_2 = \begin{pmatrix} 1 \\ -1 \end{pmatrix} \tag{9.39}$$

[2] In this one-dimensional quantum model, the flow speed is proportional to the number density, $u = c_s(1 - \rho)$. Therefore, requiring $\varepsilon \sim \delta\rho$ be small implies a low Mach number constraint. The analytical development is guaranteed to be valid only in the subsonic limit where $u \ll c_s$.

with associated eigenvalues $\lambda_1 = 0$ and $\lambda_2 = J_+ - J_-$. $\xi^i \xi_j = \delta_{ij}$. $\mathbf{J}$ may be rewritten as

$$\mathbf{J} = \lambda_2 \xi_2 \xi^2 = \begin{pmatrix} J_+ & J_- \\ -J_+ & -J_- \end{pmatrix} \tag{9.40}$$

$\mathbf{J}$ is singular. Its Moore-Penrose generalized inverse [Penrose, 1955] is the following:

$$\mathbf{J}^{-1}_{\text{gen}} = \frac{1}{\lambda_2} \xi_2 \xi^2 = \frac{1}{J_+ - J_-} \mathbf{J}. \tag{9.41}$$

Now we invoke the continuum limit where $\delta x \to 0$ and $\delta t \to 0$ so $\mathbf{f}$ is a continuous and differentiable two-component field. We obtain a first-order equation by Taylor expanding (9.36) in x and t and keeping only terms that are first order in ε:

$$\sigma_z \delta x \partial_x \mathbf{d} = \mathbf{J} \delta \mathbf{f} + \mathcal{O}(\varepsilon^2), \tag{9.42}$$

where $\sigma_z = \begin{pmatrix} 1 & 0 \\ 0 & -1 \end{pmatrix}$. Multiplying (9.42) on the left by $\mathbf{J}$ gives

$$\mathbf{J} \sigma_z \delta x \partial_x \mathbf{d} = (J_+ - J_-) \mathbf{J} \delta \mathbf{f} + \mathcal{O}(\varepsilon^2), \tag{9.43}$$

which has the nontrivial solution

$$\delta \mathbf{f} = \frac{1}{J_+ - J_-} \sigma_z \delta x \partial_x \mathbf{d} + \mathcal{O}(\varepsilon^2) \tag{9.44}$$

consistent with (9.41). Taking the difference of the respective components gives

$$\delta f_+ - \delta f_- = \frac{1}{J_+ - J_-} \delta x \partial_x \rho + \mathcal{O}(\varepsilon^2). \tag{9.45}$$

Similarly from (9.36), we obtain the second order equation:

$$\begin{aligned} \delta t \partial_t \mathbf{d} \;&+\; \sigma_z \delta x \partial_x \left(\mathbf{d} + \delta \mathbf{f} \right) \\ &+\; \frac{\delta x^2}{2} \partial_{xx} d + \mathcal{O}(\varepsilon^3) = \begin{pmatrix} \Omega \\ -\Omega \end{pmatrix}. \end{aligned} \tag{9.46}$$

We now take the sum of the respective components:

$$\begin{aligned} \delta t \partial_t \rho \;&+\; \delta x \partial_x \left(d_+ - d_- + \delta f_+ - \delta f_- \right) \\ &+\; \frac{\delta x^2}{2} \partial_{xx} \rho + \mathcal{O}(\varepsilon^3) = 0. \end{aligned} \tag{9.47}$$

Inserting (9.45) into the above equation gives the general effective field theory for any one-dimensional two-qubit-per-site lattice gas that conserves particle number

$$\begin{aligned} \partial_t \rho \;&+\; c \partial_x \left(d_+ - d_- \right) + \frac{\delta x^2}{\delta t} \frac{\partial_x (J_+ - J_-)}{(J_+ - J_-)^2} \partial_x \rho \\ &+\; \frac{\delta x^2}{2 \delta t} \left(\frac{2}{J_+ - J_-} + 1 \right) \partial_{xx} \rho + \mathcal{O}(\varepsilon^3) = 0. \end{aligned} \tag{9.48}$$

(9.34) implies that

$$d_+ - d_- = -\frac{1}{\alpha}\left(\sqrt{1+\alpha^2} - \sqrt{1+\alpha^2(\rho-1)^2}\right). \tag{9.49}$$

Again, we compute the components of J:

$$J_\pm = \frac{\partial\Omega}{\partial p_\pm} = \sin^2\theta\left(\mp 1 - \alpha\frac{(2d_\pm - 1)d_\mp(1-d_\mp)}{\sqrt{d_+(1-d_+)d_-(1-d_-)}}\right). \tag{9.50}$$

And this implies

$$J_+ - J_- = -2\sin^2\theta(1+\alpha^2\mathcal{R}), \tag{9.51}$$

where the factor $\mathcal{R} = \mathcal{R}(\alpha,\rho)$ is too complicated an expression to write out here but has the important property that $\mathcal{R}(\alpha,\rho) = 1+\mathcal{O}(\alpha)$. Finally, substituting the two results (9.49) and (9.51) into (9.48) gives the effective field theory

$$\partial_t\rho + c\cot\theta\cos(\zeta-\xi)(1-\rho)\partial_x\rho = \frac{\cot^2\theta}{2}\frac{\delta x^2}{\delta t}\partial_{xx}\rho + \mathcal{O}(\varepsilon^3, \varepsilon\alpha^2), \tag{9.52}$$

which becomes identical to (9.1) for $u = c_s(1-\rho)$ with sound speed $c_s = c\cot\theta\cos(\zeta-\xi)$ and kinematic viscosity $\nu = \frac{1}{2}\cot^2\theta\frac{\delta x^2}{\delta t}$. c_s and ν are "programmable" by appropriately choosing the Euler angles in (9.23).

9.4 Stability considerations

9.4.1 Quantum mechanical entropy function

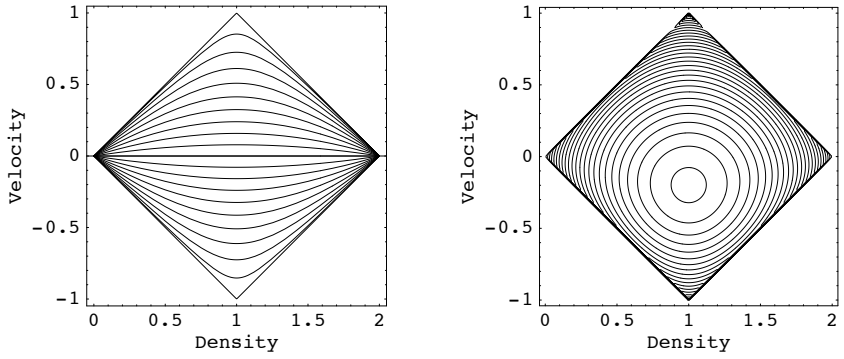

Figure 9.3: Left: equilibria contours of the kinetic mode $v^{\text{eq}} = d_+ - d_-$. Right: constant-entropy contours of $\mathcal{H}_\gamma(\rho, v)$ for $\theta = 1.5$ radians.

The unconditional numerical stability of the quantum algorithm can be understood from another vantage point which clarifies the statement of the unitarity of the quantum mechanical collision process. There exists an entropy function, denoted here as $\mathcal{H}$, that is consistent

with the unitary collision operator (9.23), the Fermi-Dirac equilibrium for the occupation probabilities of the qubit's eigenstates (9.30), quantum Boltzmann equation (9.20), and the nonlinear quantum collision function (9.28). The quantum mechanical entropy function is

$$\mathcal{H} = -\sum_{a=\pm} \left[f_a \ln(\gamma_a f_a) + (1 - f_a) \ln(1 - f_a) \right], \tag{9.53}$$

where $\gamma_+ = \sqrt{\alpha^2 + 1} + \alpha$, $\gamma_- = \frac{1}{\gamma_+} = \sqrt{\alpha^2 + 1} - \alpha$. Let $E_\pm$ denote the qubit energy eigenvalues. If we calculate the maximum of the entropy function, $\frac{\partial \mathcal{H}}{\partial f_a} = 0$, where we add the Lagrannian multiplier $\beta E_\pm f_\pm$ to $\mathcal{H}$ as a conserved energy constraint, we find that the solution for $f_\pm$ is (9.30). That is,

$$\frac{\partial \mathcal{H}}{\partial f_\pm} = -\ln(\gamma_\pm f_\pm) - 1 + \ln(1 - f_\pm) + 1 + \beta E_\pm, \tag{9.54}$$

from which we can solve for the non-equilibrium distribution function

$$f_\pm^{\text{noneq}} = \frac{1}{\frac{1}{\gamma_\pm} e^{\beta E_\pm - \partial_{f_\pm} \mathcal{H}} + 1}. \tag{9.55}$$

The equilibrium point occurs at $\partial_{f_\pm} \mathcal{H} = 0$, so from (9.55) we obtain the Fermi-Dirac function

$$f_\pm^{\text{eq}} = \frac{1}{\frac{1}{\gamma_\pm} e^{\beta E_\pm} + 1}. \tag{9.56}$$

We can also check whether (9.53) is consistent with the quantum collision function (9.28). To do this, we express (9.28) in terms of the macroscopic variables $\rho = f_+ + f_-$ and $v \equiv f_+ - f_-$ as follows:

$$\begin{aligned} \Omega_{\text{qu}}(\rho, v) &= -\sin^2\theta\, v \\ &+ \frac{1}{2} \sin 2\theta \cos\xi \sqrt{(\rho^2 - v^2) \left[1 - \rho + \frac{1}{4}(\rho^2 - v^2) \right]}. \end{aligned} \tag{9.57}$$

The equilibria contours of constant v, the kinetic mode defined by (9.49), are shown on the left of Figure 9.3. Since ρ is conserved, the quantum Boltzmann equation (9.20) re-expressed in terms of the macroscopic variables acts only on the kinetic mode:

$$v' = v + 2\,\Omega_{\text{qu}}(\rho, v). \tag{9.58}$$

We can also express the entropy function in terms of the macroscopic variables:

$$\begin{aligned} \mathcal{H}_\gamma(\rho, v) &= 2\ln 2 - \frac{1}{2}\{(\rho + v) \ln[\gamma(\rho + v)] + (\rho - v) \ln \frac{\rho - v}{\gamma} + (2 - \rho + v) \ln(2 - \rho + v) \\ &+ (2 - \rho - v) \ln(2 - \rho - v)\}. \end{aligned} \tag{9.59}$$

The entropy function $\mathcal{H} = \mathcal{H}_\gamma(\rho, v)$ is indirectly a function of the Euler angles of the quantum logic gate since $\gamma = \gamma(\theta, \xi, \zeta)$. Constant entropy contours of the surface defined by (9.59) are shown at the right of Figure 9.3.

9.4.2 Detailed balance

Transition matrix and detailed-balance

With two qubits located per lattice node, there are four basis states:

$$\begin{array}{llll} s_0 = |00\rangle & f_+ = 0 & f_- = 0 & P_0 = (1-d_+)(1-d_-) \\ s_1 = |01\rangle & f_+ = 0 & f_- = 1 & P_1 = (1-d_+)d_- \\ s_2 = |10\rangle & f_+ = 1 & f_- = 0 & P_2 = d_+(1-d_-) \\ s_3 = |11\rangle & f_+ = 1 & f_- = 1 & P_3 = d_+d_-. \end{array} \tag{9.60}$$

In (9.60), the configuration probabilites P_i, for $i = 0, 1, 2, 3$, are mean-field estimates neglecting qubit-qubit correlations. Using Q qubits to encode up to Q fermions, there are 2^Q quantum states. We shall consider the $Q = 2$ case:

$$\begin{pmatrix} P'_0 \\ P'_1 \\ P'_2 \\ P'_3 \end{pmatrix} = \underbrace{\begin{pmatrix} T_{00} & T_{01} & T_{02} & T_{03} \\ T_{10} & T_{11} & T_{12} & T_{13} \\ T_{20} & T_{21} & T_{22} & T_{23} \\ T_{30} & T_{31} & T_{32} & T_{33} \end{pmatrix}}_{\text{transition matrix}} \begin{pmatrix} P_0 \\ P_1 \\ P_2 \\ P_3 \end{pmatrix} \tag{9.61}$$

Conservation of probability condition is:

$$\sum_{i=0}^{2^Q-1} P'_i = \sum_{i=0}^{2^Q-1} P_i, \tag{9.62}$$

which implies

$$\begin{aligned} \sum_{i=0}^{2^Q-1} \left(\sum_{j=0}^{2^Q-1} T_{ij} P_j - P_i \right) &= \sum_{j=0}^{2^Q-1} P_j \left(\sum_{i=0}^{2^n-1} T_{ij} \right) - \sum_{j=0}^{2^Q-1} P_j \\ &= 0 \end{aligned} \tag{9.63}$$

provided the columns of the transition matrix sum to unity. Hence, to conserve probability, we require:

$$\sum_{i=0}^{2^Q-1} T_{ij} = 1. \tag{9.64}$$

Conservative transition matrix

The detailed-balance condition is stated as follows:

$$T_{ij} P_i = T_{ji} P_j, \tag{9.65}$$

for $i \neq j$. To conserve particle number, the transition matrix for the $Q = 2$ case is constrained to have the form:

$$\mathbf{T}_{\text{conservative}} = \begin{pmatrix} 1 & 0 & 0 & 0 \\ 0 & 1-A-C & A+D & 0 \\ 0 & B+C & 1-B-D & 0 \\ 0 & 0 & 0 & 1 \end{pmatrix}, \tag{9.66}$$

where the rows sum to unity according to (9.64) to preserve probability ($P_1' + P_2' = P_1 + P_2$), so we have

$$\begin{aligned} P_1' + P_2' &= (1-A-C)P_1 + (A+D)P_2 \\ &\quad +(B+C)P_1 + (1-B-D)P_2. \end{aligned} \tag{9.67}$$

This implies

$$P_1 + P_2 = (1-A+B)P_1 + (1+A-B)P_2 \tag{9.68}$$

or

$$(B-A)(P_1 - P_2) = 0. \tag{9.69}$$

The detailed-balance condition (9.65) for $i = 1$ and $j = 2$ is:

$$(A+D)P_1 = (B+C)P_2. \tag{9.70}$$

The set of equations (9.69) and (9.70) admit two solutions. The first solution (diffusion case) is the following: $A = B$ and $C = D$ with identical local equilibria $P_1 = P_2$. In the mean-field limit, we can write $P_1 = (1-d_+)d_-$ and $P_2 = d_+(1-d_-)$, so the equality $P_1 = P_2$ implies the equilibrium occupation probabilities are equal as well, $d_+ = d_-$. This solution can be parametrized by an angle θ where in (9.66) $A = B = \sin^2\theta$:

$$\mathbf{T}_{\text{doubly stochastic}} = \begin{pmatrix} 1 & 0 & 0 & 0 \\ 0 & \cos^2\theta - C & \sin^2\theta + C & 0 \\ 0 & \sin^2\theta + C & \cos^2\theta - C & 0 \\ 0 & 0 & 0 & 1 \end{pmatrix}. \tag{9.71}$$

(9.71) leads to the constraint $\left(\frac{P_2}{P_1} - 1\right)(\sin^2\theta + C) = 0$, which in turn gives $P_1 = P_2$.

The second solution (Burgers case) of (9.69) and (9.70) is the following: $A = B$ and $C \neq D$ with non-equal local equilibria $P_1 \neq P_2$. In this case, the transition matrix is not doubly stochastic. There is no transition matrix that is doubly stochastic that gives rise to a situation where $P_1 \neq P_2$. We will see in the next section Section 9.4.2 that the transition matrix of the quantum model has this second form:

$$\mathbf{T}_{\text{qm}} = \begin{pmatrix} 1 & 0 & 0 & 0 \\ 0 & \cos^2\theta - C & \sin^2\theta + D & 0 \\ 0 & \sin^2\theta + C & \cos^2\theta - D & 0 \\ 0 & 0 & 0 & 1 \end{pmatrix}, \tag{9.72}$$

where the particular values of $C = C(\theta, \xi, \zeta, \psi_1, \psi_2)$ and $D = D(\theta, \xi, \zeta, \psi_1, \psi_2)$ will be determined by the Euler angles in the unitary collision operator (9.23) and probability amplitudes of the quantum state vector.

At equilibrium, using (9.30), $\frac{P_1}{P_2} = \gamma^2$, so the detailed-balance condition (9.70) in this case is

$$\gamma^2 = \frac{\sin^2\theta + C}{\sin^2\theta + D}. \tag{9.73}$$

A solution is the following:

$$C = \frac{\gamma \sin 2\theta}{2} e^{i(\xi-\zeta)} \tag{9.74a}$$

$$D = -\frac{\sin 2\theta}{2\gamma} e^{-i(\xi-\zeta)}. \tag{9.74b}$$

Since C and D depend on γ, this means the components of the transition matrix will in turn depend on the state probabilities because $\gamma = \sqrt{\frac{P_1}{P_2}}$. The dynamics remains intrinsically nonlinear. Inserting (9.74) into (9.73), gives the following quadratic equation for γ:

$$\sin^2\theta\gamma^2 - \sin 2\theta \cos(\xi - \zeta)\gamma - \sin^2\theta = 0. \tag{9.75}$$

This has a solution

$$\gamma = \sqrt{\cot^2\theta \cos^2(\xi - \zeta) + 1} + \cot\theta \cos(\xi - \zeta), \tag{9.76}$$

which is exactly (9.31). Hence, (9.74) is a consistent solution since $\gamma = \gamma(\theta, \xi, \zeta)$.

Quantum transitions

Here we derive the mesoscopic stochastic transition matrix (9.72) along with the parameters (9.74) by starting directly from the quantum unitary evolution. To do this, we begin by writing the quantum mechanical collision transformation acting on the microscopic quantum state as a general block-diagonal unitary matrix with complex coefficients:

$$\begin{pmatrix} \psi_0' \\ \psi_1' \\ \psi_2' \\ \psi_3' \end{pmatrix} = \begin{pmatrix} 1 & 0 & 0 & 0 \\ 0 & U_{11} & U_{12} & 0 \\ 0 & U_{21} & U_{22} & 0 \\ 0 & 0 & 0 & U_{33} \end{pmatrix} \begin{pmatrix} \psi_0 \\ \psi_1 \\ \psi_2 \\ \psi_3 \end{pmatrix} \tag{9.77}$$

The unitarity condition ($\hat{U}^\dagger \hat{U} = \mathbf{I}$) constrains the complex coefficients as follows:

$$\begin{array}{cc} |U_{11}|^2 + |U_{21}|^2 = 1 & U_{11}^* U_{12} + U_{21}^* U_{22} = 0 \\ U_{12}^* U_{11} + U_{22}^* U_{21} = 0 & |U_{12}|^2 + |U_{22}|^2 = 1 \\ U_{33}^* U_{33} = 1. & \end{array} \tag{9.78}$$

The quantum state incoming probabilities are defined as follows:

$$P_0 \equiv |\psi_0|^2 \qquad P_1 \equiv |\psi_1|^2 \qquad P_2 \equiv |\psi_2|^2 \qquad P_3 \equiv |\psi_3|^2, \tag{9.79}$$

and, likewise, the quantum state outgoing probabilities are:

$$P'_0 \equiv |\psi'_0|^2 \qquad P'_1 \equiv |\psi'_1|^2 \qquad P'_2 \equiv |\psi'_2|^2 \qquad P'_3 \equiv |\psi'_3|^2. \tag{9.80}$$

From (9.77) we see that

$$\begin{aligned}
|\psi'_0|^2 &= |\psi_0|^2 && \text{(9.81a)}\\
|\psi'_1|^2 &= (U^*_{11}\psi^*_1 + U^*_{12}\psi^*_2)(U_{11}\psi_1 + U_{12}\psi_2) && \text{(9.81b)}\\
|\psi'_2|^2 &= (U^*_{21}\psi^*_1 + U^*_{22}\psi^*_2)(U_{21}\psi_1 + U_{22}\psi_2) && \text{(9.81c)}\\
|\psi'_3|^2 &= |\psi_3|^2, && \text{(9.81d)}
\end{aligned}$$

which can be rewritten as a quantum transition map:

$$\begin{aligned}
P'_0 &= P_0 && \text{(9.82a)}\\
P'_1 &= |U_{11}|^2 P_1 + |U_{12}|^2 P_2 && \text{(9.82b)}\\
&\quad + U^*_{11}U_{12}\psi^*_1\psi_2 + U^*_{12}U_{11}\psi_1\psi^*_2 \\
P'_2 &= |U_{21}|^2 P_1 + |U_{22}|^2 P_2 && \text{(9.82c)}\\
&\quad + U^*_{21}U_{22}\psi^*_1\psi_2 + U^*_{22}U_{21}\psi_1\psi^*_2 \\
P'_3 &= P_3. && \text{(9.82d)}
\end{aligned}$$

In matrix form this becomes

$$\begin{pmatrix} P'_0 \\ P'_1 \\ P'_2 \\ P'_3 \end{pmatrix} = \underbrace{\begin{pmatrix} 1 & 0 & 0 & 0 \\ 0 & |U_{11}|^2 & |U_{12}|^2 & 0 \\ 0 & |U_{21}|^2 & |U_{22}|^2 & 0 \\ 0 & 0 & 0 & 1 \end{pmatrix}}_{\text{classical diffusive part}} \begin{pmatrix} P_0 \\ P_1 \\ P_2 \\ P_3 \end{pmatrix} + \underbrace{\begin{pmatrix} 0 \\ U^*_{11}U_{12}\psi^*_1\psi_2 + U^*_{12}U_{11}\psi_1\psi^*_2 \\ U^*_{21}U_{22}\psi^*_1\psi_2 + U^*_{22}U_{21}\psi_1\psi^*_2 \\ 0 \end{pmatrix}}_{\text{quantum mechanical part}}. \tag{9.83}$$

The classical part of (9.83) is exactly (9.71). The quantum mechanical part gives rise to non-diffusive advective behavior, which leads to nonlinear shock formation characteristic of

the Burgers equation. Finally, from (9.83) we have a quantum transition matrix:

$$\mathbf{T}_{\rm qm} = \begin{pmatrix} 1 & 0 & 0 & 0 \\ 0 & |U_{11}|^2 + U_{11}^* U_{12} \frac{\psi_2}{\psi_1} & |U_{12}|^2 + U_{12}^* U_{11} \frac{\psi_1}{\psi_2} & 0 \\ 0 & |U_{21}|^2 + U_{21}^* U_{22} \frac{\psi_2}{\psi_1} & |U_{22}|^2 + U_{22}^* U_{21} \frac{\psi_1}{\psi_2} & 0 \\ 0 & 0 & 0 & 1 \end{pmatrix} \tag{9.84}$$

(9.84) conserves probability ($\sum_i^3 P_i' = \sum_i^3 P_i$) due to unitarity, so its columns sum to unity owing to the unitary condition (9.78).

Now with the equilibrium probability amplitudes

$$\psi_0 = \sqrt{(1-d_+)(1-d_-)} \tag{9.85a}$$
$$\psi_1 = \sqrt{(1-d_+)d_-} \tag{9.85b}$$
$$\psi_2 = \sqrt{(d_+(1-d_-)} \tag{9.85c}$$
$$\psi_3 = \sqrt{d_+ d_-}, \tag{9.85d}$$

and using (9.30), we see that $\frac{\psi_1}{\psi_2} = \sqrt{\left(\frac{d_-}{1-d_-}\right)\left(\frac{1-d_+}{d_+}\right)} = \gamma$, so that (9.84) becomes:

$$\mathbf{T}_{\rm qm}^{\rm eq} = \begin{pmatrix} 1 & 0 & 0 & 0 \\ 0 & \cos^2\theta - \frac{e^{i(\xi-\zeta)}\sin 2\theta}{2\gamma} & \sin^2\theta - \frac{\gamma e^{-i(\xi-\zeta)}\sin 2\theta}{2} & 0 \\ 0 & \sin^2\theta + \frac{e^{i(\xi-\zeta)}\sin 2\theta}{2\gamma} & \cos^2\theta + \frac{\gamma e^{-i(\xi-\zeta)}\sin 2\theta}{2} & 0 \\ 0 & 0 & 0 & 1 \end{pmatrix}, \tag{9.86}$$

where γ is determined by (9.31). The equilibrium value of the quantum transition matrix (9.86) is identical to (9.72) with components (9.74).

9.5 Simulation results

9.5.1 Consistency of the entropy and collision functions

Figure 9.4 is a composite plot showing the $\mathcal{H}_\gamma$ function constant-density contours graphed for $\rho = 0.7$ and $\xi = \zeta = 0$, but each curve has a different θ Euler angle. The top curve is for $\theta = 0.5708$ radians, which corresponds to a high viscosity model with $\nu = 2.42548\frac{\delta x^2}{\delta t}$. The intermediate $\mathcal{H}_\gamma$ curves are plotted with θ incremented by $\Delta\theta = 0.05$ radians. The bottom curve has $\theta = 1.5708$ radians $\simeq \frac{\pi}{2}$, which is a nearly inviscid contour of the entropy surface corresponding to an extremely low viscosity of $\nu = 1.34 \times 10^{-11}\frac{\delta x^2}{\delta t}$. The abscissa is the kinetic mode $v = f_+ - f_-$ plotted over the range $-\rho \geq v \geq \rho$ for $\rho = 0.7$. The ordinate is the $\mathcal{H}_\gamma$ function plotted over the range $-0.5 \geq \mathcal{H}_\gamma \geq 2.0$. Each set of dynamical trajectory points computed using (9.58) exactly lies on the respective $\mathcal{H}_\gamma$ function contour,

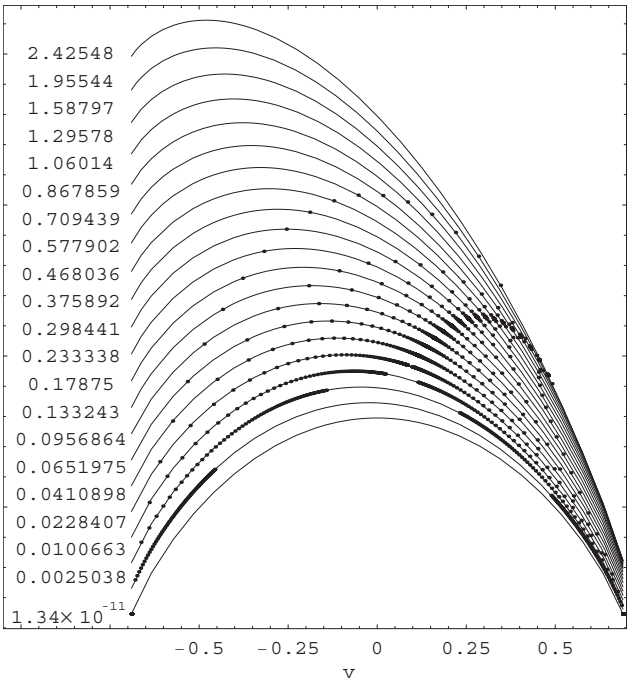

Figure 9.4: $\mathcal{H}_\gamma$ function constant-density contours of the entropy surface (solid gray curves), which are vertically stacked over one another for graphical clarity. The x-axis is $v = f_+ - f_-$ and the y-axis is entropy as defined by (9.59). The dynamical trajectories (black dots) were computed using the nonlinear quantum collision function $\Omega_{\rm qu}(\rho, v)$ for different values of the shear viscosity for a relatively high value of $\nu = 2.42548 \frac{\delta x^2}{\delta t}$ (on the top) down to an extremely low value of $\nu = 1.34 \times 10^{-11} \frac{\delta x^2}{\delta t}$ (at the bottom). Viscosity values are labeled on the left of the respective $\mathcal{H}_\gamma$ contours, not numerical values of entropy.

demonstrating the consistency of the quantum Boltzmann equation and the entropy function descriptions.

In the inviscid limit where $\theta \to \frac{\pi}{2}$, the quantum collision function reduces to $\Omega_{\rm qu}(\rho, v) = -v$, and in turn (9.58) reduces to $v' = -v$. So as the fluid's viscosity is reduced, the collision process causes the sign of velocity field to alternate. This is shown in Figure 9.4, where for the lower viscosity cases, the value of the kinetic mode jumps back and forth from the left $(-v)$ to the right side $(+v)$ of the entropy contour and back again.

9.5.2 Comparison to the Cole-Hopf solution

Choosing three sets of "Euler" angles in (9.23) to be $\theta = \frac{\pi}{12.8239}$ (case A), $\theta = \frac{\pi}{6.77582}$ (case B), and $\theta = \frac{\pi}{4}$ (case C) and $\theta = \frac{\pi}{2.36955}$ (case D), and $\xi = \zeta$, then $\nu = 8\frac{\delta x^2}{\delta t}$ (case A), $\nu = 2\frac{\delta x^2}{\delta t}$ (case B), $\nu = \frac{1}{2}\frac{\delta x^2}{\delta t}$ (case C), and $\nu = \frac{1}{32}\frac{\delta x^2}{\delta t}$ (case D) are the respective shear viscosity transport coefficients. For these four cases, we compare the numerical prediction that the macroscopic scale behavior of the quantum algorithm is governed by the Burgers equation (9.1) with the exact solutions obtained by analytical means. For the purposes of the numerical tests, the system is simulated directly at the mesoscopic scale using (9.26), and all initialized with the same sinusoidal profile in the number density field

$$\rho(x_l, 0) = \rho_a \cos\left(\frac{2\pi l}{L}\right) + \rho_b, \tag{9.87}$$

where $\rho_a = 0.4$ and $\rho_b = 1$, and $L = 256$. A time history of the dynamical evolution of the number density fields is plotted in Figure 9.5. The analytical solution of the Burgers equation is obtained by application of the Cole-Hopf transformation [3]

$$\rho = \rho_a + \frac{2\nu}{c\psi}\frac{\partial \psi}{\partial x}, \tag{9.88}$$

where

$$\psi \equiv I_0(z) + 2\sum_{\ell=1}^{\infty}(-1)^{\text{Floor}[\ell/2]} I_\ell(z) F_\ell(2\pi\ell x + \nu_\ell t) e^{-\mu_\ell t}, \tag{9.89}$$

and where $z \equiv \frac{c_s \rho_b}{4\pi\nu}$, $\mu_\ell \equiv \nu(2\pi\ell)^2$, $\nu_\ell \equiv c_s(1-\rho_a)(2\pi\ell)$, the I_ℓ's are modified Bessel functions, and the function F_ℓ denotes the sine or cosine function when ℓ is odd or even, respectively,

$$F_\ell(x) \equiv \frac{(-1)^\ell + 1}{2}\cos(x) - \frac{(-1)^\ell - 1}{2}\sin(x). \tag{9.90}$$

[3] It is possible to add an external noise term of the form $\frac{\partial \eta(x,t)}{\partial x}$ into the right-hand side of the Burgers equation (9.1). The potential field $h(x,t)$ is defined as follows: $\frac{\partial h(x,t)}{\partial x} \equiv u(x,t)$. Then $h(x,t)$ satisfies the Kardar-Parisi-Zhang equation [Kardar et al., 1986].

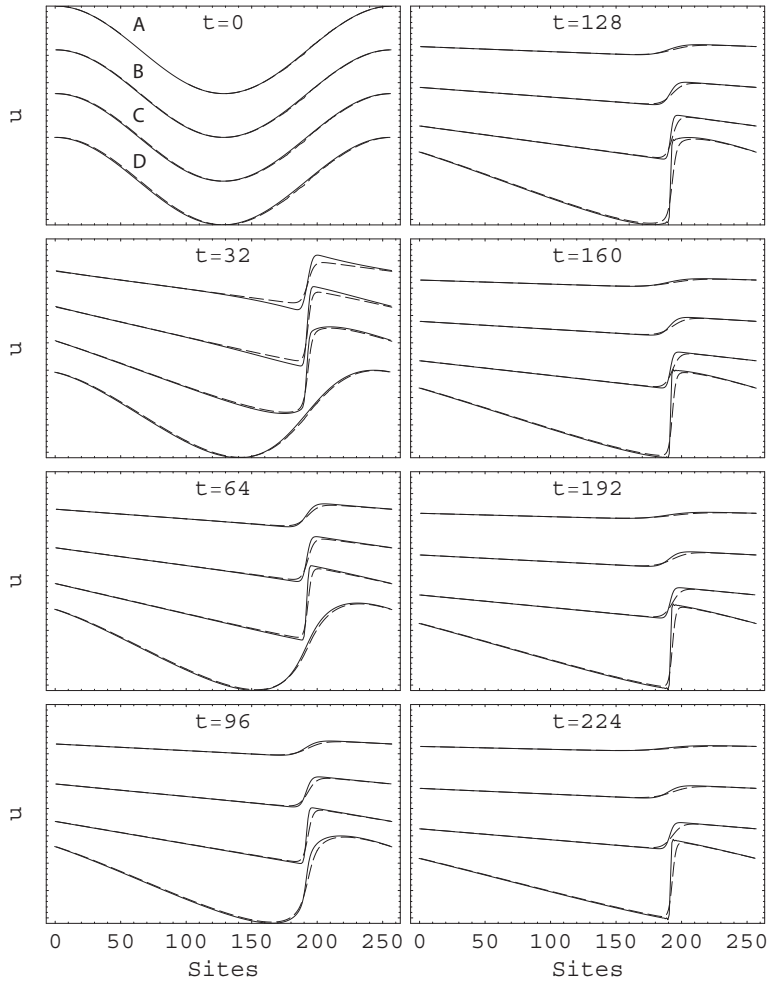

Figure 9.5: Development of a shock front in the flow field $u(x,t)$ after the system is initialized with a sinusoidal profile on an $L = 256$ site lattice for four different viscosities: (A) $\nu = 8$, (B) $\nu = 2$, (C) $\nu = \frac{1}{2}$, (D) $\nu = \frac{1}{32}$, where the viscosity is in lattice units $\frac{\delta x^2}{\delta t}$. The curves are shifted vertically one from the other by $\Delta\rho = \frac{1}{2}$ to avoid overlapping. Agreement between the numerical data (solid curves) and the analytical solution (dashed curves) is excellent. The shock fronts of the analytical solutions are slightly wider than the shock fronts of the numerical simulations which have much sharper edges. This is because these plotted analytical solutions are slightly over-damped to help stabilize the series solution (9.89), so the quantum model data is more accurate approximation of the time-dependent solution to the Burgers equation. All four cases were initialized using (9.87) with $\rho_a = 1$ and $\rho_b = 0.4$.

To match the numerical simulations, the parameters in the analytical solution (9.89) were set to $c = Lc_s = 256 \cot\theta \frac{\delta x}{\delta t}$ and $\nu = \frac{1}{2}\cot^2\theta \frac{\delta x^2}{\delta t}$. Also in (9.89) the size of the system is set to unit length, $0 \leq x \leq 1$.

The agreement between the numerical prediction and the analytical solution is excellent for all cases, as shown in Figure 9.5. There is a slight discrepancy between the analytical and numerical results after the shock front has developed in the flow field. The discrepancy occurs at the corners or edges of the shock. The analytical solution appears to be smoother across the shock front than the numerical solution. To plot the analytical solution, it was not possible to include all terms in the series expansion (9.89) from $\ell = 1$ up to $\ell = \infty$. Instead, an approximation was made using only the first 80 terms in the expansion (9.89). For cases when the shock front is too steep, the analytical solution diverges at shock front while the quantum algorithm remains unconditionally stable; it becomes computationally difficult to compute the analytically predicted exact solution using (9.89). To avoid this situation, some additional damping was added to the analytical series solution to ensure its convergence. This explains the observed discrepancy.

9.5.3 Near inviscid flow

Figure 9.6 shows the time evolution of the same quantum lattice gas system with $L = 256$ nodes. There are two situations with the collision operators set with different values for the Euler angles: $\nu = \frac{1}{2}\frac{\delta x^2}{\delta t}$ (dotted curve) and $\nu = 0.00251446\frac{\delta x^2}{\delta t}$ (solid curve) cases. The vertical axis is ρ plotted in the range of $\frac{1}{2} \leq \rho \leq \frac{3}{2}$. The time step is in the upper left corner of each snapshot. The viscosity of the quantum model is close to zero. The quantum algorithm is unconditionaly stable and obeys the principle of detailed-balance. Having a variable transport coefficient that can be made small, it is consistent with the inviscid Burgers equations when the Euler angle $\theta \simeq \frac{\pi}{2}$. The numerical simulation result plotted in Fig. 9.7 manifests a characteristic property of a type-II quantum algorithm. The expected value of the occupancy of the ground state and excited state of a microscopic qubit contained within a quantum mechanical node of the lattice are shifted. The expectation value of the excited state is plotted in the blue curve shown in in Fig. 9.7b. Regardless of the dissipation regime (high or low viscosity), there is a gap in value of the occupation probabilites; hence, $d_+ \neq d_-$. The physical cause of this gap is the following. The microscopic dynamics is interpreted as the motion of qubits moving left and right through a chain of quantum processors. If the likelihood of a qubit exiting left or right from a quantum processor is equal, then the excited state energies encoding the left- and right-going probabilities would be degenerate. The equilibrium probabilities must overlap: $d_+ = d_-$. The macroscopic effective field theory would be strictly diffusive as any qubit would move up and down the one dimensional chain

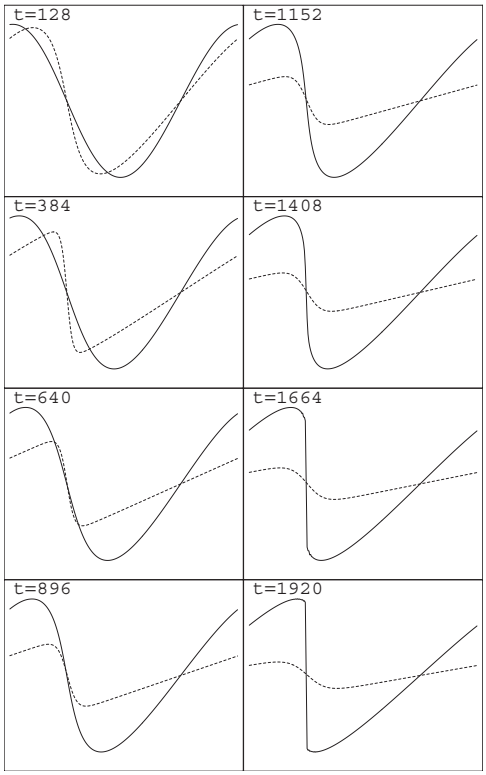

Figure 9.6: Two scenarios: the quantum lattice gas with $\theta = 1.5$ radians and $\zeta = \xi = 0$ (solid curve) and $\theta = \frac{\pi}{4}$ and $\zeta = \xi = 0$ (dotted curve).This demonstrates a quantum lattice gas modeling a low viscosity fluid when $\theta \simeq \frac{\pi}{2}$.

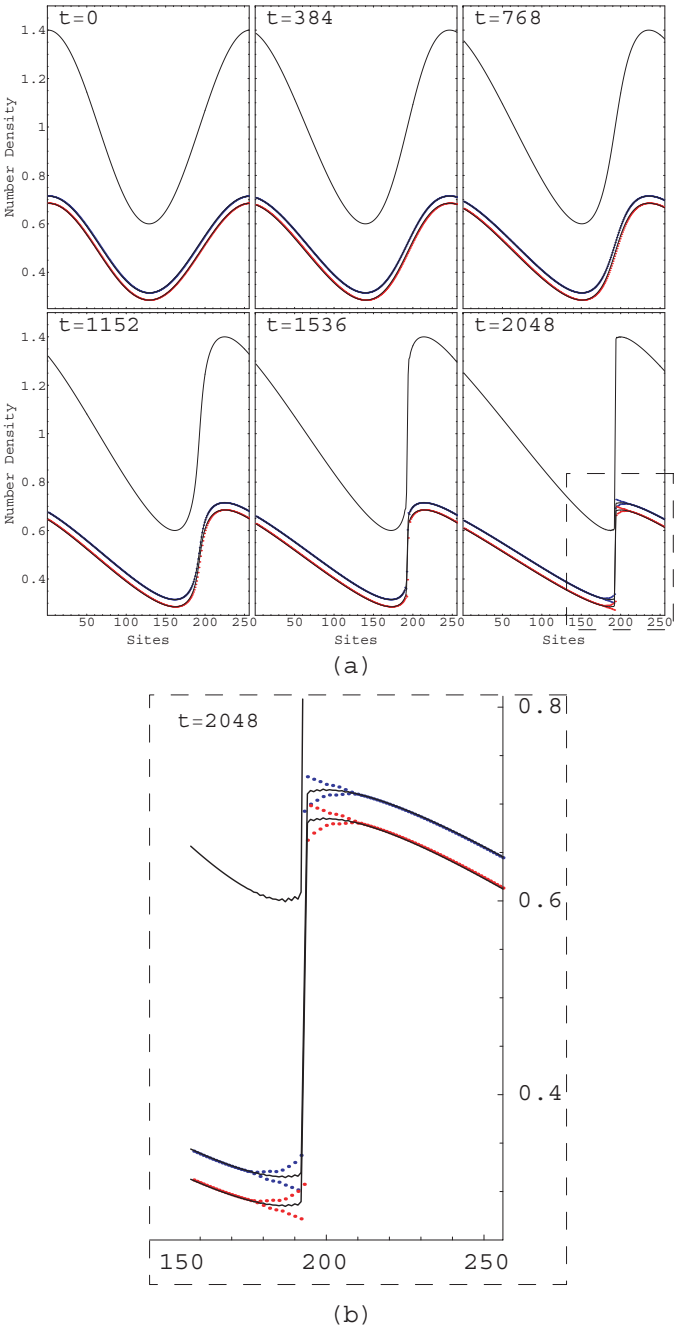

Figure 9.7: Highly under-resolved simulation with $\theta = 1.5$ radians with $L = 256\delta x$. (a) Six successive snapshots of the flow field data (black curve) and the numerical prediction of the occupancy probabilities f_+ (blue dots) and f_- (red dots). The analytically predicted equilibria, d_+ and d_-, are over plotted (black curves). There is excellent agreement between theory and simulation, with a deviation occurring at late times after the shock front is fully formed. (b) An expanded view of the shock front at $t = 2048\frac{\delta x}{\delta t}$. The width of the shock front is much less than δx so a kind of Gibbs oscillations emerges.

of quantum processors in an unbiased random walk fashion. However, if the likelihood of a qubit exiting a quantum processor to the left does not equal the likelihood it will exit to the right, then the degeneracy in the distribution functions is lifted and an energy gap appears as demonstrated Figs. 9.7. In this case, the macroscopic effective field theory would not be strictly diffusive; there would be an overall net advection of qubits in one direction (the symmetry of the lattice is broken and this causes an energy gap in excited state energy levels). This net advection gives rise to the nonlinear terms in (9.1).

In regions of $\frac{\partial v}{\partial x} < 0$, shocks tend to form in the v-field. Asymptotically, v attains a constant slope with shock discontinuities. In Fig. 9.7, the extent of the Gibbs oscillations at the shock front is greater at the mesoscopic than at themacroscopic scale because of a fortuitous cancellation of errors. In Figure 9.8, we compare the analytically predicted values

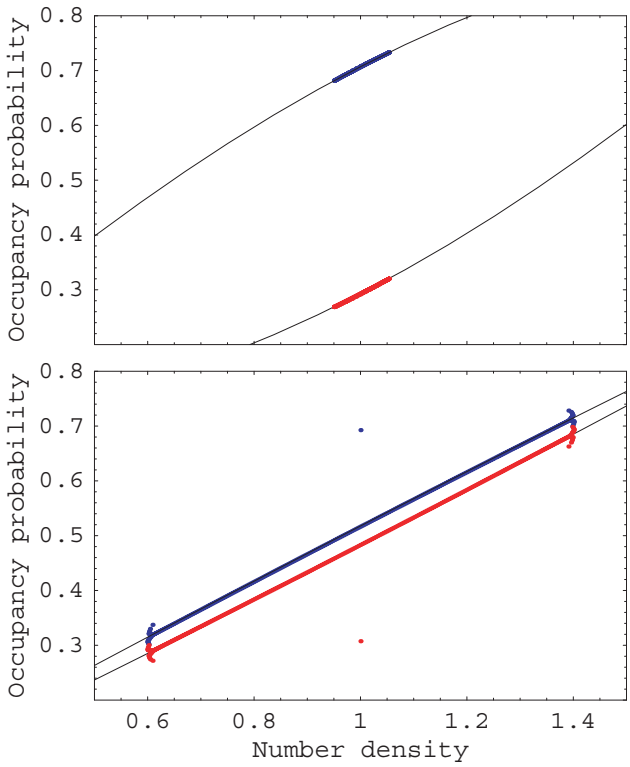

Figure 9.8: Analytical versus numerical equilibria: (top plot) high viscosity $\theta = \frac{\pi}{4}$ radians, and (bottom plot) low viscosity $\theta = 1.5$ radians. The numerical data of the occupancy probabilities f_+ (blue dots) and f_- (red dots) are shown for the flow field at $t = 2048\delta t$. The analytically predicted equilibria, d_+ and d_-, plotted as well (black curves). In the low viscosity case, the deviation of the occupancy probabilities for the highest and lowest values of the number density correspond to the aberrant Gibbs oscillations seen in Fig. 9.7 of the under resolved flow.

of the equilibrium distribution to the numerically obtained distribution. There is excellent agreement in the high dissipation regime, shown in the top graph in Figure 9.8. However, a

discrepancy emerges in the extremely low dissipation regime, shown in the bottom graph in Figure 9.8, which corresponds to the under-resolved shock front.

9.6 Summary

In summary, the type-II quantum algorithm:

- uses conservative quantum logic that is easily implementable
- is fourth-order accurate in space
- is unconditionally stable
- has a well-defined entropy function
- obeys detailed-balance due to the unitarity of the quantum collision process
- has tunable transport coefficients, for example sound-speed and viscosity coefficients
- is valid for highly nonlinear dynamics, for example the inviscid Burgers equations when the Euler angle $\theta \simeq \frac{\pi}{2}$ of a conservative $\sqrt{\text{SWAP}}$ quantum logic gate
- is valid for highly nonlinear dynamics, for example it can achieve arbitrarily high Reynolds numbers
- uses exponentially fewer local resources because of efficient microscopic Hamiltonian encoding of the particle-particle collisions
- is computationally efficient, for example with a speedup scaling as $\text{Re}^{\frac{1}{2}}$ for the Burgers equation and Re for the Navier-Stokes equation.

The quantum algorithm for modeling the Burgers equation is the simplest case (two qubits per node) of a more general quantum algorithmic approach using many qubits per node for modeling classical nonlinear dynamical fluid systems that shows an advantage over classical algorithms. It is the simplest way to demonstrate the source of quantum efficiency in computational physics applications in the same spirit as demonstrating the source of quantum efficiency in quantum information processing by using the Deutsch-Josza quantum algorithm for checking whether a function is constant or balanced [4].

[4]The efficiency of the Deutsch-Josza algorithm can be explained as follows. Classically, to find out if a coin is fair or not, both sides must be observed; two bits of information are used. Quantum mechanically, this determination can be made with a single observation of a qubit; only one bit of information is used.

9.7 Final remarks

An open system quantum model for the nonlinear Burgers equations was presented. A salient feature of this microscopic quantum model is that at the mesoscopic scale the model effectively behaves as a kinetic system of qubits accurately governed by a quantum Boltzmann equation of motion. As a consequence of the microscopic unitarity of the quantum mechanical evolution operator, the mesoscopic scale qubit dynamics obeys statistical detail-balance in its collisions. Furthermore, the dynamics obeys an entropy theorem consistent with the second law of thermodynamics. A feature of the model is that it allows for arbitrary tuning of the macroscopic scale shear viscosity transport coefficient. Localization of the microscopic dynamics, for example through state reduction via a measurement process, allows for tuning the level of the consequent macroscopic scale dissipation. This feature is important from a computational physics perspective because the model, seen as a quantum algorithm, remains unconditionally stable at extremely low dissipation regimes. This allows us to use the quantum algorithm for modeling highly nonlinear shock formation, even severely under-resolved shock fronts, without the model breaking down. All numerical tests of the algorithm indicate that the analytical treatment of the quantum model is correct.

The quantum Boltzmann equation that represents our quantum algorithm can be directly implemented on a present-day classical computer (so long as the number of qubits per quantum node is small) and constitutes a new modeling tool for numerically predicting the time-dependent behavior of hydrodynamic flow and shock formation. This quantum Boltzmann equation method, which is akin to the entropic lattice Boltzmann equation method [Karlin and Gorban, 1998, Karlin et al., 1999, Ansumali and Karlin, 2000, Boghosian etal., 2001, Ansumali and Karlin, 2002, Ansumali et al., 2003, Boghosian et al., 2004b, Boghosian et al., 2004a], and which in turn was an offshoot of the lattice Boltzmann equation method [R. Benzia and Vergassola, 1992], when implemented on a present-day supercomputer can be generalized to model Navier-Stokes turbulence.

The quantum Boltzmann equation method in this chapter has also been extended to handle magnetohydrodynamics in one spatial dimension where the shear viscosity and resistivity transport coefficients are both arbitrarily tunable [Yepez et al., 2005].

It remains an open problem whether the method presented here can be extended to directly recover the Burgers equation, the equations of compressible thermohydrodynamics, and the equations of magnetohydrodynamics in two and three spatial dimensions. These extensions will require using the Chapman-Enskog technique presented in this paper but for quantum models with significantly many more qubits per lattice node, say several dozen per node. Therefore efficient implementation of open quantum system models of classical

turbulence in higher spatial dimensions will require a quantum computer. Fortunately, such an implementation on a future quantum computer should be possible because this quantum modeling method has a well-defined microscopic quantum mechanical dynamics generated by a Hamiltonian with only local qubit-qubit interactions.

Chapter 10

Magnetohydrodynamic Burgers equation

10.1 Introduction

The solution of nonlinear equations poses major challenge for parallel computational techniques. This has led to the development of mesoscopic algorithms which are ideally parallelized (on classical computers), like lattice Boltzmann methods. However the straightforward application of lattice Boltzmann methods lead to severe numerical instabilities as the transport coefficients tend to zero. To overcome these instabilities, entropic constraints are introduced into the lattice Boltzmann algorithm which enforce positive-definiteness of the distribution functions. While these entropic algorithms, when they exist, are unconditionally stable and still permit excellent parallelization, they require at every time step and at every grid point a Newton-Raphson root finder algorithm which enforce bounds to remain on a constant entropic surface. Quantum algorithms are also being developed for nonlinear equations which have intrinsic classical and quantum parallelization, and which are unconditionally stable algorithms (because of the unitary collision and streaming operators) without the need of expensive root-finding routines of entropic lattice Boltzmann.

Parallel quantum algorithms [Yepez, 1998] have been developed to numerically predict time-dependent field solutions of the diffusion equation [Yepez, 2001b], the nonlinear Burgers equation [Yepez, 2002c, Yepez, 2002a], the one dimensional equations for magnetohydrodynamic turbulence with fixed (large) transport coefficients [Vahala et al., 2003c], the Korteweg de Vries equation [Vahala et al., 2003b], the nonlinear Schroedinger equation in 1D and 2D [Vahala et al., 2003b, Vahala et al., 2004b], and the Manakov equations [Vahala et al., 2003a, Vahala et al., 2004a]. The first parallel quantum algorithms for the diffusion and Burgers equations have with success been experimentally tested on quantum information processing prototypes of parallel quantum computers (or type-II quantum computers [Yepez, 2001c]) us-

ing spatial nuclear magnetic resonance spectroscopy on a linear array (in space and in reciprocal space) of segmented ensembles of two-qubit labeled chloroform molecules [Pravia et al., 2002, Pravia et al., 2003, Chen et al., 2006a].

Here, we generalize our parallel quantum algorithm for modeling magnetohydrodynamic (MHD) turbulence but to now handle arbitrary transport coefficients. This algorithm is based upon the quantum algorithms for the diffusion [Yepez, 2001b] and Burgers equations [Yepez, 2002c, Yepez, 2002a]; it can be implemented on a parallel quantum computer with pairs of labeled chloroform molecules. The intent of this paper is solely to demonstrate the quantum Boltzmann equation method, so all the details about the microscopic quantum mechanical implementation of the method have been replaced with a simpler and friendlier mesoscopic treatment. The quantum mechanical foundation of the method lends it several advantageous features as a tool for computational physics. First, there is inherent numerical stability. Second, there is a corresponding entropy function description of the model dynamics and an entropy theorem, although for economy and brevity the details of the entropy function are not presented here. The Boltzmann collision function can be computed directly without the need of root finding as is required for entropic lattice Boltzmann equation models of turbulence [Boghosian et al., 2001, Boghosian et al., 2003, Boghosian et al., 2004a]. Although the quantum algorithm presented here was originally developed for a parallel quantum computing architecture, the quantum Boltzmann equation is a practical algorithmic method for presentday classical computers.

Turbulence is plagued by spatiotemporal intermittency involving coherent structures – structures that are at odds with the simple scale-similarity arguments. Insight into these coherent structures comes by examining simplified models and the simplest model exhibiting Alfvenization (the exchange of fluid and magnetic energies) are the 1D equations [Thomas, 1968, Fleischer and Diamond, 2000]

$$\frac{\partial v}{\partial t} + v\frac{\partial v}{\partial x} = -\frac{\partial}{\partial x}\left(\frac{B^2}{2}\right) + \mu\frac{\partial^2 v}{\partial x^2} \tag{10.1a}$$

$$\frac{\partial B}{\partial t} + \frac{\partial}{\partial x}(vB) = \eta\frac{\partial^2 B}{\partial x^2} \tag{10.1b}$$

for the velocity field $\vec{v} = v(x)\hat{x}$ and the magnetic field $\vec{B} = B(x)\hat{z}$. The transport coefficients are μ the fluid viscosity, and η the plasma resistivity. These 1D equations are derived from the full MHD equations when the fluid density length scales are much longer than those of the B field [Thomas, 1968, Fleischer and Diamond, 2000]. To leading order, this results in a constant density so that (10.1) forms a closed set of equations for v and B. Adding a y-component of the magnetic field gives a 1D model for solar flares [Galtier, 1999]. In

Elsasser variables $z_\pm = v \pm B$, (10.1) can be written in symmetric form

$$\frac{\partial z_\pm}{\partial t} + z_\pm \frac{\partial z_\pm}{\partial x} = \mu \frac{\partial^2 z_\pm}{\partial x^2} \pm \frac{1}{2}(\eta - \mu)\frac{\partial^2 (z_+ - z_-)}{\partial x^2}. \tag{10.2}$$

If the transport coefficients are equal, $\eta = \mu$, then (10.2) reduces to two uncoupled nonlinear Burgers equations for $z_\pm$. [In the limit $B \equiv 0$, (10.1) reduces to Burgers equation for v]. The Burgers equation [Woyczynski, 1998] is a well-known paradigm for Navier-Stokes turbulence and has also been studied extensively for many decades as a simplified model for boundary layer behavior, shock wave formation, mass transport, self-organized criticality and growing interfaces. It is also a test-bed for numerical methods since a general analytic solution exists [Hopf, 1950, Cole, 1951]. In Burgers turbulence, regions where $\frac{\partial v}{\partial x} < 0$ steepen into shock singularities, while regions where $\frac{\partial v}{\partial x} > 0$ become smoother. However, with the inclusion of the B field, there is now a magnetic back-pressure in (10.1) that is absent from the Burgers equation. In particular, the B field will concentrate in regions of the velocity shock, softening the shock front. For $\eta \neq \mu$, (10.1) is non-integrable. Our initial attempt at a quantum algorithm for (2) was restricted to the case $\mu = 1/2$ and $\eta = 1$, in lattice units. Here we present a quantum lattice Boltzmann algorithm that permits arbitrary transport coefficients – a nontrivial generalization.

10.2 Quantum algorithm

To model (10.1) we use two quantum Boltzmann equations: we employ a two phase algorithm for an ordered one dimensional array of L nodes, enumerated by a "spatial" integer coordinate $x = 1, 2, ..., L$. At each node there are four probability values $0 \leq p_a \leq 1$, for $a = 1, 2, 3, 4$ which we shall call *occupation probabilities*. In first phase of the algorithm, the occupation probabilities are encoded using the Elsasser variables $1 + v(x) + B(x)$ and $1 + v(x) - B(x)$, whereas in the second phase of the algorithm, the occupation probabilities are encoded using the $1 + v(x)$ and $B(x)$ fields as density variables. In the first phase of the algorithm, the evolution of the occupation probabilities is carried out using the quantum Boltzmann equation for the nonlinear Burgers; and in the second phase, the evolution is carried out using the quantum Boltzmann equation for linear diffusion. A unitary matrix, denoted T, is employed to transform the occupation probability distribution back and forth between the Elsasser and density variable representations. During the evolution steps of the first and second phases of the algorithm, the probabilities are updated independently in pairs: (p_1, p_2) and (p_3, p_4). In the transformation steps, the probabilities are adjusted in the alternate pairs: (p_1, p_3) and (p_2, p_4). Therefore, this quantum algorithm is a four-qubit algorithm.

10.2.1 Initialization step

The zeroth step encodes all four probability fields at $t = 0$ using the initial $v(x)$ and $B(x)$ fields:

$$p_{1,2}(x) = d_{1,2}[\cot\theta, 1 + v(x) + B(x)] \tag{10.3a}$$

$$p_{3,4}(x) = d_{1,2}[\cot\theta, 1 + v(x) - B(x)], \tag{10.3b}$$

where the local equilibrium functions

$$d_1(\alpha,\rho) = \frac{\rho}{2} + \frac{1}{2\alpha}\left[\sqrt{1+\alpha^2} - \sqrt{1+\alpha^2(\rho-1)^2}\right] \tag{10.4a}$$

$$d_2(\alpha,\rho) = \frac{\rho}{2} - \frac{1}{2\alpha}\left[\sqrt{1+\alpha^2} - \sqrt{1+\alpha^2(\rho-1)^2}\right] \tag{10.4b}$$

are the zeros of the full quantum collision function [Yepez, 2006]. This step occurs only in the first pass through the algorithmic loop.

10.2.2 Quantum Boltzmann equation for nonlinear Burgers

The first evolution step uses the full quantum Boltzmann equation to update all the probability fields:

$$p_{1,2}(x \mp 1) = p_{1,2}(x) \mp [p_1(x) - p_2(x)]\sin\theta \pm \sqrt{p_1(x)[1-p_1(x)]p_2(x)[1-p_2(x)]}\sin 2\theta \tag{10.5a}$$

$$p_{3,4}(x \mp 1) = p_{3,4}(x) \mp [p_3(x) - p_4(x)]\sin\theta \pm \sqrt{p_3(x)[1-p_3(x)]p_4(x)[1-p_4(x)]}\sin 2\theta. \tag{10.5b}$$

10.2.3 Transformation to density variables

The second step of the algorithm transforms the local probability distribution from the Elsasser variables representation to the density variables representation:

$$p_a(x) = T_{ab}\, p_b(x), \tag{10.6}$$

where there is an implied summation over the repeated index and the unitary transformation matrix is

$$T = \frac{1}{\sqrt{2}}\begin{pmatrix} 1 & 0 & 1 & 0 \\ 0 & 1 & 0 & 1 \\ 1 & 0 & -1 & 0 \\ 0 & 1 & 0 & -1 \end{pmatrix}. \tag{10.7}$$

Here, the density assignments to evaluate the $v(x)$ and $B(x)$ fields are:

$$v(x) = p_1(x) + p_2(x) - 1 \tag{10.8a}$$

$$B(x) = p_3(x) + p_4(x). \tag{10.8b}$$

(10.8) are not part of the mesoscopic quantum algorithm, merely diagnostic evaluation of the dynamics–a kind of "observation" that does not affect the dynamics.

10.2.4 Quantum Boltzmann equation for linear diffusion

The third step uses the following quantum Boltzmann equation to independently update the probability fields associated v and B fields:

$$p_{1,2}(x \mp 1) = p_{1,2}(x) \mp [p_1(x) - p_2(x)] \sin^2 \alpha \tag{10.9a}$$

$$p_{3,4}(x \mp 1) = p_{3,4}(x) \mp [p_3(x) - p_4(x)] \sin^2 \beta. \tag{10.9b}$$

To improve the numerical convergence of the quantum algorithm overall, this diffusion step should be implemented with a fourth-order accurate scheme employing interleaving. The details have been omitted here for the sake of brevity, but can be found in [Yepez, 2001b].

10.2.5 Transformation to Elsasser variables

The fourth step of the algorithm re-encodes the local probability distribution p_a into probabilities associated with the Elsasser variables $v + B$ and $v - B$:

$$p_a(x) = T^\dagger_{ab}\, p_b(x). \tag{10.10}$$

Note that $T^\dagger = T$, the variable transformation is self-adjoint. At this point, one iteration of the algorithm is completed and time is advanced by one unit Δt.

Here, the Elsasser assignments to evaluate the macroscopic scale $v(x)$ and $B(x)$ fields from the occupation probabilities are the following formulae:

$$v(x) = \frac{1}{2}\left[p_1(x) + p_2(x) + p_3(x) + p_4(x)\right] - 1 \tag{10.11a}$$

$$B(x) = \frac{1}{2}\left[p_1(x) + p_2(x) - p_3(x) - p_4(x)\right]. \tag{10.11b}$$

In this way, a time history of the $v(x)$ and $B(x)$ fields can be generated by looping back to the first step. Like (10.8), (10.11) is not part of the mesoscopic quantum algorithm, merely a diagnostic evaluation of the dynamics. Now we can see why the inverse of (10.11), which is

$$p_{1,2}(x) = \frac{1}{2}[1 + v(x) \pm B(x)] = p_{3,4}(x), \tag{10.12}$$

was used in (10.3) to encode the probability fields using the initial $v(x)$ and $B(x)$ fields at $t = 0$. That is, we initially start out in the Elsasser variable representation.

10.2.6 Basic algorithmic steps summarized

In summary, the mesoscopic quantum algorithm is the following:

STEP 0: INITIALIZATION USING (10.3).

STEP 1: NONLINEAR EVOLUTION USING (10.5).

STEP 2: TRANSFORMATION TO DENSITY VARIABLES USING (10.6).

STEP 3: LINEAR EVOLUTION USING (10.9).

STEP 4: TRANSFORMATION TO DENSITY VARIABLES USING (10.10), WHICH IS IDENTICAL TO (10.6).

Following Step 4, time advances $t \to t + \Delta t$, and we loop back to Step 1. It is also interesting to note that the unitary transformation T acts not on the probability amplitudes but on the actual probabilities themselves. This does not destroy the overall unitariness of the algorithm since $T^\dagger = T$.

10.3 Effective Field Theory

We shall not present the effective field theory for arbitrary transport coefficients since the resulting finite difference equations are far too complex and lengthy to present here [1].. Instead, we shall discuss the effective field theory for two special choices of α, β, θ

For the special case of $\alpha = 0$ and $\beta = 0$ and $\theta = \frac{\pi}{4}$, it can be shown that the mesoscopic transport equation (10.5) can be written directly as a finite difference equation in the $v(x)$ and $B(x)$ fields:

$$\begin{aligned} v'(x) &= \frac{1}{2}\left[v(x-1) + v(x+1)\right] && \text{(10.13a)} \\ &+ \frac{1}{4}\left[v(x-1)^2 - v(x+1)^2\right] \\ &+ \frac{1}{4}\left[B(x-1)^2 - B(x+1)^2\right] \\ B'(x) &= \frac{1}{2}\left[B(x+1) + B(x-1)\right] && \text{(10.13b)} \\ &+ \frac{1}{2}\left[v(x-1)B(x-1) - v(x+1)B(x+1)\right]. \end{aligned}$$

[1] The unitary collision operators are implemented with perfect control and the occupation probabilities are measured exactly. These assumptions hold only for an ideal experimental setup. We address actual quantum control and Von Neuman projective shot noise in our papers on experimental parallel quantum computing with NMR [Pravia et al., 2002, Pravia et al., 2003, Chen et al., 2006a].

The macroscopic scale effective field theory for $v(x,t)$ and $B(x,t)$ follows from taking the continuum limit of (10.13) with the ordering $\Delta x \sim \mathcal{O}(\varepsilon)$ and $\Delta t \sim \mathcal{O}(\varepsilon^2)$. We obtain (in lattice units $\Delta x = 1 = \Delta t$)

$$\frac{\partial v}{\partial t} + v\frac{\partial v}{\partial x} = \frac{1}{2}\frac{\partial^2 v}{\partial x^2} - B\frac{\partial B}{\partial x} + \mathcal{O}(\varepsilon^3) \tag{10.14a}$$

$$\frac{\partial B}{\partial t} + v\frac{\partial B}{\partial x} = \frac{1}{2}\frac{\partial^2 B}{\partial x^2} - B\frac{\partial v}{\partial x} + \mathcal{O}(\varepsilon^3). \tag{10.14b}$$

This is just the 1D MHD (10.1) in the special case where the kinematic shear viscosity and resistivity transport coefficients are equal, $\mu = \eta = 0.5$. If we make an Elsasser variables substitution, $z_\pm = v \pm B$, then (10.14a) and (10.14b) simplify into two uncoupled nonlinear Burgers equations for $z_\pm$, see (10.2). We now proceed from the integrable 1D MHD with $\mu = \eta$ to the non-integrable case of unequal transport coefficients, $\mu \neq \eta$.

After some algebra for the special case where $\alpha = 0$ and $\beta = \frac{\pi}{4}$ and $\theta = \frac{\pi}{4}$, it follows that the dynamics of the $v(x)$ and $B(x)$ fields can be written directly as a finite difference equation:

$$\begin{aligned} v'(x) &= \frac{1}{2}\left[v(x-1) + v(x+1)\right] + \frac{1}{4}\left[v(x-1)^2 - v(x+1)^2\right] \\ &+ \frac{1}{16}\left[B(x-2) - B(x+2)\right]\left[B(x-1) + 2B(x) + B(x+1)\right] \end{aligned} \tag{10.15a}$$

$$\begin{aligned} B'(x) &= \frac{1}{4}\left[B(x-2) + 2B(x) + B(x+2)\right] \\ &+ \frac{1}{4}\left[v(x-1)B(x-2) + \left[v(x-1) - v(x+1)\right]B(x) - v(x+1)B(x+2)\right]. \end{aligned} \tag{10.15b}$$

Again proceeding to the continuum limit by Taylor expanding (10.15), we obtain our desired 1D MHD equations with unequal transport coefficients: viscosity $\mu = \frac{\Delta x^2}{2\Delta t}$ and resisitivity $\eta = \frac{\Delta x^2}{\Delta t}$.

In the general case where $\frac{\pi}{4} \leq \theta < \frac{\pi}{2}$, $0 \leq \alpha < \frac{\pi}{2}$, and $0 \leq \beta < \frac{\pi}{2}$, we obtain the following effective field theory:

$$\frac{\partial v}{\partial t} + v\frac{\partial v}{\partial x} = \mu\frac{\partial^2 v}{\partial x^2} - B\frac{\partial B}{\partial x} + \mathcal{O}(\varepsilon^3) \tag{10.16a}$$

$$\frac{\partial B}{\partial t} + v\frac{\partial B}{\partial x} = \eta\frac{\partial^2 B}{\partial x^2} - B\frac{\partial v}{\partial x} + \mathcal{O}(\varepsilon^3), \tag{10.16b}$$

with adjustable transport coefficients for the viscosity and resistivity:

$$\mu(\theta,\alpha) = \frac{1}{2}\left(\cot^2\theta + \tan^2\alpha\right)\frac{\Delta x^2}{\Delta t} \tag{10.17a}$$

$$\eta(\theta,\beta) = \frac{1}{2}\left(\cot^2\theta + \tan^2\beta\right)\frac{\Delta x^2}{\Delta t}. \tag{10.17b}$$

The equations for (10.17a) are based on a previous result from the quantum algorithm for modeling the Burgers equation [Yepez, 2006], and the dependence of the transport coefficients on the Euler angles in (10.17a) have been confirmed numerically, see Section 10.4 below.

10.4 Numerical Tests

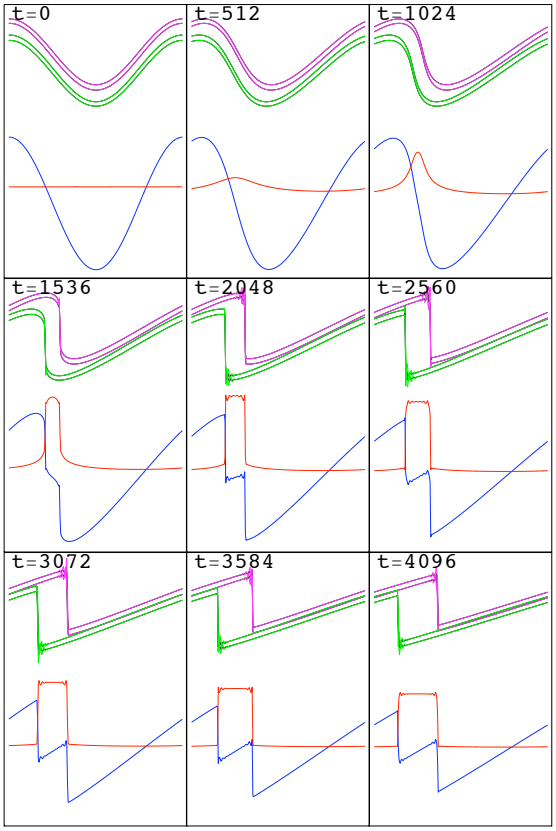

Figure 10.1: Simulation results in the low dissipation regime $\alpha = 0$, $\beta = 0$ and $\theta = 1.5$ radians, which corresponds to $\mu = \eta = 0.0025$. The simulation was carried out on a lattice with 256 nodes, used as the spatial coordinates along the $\hat{x}$-axis. The following values of four field quantities are plotted along the $\hat{y}$-axis. The blue curve is the velocity field, $-1 \leq v(x) \leq 1$. The red curve is the magnetic field, $0 \leq B(x) \leq 1$. The purple curves are the first and second occupation probability fields, $0 \leq p_1 \leq 1$ and $0 \leq p_2 \leq 1$. The green curves are the third and fourth occupation probability fields, $0 \leq p_3 \leq 1$ and $0 \leq p_4 \leq 1$. There are four black curves; these are analytical predictions, based on the computed macroscopic field profiles, of the equilibrium occupation probabilities and they are in excellent agreement with the numerical predictions. The mesoscopic fields remain in local equilibrium. Snapshots are shown at every 512 time steps. In regions of $\frac{\partial v}{\partial x} < 0$, shocks tend to form in the v-field with localized enhancement of the B-field. Asymptotically, v attains a constant slope with shock discontinuities while the B field is constant with discontinuities at the leading edges of the front. The extent of the Gibbs oscillations at the shock front is greater at the mesoscopic than at the macroscopic scale because of a fortuitous cancellation of oscillations.

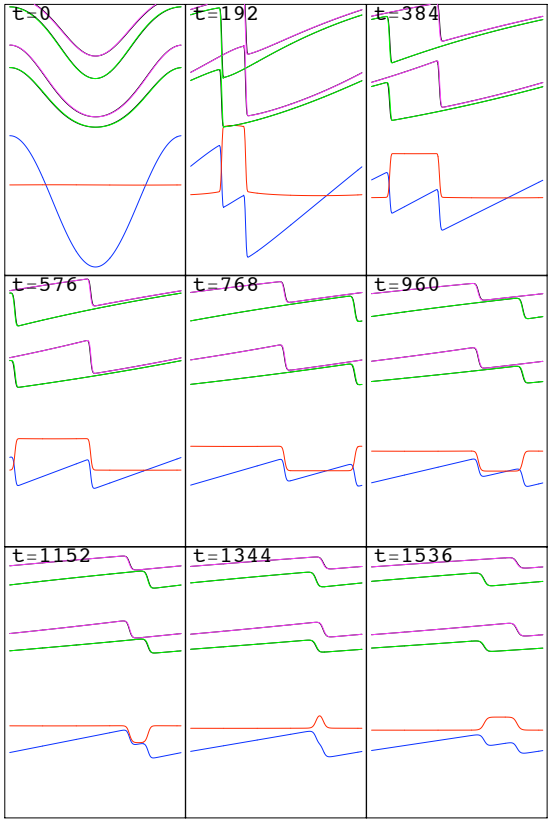

Figure 10.2: Simulation results in the highly dissipation regime : $\alpha = 0$, $\beta = 0$ and $\theta = \frac{\pi}{4}$ yielding $\mu = \eta = 0.5$, but otherwise similar to the previous figure (see Fig. 10.1 caption). No Gibbs oscillations occur since the shock front is spatially resolved. The color codings and lattice parameters are the same as those used in Fig. 10.1.

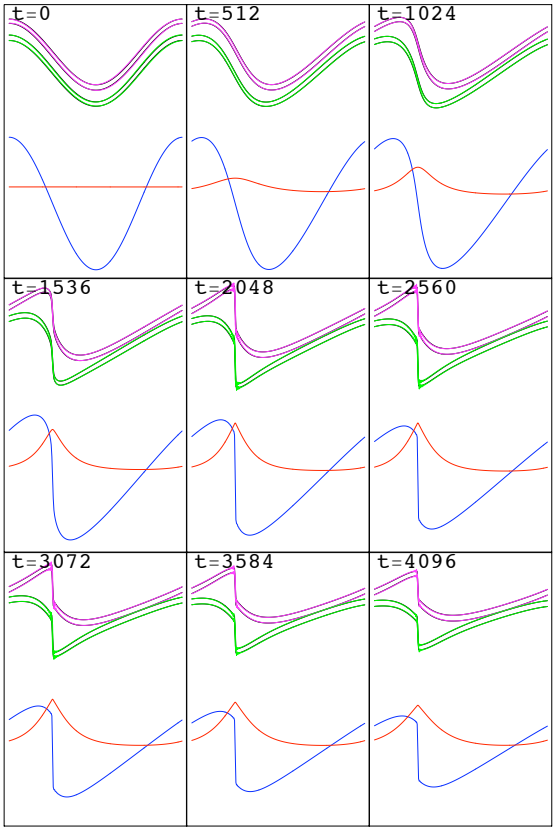

Figure 10.3: Simulation results with $\alpha = 0$ (low viscosity), $\beta = 1.0$ radian (high resistivity), and $\theta = 1.5$ radians (*i.e.*, $\mu = 0.0025, \eta = 1.22$). Slight Gibbs oscillations occurs as a steep unbifurcated shock front forms in the velocity profile since (10.16a) asymptotically becomes the Burgers equation. The caustic in the magnetic field is diffusion dominated, with tails emanating from the location of the shock front. The color codings and lattice parameters are the same as those used in Fig. 10.1.

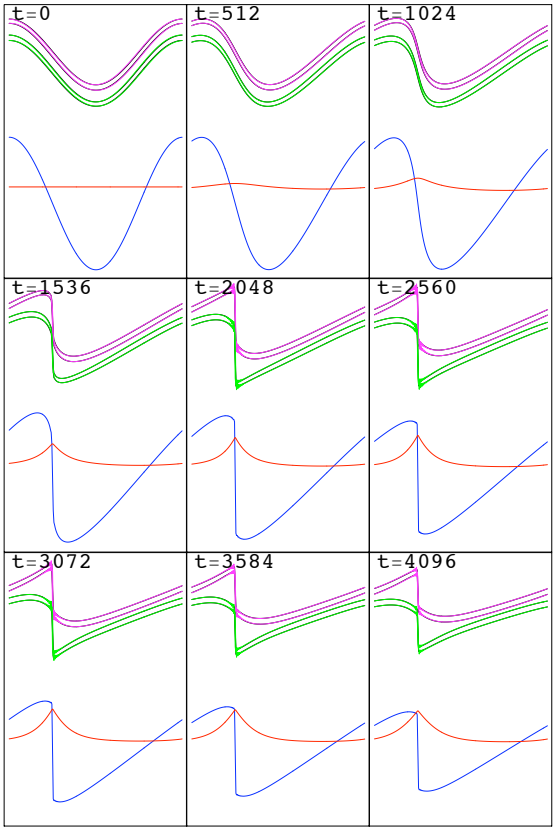

Figure 10.4: Simulation results with $\alpha = 0$ (low viscosity), $\beta = 1.2$ radians (high resistivity), and $\theta = 1.5$ radians (*i.e.*, $\mu = 0.0025, \eta = 3.31$). Slight Gibbs oscillations occurs as a steep unbifurcated shock front forms in the velocity profile since (10.16a) asymptotically becomes the Burgers equation. The caustic in the magnetic field is diffusion dominated, with tails emanating from the location of the shock front. The color codings and lattice parameters are the same as those used in Fig. 10.1.

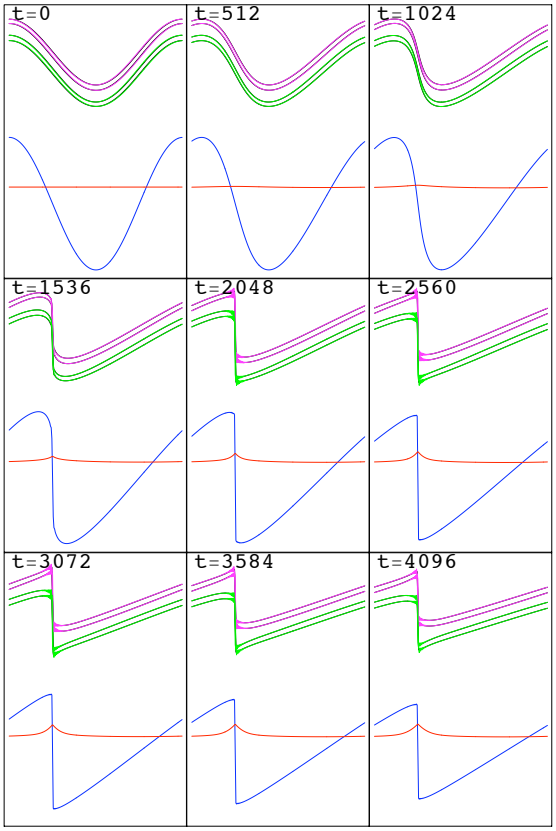

Figure 10.5: Simulation results with $\alpha = 0$ (low viscosity), $\beta = 1.4$ radians (high resistivity), and $\theta = 1.5$ radians (*i.e.*, $\mu = 0.0025, \eta = 16.81$). Slight Gibbs oscillations occurs as a steep unbifurcated shock front forms in the velocity profile since (10.16a) asymptotically becomes the Burgers equation. The caustic in the magnetic field is diffusion dominated, with approximately exponential tails emanating from the location of the shock front. The color codings and lattice parameters are the same as those used in Fig. 10.1.

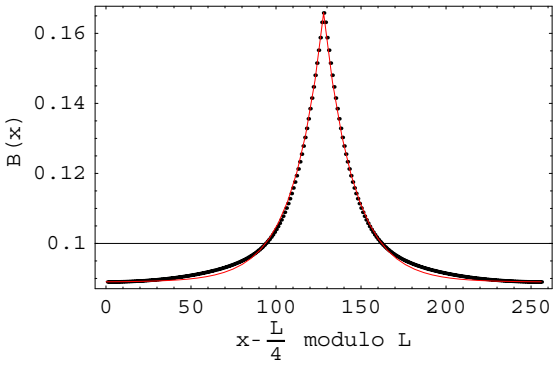

Figure 10.6: Comparison of theory versus numerical data for the magnetic field profile near a shock front with $\alpha = 0$ (low viscosity), $\beta = 1.4$ radians (high resistivity), and $\theta = 1.5$ radians (*i.e.*, $\mu = 0.0025, \eta = 16.81$). The caustic in the magnetic field (black dots) is diffusion dominated, with theoretically predicted exponential tails (red curve) emanating from the location of the shock front on a grid of size $L = 256\Delta x$. The data is shifted to the left by a distance of $\frac{L}{4}$

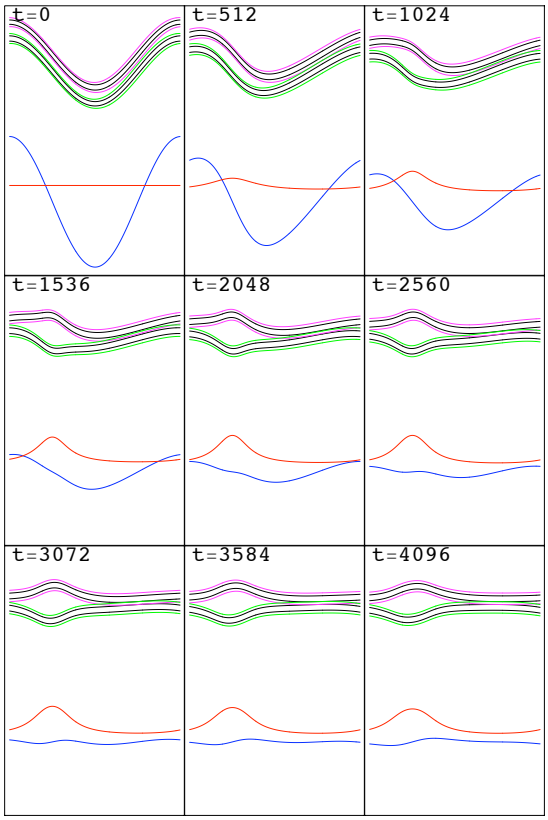

Figure 10.7: Simulation results with $\alpha = 0.8$ radians (high viscosity), $\beta = 0$ (low resistivity), and $\theta = 1.5$ radians (i.e.,$\mu = 0.53, \eta = 0.0025$). No Gibbs oscillations occurs and no shock front forms in the velocity field, which is diffusion dominated. The solitary and persistent pulse in the magnetic profile is caused by the forcing of the initial sinusoidal velocity field. The color codings and lattice parameters are the same as those used in Fig. 10.1.

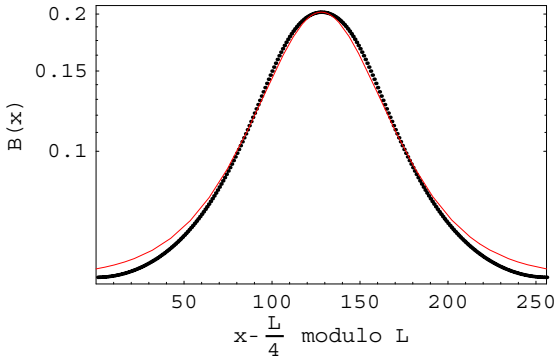

Figure 10.8: Comparison of theory versus numerical simulation results with $\alpha = 0.8$ radians (high viscosity), $\beta = 0$ (low resistivity), and $\theta = 1.5$ radians (*i.e.*, $\mu = 0.53, \eta = 0.0025$). The solitary and persistent pulse in the magnetic profile (black dots) has an approximately hyperbolic secant profile (red theoretical curve). The data is shifted to the left by a distance of $\frac{L}{4}$.

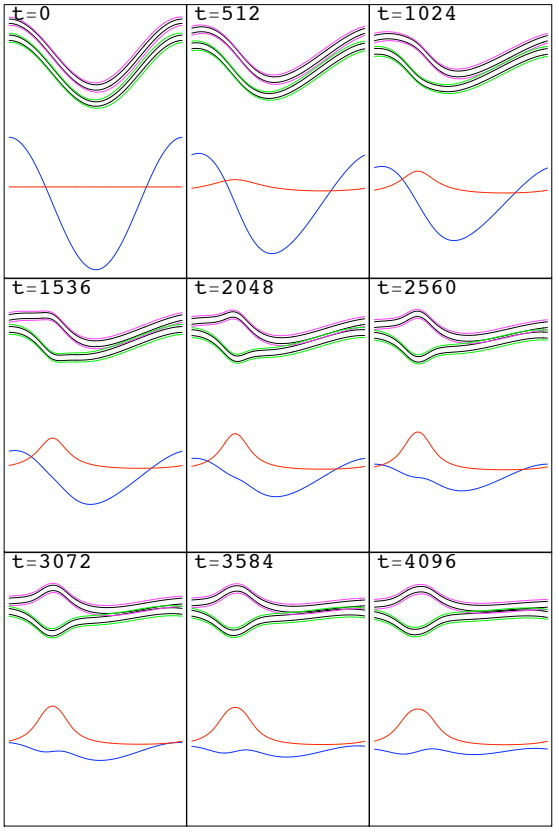

Figure 10.9: Simulation results with $\alpha = 1.0$ radian (high viscosity), $\beta = 0$ (low resistivity), and $\theta = 1.5$ radians (*i.e.*, $\mu = 1.22, \eta = 0.0025$). No Gibbs oscillations occurs and no shock front forms in the velocity field, which is diffusion dominated. The solitary and persistent pulse in the magnetic profile is caused by the forcing of the initial sinusoidal velocity field. The color codings and lattice parameters are the same as those used in Fig. 10.1.

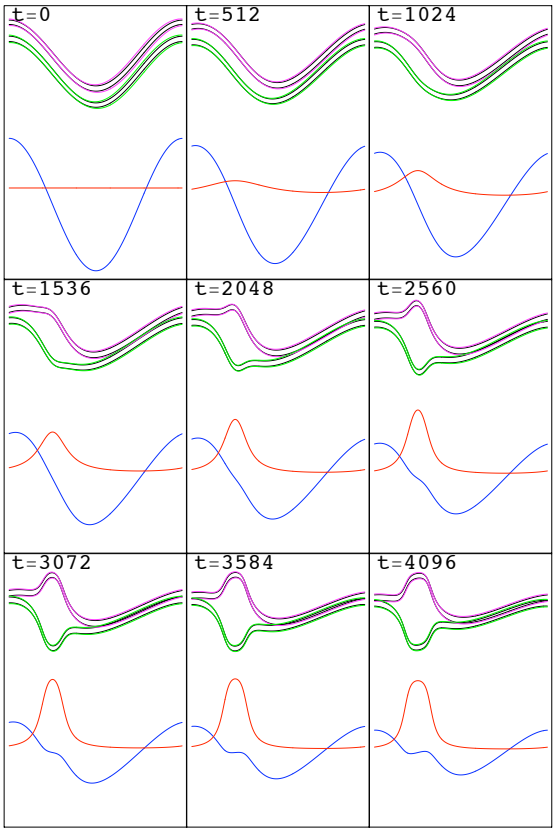

Figure 10.10: Simulation results with $\alpha = 1.2$ radian (high viscosity), $\beta = 0$ (low resistivity), and $\theta = 1.5$ radians (*i.e.*, $\mu = 3.31, \eta = 0.0025$). No Gibbs oscillations occurs and no shock front forms in the velocity field, which is diffusion dominated. The solitary and persistent pulse in the magnetic profile was caused by the forcing of the initial sinusoidal velocity field. The magnetic solitary pulse begin to cause a step discontinuity in the sinusoidal velocity profile. The color codings and lattice parameters are the same as those used in Fig. 10.1.

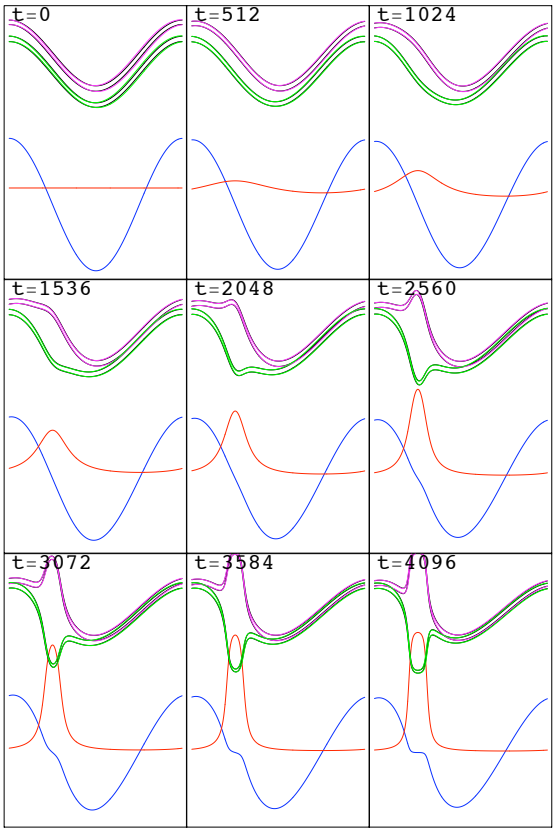

Figure 10.11: Simulation results with $\alpha = 1.4$ radians (very high viscosity), $\beta = 0$ (low resistivity), and $\theta = 1.5$ radians (*i.e.*, $\mu = 16.81, \eta = 0.0025$). No Gibbs oscillations occurs and no shock front forms in the velocity field, which is diffusion dominated. A very strong solitary and persistent pulse in the magnetic profile is caused by the forcing of the initial sinusoidal velocity field. This magnetic solitary pulse clearly causes a step discontinuity in the sinusoidal velocity profile. The color codings and lattice parameters are the same as those used in Fig. 10.1.

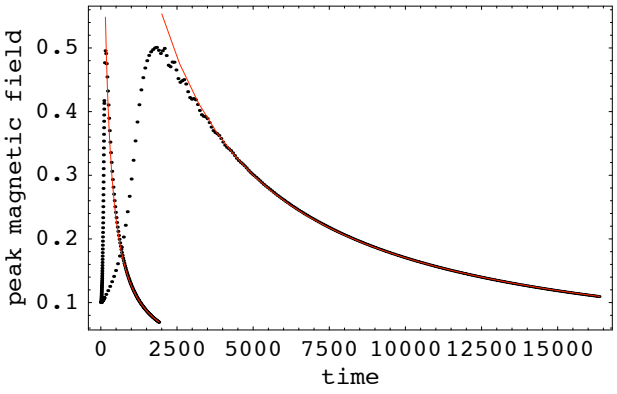

Figure 10.12: The time evolution of the B field at location $x = 192$ determined from the quantum algorithm (dotted curve). Two cases are shown. For the $\theta = \frac{\pi}{4}$ case, after the shock formation around $t \sim 200\Delta t$. For the $\theta = 1.5$ radians case, shock formation occurs latter in time at around $t \sim 2500\Delta t$. The analytical asymptotic solutions (red curves) shows the B field decays like t^{-1} as expected, see (10.19). There is excellent agreement between theory and the numerical solution over the whole dissipative regime from high to low resistivity.

The 1D MHD equations are solved using the quantum Boltzmann equation method described above for initial profiles $v(x,0) = 0.4\cos\left(\frac{2\pi}{L}\right)$ and $B(x,0) = 0.1$ on a $L = 256\Delta x$ grid. The evolution of the fields are shown in Fig. 10.1 (low dissipation regime) and Fig. 10.2 (high dissipation regime). Regions of $\frac{\partial v}{\partial x} < 0$ steepen towards shocks while regions of $\frac{\partial v}{\partial x} > 0$ smooth. At first the B field rapidly increases by a factor of 10 and concentrates where velocity shocks form. Asymptotically in time (but when the nonlinear terms are important and before the profile linearly diffuses away) the velocity profile bifurcates and eventually becomes linear in x except at the shocks. There is a surprising cancellation of errors. If one looks at the profiles of the occupation probabilities in Fig. 10.1 (low dissipation regime), they separately each have Gibbs oscillations. However, when the two occupation probability fields are added together forming the $v(x)$ field or subtracted forming the $B(x)$ field, the oscillations substantially cancel out because they are out of phase. The Gibbs oscillations subside altogether with higher grid resolution since its source is an under resolved shock front.

The B field asymptotically tends to a constant with spatial jumps around the velocity shock fronts. The linear sloped v field decays in time as does the constant B field. Indeed, we can check our model in this asymptotic region. Assuming $v(x,t) \longrightarrow a(t)x + b(t)$ and $B(x,t) \longrightarrow B(t)$, except at isolated locations corresponding to shock fronts, (10.1) yield constraint equations for $a(t)$, $c(t)$, and $B(t)$:

$$\frac{da}{dt} + a^2 = 0 \qquad \frac{db}{dt} + ab = 0 \qquad \frac{dB}{dt} + aB = 0. \tag{10.18}$$

The analytical solution of (10.18) yield asymptotic v and B field profiles

$$v(x,t) = \frac{x + k_2}{t + k_1} \qquad B(t) = \frac{k_3}{t + k_1}, \tag{10.19}$$

with constants of integration k_1, k_2 and k_3. From the quantum simulations shown in Figs. 10.1 and 10.2, we plotted in Fig. 10.12 the B field at $x = 192$ as a time series (black dots). The solid curve is the asymptotic decay (10.19) derived from (10.1). The decay is fast for the high resistivity case and it is slow for the low resistivity case. There is excellent agreement after the shock has fully formed with the analytical asymptotic solutions (red curves) validating our model for 1D MHD with unequal and arbitrary transport coefficients.

10.5 Final remarks

The numerical simulation results plotted in Figs. 10.1 and 10.2 manifest a characteristic property of a type-II quantum algorithm. The expected value of the occupancy of the ground state and excited state of a microscopic qubit contained within a quantum mechanical node of the lattice (in the 1D MHD model presented here there would be four qubits per node) are shifted. The expectation value of the excited state is plotted in the purple and green curves shown in in Figs. 10.1 and 10.2. Regardless of the dissipation regime (high or low viscosity and resistivity), there is a gap in value of the occupation probabilites; hence, $p_1^{\text{eq}} \neq p_2^{\text{eq}}$ (two purple curves) and $p_3^{\text{eq}} \neq p_4^{\text{eq}}$ (two green curves). The physical cause of this gap is the following. The microscopic dynamics is interpreted as the motion of quantum particles moving left and right through a chain of quantum processors. If the likelihood of a quantum particle exiting left or right from a quantum processor is equal, then the excited state energies encoding the left- and right-going probabilities would be degenerate. The equilibrium probabilities must overlap: $p_1^{\text{eq}} = p_2^{\text{eq}}$ and $p_3^{\text{eq}} = p_4^{\text{eq}}$. This degeneracy occurs in pairs because there are four occupation probabilities and only two macroscopic field quantities. The macroscopic effective field theory would be strictly diffusive as any quantum particle would move up and down the one dimensional chain of quantum processors in an unbiased random walk fashion. However, if the likelihood of a quantum particle exiting a quantum processor to the left does not equal the likelihood it will exit to the right, then the degeneracy in the distribution functions would be lifted and an energy gap would appear as demonstrated Figs. 10.1 and 10.2. In this case, the macroscopic effective field theory would not be strictly diffusive; there would be an overall net advection of quantum particles in one direction (the symmetry of the lattice is broken and this causes an energy gap in excited state energy levels). This net advection gives rise to the nonlinear terms in (10.16).

It is also interesting to note the strong asymmetry at the macroscopic level between the

v-field and the B-field, while at the quantum mesoscopic level there is symmetry in the four probabilities. The root of this macroscopic asymmetry is evident from the full 3D MHD equations where the momentum equation has a gradient of a symmetric tensor while the evolution of the magnetic flux is governed by the gradient of an anti-symmetric tensor. To clarify that we recover the macroscopic asymmetry, we have interchanged the initial profiles for v and B and chosen transport coefficients corresponding to Fig. 10.1: $\mu = \eta = 0.0025$. One notices that the initially constant v-profile develops a doubly periodic oscillation (driven by the single oscillation in the B-field) which then undergo shock formation at the two regions in which $\frac{\partial v}{\partial x} < 0$, see Fig. 10.13.

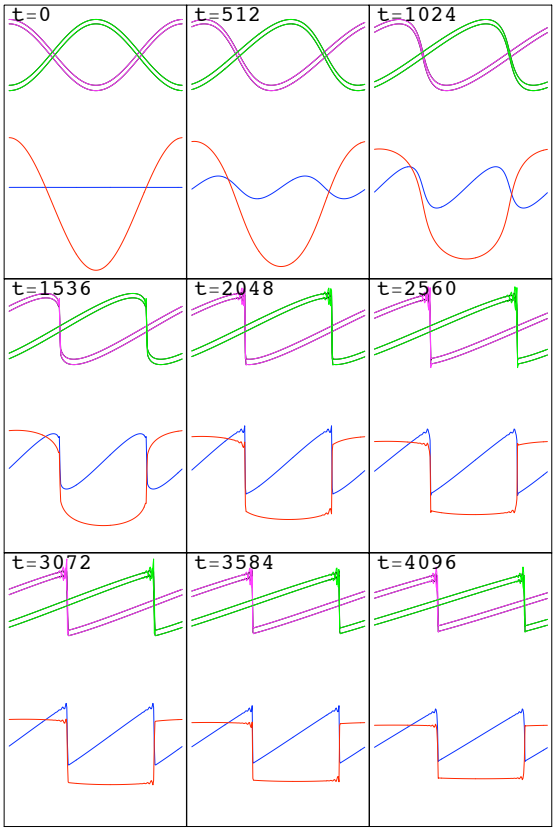

Figure 10.13: Simulation results in the low dissipation regime $\alpha = 0$, $\beta = 0$ and $\theta = 1.5$ radians, which corresponds to $\mu = \eta = 0.0025$. but for the initial conditions: $B(x,0) = 0.4\cos\left(\frac{2\pi}{L}\right)$ and $v(x,0) = 0.1$. The blue curve is the velocity field. The red curve is the magnetic field. The purple curves are the first and second occupation probability fields (p_1 and p_2). The green curves are the third and fourth occupation probability fields (p_3 and p_4).

The quantum Boltzmann equation is a new unconditionally stable algorithm for numerically predicting the time-dependent behavior of magnetohydrodynamic turbulence and shock formation for tunable transport coefficients. In contrast, the standard lattice Boltz-

mann algorithm becomes numerically unstable at low transport coefficients which are over a magnitude greater than those considered in Fig. 10.1. An open and very interesting problem is the extension of this quantum algorithm to MHD turbulence in 2+1 and 3+1 dimensions.

Chapter 11

The Navier-Stokes equation

11.1 Introduction

In the defense community there are a plethora of neutral-fluid flows problems, particularly flows by regions with non-trivial spatial boundaries, such around an aircraft fuselage or a ship hull, through a jet engine compartment, or over the Earth's surface. While analytical solutions to such problems remain elusive and generally intractable, today they are within the reach of the computational physicist. To tackle such problems, practitioners usually resort to direct numerical simulation methods, yet here the amount of computer memory and processing time grows faster that the number of desired computed field points. Even in cases with simple or periodic boundaries, where more efficient numerical representations are available (such as a psuedo spectral approach pioneered by G.I. Taylor in the 1930's and S.A. Orszag *et al.* in the 1970's [Orszag and Patterson, 1972]), the scaling of computer resources with grid size is daunting. This computational complexity has translated into significant annual costs to defense department high performance computing offices purchasing large numbers of processing elements (typically thousands or ten of thousands), configured in massive parallel computing arrays. But this cost, increasing year after year, has been borne so engineers can solve mission critical fluid problems, perpetually requiring higher resolution grids and more accurate and faithful simulations. For example, high resolution flow simulations like those shown in Figure 11.1 are vital to aeronautical engineers designing the shape of advanced fighter jets or unmanned aerial vehicles or submarines to economize on fuel consumption and minimize maneuvering instabilities and wakes, to propulsion engineers designing nozzle and flow control orifices to maximize thrust, or to meteorologists trying to understand intermittent turbulence induced in the upper atmosphere under the jet stream to maximize laser propagation from airborne platforms. Yet to the theoretical physicist, the situation is even more dire: the prediction of any aspects of turbulence (beyond Kolmogorov's 1941 universality hypothesis), using advanced statistical methods and perturbation methods,

borrowed from triumphant quantum field theory and statistical mechanics, remains the oldest and most prominent of classical grand challenge problems, open now for over 150 years.

This dire situation arises because, even in the macroscopic limit, strong correlations and feedback mechanisms between large scale and small scale flow structures, over many decades of spatial separation, dominate the overall flow evolution. The clearest high level picture capturing the essential physics of this problem, with restrictioned attention to divergence free and low Mach number flows, are the incompressible Navier-Stokes equations. The strong correlation between disparate scales is captured by the extremely simple non-local convective derivative (the second order nonlinearity in the velocity field).

11.1.1 Laminar to turbulent flow transition

The lattice model now affords a deep insight into the origin and essential inner workings of free shear turbulence. This is a *kinetic lattice gas model*, the clearest low level picture correctly capturing the essential physics and hydrodynamics of the problem. As the well known Ising lattice gas model is fundamental to a statistical mechanics understanding of the essential physics of ferromagnetism and the order-disorder phase transition, the kinetic lattice gas model is fundamental to a dynamical mechanics understanding of fluids and the laminar-to-turbulent flow transition.

A new universal feature of the laminar-to-turbulent transition becomes clear in high Reynolds number simulations. Following an initial period of laminar flow with vortex sheet stretching, and preceding the final inertial subrange period of isotropic and homogeneous turbulent flow with self-similar vortex tubes, there exists a well-defined interim period, here termed the *breaking subrange*. The hypothesis is that this subrange manifests self-organized criticality. The breaking subrange is dominated by anisotropic and non-homogeneous turbulent flow. Avalanches occur intermittently, where large coherent spatial structures grow, become unstable under maximal shear, and subsequently break into isotropic and homogeneous turbulence. These avalanches occur progressively in time across the entire space. See the bottom image of Fig. 11.1 showing the kind of anisotropic turbulent flow that occurs during an avalanche event, with young vortex tendrils. The time rate of change of the enstrophy, $\frac{\partial \mathscr{E}}{\partial t}$, has a generally negatively sloped avalanche cascade, with marked peaks, indicating the successive breaking points, as shown in Fig. 11.3.

By carefully comparing the renderings in Fig. 11.2 to the enstrophy plots in in Fig. 11.3, it is possible to see three distinct morphological stages of the flow: vortex stretching range, breaking subrange, and the inertial subrange. The morphological evolution transitions from (1) large vortex sheets to (2) convoluted vortex sheets with virgin vortex tendrils to (3) small entangled vortex tubes.

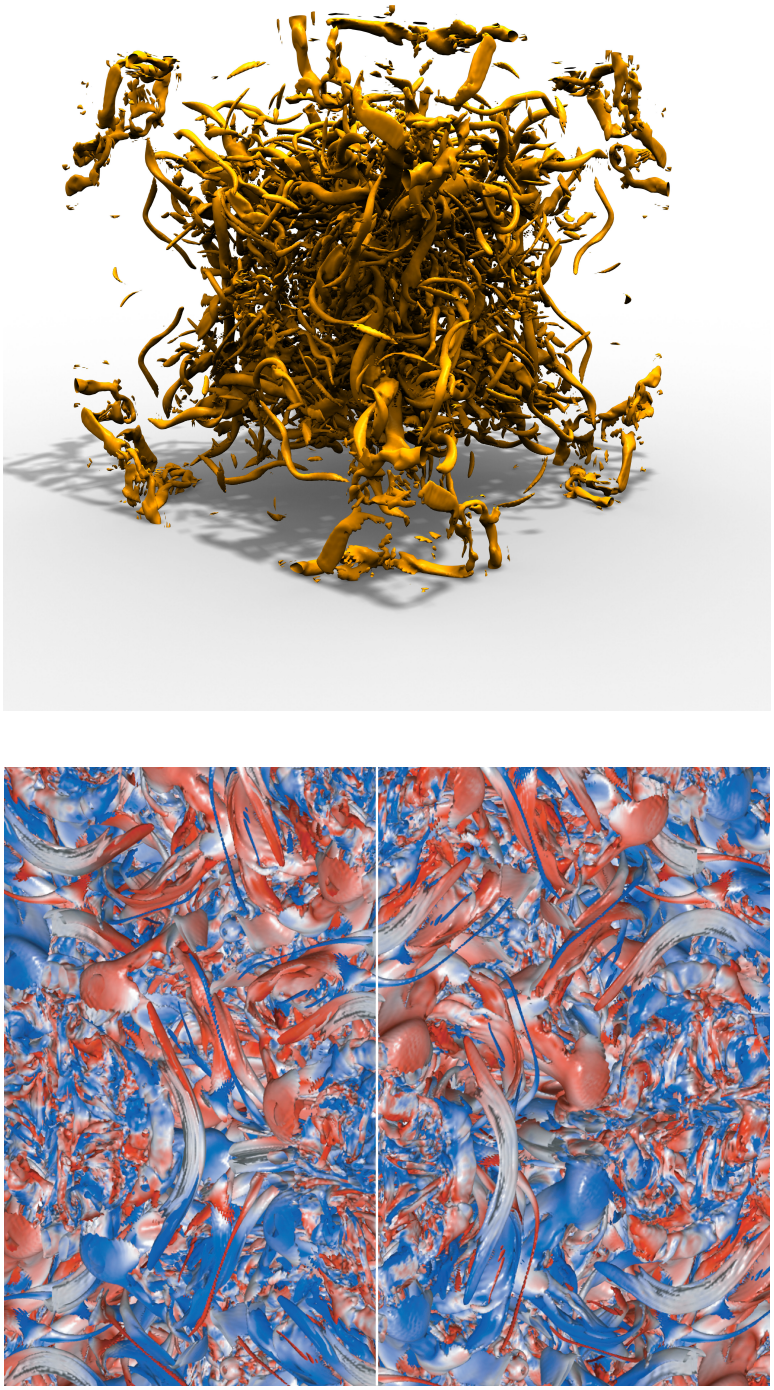

Figure 11.1: Supercomputer simulation of Navier-Stokes turbulence. Surface of constant vorticity in turbulent flow, showing entangled vortex tubes (top) and anisotropic flow in the *breaking subrange* (bottom). The dot product of the velocity and vorticity fields are displayed in the red-blue color coding. The bottom image is a zoomed view at $t = 5K\Delta t$ of Fig. 11.2, where the vertical white line is one edge of the cubical simulation grid. Long vortex tendrils are easily seen. Large-scale simulations offer a way to see the morphological evolution and structural development of turbulence in fluids, but they also give a preview of the kind of numerical output to be available from future quantum computers.

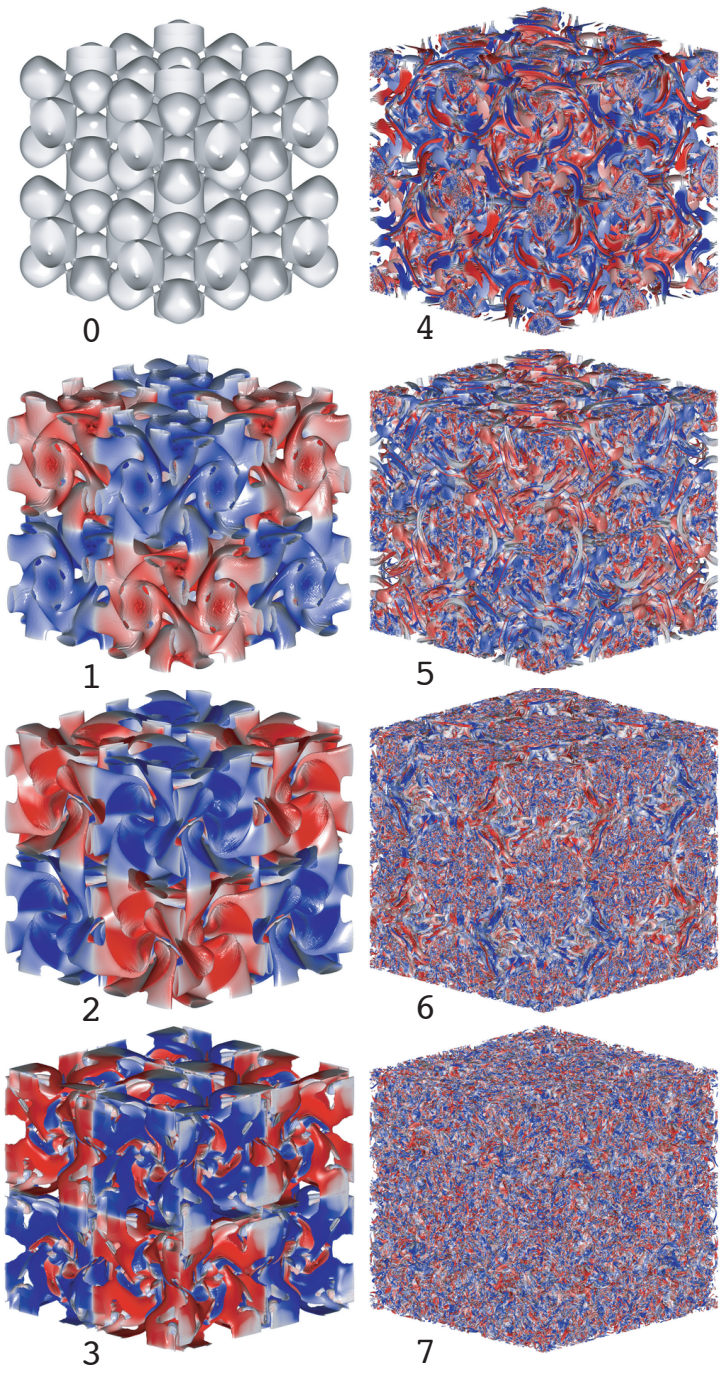

Figure 11.2: Surfaces of constant enstrophy ($\mathscr{E} = \frac{1}{2}\int dV|\vec{\omega}|^2$ where $\vec{\omega} = \nabla \times \vec{u}$) illustrating an incompressible fluid's morphological evolution from $t = 0$ up to $t = 7,000\Delta t$ iterations, in time steps of $1,000\Delta t$ on a cubical cartesian grid of size $L = 512\Delta x$. Surface coloring uses $\vec{u} \cdot \vec{\omega}$ (red equals -1 and blue 1). This 3+1 dimensional turbulent neutral fluid simulation run using the entropic lattice Boltzmann equation with 15-body particle-particle collisions (ELB-Q15 model) computed at every lattice site at each time step. At each site, local relaxation of the single-particle probability distribution a desired equilibrium function, represented as a low Mach number polynomial expansion. The initial flow is a Kida and Murakami profile [Kida and Murakami, 1987] with a super cell size set to $L_\circ = 512\Delta x$, the total grid size. So the flow configurations within all 8 octants of the large grid are initially identical. The characteristic flow speed is $u_\circ = 0.07071\frac{\Delta x}{\Delta t}$. The collisional inversion parameter is set to $\beta = 0.99592$, corresponding to a kinematic viscosity of $\nu_\circ = 6.8 \times 10^{-4}\frac{\Delta x^2}{\Delta t}$, for $\alpha = 2$.

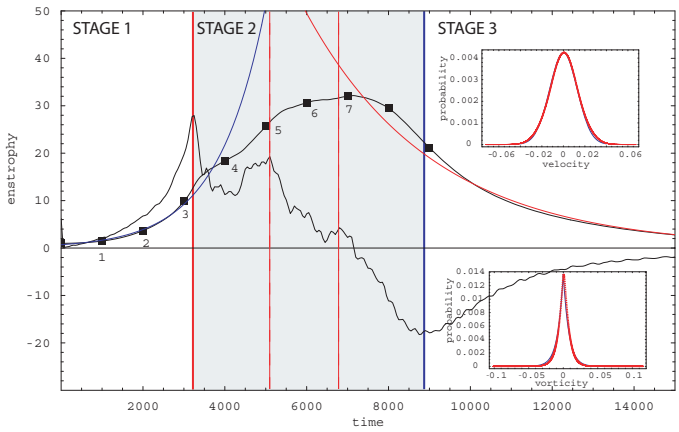

Figure 11.3: Plot of enstrophy versus time (smooth black curve) showing three stages in the morphological evolution: (1) vortex stretching range ($t < 3,200\Delta t$), (2) breaking subrange ($3,200 < t < 9,000\Delta t$), and (3) inertial subrange ($t > 9,000\Delta t$). The enstrophy is normalized so that at $t = 0$ it is unity. The isovalues used to visualize the 8 images in Fig. 11.2 are shown (black squares). STAGE 1: The initial exponential increase (blue curve) of enstrophy designates the initial *vortex stretching range* with characteristic laminar flow. There is excellent agreement between the analytical fit (blue curve) and the enstrophy data (black curve). STAGE 2: The time derivative of the enstrophy curve (jagged black curve) is also plotted. The time period of generally negative slope of the enstrophy derivative (gray shaded region) is here termed the *breaking subrange*, where large scale anisotropic ordering of turbulence occurs and intermittently breaks down over time. The first major breaking point occurs at about $t = 3,200\Delta t$ (vertical red line) and subsequent intermediate avalanches occur at about $t = 5,100\Delta t$ and $t = 6,750\Delta t$ (thin vertical red lines), respectively. STAGE 3: The final exponential decrease of enstrophy (red curve) designates the *inertial subrange* where the homogeneous and isotropic "small scale" turbulent flow morphology, with characteristic entangled vortex tubes, is organized in a spatially self-similar way. Here the energy spectral density obeys the Kolmogorov universality hypothesis, the famous $k^{-\frac{5}{3}}$ power law for energy cascade downward to smaller scales. The onset of the inertial subrange occurs close to $t = 9,000\Delta t$ (vertical blue line). Here the velocity probability distribution functions, for each component, are Gaussian (top inset) and the vorticity probability distribution function approaches an exponential (bottom inset). There is excellent agreement between the analytical fit (blue curve) and the enstrophy data (black curve). There exists a fourth stage of the morphology of turbulence at late times ($t > 14,000\Delta t$), not shown here, called the *viscous subrange*.

11.1.2 Q versus S models: closure of sub-grid effects

The continuum hydrodynamical equations are projections of the entropic lattice Boltzmann (ELB) equation, a projection down from the $Q \times L^D$-dimensional kinetic phase space on to a $4 \times L^D$-dimensional hydrodynamic null space [1]. This projection recovers the Navier-Stokes equations in the Chapman-Enskog limit. This has an important consequence: there exist many "qubit" models (or Q models for short) with a different local stencils (*i.e.* lattice vectors sets with different finite point group symmetries and coordination number), which will also recover the Navier-Stokes equations asymptotically (continuous rotational symmetry).

ELB is ideal for large eddy simulation (LES) closures since in LES one typically deals with mean strain rates for modeling the eddy viscosity. These nonlocal fluid calculations are immediately recovered from simple local moments in ELB.

At this stage, the ELB runs are a validation of the method and this is important because ELB is a crucial precursor to a viable quantum lattice Boltzmann method [Yepez, 2001a]. The good numerical agreement between the LES-LB (lattice Boltzmann equation with sub-grid Smagorinsky closure here referred to as an S model) and the basic ELB Q models is encouraging. Now fully convinced of the validity of ELB, work to speed it up for present day supercomputer implementations is underway. But the most promising opportunity is to simply build a type-II quantum computer [Pravia et al., 2002, Chen et al., 2006b], which could far outstrip any classical supercomputers, for turbulence fluid simulations. In the fullness of time, the ELB will outpace the LES-LB, even without quantum computers.

There are a few reasons for this view. First, the kinetic lattice gases obey detail balance while sub-grid closure methods, such as the LES-LB, do not. And another advantage of the ELB over LES-LB is that ELB obeys the second law of thermodynamics while LES-LB and other LES methods do not necessarily obey the second law. Third, in the LES-LB the strain tensor must be computed at every site. With no-slip boundaries, computing the strain tensor becomes problematic. In contrast, ELB is purely local, so grid sites near boundaries are handled as easily as sites far away from boundaries. All these are important differences when the model is used for practical engineering grade applications.

11.1.3 Timings and scaling

Turbulent dynamics are easily solved since the underlying kinetic equation (11.8) has only local algebraic nonlinearities in the macroscopic variables and simple linear advection. At

[1] A subset of all the eigenvectors in the Q-dimensional kinetic space, have zero eigenvalues. These eigenvectors span the hydrodynamic null space. It is 4 dimensional because the kinetic lattice gas model conserves probability (mass) and probability flux along the spatially orthogonal directions (three components of the momentum vector).

this mesoscopic level there are various kinetic lattices (Q=15, 19, or 27) with different lattice vectors on a cubic lattice, which model the Navier-Stokes equation to leading order in the Chapman-Enskog perturbative asymptotics.

With the CAP data obtained on BABBAGE, the effects of the underlying lattice symmetry on the fluid turbulence statistics (through autocorrelation tensors of velocity, vorticity, pdfs of vorticity, and the like) can be determined, but there is not have sufficient space to preset details here. The Q15 model seems to be the most efficient model. An example output of this model is shown in Fig. 11.2. Even on a relatively modest size 512^3 grid, we can achieve such a high degree of resolved nonlinearity (Re=26,512) that the consequent isotropic turbulence at the onset of the inertial subrange (at about $t \sim 9,000\Delta t$) outstrips the ability to visualize the myriad vortex tubes. Fig. 11.2 is just a test case. The sustained floating point per seconds (MFLOPS/PE) we achieved are the best of all scientific codes run, for example on the Earth Simulator, attaining over 67% of peak performance on 4,800 processors. Achieving the world's highest Reynolds number in the field of computational fluid dynamics should also occur in the near future. The current tested code on BABBAGE, on $1,600^3$ grid with 2,048 processing elements, can achieve a Reynold's number of Re=565,667. Modeling atmospheric scale turbulence, in the range of Re $\sim 10^6$ is possible today, for the first time in the half century long history of numerical digital computers applied to aerodynamics.

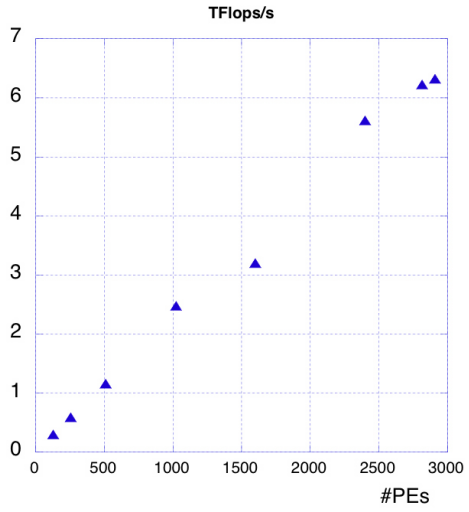

Figure 11.4: TFlops/sec scaling of ELB-Q27 code on BABBAGE with number of CPUs.

Some runs with these models–in particular the Q15, Q19, Q27 and S27 models–have been completed. The advantages of these lower Q models are reduced wallclock times with less memory demands. The nonlinear convective derivatives of in the Navier-Stokes equation are recovered from purely local moments of kinetic space distribution function. This is the basic

reason why ELB scales so well with PEs: the algorithm consists of simple local computations and streaming of information only to near neighbor grid sites.

No. PEs	GRID	MODEL	WALLCLOCK (s)	GFlops/s per PE
2912	1950^3	ELB-Q27	7,554.7	2.17
2912	1950^3	ELB-Q19	5,602.7	2.24
2912	1950^3	ELB-Q15	4,798.4	2.05
2912	1950^3	LES-LB-S27	4,451.2	1.05

Table 11.1: The gigaflops per second per processor element for 2912 CPU runs on a $1952 \times 1946 \times 1950$ grid for four lattice Boltzmann codes variants. The wallclock time is for $2{,}000\Delta t$ (lattice time steps). A full turbulence simulation takes about 54,000 time steps.

During Phase I, investigating the scaling properties of the Q27 code, over 6.3 tera flops per second on the full 2912 processor elements available on BABBAGE was achieved, see Fig. 11.4.

The LES-LB-S27 code, which no longer needs the solution of an entropy constraint equation, has also been tested in Phase I. It is less computationally intensive (due to the avoidance of log-calls and the need for a Newton-Raphson root finder at each spatial node and time iteration) and shorter wallclock time than the ELB-Q27 code, see Table 11.1.

11.1.4 Quantum information processing

Quantum information processing (QIP) and quantum communications will be integral to the 21st century. For many years, QIP has been included in the Developing Science and Technologies List, in the section of critical information systems technology. It appears that superconductive quantum information processing may soon be elevated to the status of a militarily critical technology. There now exists the rather imminent possibility of the development of large quantum computer arrays, potentially far outstripping any supercomputers now used for defense department computations.

On BABBAGE Q27, Q19, Q15 lattice Boltzmann codes were tested, like the one shown in Figure 11.1. Using 2,048 processors it took two days to complete a single job. A $1,024^3$ grid takes about 44 hours for Q27 on 512 processors, while the corresponding run for Q15 takes about 28 hours. The cost of the largest supercomputer parallel arrays annually adds to a significant fraction of a billion dollars for new government-owned systems in the United States (*e.g.* 19,000 processor Franklin at DOE/NERSC cost about $50 million and occupies the space of a gymnasium). Remarkably, exploiting quantum mechanical complexity new quantum device technology available today can be used to efficiently compute the collision operator of the Q15 lattice Boltzmann code, the basic engine of the code.

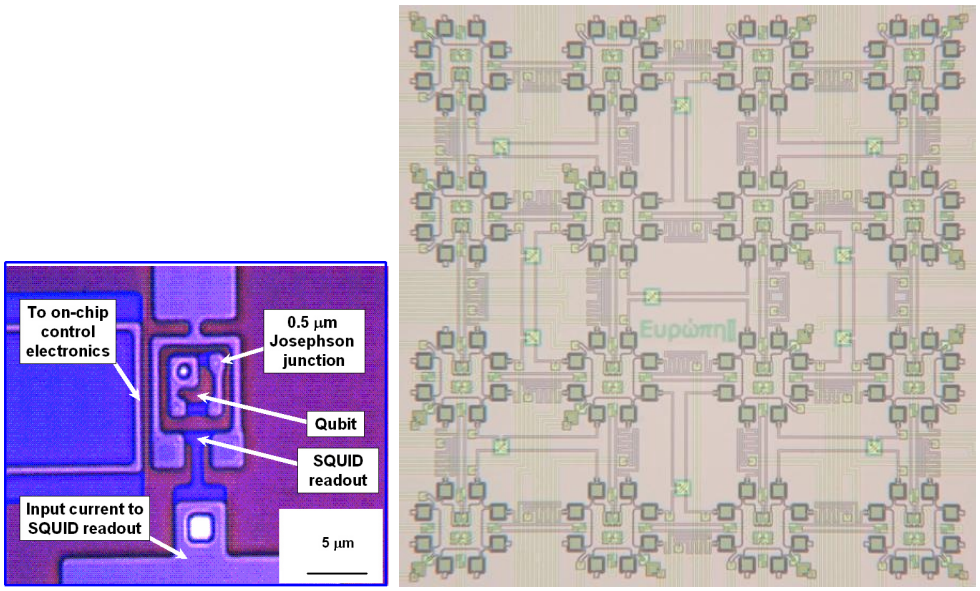

Figure 11.5: Shown here is a quantum information processor circuit to embody a qubit (top), a basic device for storing quantum information, designed by Terry Orlando of MIT and build at MIT Lincoln Laboratory at Hanscom AFB in 2000 [Mooij et al., 1999, Orlando et al., 1999]. The circuit must be placed in a dilution refrigerator. Air Force Office of Scientific Research (AFOSR) supported novel quantum computing technology based on superconductive electronics under the Quantum Computation for Physical Modeling (QCPM) theme, and this research has recently found follow-on use. A superconducting wire loop with multiple Josephson junctions forms a qubit and such qubits are coupled together to make quantum logic gates. AFOSR funded this new solid-state technology, fabricated at the superconductive electronics foundry at MIT Lincoln laboratory. This helped establish the basic fabrication techniques to build scalable quantum computers and mapped the quantum control methodology, proven with NMR spectroscopy [Pravia et al., 2002, Chen et al., 2006b], onto the field of superconductive electronics for quantum information processing, mapping pulse protocols to allow qubit-qubit logical operations, constituting a basic 2-qubit quantum processor. Going from a 2-qubit processor to a 16-qubit processor necessarily entails a significant applied research effort recently announced by D-Wave, a Canadian start-up company. D-Wave's 16-qubit processor, fabricated by NASA, is shown (bottom).

Therefore, a relatively low cost and small type-II quantum computer with a few thousand 16-qubit quantum processor chips, perhaps cooled with dilution refrigeration, could handle the same supercomputing job. It could cost a few million dollars to assemble, a couple orders of magnitude less expensive than classical digital electronics based supercomputers, such as BABBAGE, and physically smaller by many orders of magnitude as well. Furthermore, future quantum processor arrays with more qubits per node, in the very near future, should outstrip any traditional parallel supercomputer purchased under the department of defense high performance computing modernization program.

The kinetic lattice gas model has proven to be a state-of-the-art tool for understanding the morphological evolution of turbulence.

11.2 Brief review of fluid dynamics

The long wavelength hydrodynamic behavior of a many-body system of particles can be modeled at the macroscopic scale by an effective field theory, a set of coupled partial differential equations. The smooth fields of mass density, ρ, and flow velocity, $\vec{v}$, obey a mass continuity equation and a viscous Navier-Stokes fluid equation of motion. There is also a parabolic heat equation for the energy density, yet for simplicity, I will not consider the heat equation here, and instead I shall consider an athermal fluid.

Because the mass increase within a region $\mathcal{R}$ is entirely accounted for by the flux of particles into $\mathcal{R}$ through its boundary $\partial\mathcal{R}$, the ρ and $\vec{v}$ fields obey the continuity equation

$$\partial_t \rho + \partial_i(\rho v_i) = 0. \tag{11.1}$$

This is the first equation of motion. Here the shorthand notation for partial derivatives is used: $\partial_t \equiv \partial/\partial_t$ and $\partial_i \equiv \partial/\partial x_i$. The field equation embodying Newton's second law, for a region $\mathcal{R}$ expressing the change in the momentum density in terms of the stress applied at the boundary $\partial\mathcal{R}$, is Euler's equation

$$\partial_t(\rho v_i) + \partial_j \Pi_{ij} = 0. \tag{11.2}$$

Now following Landau and Lifshitz [Landau and Lifshitz, 1987], the momentum flux density tensor is written as[2]

$$\Pi_{ij} = P\delta_{ij} + \rho v_i v_j - \eta(\partial_i v_j + \partial_j v_i - \frac{2}{D}\partial_k v_k \delta_{ij}) - \zeta \delta_{ij}\partial_k v_k. \tag{11.3}$$

The viscous stress tensor is $\sigma'_{ij} = \eta(\partial_i v_j + \partial_j v_i - \frac{2}{D}\partial_k v_k \delta_{ij}) + \zeta\delta_{ij}\partial_k v_k$, where η and ζ are the transport coefficients for the shear viscosity and bulk viscosity, respectively, and D is

[2] For non-divergent flow ($\partial_j v_j = 0$) in the incompressible fluid limit, (11.3) is $\Pi_{ij} = P\delta_{ij} + \rho v_i v_j + \eta(\partial_i v_j + \partial_j v_i)$. Furthermore, the term $\eta\partial_i v_j$ in the Euler equation vanishes in this limit.

the number of spatial dimensions of the system. The first two terms in (11.3) represent the *ideal part* of the momentum flux density tensor, which is the sum of the pressure term, P, plus the convective term, $\rho\vec{v}\vec{v}$, which is nonlinear in the velocity.

In general the pressure, P, is a function of the mass density field, $\rho = \rho(\vec{x}, t)$, and for a thermal fluid it also is a function of the temperature field, $T = T(\vec{x}, t)$. The pressure tensor is diagonal because the fluid is *isotropic*. $P = P(\rho, T)$ is termed the *equation of state*. For a *neutral fluid* comprosed of independently moving particles, the pressure depends linearly on the mass density, $P = c_s^2\rho$, where c_s is the *speed of sound* in the fluid. In a thermohydrodynamic system, the sound speed is temperature dependent, $c_s = \sqrt{\frac{k_{\rm B}T}{m}}$ (where $k_{\rm B}$ is the Boltzmann constant and m is the mass of a single particle). In this case the pressure obeys the well known *ideal gas law*, $P = nk_{\rm B}T$, where $n = \frac{\rho}{m}$ is the particle number density. For an athermal hydrodynamic system (one where the system is at uniform homogeneous temperture, and where heat transport is neglected), c_s is a constant.

Substituting (11.3) into Euler's equation (11.2), gives us the second equation of motion for a viscous isotropic fluid

$$\rho\left(\partial_t v_i + v_j\partial_j v_i\right) = -\partial_i P + \rho\nu\partial^2 v_i + \left(\zeta + \frac{\eta}{D}\right)\partial_i\partial_j v_j. \tag{11.4}$$

This is the called the *Navier-Stokes* equation. In (11.4), η is the *shear viscosity* and ζ is the *bulk viscosity*. The transport coefficient for momentum diffusion, $\nu \equiv \frac{\eta}{\rho}$, is the *kinematic viscosity*. It gives a measure for the rate of decay of local shears in the fluid and determines how fast a perturbed fluid will relax from an anisotropic flow profile at the macroscopic scale to an isotropic steady state profile. Both the shear viscosity and the bulk viscosity cause damping of compressional waves in the mass density field. The shear viscosity alone causes damping of shear waves in the momentum density field. In general, for a nonisotropic fluid, there may also exist a *cubic viscosity*. However, in our case we shall deal with isotropic fluids where the shear and cubic viscosities coincide.

11.2.1 Dimensionless numbers

Let L and T denote the characteristic length and time scales, respectively, of a hydrodynamic scale fluctuation. That is, L and T are quantities characterizing the fluid's configuration at the macroscopic scale. Examples of the characteristic length scale for hydrodynamic flow are the wavelength of a compressional wave in the mass density field, the wavelength of a shear wave in the momentum density field, or the diameter of a fluid vortex. The mean free path is the average distance a particle travels between collisions. Let λ and τ denote the mean-free length and time, respectively, characterizing the microscopic particle collisions. Relevant hydrodynamic quantities are the

- *characteristic flow speed*, $u \sim \frac{L}{T}$;
- *sound speed*, $c_s \sim \frac{\lambda}{\tau}$;
- *shear viscosity*, η (and the *kinematic viscosity*, $\nu \equiv \frac{\eta}{\rho} \sim \frac{\lambda^2}{\tau}$); and,
- *bulk viscosity*, ζ.

The relevant dimensionless quantities are the

- *Knudsen number*, Kn, defined as the ratio of the mean-free path to the characteristic length scale ($\mathrm{Kn} \equiv \frac{\lambda}{L}$);
- *Strouhal number*, Sh, defined as the ratio of the mean-free time to the characteristic time scale ($\mathrm{Sh} \equiv \frac{\tau}{T}$);
- *Mach number*, M, defined as the ratio of the characteristic velocity to the sound speed ($\mathrm{M} \equiv \frac{u}{c_s}$);
- *Reynolds number*, Re, defined as the ratio of the product of the characteristic velocity times characteristic length to the kinematic viscosity ($\mathrm{Re} \equiv \frac{uL}{\nu} \sim \frac{\mathrm{M}}{\mathrm{Kn}}$); and,
- *fractional mass density variation*, $\frac{\delta\rho}{\rho}$.

11.3 Microscopic lattice model

In the lattice model, dynamics is projected into a discrete kinetic phase space (a product space over the position and momentum degrees of freedom). The logical "1" state (the excited state) of a qubit $|q\rangle$ associated with the spacetime point $(\vec{x}, t)$ encodes the probability f_q of the existence of a particle at that point moving with velocity $\vec{c}_q = \frac{\Delta\vec{x}_q}{\Delta t}$, where $\Delta\vec{x}_q$ are lattice vectors, for $q = 1, 2, \ldots, Q$. Similarly, the logical "0" state (the ground state) of a qubit $|q\rangle$ associated with the spacetime point $(\vec{x}, t)$ encodes the probability $1 - f_q$ of the existence of a hole at that point.

A fundamental property of the lattice model is that particle motions in momentum space and position space occur independently [Yepez, 2005]. Particle momentum and position space motions are generated by the combination of an engineered qubit-qubit interaction Hamiltonian H' and a free Hamiltonian $-i\hbar \sum_q \vec{c}_q \cdot \nabla$, respectively.

11.3.1 Interaction Hamiltonian

All positive indices of ladder operators are taken modulo Q, and negative indices are converted to positive indices $-q = q + \frac{Q}{2}$, for even Q. All sums are taken in increments of unity. The interaction Hamiltonian can be written as follows:

$$H' = A \sum_{q=\frac{1}{2}}^{\frac{Q}{2}} a_{2q}^{\dagger} a_{-2q}^{\dagger} a_{2q+1} a_{-2q-1} + B \sum_{q=\frac{1}{2}}^{\frac{Q}{2}} a_{2q}^{\dagger} a_{2q+1} + \text{h.c.} \tag{11.5a}$$

$$= \frac{A}{2} \sum_{q=1}^{Q} a_{2q}^{\dagger} a_{-2q}^{\dagger} a_{2q+1} a_{-2q-1} + \frac{B}{2} \sum_{q=1}^{Q} a_{2q-1}^{\dagger} a_{2q} + \text{h.c.}, \tag{11.5b}$$

where A and B are energy constants. The factor of $\frac{1}{2}$ is inserted to avoid double counting.

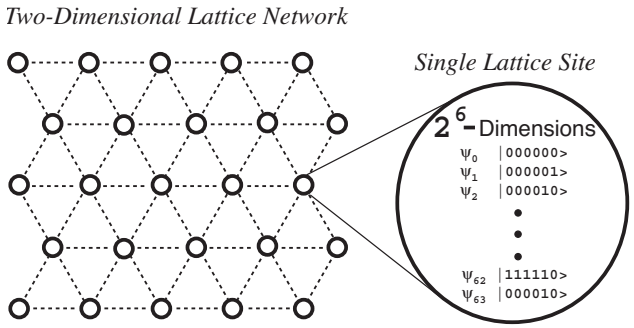

Figure 11.6: An triangular lattice of quantum nodes (depicted as circles) arranged in a 2-dimensions. The large circle on the right is an expanded view of a single node at one site of the lattice. It depicts the on-site submanifold, $\mathcal{H}$. Each quantum node has $Q = 6$ qubits so the on-site ket $\mid \psi\rangle$ resides in a 64-dimensional Hilbert space. Each node is coupled to its 6 nearest neighbors by a mechanism allowing for the exchange (or teleportation) of qubit states.

The following is an explicit example of the Hamiltonian of a quantum lattice gas in 2+1 dimensions that generates all the collisions of a system of particles moving on a triangular lattice.

$$\begin{aligned} H' &= A \left(a_1^{\dagger} a_2 a_4{}^{\dagger} a_5 + a_3^{\dagger} a_4 a_6^{\dagger} a_1 + a_5^{\dagger} a_6 a_2^{\dagger} a_3 + \text{h.c.} \right) \\ &+ B \left(a_1^{\dagger} a_2 + a_3^{\dagger} a_4 + a_5^{\dagger} a_6 + \text{h.c.} \right) \end{aligned} \tag{11.6}$$

The triangular lattice is shown in Fig. 11.6. A comparison between classical lattice gas and quantum lattice gas simulations are shown in Fig. 11.7.

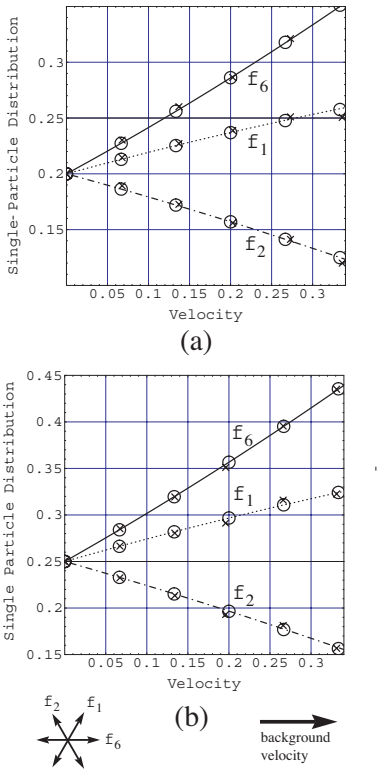

Figure 11.7: Theory versus simulation comparison of the velocity dependence of the single-particle distribution function in the non-Galilean parameterization: $f_a = \langle\psi|\hat{n}_a|\psi\rangle = d + dD\hat{e}_a \cdot \vec{v} + gdD(D/2+1)\hat{Q}_a : \vec{v}\vec{v}$. FHP simulation data is overplotted on this predicted mesoscopic distribution function. Plots (a) and (b) are for background densities of $d = .20$ and $d = 0.25$, respectively. A velocity shift is imparted along the x-axis; that is, along the f_1 direction indicated in the figure. Data were collected from a 128×128 classical FHP simulation (crosses) and was coarse-grained averaged over 1600 time steps from time step $t = 400$ to $t = 2000$. Data were also collected from a smaller 32×32 quantum FHP simulation (circles) and were measured at a single time step at $t = 200$.

11.3.2 Local quantum dynamics

The initial local quantum state is a tensor product over the qubits $\psi(\vec{x},t) = \bigotimes_{q=1}^{Q} |q(\vec{x},t)\rangle$.

$$\psi'(\vec{x},t) = e^{\frac{-iH'\Delta t}{\hbar}}\psi(\vec{x},t) \tag{11.7a}$$

$$|q(\vec{x},t+\Delta t)\rangle = e^{-i\hbar\vec{c}_q\cdot\nabla}|q'(\vec{x}-\Delta\vec{x}_q,t)\rangle. \tag{11.7b}$$

All the particle-particle interactions, 2-body up to and including $(Q-2)$-body interactions, generated by H' are mapped to a local collision function $H' \mapsto \Omega_q$ that depends on the f_q's at the lattice site [Yepez, 2001a].

In the type-II quantum computing case, quantum entanglement is localized among qubits associated with the same $(\vec{x},t)$ [Yepez, 2006], so we have:

$$f'_q(\vec{x},t) = f_q(\vec{x},t) + \Omega_q(f_1, f_2, \ldots f_Q) \tag{11.8a}$$

$$f_q(\vec{x},t) = f'_q(\vec{x}-\Delta\vec{x}_q, t-\Delta t), \tag{11.8b}$$

where f_q and f'_q are called the *incoming* and *outgoing* probabilities, respectively. In the classical limit, there exists a fundamental entropy function

$$\mathscr{H}(f_1,\ldots,f_Q) = \sum_{q=1}^{Q} \left(f_q \ln(\gamma_q f_q) + (1-f_q)\ln(1-f_q)\right), \tag{11.9}$$

where the γ_q are weights determined by the microscopic collision operator.

11.4 The approach to local equilibrium

Our lattice-based quantum system is said to be in *local equilibrium* when the system ket $|\Psi^{\text{eq}}(t)\rangle$ is an eigenvector, with unity eigenvalue, of the collision operator $\hat{C}$

$$\hat{C}|\Psi^{\text{eq}}\rangle \equiv |\Psi^{\text{eq}}\rangle. \tag{11.10}$$

The value of the probability of occupancy (7.4) is then determined from $|\Psi^{\text{eq}}\rangle$ as follows

$$f_a^{\text{eq}}(\vec{x},t) = \langle\Psi^{\text{eq}}(t)|\hat{n}_\alpha|\Psi^{\text{eq}}(t)\rangle. \tag{11.11}$$

Notice by the definition (11.10) for local equilibrium, the collision term (7.13) in the lattice Boltzmann equation vanishes

$$\Omega_a^{\text{meso}}(|\Psi^{\text{eq}}\rangle) = 0. \tag{11.12}$$

At steady-state equilibrium, the occupancy probabilities are unchanging over time. That is, $|\Psi^{\text{eq}}\rangle$ is the ground state of the system. At local equilibrium, the distribution along the

momentum directions of the particle occupancies are uniform, so the local configurations are perfectly symmetric, and Ω_a^{meso} cannot cause any further changes.

Let us predict the non-equilibrium behavior of the quantum lattice-gas system when it is near and approaching local equilibrium. Since continuous macroscopic fields for the mass and momentum densities are defined for the quantum lattice-gas system in the continuum limit, by (7.5) and (7.7), we can characterize the system using the dimensionless quantities traditionally used to characterize fluid systems. Given the *law of similarity*[3], if the macroscopic scale behavior of the quantum lattice gas is fluid-like, then it may be compared to a natural fluid characterized by the same dimensionless quantities.

Several dimensionless quantities (the Knudsen, Strouhal, Mach, and Reynolds numbers, and fractional mass density variation defined above in Section 11.2.1) allow us to quantify how close the system is to local equilibrium. At local equilibrium all the dimensionless numbers vanish (only the Mach number may be nonzero at equilibrium if there is a global uniform background flow, however this can be avoided by an appropriate choice of the Galilean frame-of-reference). In nonequilibrium situations far from steady-state, Kn, Sh, M, and $\frac{\delta\rho}{\rho}$ are order unity.

Hydrodynamic behavior is attained in the long wavelength limit where Kn and Sh are close to zero. *Viscous* hydrodynamic behavior is attained in the long wavelength limit when $\text{Sh} \sim \text{Kn}^2$ and $\frac{\delta\rho}{\rho} \sim \text{Kn}$. This is called *diffusive ordering* which is characteristic of random walk processes.[4]. *Incompressible* viscous hydrodynamics occurs when we also have $\text{M} \sim \text{Kn}$ so that $\text{Re} \sim \mathcal{O}(1)$ and $\frac{\delta\rho}{\rho} \sim \text{Kn}^2$. A procedure for linearizing the mesoscopic quantum Boltzmann equation and comparing the resulting dispersion relations to the solution of the effective field theory equations of motions (11.1) and (11.4) is given immediately below in Section 11.4.1. The procedure involves a series of expansions in $\frac{\delta\rho}{\rho}$. A Mach number expansion of the probability of occupancy is used (see Appendix I). Then, a Chapman-Enskog procedure, given in Section 11.5.2, is used, which is necessary for the derivation of the macroscopic equations of motion and which involves perturbative expansions in Kn and Sh, given in Section 11.5.3.

At $t = \infty$, an infinite lattice-gas system completely relaxes to steady-state equilibrium, where the mass density field is uniformly constant. The steady-state equilibrium occupation probability, denoted by d, is the same everywhere, $f_a(\vec{x}, \infty) = d$, for all a and all $\vec{x}$. For a lattice of finite size, the number of phase space points is also finite, although extremely large. The number of phase space points equals 2^{BV}, where B is the number of local states

[3]See page 56 of Fluid Mechanics by Laudau and Lifshitz [Landau and Lifshitz, 1987].

[4]A tagged particle in a lattice gas undergoes a random walk, and the observed diffusive behavior of tagged particles in lattice-gas simulations agrees well with analytical results [Binder, 1988, Brito and Ernst, 1992]

per site and V is the total number of sites. Hence the Poincaré recurrence time, which is the number of phase space points of a closed loop trajectory, is also finite and the state of the finite-lattice gas system is not defined at $t = \infty$. Hence, we may instead say that the lattice-system has completely relaxed to a steady state on a time scale much much larger than the characteristic time ($\frac{\tau}{\mathrm{Sh}}$) for the largest hydrodynamic scale fluctuation.

11.4.1 Linearized quantum Boltzmann equation

Our first step towards analyzing the nonsteady-state behavior of the system will be to expand f_a^{noneq} about d. We write the occupancy probability as a constant part ($d \equiv \frac{\rho}{mB}$) and a fluctuating part $\delta f_a(\vec{x}, t) \ll d$

$$f_a(\vec{x}, t) = d + \delta f_a(\vec{x}, t). \tag{11.13}$$

We can also expand the collision term about steady-state equilibrium

$$\Omega_a^{\mathrm{meso}}(|\Psi\rangle) = \Omega_a^{\mathrm{meso}}(|\Psi^{\mathrm{eq}}\rangle) + \delta\Omega_a^{\mathrm{meso}}. \tag{11.14}$$

Now the first term on the R.H.S. vanishes according to (11.12) and the second term on the R.H.S. arises because of fluctuations in the probability of occupancies of all the local states in the entire system. This is because the fluctuations of the collision term depend on fluctuations of the system ket $|\Psi\rangle$, which may have global superposition of the qubit states. Hence, we can formally write the collision term as a function of the occupancy probabilites of all Q qubits in the system

$$\Omega_a^{\mathrm{meso}}(|\Psi\rangle) = \Omega_a^{\mathrm{meso}}(f_1, f_2, \ldots, f_Q). \tag{11.15}$$

This functional form of the collision term is quite different than in the classical case where $\hat{C}$ is an orthogonal matrix. In the classical case, the collision term Ω_a^{meso} is only a function of the local occupation probabilities at a single site in the system. Because of global superposition and entanglement, Ω_a^{meso}, expressed in (7.36), for the quantum case, is a complicated function of the occupation probabilities.

At the mesoscopic scale, we regard each of the occupancy probabilities, f_α, as a continuous variable. The basic approach is that Ω_a is a continuous and differentiable function of the occupation variables. With this understanding, using the chain rule, we can write the collision term (11.14) as follows

$$\Omega_a^{\mathrm{meso}}(|\Psi\rangle) = \delta\Omega_a^{\mathrm{meso}} = \sum_{b=1}^{B} \left.\frac{\partial\Omega_a^{\mathrm{meso}}}{\partial f_b}\right|_{f_*=d} \delta f_b + \mathcal{O}(\delta f^2). \tag{11.16}$$

The asterisk symbol used as a subscripted index on the occupation probability, as f_*, denotes the dependence on all the possible values of the index. Using (11.13) and (11.16), we can

write the quantum Boltzmann equation (7.12) in linearized form

$$\delta f_a(\vec{x} + \ell_s \hat{e}_a, t + \tau) = \delta f_a(\vec{x}, t) + J_{ab} \delta f_b(\vec{r}, t), \tag{11.17}$$

where the *Jacobian of the collision term* is defined as

$$J_{ab} \equiv \left. \frac{\partial \Omega_a^{\text{meso}}}{\partial f_b} \right|_{f_* = d}. \tag{11.18}$$

Let $\tilde{f}_a(\vec{k}, \omega)$ denote the discrete Fourier transform of the occupation probability $f_a(\vec{x}, t)$ (see Appendix H.1). Then taking the discrete Fourier transform of the linearized Boltzmann equation (11.17) we obtain the following characteristic equation

$$e^{i(\ell_s \hat{e}_a \cdot \vec{k} + \omega\tau)} \delta \tilde{f}_a(\vec{k}, \omega) = \delta \tilde{f}_a(\vec{k}, \omega) + J_{ab} \delta \tilde{f}_b(\vec{k}, \omega), \tag{11.19}$$

which we rewrite as

$$\left[\left(e^{i(\ell_s \hat{e}_a \cdot \vec{k} + \omega\tau)} - 1 \right) \delta_{ab} - J_{ab} \right] \delta \tilde{f}_b(\vec{k}, \omega) = 0. \tag{11.20}$$

Therefore, we have the following matrix equation

$$\mathbf{M} \; \delta \tilde{\mathbf{f}} = 0, \tag{11.21}$$

where $\tilde{\delta}\mathbf{f} = (\tilde{\delta} f_0, \tilde{\delta} f_1, \ldots, \tilde{\delta} f_{B-1})$ and the components of the square matrix $\mathbf{M}$ are

$$M_{ab} \equiv \left(e^{i(\ell_s \hat{e}_a \cdot \vec{k} + \omega\tau)} - 1 \right) \delta_{ab} - J_{ab}. \tag{11.22}$$

Solving (11.21) gives us the dispersion relations for the system obeying what is called *generalized hydrodynamics*. The generalized hydrodynamics for classical lattice-gas systems have been previously worked out [Das et al., 1993, Grosfils et al., 1993]. The development given here for the quantum lattice-gas system follows Das and Ernst's treatment of a classical lattice-gas system [Das et al., 1993]. However, in the present treatment, I do not use differential point form notation for mesoscopic fields (since technically this is unwarranted and allowed only in the continuum limit). Instead, to be absolutely rigorous, I have applied the discrete Fourier transform to the mesoscopic field to obtain (11.21) and (11.22). So, up to this point in the analytical treatment, I have not invoked the continuum limit.

11.4.2 Dispersion relations

To solve (11.21) for the dispersion relation $\omega = \omega(\vec{k})$, we must find the B roots of the secular determinant of the matrix $\mathbf{M}$ [Das et al., 1993, Grosfils et al., 1993]. In general, there are

two types of long wavelength excitations ($\vec{k} \to 0$), and they are called *hard kinetic modes* and *soft hydrodynamic modes*.

In the long-wavelength limit, the kinetic modes are nonvanishing at first order. The kinetic modes decay rapidly in the lattice-gas system because of a positive imaginary part in the eigenvalue spectrum of ω, ($\mathrm{Im}(\omega) > 0$), at $k = 0$. In contrast, the soft hydrodynamic modes decay over a long-time scale. They are associated with eigenvalues that vanish in the long-wavelength limit, ($\mathrm{Im}(\omega) = 0$), at $k = 0$. These vanishing eigenvalues in turn are associated with the conserved quantities in the lattice-gas system.

In the long-wavelength limit, $k \sim 0$, the dispersion relation for the 1D3Px lattice-gas corresponds to a damped sound mode

$$\omega(\vec{k}) = \pm c_s k + i\Gamma(\rho)k^2. \tag{11.23}$$

The real part of ω is linear in the wave number. Since $\mathrm{Re}(\omega)$ is linear in the wave number, the sound mode excitation propagates at the sound velocity corresponding to the slope, which is denoted here by c_s. Furthermore, the sound mode is damped in the *viscous hydrodynamic regime* characterized by diffusive ordering where the dispersion relation is parabolic in wavenumber, $\mathrm{Im}(\omega) \sim \mathcal{O}(k^2)$. In general, in a single-speed lattice gas, the decay of the hydrodynamic modes depends on shear viscosity and sound damping (there is no mode related to bulk viscosity).

11.4.3 Criterion for deviations from local equilibria

At local equilibrium, we assume that the occupancies of the local states at each site in the system are isotropic. This is called the *subsonic limit*. A stronger definition of the subsonic limit is when the fractional variation of the occupancy probabilities, $|\delta f_a|/f_a^{\mathrm{eq}}$, at all lattice sites, are assumed to be uniformly distributed along all the momentum directions, $1 \le a \le B$. Hence, the criterion for a fractional mass density variation on the order of the Knudsen number, can be expressed as[5]

$$\frac{|\delta f_a|}{f_a^{\mathrm{eq}}} \sim \frac{\lambda}{BL}. \tag{11.24}$$

The maximum size of the simulation volume is limited by the amount of physical computational resources available. In a microscopic quantum lattice-gas simulation, the occupation

[5] Suppose, as a concrete example, that an initial nonequilibrium state of the system is chosen with a characteristic feature size on the order of say one hundred lattice grid units, $L \sim 100\ell$. Next, suppose the mean-free path length is on the order of the size of a single primitive lattice cell, $\lambda \sim \ell$. If the fractional mass density variation, which must be on the order of the Knudsen number is $\frac{\delta\rho}{\rho} \sim \frac{\lambda}{L} \sim 0.01$, then the lattice gas would accurately model the dynamical fluid behavior in the regime of incompressible viscous hydrodynamics. Continuing the example, if $B = 6$ then $|\delta f_a|/f_a^{\mathrm{eq}} \sim 0.002$.

probabilities, f_a, must be determined by either partitioning the maximum size simulation into ensemble realizations or coarse-grain blocks. Let us, for the moment, revisit the subject of averaging over the microscopic quantities to obtain the mesoscopic values. There are more details to discuss.

In ensemble averaging, many realizations of the quantum lattice-gas system, which are identical at the macroscopic scale, are computed independently. Measurements are separately made from each realization, and all the resulting measurements are then averaged. For example, the state of the α^{th} qubit is measured for each copy of the system, which results in a series of 1's and 0's, and the average value is an estimate of f_α. In coarse-grain averaging, one measures the occupancy of all the local states, occupied by a particle with momentum $mc\hat{e}_a$, at all the sites within a spacetime block of a large microscopic system. Again, this results in a series of 1's and 0's, which are then averaged to estimate $f_a(\vec{X}, T)$, where $\vec{X}$ and T denote the coordinates of the centroid of a spacetime block within the superlattice.

In either case, whether ensemble or coarse-grain averaging is employed, all the available computational resources are expended. However, the numerical results can be quite different, for two reasons: because lattice-gas systems obey diffusive ordering and because of renormalization effects arising from particle-particle correlations.

Let us first consider the consequences of diffusive ordering. If one doubles the system size, $L \to 2L$, one must quadruple the simulation time, $T \to 4T$, to evolve to a macroscopic state similar to the one obtained by running a simulation of size L for time T. Consequently, if the fixed amount of computational resource is partitioned to do ensemble averaging, then many "small" systems are simulated which "rapidly" relax towards steady-state equilibrium. If the fixed amount of computation resource is partitioned to do coarse-grain averaging, then one "large" system is simulated which "slowly" relaxes towards steady state. Therefore, estimates can be made more quickly using ensemble averaging, but only in those situations were particle-particle correlations can be neglected.

This brings us to the issue of renormalization. In a large system simulation, there is sufficient time for many particle collision events to occur allowing the particle occupancies to become correlated. These particle-particle correlations, in certain situations, may have an appreciable effect on the value of the transport coefficients [Boghosian, 1995]. One enumerates all *connected diagrams* corresponding to the pathways by which outgoing particles, initially correlated by a collision, move through the system, interact with other particles, and eventually return as incoming particles to a final collision event. Each connected diagram corresponds to a term in an asymptotic series expansion of the collision operator, which is summed to give a *renormalized* collision operator. If the ultimate aim of is to estimate a transport coefficient, which strongly depends on particle-particle correlations, then

coarse-graining averaging must be used [Bussemaker et al., 1995, Boghosian, 1995].

In either case, it is necessary to satisfy the criterion that $(\delta f_a / f_a^{\mathrm{eq}}) \sim \mathcal{O}(\mathrm{Kn})$ or smaller for all a. If this criterion is satisfied, the linearized quantum Boltzmann equation (11.17) can accurately describe Navier-Stokes hydrodynamics. This is a stronger requirement then $\frac{\delta\rho}{\rho} \sim \mathcal{O}(\mathrm{Kn})$. The requirement that $(\delta f_a / f_a^{\mathrm{eq}}) \sim \mathcal{O}(\mathrm{Kn})$ for viscous hydrodynamics (or the more stringent requirement that $(\delta f_a / f_a^{\mathrm{eq}}) \sim \mathcal{O}(\mathrm{Kn}^2)$ for incompressible viscous hydrodynamics) implies a lower bound for the number of states used in an ensemble average or for the minimum size of the spacetime block used in a coarse-grain average. All these considerations, usually applied to classical lattice-gas simulation, are also relevant to quantum lattice-gas simulations.

11.5 Macroscopic scale

11.5.1 Eigensystem of the linearized collision operator

In the long wavelength ($\vec{k} \to 0$) limit, the characteristic equation (11.20) reduces to the simple form

$$[(e^{\omega\tau} - 1)\mathbf{1} - \mathbf{J}] \;\; \delta\tilde{\mathbf{f}} = 0. \tag{11.25}$$

Expanding to first order in Sh (second order in ε) this becomes the eigenvalue equation

$$\mathbf{J} \;\; \delta\tilde{\mathbf{f}} = \omega\tau\delta\tilde{\mathbf{f}} + \mathcal{O}(\varepsilon^3). \tag{11.26}$$

Therefore, in the long-wavelength and low-frequency limits, the eigenvalues of J determine possible values for ω and in turn the hydrodynamic and kinetic behavior of the lattice-gas system. This eigenvalue problem is analytically solvable, without the need for any numerical treatment as is needed for finding the $\vec{k}$-dependent roots of the secular determinant of the matrix M in (11.22).

Consider the following eigenvalue equation

$$J_{ab}\xi_b^\alpha = \kappa_\alpha \xi_a^\alpha, \tag{11.27}$$

with eigenvectors ξ^α and eigenvalues κ_α, where $\alpha = 1, \ldots, B$.

The problem is simplified if J is circulant [Wolfram, 1986]. The components of J can be specified by the difference of the indices, $J_{ab} = J_{a-b}$. Hence, we make the ansatz that the eigenvectors ξ^α have the following form

$$\xi_a^\alpha = e^{2\pi i a\alpha/B}. \tag{11.28}$$

Then inserting (11.28) into (11.27) and taking $m = a - b$, gives a solution for the eigenvalues

$$\kappa_\alpha = \sum_{m=1}^{B} J_m e^{2\pi i m\alpha/B}. \tag{11.29}$$

Let us see why there will be as many zero eigenvalues as there are conserved quantities in the lattice gas dynamics. For convenience, we will use ket notation where $|\alpha\rangle \equiv (\xi_1^\alpha, \xi_2^\alpha, \ldots, \xi_B^\alpha)$ and $|\delta\tilde{f}\rangle \equiv (\delta\tilde{f}_1, \delta\tilde{f}_2, \ldots, \delta\tilde{f}_B)$. We can write J as follows

$$J = \sum_{\alpha=1}^{B} \kappa_\alpha |\alpha\rangle\langle\alpha|, \tag{11.30}$$

so (11.26) becomes

$$\sum_{\alpha=1}^{B} \kappa_\alpha |\alpha\rangle\langle\alpha|\delta\tilde{f}\rangle = \omega\tau|\delta\tilde{f}\rangle. \tag{11.31}$$

All the scalars $\langle\alpha|\delta\tilde{f}^{(1)}\rangle$ for which $\kappa_\alpha = 0$ have no effect on the dynamics since $J|\delta\tilde{f}\rangle = 0$ and so correspond to the conserved quantities of the system. The set of eigenvectors with degenerate eigenvalue of zero span what is called the *hydrodynamic space*, which I denote by $\mathcal{H}$. The remaining set of eigenvectors (with nonzero eigenvalues) span what is called the *kinetic space*, which I denote as $\mathcal{K}$. Therefore J can be explicitly written as a linear combination over eigenvectors in the kinetic space

$$J = \sum_{\alpha\in\mathcal{K}} \kappa_\alpha |\alpha\rangle\langle\alpha|. \tag{11.32}$$

In an athermal system, there are $1 + D$ conserved quantities, the mass plus the momentum for each dimension of the space. So $\mathcal{H}$ is a $D + 1$ dimensional space and $\mathcal{K}$ is a $B - D - 1$ dimensional space. Let us denote the kinetic eigenkets as follows, $|D + 2\rangle, |D + 3\rangle, \ldots, |B\rangle$, which span the kinetic subspace $\mathcal{K}$. Then, the generalized inverse of J is defined over $\mathcal{K}$ as follows

$$J^{-1} = \underbrace{(|D+2\rangle\ |D+3\rangle \cdots |B\rangle)}_{B\times K \text{ matrix}} \underbrace{\begin{pmatrix} \frac{1}{\kappa_{D+2}} & 0 & \cdots & 0 \\ 0 & \frac{1}{\kappa_{D+3}} & \cdots & 0 \\ \vdots & & \ddots & \\ 0 & \cdots & & \frac{1}{\kappa_B} \end{pmatrix}}_{K\times K \text{ matrix}} \underbrace{\begin{pmatrix} \langle D+2| \\ \langle D+3| \\ \vdots \\ \langle B| \end{pmatrix}}_{K\times B \text{ matrix}}. \tag{11.33}$$

From (11.33), it follows by construction that

$$J^{-1}|\alpha\rangle = \frac{1}{\kappa_\alpha}|\alpha\rangle, \tag{11.34}$$

for $|\alpha\rangle \in \mathcal{K}$.

Within $\mathcal{K}$ there exists the *viscous subspace*, $\mathcal{V} \subset \mathcal{K}$ characterized by the degenerate eigenvalue κ_η. Because the collisional process is invariant under the finite point-group symmetries of the Bravais lattice, there is a lack of preference in direction for momentum diffusion in the system. That is, the system does not make diffusion any easier in one direction rather than another. Hence, there is a subspace of $\mathcal{K}$ characterized a degenerate eigenvalue which contributes positively to the shear and bulk viscosities.

A ket $|e_i e_j\rangle$ may be formed from the dyadic product $e_{ai} e_{aj}$. The ket $|\ e_i e_j\rangle$ resides in $\mathcal{V}$. Hence, it is an eigenket of the generalized inverse of the Jacobian of the collision operator, J^{-1}, and has eigenvalue $\frac{1}{\kappa_\eta}$. That is, for a hydrodynamic lattice-gas fluid

$$J^{-1}|e_i e_j\rangle = \frac{1}{\kappa_\eta}|e_i e_j\rangle. \tag{11.35}$$

The identity (11.35) will be needed in the following section.

11.5.2 Chapman-Enskog expansion

The characteristic equation (11.20) of the linearized quantum Boltzmann equation

$$\left[\left(e^{\ell_s \hat{e}_a \cdot \vec{k} + \omega\tau} - 1\right)\delta_{ab} - J_{ab}\right]\delta\tilde{f}_b(\vec{k},\omega) = 0$$

is an approximate description of the mesoscopic particle dynamics since the collision term on the R.H.S. has been expanded to first order about the equilibrium value of the occupation probability. In this approximation, the collision term, J_{ab}, acts as a linear operator on the local configuration $\delta\mathbf{f}$. I would now like to expand the L.H.S. of this characteristic equation. To do so, let us use ε as a small expansion parameter, $\varepsilon \ll 1$. In the viscous hydrodynamic regime, this expansion parameter is the Knudsen number, $\mathrm{Kn} \simeq \hat{e}_a \cdot \vec{k} = \ell_s|k| \sim \varepsilon$. And, because of diffusive ordering, the Strouhal number is $\mathrm{Sh} \simeq \omega\tau \sim \varepsilon^2$. We expect (11.20) is an appropriate description of the mesoscopic dynamics so long as the nonequilibrium occupation probabilities are close enough to their equilibrium values so that the action of the linearized collision term, J_{ab}, is sufficient to cause any such nonequilibrium configuration to relax back to an equilibrium configuration.

Begin by expanding (11.20) to first order in ε

$$(i\ell_s \hat{e}_a \cdot \vec{k}\delta_{ab} - J_{ab})\delta\tilde{f}_b \simeq 0. \tag{11.36}$$

The essential ansatz is that the deviations, $\delta\tilde{f}_a$, of the occupation probability can be expanded in powers of ε

$$\delta\tilde{f}_a = \delta\tilde{f}_a^{(0)} + \delta\tilde{f}_a^{(1)} + \mathcal{O}(\varepsilon^2), \tag{11.37}$$

where $\delta\tilde{f}_a^{(0)} \sim \varepsilon$ and $\delta\tilde{f}_a^{(1)} \sim \varepsilon^2$. The superscript on $\delta\tilde{f}^{(0)}$ denotes that it is a deviation from the steady-state equilibrium d due to bulk motion of the fluid. The superscript on $\delta\tilde{f}^{(1)}$ denotes that it is a deviation due to spatial gradients in the bulk profile. We require that the largest Mach number at any point in the system must be small, $\mathrm{M} \ll 1$, that $\delta\tilde{f}^{(0)} \sim M \sim \varepsilon$. We can insert (11.37) into the first order ε-expansion of the characteristic equation (11.36). $J_{ab}\delta\tilde{f}_b^{(0)} = 0$, and we equate the two $\mathcal{O}(\varepsilon^2)$ terms

$$i\ell_s \hat{e}_a \cdot \vec{k}\delta\tilde{f}_a^{(0)} = J_{ab}\delta\tilde{f}_b^{(1)}. \tag{11.38}$$

Since J has a well-defined generalized inverse, we can invert the Jacobian matrix according to (11.33) to solve for the second order correction to the occupation probability

$$\delta\tilde{f}^{(1)} = i\ell_s J_{ab}^{-1}\hat{e}_b \cdot \vec{k}\delta\tilde{f}_b^{(0)}. \tag{11.39}$$

Therefore, using the basic approach of the Chapman-Enskog expansion (11.37), we have the result that

$$\delta\tilde{f}_a = [\delta_{ab} + i\ell_s J_{ab}^{-1}\hat{e}_b \cdot \vec{k}]\delta\tilde{f}_b^{(0)} + \mathcal{O}(\varepsilon^3). \tag{11.40}$$

In the continuum limit, we are justified in taking the inverse Fourier transform of (11.40), which gives the fluctuating part of the non-equilibrium probability occupancy in differential point form

$$\delta f_a(\vec{x}, t) = [\delta_{ab} + \ell_s J_{ab}^{-1}\hat{e}_b \cdot \nabla]\delta f_b^{(0)}(\vec{x}, t) + \mathcal{O}(\varepsilon^3). \tag{11.41}$$

Then using (11.13), the probability of occupancy in the continuum limit is

$$f_a(\vec{x}, t) = [\delta_{ab} + \ell_s J_{ab}^{-1}\hat{e}_b \cdot \nabla]f_b^{(0)}(\vec{x}, t) + \mathcal{O}(\varepsilon^3). \tag{11.42}$$

Assuming a Fermi-Dirac form for the occupation probability in accordance with Section 2.5, we insert the Mach number expansion (I.20) from Appendix I into (11.42). After some algebraic manipulation, the result is

$$f_a = d[1 + \frac{D}{c}e_{ai}v_i + g\frac{D(D+2)}{2c^2}Q_{aij}v_i v_j + \tau D J_{ab}^{-1}e_{bi}e_{bj}\partial_i v_j] + \mathcal{O}(M^3), \tag{11.43}$$

where d is the background density, D is the number of spatial dimensions, c is the unit propagation speed of particle on the lattice, v_i is the macroscopic velocity, g is a Galilean pre-factor, $Q_{aij} = e_{ai}e_{aj} - \delta_{ij}/D$ is a traceless second-rank tensor, M is the Mach number. Using the identity (11.35), that $J_{ab}^{-1}e_{bi}e_{bj} = \frac{1}{\kappa_\eta}e_{ai}e_{aj}$, (11.43) becomes

$$f_a = d[1 + \frac{D}{c}e_{ai}v_i + g\frac{D(D+2)}{2c^2}Q_{aij}v_i v_j - \frac{\tau D}{\kappa_\eta}e_{ai}e_{aj}\partial_i v_j] + \mathcal{O}(M^3). \tag{11.44}$$

The approximation (11.44) is a good one provided several conditions are met:

1. the ratio of the superlattice cell size to the characteristic scale length of the small hydrodynamics fluctuation is close to zero, $\frac{\ell_s}{L} \sim 0$ (satisfied in the continuum limit)

2. the angular distribution of particles along momentum directions is close to an isotropic one

3. the flow is subsonic ($\mathrm{M} \ll 1$)

4. spatial gradients are small ($\mathrm{Kn} \sim 0$ and $\frac{\delta\rho}{\rho}$ is small).

11.5.3 Derivation of the continuum equations

The derivation of the continuum equations of motion at the macroscopic scale is carried out in this section. The method of derivation is outlined by these following few steps:

1. Expand the quantum Boltzmann equation (7.12) to first order in time and second order in space [6].

2. In the continuum limit, calculate the first and second moments of the quantum Boltzmann equation [7].

3. Insert the mesoscopic occupancy probability given by (11.44) into the moment equations obtained in Step 2.

After some algebraic manipulations, we obtain an approximation of the equations of motion that serve as an effective field theory at the macroscopic scale. Because of diffusive ordering, the result is that the macroscopic equations of motion are a set of coupled parabolic partial differential equations. In the present derivation, I do not give a multi-scale analysis such as the one carried out by Frisch *et al.* [Frisch et al., 1987] in their treatment of 2 and 3 dimensional lattice-gas hydrodynamics. This omission is justified because only a single time-scale is needed for most lattice-gas systems since the transport coefficients are very large. That is, there is little or no separation between the short time scale associated with sound mode excitations and the longer time scale associated with viscous mode excitations arising from momentum diffusion. Viscous damping in lattice-gas fluids is observed over relatively short-time scales and therefore significantly affects, and is mixed in with, sound wave propagation and convection. Nevertheless, at the end of this section, I will divide the

[6] Only a first order time derivative is needed because of the long-time scales associated with viscous damping. Time and spatial scales are related parabolically ($T \sim L^2$ or $\varepsilon^2 \sim \delta x^2 \sim \delta t$) in lattice-gas systems.

[7] This is done because for each additive conserved quantity of the dynamics, a macroscopic field is expressed as a moment of the mesoscopic field of probability of occupancies. In the present case, ρ and $\vec{v}$ are expressed in terms of the f_a's according (7.5) and (7.7).

effective field theory into two sets of equations that apply at short and long time scales, respectively.

We determine the macroscopic equations of motion using the quantum Boltzmann equation (7.27) of Section 7.5

$$\frac{df_a}{dt} = \lim_{\substack{\tau\to 0\\ \ell_s\to 0}} \frac{\Omega_a^{\rm meso}}{\tau}. \tag{11.45}$$

In consideration of diffusive ordering, we expand the L.H.S. of this equation to first-order in time and second-order in space

$$\frac{\partial f_a}{\partial t} + c\hat{e}_a\cdot\nabla f_a + \frac{\ell_s^2}{2\tau}(\hat{e}_a\cdot\nabla)^2 f_a + \mathcal{O}({\rm Kn}^3,{\rm Sh}^2) = \lim_{\substack{\tau\to 0\\ \ell_s\to 0}} \frac{\Omega_a^{\rm meso}}{\tau}. \tag{11.46}$$

This is the *quantum lattice-Boltzmann equation*, where $\Omega_a^{\rm meso}$ is defined by (7.13). Since $\sum_a \Omega_a^{\rm meso} = 0$, the zeroth moment of (11.46) is

$$\begin{aligned}&\partial_t\left(m\sum_a f_a\right) + \partial_i\left(mc\sum_a e_{ai} f_a\right)\\ &+\frac{\ell_s^2}{2\tau}\partial_i\partial_j\left(\sum_a e_{ai}e_{aj}f_a\right) + \mathcal{O}({\rm Kn}^3,{\rm Sh}^2) = 0.\end{aligned} \tag{11.47}$$

Using the identities (J.11) from Appendix J, the corrected occupancy probability (11.44), along with definitions for the mass density (7.5) and momentum density (7.7), this reduces to a mass continuity equation in the long-wavelength, low-frequency, and subsonic limits

$$\partial_t\rho + \partial_i(\rho v_i) + \mathcal{O}({\rm Kn}^3,{\rm Sh}^2,{\rm M}^3) = 0. \tag{11.48}$$

Since $\sum_a e_{ai}\Omega_a^{\rm meso} = 0$ too, the first moment of (11.46) is

$$\begin{aligned}&\partial_t\left(mc\sum_a e_{ai} f_a\right) + \partial_j\left(mc^2\sum_a e_{ai}e_{aj}f_a\right)\\ &+\frac{\ell_s^2}{2\tau}\partial_j\partial_k\left(mc\sum_a e_{ai}e_{aj}e_{ak}f_a\right) + \mathcal{O}({\rm Kn}^3,{\rm Sh}^2) = 0.\end{aligned} \tag{11.49}$$

This reduces to Euler's equation in the long-wavelength, low-frequency, and subsonic limits

$$\partial_t(\rho v_i) + \partial_j\Pi_{ij} + \mathcal{O}({\rm Kn}^3,{\rm Sh}^2,{\rm M}^3) = 0, \tag{11.50}$$

where the momentum flux density is

$$\Pi_{ij} = P_{ij} + g\rho v_i v_j - \frac{\rho\ell_s^2}{(D+2)\tau\kappa_\eta}\partial_j v_i + \frac{\ell_s^2}{2\tau}\frac{\rho}{(D+2)}\partial_j v_i \tag{11.51}$$

or

$$\Pi_{ij} = P_{ij} + g\rho v_i v_j - \frac{\rho \ell_s^2}{(D+2)\tau}(\frac{1}{\kappa_\eta} - \frac{1}{2})\partial_j v_i. \tag{11.52}$$

The shift of $-\frac{1}{2}$ is a constant negative contribution to the shear viscosity by a lattice effect. With sound speed $c_s \equiv \frac{\ell_s}{\tau\sqrt{D}}$, identify the isotropic pressure tensor as

$$P_{ij} = \rho c_s^2 \left(1 - g\frac{v^2}{c^2}\frac{\ell^2}{\ell_s^2}\right)\delta_{ij}. \tag{11.53}$$

Finally, inserting (11.52) into Euler's equation (11.50), the momentum equation for viscous flow is

$$\begin{aligned} &\partial_t(\rho v_i) + \partial_j(g\rho v_i v_j) + \mathcal{O}(\mathrm{Kn}^3, \mathrm{Sh}^2, \mathrm{M}^3) = \\ &-\partial_i P + \eta\partial^2 v_i + \left(\zeta + \frac{\eta}{D}\right)\partial_i\partial_j v_j. \end{aligned} \tag{11.54}$$

with shear viscosity

$$\eta = \frac{\rho\ell_s^2}{\tau}\frac{1}{D+2}\left(\frac{1}{\kappa_\eta} - \frac{1}{2}\right), \tag{11.55}$$

and bulk viscosity

$$\zeta = \frac{\rho\ell_s^2}{\tau}\frac{2D-1}{D(D+2)}\left(\frac{1}{\kappa_\eta} - \frac{1}{2}\right). \tag{11.56}$$

With small Knudsen, Strouhal, and Mach numbers, the momentum equation (11.54) approximates the Navier-Stokes equation (11.4) except that there is an extra density-dependent factor, $g(d)$, in the convective term in (11.54). If g is not unity, the effective field theory is not Galilean invariant. For computational fluid dynamics modeling applications, it would be advantageous to alter the collision term in the quantum Boltzmann equation so that $g = 1$. In a classical setting, this was done by H. Chen, S. Chen, and Mattaeus in 1992 [Chen et al, 1992], but their approach violated detailed balance, and consequently the algorithm is subject to unphysical numerical instabilities. Unconditionally numerically stable lattice-gas methods that obey the principle of detailed balance gave been found to set $g = 1$ [Texiera, 1992, Boghosian et al., 1997] and these kinds of techniques may be adapted to our quantum mechanical construction.

For fluidic systems with low viscosity [Dubrulle et al., 1991], it is appropriate to consider two separate effective field theories for short-time and long-time hydrodynamic behavior. The short and long hydrodynamic time scales are denoted by t_1 and t_2, respectively. A multi-scale formalism is used where $\partial_t \longrightarrow \partial_{t_1} + \partial_{t_2}$ [Frisch et al., 1987]. Then the effective field theory defined by the continuity equation (11.48) and the Navier-Stokes equation (11.50) reduces at the short-time hydrodynamic scale to the following set

$$\partial_{t_1}\rho + \partial_i(\rho v_i) = 0 \tag{11.57}$$

$$\partial_{t_1}(\rho v_i) = -\partial_j P \tag{11.58}$$

at the short-time hydrodynamic scale. This set models sound wave propagation induced by pressure gradients in a compressible fluid. At the long-time hydrodynamics scale, (11.48) and (11.50) reduce to

$$\partial_{t_2}\rho = 0 \tag{11.59}$$

$$\partial_{t_2}(\rho v_i) + \partial_j(g\rho v_i v_j) = \eta\partial^2 v_i + \left(\zeta + \frac{\eta}{D}\right)\partial_i\partial_j v_j. \tag{11.60}$$

This set of equations describes viscous damping and convection in the incompressible fluid limit.

11.6 Quantum efficiency

We consider the algorithmic complexity required to numerically model fluids at a sufficiently high resolution to capture the smallest scale for which the dynamics is physically relevant. For both classical and the quantum mechanical methods, we shall estimate the algorithmic complexity of numerically modeling fluidic behavior at the macroscopic scale as a function of Re.

We consider two cases: the one-dimensional Burgers equation, and the three-dimensional Navier-Stokes equation. The scaling arguments are different in each case and lead to different results, but in both cases there exists a significant quantum computational speedup.

11.6.1 Ensemble size, grid size, and time steps estimate

Multiplying (9.1) by u and integrating over all space, with periodic boundaries, gives a relation for energy conservation where the time rate of change of the turbulent kinetic energy density $\partial_t(\frac{u^2}{2})$ is balanced by the viscous dissipation $\varepsilon \equiv \nu\left(\frac{\partial u}{\partial x}\right)^2 \sim \frac{u_\circ^3}{\mathcal{L}}$, where $\mathcal{L}$ is the characteristic scale of the largest feature in the flow field and $u_\circ$ is the standard deviation of the turbulent kinetic energy or eddy velocity at that scale.

The flow velocity, the kinematic viscosity, and the viscous dissipation quantities have the dimensions: $[u] = \frac{L}{T}$, $[\nu] = \frac{L^2}{T}$, and $[\varepsilon] = \frac{L^2}{T^3}$. The dissipation scale $\lambda \equiv \left(\frac{\nu^3}{\varepsilon}\right)^{\frac{1}{4}}$ is the smallest spatial scale where macroscopic effective field theory (9.52) is physically applicable and the smallest physical velocity at the dissipation scale is the *dissipation-scale velocity* $u_\lambda \equiv (\nu\varepsilon)^{\frac{1}{4}} = \frac{\nu}{\lambda}$.

The Reynolds number characterizing the fluid's nonlinearity is

$$\mathrm{Re} \equiv \frac{\mathcal{L}}{\lambda}\frac{u_\circ}{u_\lambda} = \frac{\mathcal{L}u_\circ}{\nu}, \tag{11.61}$$

and using $\varepsilon = \frac{u_o^3}{\mathcal{L}}$ to eliminate $\mathcal{L}$, we also have

$$\mathrm{Re} = \frac{u_o^4}{\nu\varepsilon} = \left(\frac{u_o^2}{u_\lambda^2}\right)^2 = \left(\frac{\mathcal{L}}{\lambda}\right)^{\frac{4}{3}}. \tag{11.62}$$

We can estimate the ensemble size N by determining the physical limits of the quantity $|\delta p_\pm|$. Since the occupation probabilities are measured by ensemble averaging over N independent microscopic realizations, $|\delta p_\pm| \simeq \frac{1}{\sqrt{N}}$, which is due to stochastic quantum mechanical projective measurement. Following Orszag and Yakhot [Orszag and Yakhot, 1986], the value of the statistical fluctuation $\delta u(x,t)$ of the numerical flow field must be much much less than $u_\lambda(x,t)$ of the macroscopic effective field theory (9.1). Using the assumption of convective ordering, $\Delta x\ u_o \sim \Delta t$, we have $u_\lambda \gg u_o(\delta a + \delta b) \sim \frac{u_o}{\sqrt{N}}$. Hence, using (11.62), the required ensemble size is

$$N \gg \frac{u_o^2}{u_\lambda^2} \sim \mathrm{Re}^{\frac{1}{2}}. \tag{11.63}$$

THE BURGERS EQUATION

In the case of the Burgers equation, the smallest spatial scale is the width of a shock front, denoted here as $\Delta\mathcal{L}$. Taking the potential solution $u = \partial_x h$, then (9.1) becomes the Kardar-Parisi-Zhang (KPZ) equation $\partial_t h + \frac{1}{2}(\partial_x)^2 = \nu\partial_{xx}h$. Taking the Cole-Hopf logarithmic solution $h = -2\nu \ln\psi$, then the KPZ equation becomes the diffusion equation $\partial_t\psi = \nu\partial_{xx}\psi$ with the analytical solution:

$$\psi = \sum_{\ell=0}^{\infty} \left(a_\ell \sin k_\ell x + b_\ell \cos k_\ell x\right) e^{-\nu k_\ell^2 t}, \tag{11.64}$$

where the wave number is $k_\ell \equiv \ell\frac{2\pi}{\mathcal{L}}$. The shock front is resolved by all modes corresponding to wave numbers for which the damping constant νk_ℓ^2 is small. Therefore, over the characteristic time $t \sim \frac{\mathcal{L}}{u_o}$, the critical condition for the width of the shock front becomes: $\nu\left(\frac{2\pi}{\Delta\mathcal{L}}\right)^2 \frac{\mathcal{L}}{u_o} \sim 1$, and hence $\Delta\mathcal{L} \sim \sqrt{\frac{\nu\mathcal{L}}{u_o}}$. Now according to (11.61), the Reynolds number scales inversely to the kinematic viscosity, so we obtain the result $\Delta\mathcal{L} \sim \mathrm{Re}^{-\frac{1}{2}}\mathcal{L}$. Therefore, the number of grid points N_x required to resolve this smallest feature of the flow then goes as

$$N_x \equiv \frac{\mathcal{L}}{\Delta\mathcal{L}} \sim \mathrm{Re}^{\frac{1}{2}}. \tag{11.65}$$

THE NAVIER-STOKES EQUATION

Using (11.62), we know that the number of grid points N_x to sufficiently resolve a turbulent flow field down to the dissipation scale is

$$N_x \equiv \frac{\mathcal{L}}{\lambda} = \mathrm{Re}^{\frac{3}{4}}. \tag{11.66}$$

Diffusive Ordering

In the case of the diffusive ordering, characteristic of parabolic differential equations such as the Burgers and Navier-Stokes equation, the relation between the lattice cell size and the update time is $\Delta x^2 \sim \nu \Delta t$. Hence, using (11.61), the lattice grid size N_x and the number of time steps N_t are related as follows:

$$N_t \sim \frac{1}{\mathrm{Re}} N_x^2. \tag{11.67}$$

We combine the results for the two cases (11.65) and (11.66) as follows:

$$N_x \sim \mathrm{Re}^{\beta} \tag{11.68}$$

where $\beta = \frac{1}{2}$ for the Burgers equation and $\beta = \frac{3}{4}$ for the Navier-Stokes equation. Inserting (11.68) into (11.67), we have

$$N_t \sim \mathrm{Re}^{2\beta - 1} \tag{11.69}$$

Convective ordering

In the case of convective ordering, the relation between the lattice cell size and the update time is a linear one $\Delta x \sim u_{\circ} \Delta t$. Hence, the lattice grid size and the number of time steps are equal: $N_t \sim N_x$, so in this case $N_t \sim \mathrm{Re}^{\beta}$.

11.6.2 Algorithmic complexity

Classical case

The total algorithmic complexity of computation of a unit of physical time of the classical lattice-gas model is the product of the ensemble of size N, the number of interaction required to complete the numerical simulation N_t, the lattice grid size N_x, and local resources of size ϱ

$$C_{\mathrm{cl}} \equiv N N_t N_x^D \varrho, \tag{11.70}$$

where D is the spatial dimension. The quantity ϱ is the amount of resources needed to encode and evaluate the function for the local microscopic collisions.

For a fixed viscosity fluid model, inserting (11.63), (11.68), and (11.69) into (11.70), the classical algorithmic complexity becomes

$$C_{\mathrm{cl}} = \left(\mathrm{Re}^{\frac{1}{2}}\right)\left(\mathrm{Re}^{2\beta-1}\right)\left(\mathrm{Re}^{\beta D}\right)\rho = \rho \mathrm{Re}^{(D+2)\beta - \frac{1}{2}}. \tag{11.71}$$

Quantum mechanical case

There are three advantages of nano-scale quantum computing technology that significantly reduce the algorithmic complexity of computational fluid dynamics.

First, a crucial advantage comes from the quantum algorithmic approach itself where the fluid viscosity can be made arbitrarily small without inducing numerical instabilities and without any additional computational overhead. The kinematic viscosity is a freely tunable parameter. We cannot reduce the kinematic viscosity to zero because that would, in turn, require infinite lattice resolution to resolve the resulting infinitesimal features of the fluid. In a quantum model, we can however reduce the viscosity to the minimum value compatible with a given lattice grid size. Our basic approach is to set the viscosity as follows:

$$\nu \equiv \frac{\mathcal{L} u_\circ}{N_x^2}. \tag{11.72}$$

In this way, the number of time steps is always order unity $N_t \sim 1$ regardless of the grid size, so the algorithmic complexity becomes significantly lower than the fixed viscosity case.

Second, because of wave function collapse by Von Neumann projective measurement, ensemble averaging is required just as in the classical case. However, by using the nano-scale device technology to store and process information at extremely high densities approaching atomic liquid-state or solid-state densities using extremely short logic gate switching times, it becomes practical to physically build the mechanism for ensemble averaging directly into the "hardware" of the quantum computer. A proof-of-concept of this approach has been achieved using state-of-the-art spatial nuclear magnetic resonance spectroscopy [Pravia et al., 2002, Pravia et al., 2003]. Hence, the algorithmic complexity of ensemble averaging may be counted as order unity overhead: $N \sim 1$.

Third, because it is possible to exploit quantum entanglement within each node of the type-II quantum computer, the amount of required local resources needed to compute the nonlinear collision function goes as $\log_2 \varrho$, which is exponentially less than the required classical resources needed to compute the same function. Relating ϱ to the minimum number of bits per node needed to encode (**??**), our parsimonious quantum algorithm for the Burgers equation is a demonstration of quantum efficiency: (9.1) can be modeled classically with 3 bits per node whereas we prove only 2 qubits per node is required quantum mechanically. Furthermore, the evaluation of $\Omega_{\text{cl}}(a, b)$ requires 8 floating-point operations, whereas the evaluation of $\Omega_{\text{qu}}(a, b)$ requires only 1 quantum logic gate operation. Therefore, with the three advantages of tunable viscosity, inherent ensemble averaging, and localized quantum entanglement, the quantum mechanical algorithmic complexity is

$$C_{\text{qu}} \geq N_x^D \log_2 \varrho. \tag{11.73}$$

With a quantum computer, since we are modeling the time evolution of a classical system, the value of $u(x, t)$ must be known everywhere at every time step whence the need for continual measurement in any quantum mechanical computing device. Therefore, the

memory load factor for the lattice is still N_x^D in (11.73) and not $\log_2 N_x^D$ in the quantum case [Yepez, 2001c].

Inserting (11.68) into (11.73), we obtain the result:

$$C_{\text{qu}} = \text{Re}^{D\beta} \log_2 \varrho, \tag{11.74}$$

which represents a significant quantum speedup. In comprehensive fluid models capturing thermohydrodynamics, phase transitions, multi-species reaction processes, or magnetohydrodynamics, the quantity of qubits required per node is numbered in the hundreds. In these cases, classical algorithmic approaches become intractable while the quantum mechanical algorithmic approach is still practical in principle according to (11.74).

Chapter 12

Conclusion

12.1 Quantum information age

In the middle of last century, scientists had a veritable bonanza. They broke through barriers that seemed nearly insurmountable, including splitting the atom, supersonic flight, and breaking enemy codes. On July 16, 1945, the Office of Scientific Research and Development of the War Department reached a historical technology transition with a detonation of the first atomic bomb at the Trinity site in the desert of central New Mexico. On October 14, 1947, US Air Force Captain Chuck Yeager broke the sound barrier flying faster than the speed of sound in the bullet-like X-1, built by NASA and Bell Laboratories, producing the first man-made aerodynamic shock wave. On June 1, 1944, just 5 days before the Allied amphibious landing on the beaches of Normandy to emancipate Europe from the Nazis grip, the Colossus I went into operation just in time to crack the German 'Fish' material that confirmed Hilter swallowed the Allied deception plans to attack Pas-de-Calais instead.

Thus the atomic age, the age of supersonic rocket powered flight as a prelude to the space age, and the digital information age were borne. Today we are at the dawn of a new age, the *quantum information age*.

12.2 Technology transition

As we seek to make logical gates smaller and smaller, we are approaching the point in time where to one must abandon a classical or semi-classical physics approach in favor of a purely quantum mechanical one. For example, in 2002 Intel introduced a 90 nanometer lithography process on silicon dioxide for static random access memory embedded in the Itanium 64-bit word size processor, and in the year in 2003 Toshiba and Sony announced a 65 nanometer process. By 2004 a 25 nanometer process was invented, an authentic nanotechnology. Here the engineered bit, contained in a static random access memory cell, is so small that a single

stray cosmic ray such as an alpha particle impacting a memory cell will not only ionize that cell but also neighboring cells, potentially causing many bit-flip errors. That point in time when we are forced to abandon classical engineering technologies is the moment we hit the quantum barrier.

It is expensive to cross this barrier because new and untested quantum technologies must emerge from the tried and true basic science of quantum mechanics and progress to the status of a robust and easily reproducible engineering technology. Successfully crossing this barrier will not only represent the greatest technical transition in the Department of Defense but perhaps also the greatest technology in the history of the world to date. This classical to quantum technical transition will even surpass the historic tech-transitions of thermodynamics to the steam engine, and of optics, chemistry, and electronics, and condensed matter physics to the photolithographically integrated solid-state circuit. The scale of the scientific effort needed to surmount the quantum barrier can be easily underestimated, as is the importance of breaking through this barrier.

This technical transition will likely also be the most expensive one to date. The scale of the engineering effort of the quantum tech-transition needed to produce a state-of-the-art type II quantum computer could be comparable to, and actually may supersede, the scale of the effort that occurred during the Manhattan project during World War II[1].

During the Manhattan project the well developed basic science of atomic and nuclear physics, which by the way was substantially semi-classical physics, was transitioned to the military as a technology for nuclear bomb making. Similarly, today the well developed basic quantum mechanical science of atomic, nuclear, superconductive, optical, and condensed matter physics, all entailing full-fledged many-body quantum physics, will be transitioned in various incarnations as novel technologies for communication and then computation. This is a tall order.

12.3 Massive parallelism

One way to understand these analogous technical transitions, and in a way which is consistent with Moore's second law, is by considering the following imaginary scenario. Imagine we are displaced back in time from the present we again must contend with the seemingly indomitable Nazis. Imagine also that as a nation we in the United States lacked the resolve to tackle the monumental task of tech-transitioning nuclear physics to nuclear bomb making. Instead, suppose we took the more practical and familiar road. Therefore, instead of

[1]I presented this viewpoint in more detail in an invited talk on type II quantum computing at the 2002 Air Force Office of Scientific Research Computational Mathematics Meeting held at University of Florida Graduate Engineering and Research Center

developing the 4.5 ton Little Boy atomic bomb that the United States dropped on Hiroshima on the 6th of August 1945 which had the equivalent of 13,000 tons of trinitrotoluene (TNT) or the 5.15 ton Fat Man plutonium-implosion bomb dropped on Nagasaki three days later which had the equivalent of 20,000 tons of TNT, suppose in our fictitious scenario the United States followed a conventional-bomb program instead of the fateful nuclear-bomb program.

Figure 12.1: Large B-17 formation: This is a large B-17 formation from the Fifteenth Air Force, 463rd Bomb Group. The Flying Fortress in one of the most famous airplanes ever built. The B-17 prototype first flew on July 28, 1935. Few B-17's were in service on December 7, 1941, but production quickly accelerated. Production ended in May 1945 and totalled 12,726. They served in every WW II combat zone, but are best known for daylight strategic bombing of German industrial targets.

We could have deployed a large array of one thousand B-29 Super-fortresses, similar to the large arrays of B-17 Flying Fortresses shown in Figure 12.1. With each B-29 loaded with 10 tons of explosives, the entire array deployed as a single formation could have delivered a fierce 20,000 ton blast over Nagasaki–the equivalent blast of the Fat Man. At the cost of approximately $600,000 per Super-fortress, this massively parallel array of B-29s would have cost only 600 million dollars. In comparison to the nuclear approach, this is a bargain because it is much less than the $2 billion dollar price tag actually spent for the three secret cities built for atomic bomb development at Oak Ridge, Tennessee, Hanford, Washington, and Los Alamos, New Mexico. Furthermore, B-17 Flying Fortress formations had already been used in precise daylight bombing raids over Europe and hence formation flying was a successfully proven technology. In fact, Boeing manufactured some 12,730 Flying Fortresses, so producing massive numbers of bombers was also a proven technological feat.

At the time, one might have argued that the massively parallel approach of using large bomber formations could not keep pace with the highly efficient output of the nuclear technology approach which eventually produced fusion bombs. After all, following a mere decade of research we had achieved an efficiency of three-orders of magnitude where a 5 ton bomb

yielded the equivalent of 20 million tons of TNT. Even with the biggest conventional bombs such as the Massive Ordnance Air Blast (the "mother of all bombs") weighing in at over 10 tons exploded in 2003 over a test site at Eglin Air Force Base in Florida as a warning to the Iraqis, or the 11 ton Grand Slam used by the British during World War II, it would have taken a million of them to equal one Mark 41 thermonuclear bomb. Clearly it would be prohibitively expensive to procure a fleet of a million bombers, a logistical nightmare of historical proportions.

In hindsight the transition of nuclear technology clearly won out over a conventional technology used in a massively-parallel configuration. But in our fictitious scenario, we wouldn't have the benefit of hindsight, and the massively parallel approach might have seemed quite attractive.

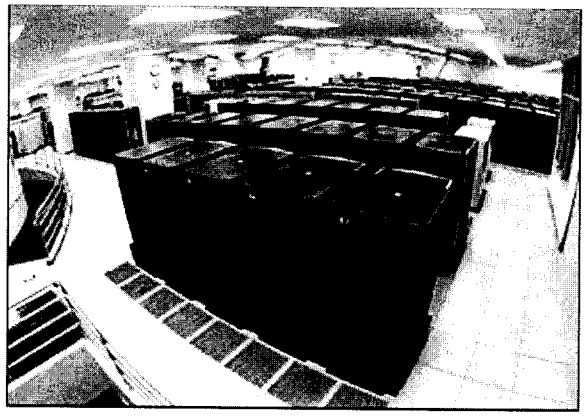

Figure 12.2: National Energy Research Scientific Computing Center IBM massively parallel supercomputer.

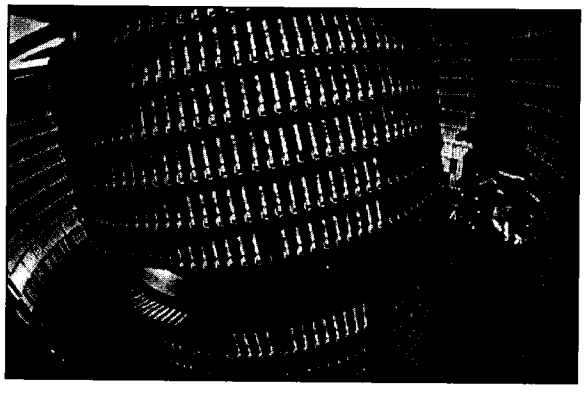

Figure 12.3: High performance storage system: One of the storage silo robots in NERSC's 8.8-petabyte high performance storage system used to archive data.

Of course, I am offering formation flying as an analogy to what we are doing today in the

construction of massively parallel supercomputers. Fortunately, we are not displaced back in time to relive the atomic age of bomb making. Yet today we are living through another historic age, the information age of computer making. The relevant question today is whether we should use a conventional massively parallel approach or instead embark on the daring alternative of using a quantum mechanical approach to achieve parallelism through quantum entanglement. Today, most government high-performance supercomputing resources for state-of-the-art computing are targeted toward conventional programs of massive classical parallelism.

The National Energy Research Scientific Computing (NERSC) Center, funded by the U.S. Department of Energy's Office of Science, put its 10 trillion floating-point operations per second (10 teraflops) IBM supercomputer with 6,656 processors into service March 3, 2003, see Figures 12.2 and 12.3. The NERSC Center, located at Lawrence Berkeley National Laboratory, serves more than 2,000 researchers at national laboratories and universities across the country in research problems such as combustion, climate modeling, fusion energy, materials science, physics, chemistry and computational biology.

The NERSC Center is only one of many national massively parallel supercomputer centers. Similarly massive centers are also operated by the Department of Defense. Presently, as the Department of Energy contracts with IBM to procure the largest and fastest supercomputer in the world, called *ASCII Purple*, the United States government is in effect taking the more practical and familiar road of massively-parallel conventional technologies to achieve a 100 teraflops milestone at a cost exceeding a quarter of a billion dollars. As we continue to try to engineer ever faster supercomputers using strictly classical principles and familiar associated technologies, the development and maintenance costs of "formation-flying" will skyrocket out of control. This in effect is presently occuring in regards to IBM's massively-parallel conventional computing project. It is a tangible aspect of Moore's second law. Clearly, logistical considerations will eventually impose limits upon the approach of using massively-parallel arrays of conventional processors. The day IBM expresses serious concern that the massively-parallel conventional computer they are building is so complex and has so many functions that fully testing it will take years is the day we know we have reached the quantum barrier.

As of yet, I do not believe we have reached that point in time. According to the historical data presented in Figure 1.2, the quantum barrier is nearly two decades in the future; it is projected to occur sometime in the middle of the year 2021. However, we have reached the point in time when it is now technologically practical embark on a basic research project to break the quantum barrier. Building a state-of-the-art supercomputer, a 1,000 teraflops type II quantum computer, could be accomplished with present day technologies, albeit at

great expense.

12.4 Physical simulation

It is an ironic twist of fate that the inhumane technology of nuclear weapon manufacture that gave birth to the atomic age can actually now push us ever deeper into the information age. To achieve such high rates and densities of computation needed to accurately model dynamical physical systems such as the behavior of nuclear detonations, we will be necessarily forced to cross the quantum barrier—no classical technology could ever achive the scale, resolution, nor degree of nonlinearity to faithfully reproduce nuclear explosions within the computational space of classical binary logic. Nuclear physics technology, through its own self-reflective simulation within the substrates of the highest-performing supercomputers, is driving supercomputing towards the application of quantum computation for physical modeling using nuclear spins and their interactions to encode information and perform fundamental logical operations to efficiently process that information[2].

Figure 12.4: F-18 shock waves: Shock waves behind the canopy and along the wings and fuselage of an F-18 fighter jet the instant it breaks the sound barrier.

If Moore's law shown in Figure 1.2 persists, sometime around 2021 the first large-scale type II quantum computer may come on line with a vast memory size of ten million terabytes. Its three-dimensional numerical grid size might be on the order of one hundred thousand lattice sites on a side. This would be sufficient to resolve a coupled set of Boltzmann equations modeling the kinetic processes capturing all the essential physics down to the dissipation scale lengths related to the viscosities and resistivities of the highly turbulent

[2] The real-time gaming industry and the animated motion pictures industry are both significant driving forces underlying continued computing advancement, but they are no economic match for the level of government investment in high-performance supercomputing.

fluid of the kind fluid flow shown in Figure 12.4, including all the relevant phase-change dynamics, thermodynamics, and shock wave processes. Today, however, we can only dream

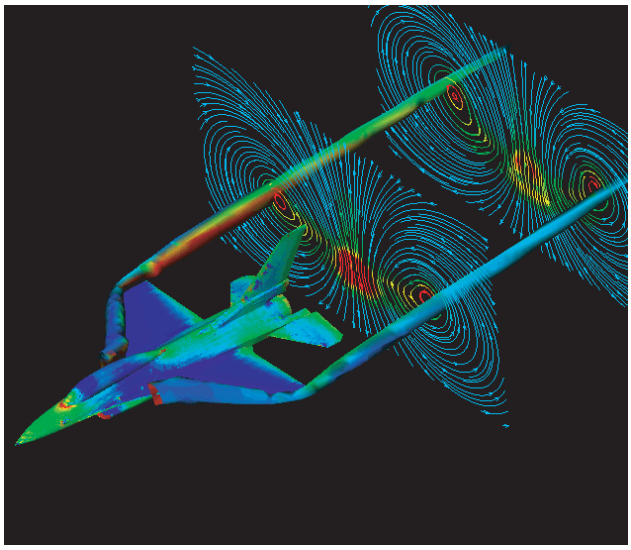

Figure 12.5: F-16 simulation: Nonlinear subsonic flow around an international F-16 fighter jet at a 7° angle of attack computed on a Silicon Graphics Origin 3200 parallel supercomputer using a computational fluid algorithm based on the lattice Boltzmann equation.

about carrying out faithful physical simulations of this kind. Using the computational fluid dynamics algorithm based on lattice Boltzmann equation, today we can model only subsonic unsteady flow such as that about the international F-16 fighter shown in Figure 12.5. Yet, it is possible that the type II quantum computing methodology will be extended to handle large scale magnetohydrodynamic flows and other complex flows using immensely large spatial simulations.

How would we make sure our quantum computer was operating correctly? How would we diagnose the output of such a large field of data? The first and most important physical principle that we would exploit in this task would be wave function collapse achieved by quantum projective measurement. This reduces the data set logarithmically. Next, we could perform consistency checks by accumulating totals for each of the conserved quantities in our numerical simulation. We would check that mass, the components of moment of the flow field, the total energy, the components of the magnetic field are globally conserved. These would be rigorous tests of the validity of the numerical simulation because of the astronomical unlikelihood of these conserved quantities being accidently and coincidentally conserved. Furthermore, we would extract reduced sets of information, such as two-dimensional slices, of the massive data set. We would also extract aggregated data at limited regions showing hydrodynamic pressure or magnetic pressure contours at those locations and do consistency

checks against analytical predictions, at least for the most simple test cases with special initial conditions and symmetries. Furthermore, quantum controls of logical gate operations, implementing conservative quantum gates would be subject to independent testing.

We will always be wedded to conventional classical computers to carry out these types of data reduction activities and diagnostics. In that sense, we will always retain fleets of conventional processing units to carry out some reasonable amount of "formation-flying."

12.5 Final remarks

Quantum algorithms for simulating the physical dynamics of classical systems can serve as an important pathway leading to quantum computers becoming a new dominant computing standard. Although this application is specialized, it can nevertheless be a springboard to more general purpose quantum computing applications, very much like the role the Earth Simulator in Japan plays in the field of high-performance supercomputing [Sato, 2003]. It is my expectation that neither Shor's factoring algorithm nor code-breaking nor Grover's search algorithm will, in the end, be the pathway causing quantum computers to become a new dominant computing standard, although these quantum algorithms have certainly been the primary pathway as the nascent field of quantum information processing has initially gained world-wide attention.

In our narrow treatment of the broad subject of quantum information processing and quantum logic, we have discussed only conservative quantum logic. The reason for doing so is that it is a natural choice as the basis for any standardized implementation of universal quantum logic because the laws of physics are themselves conservative. The use of conservative quantum logic significantly reduces fixed-cost overhead and hence remarkably simplifies the design and implementation details of quantum computer architectures. Conservative quantum logic is naturally suited to quantum computation of physical modeling applications.

It appears that a new trend has emerged in quantum computing, particularly if we look at the progress over the past seven years or so in the application of nuclear magnetic resonance spectroscopy to quantum computing. Every year or so a new chemical is found that has an additional spin-$\frac{1}{2}$ nucleus, either a proton or carbon-13 isotope, so that the computational space doubles at this pace. Moore's law can be upheld with quantum computing technologies so long as we add one qubit (per node of a type II quantum computer) every two years. And although we cannot improve upon the remarkable reduction rate of bit sizes halving every two years, we likely can bypass Moore's second law. In that regard, quantum computers can one day offer an economically advantageous solution to our computing industry.

Appendix A

Representations of conservative quantum gates

A.1 $\hat{H}^2 = \hat{H}$ case

From (2.40) and (2.46), we can solve for $\hat{H}$:

$$\hat{H} = \frac{1}{e^z - 1}(\Upsilon - \mathbf{1}) = \frac{1}{e^z - 1}\begin{pmatrix} 0 & 0 & 0 & 0 \\ 0 & A-1 & B & 0 \\ 0 & C & D-1 & 0 \\ 0 & 0 & 0 & E-1 \end{pmatrix}. \tag{A.1}$$

Let us pick a new set of variables to simplify matters:

$$\mathcal{A} = \frac{A-1}{e^z - 1} \qquad \mathcal{B} = \frac{B}{e^z - 1} \tag{A.2}$$

$$\mathcal{C} = \frac{C}{e^z - 1} \qquad \mathcal{D} = \frac{D-1}{e^z - 1} \tag{A.3}$$

$$\delta = \frac{E-1}{e^z - 1} \tag{A.4}$$

Then inserting (A.2-A.4) into (A.1), the Hamiltonian has the simple matrix and operator representation

$$\hat{H} = \begin{pmatrix} 0 & 0 & 0 & 0 \\ 0 & \mathcal{A} & \mathcal{B} & 0 \\ 0 & \mathcal{C} & \mathcal{D} & 0 \\ 0 & 0 & 0 & \delta \end{pmatrix}, \tag{A.5}$$

and from this we deduce the operator form of the idempotent Hamiltonian

$$\hat{H} = \mathcal{B}\hat{a}_2^\dagger \hat{a}_1 + \mathcal{C}\hat{a}_1^\dagger \hat{a}_2 + \mathcal{D}\hat{n}_1(\mathbf{1} - \hat{n}_2) + \mathcal{A}(\mathbf{1} - \hat{n}_1)\hat{n}_2 + \delta \hat{n}_1 \hat{n}_2. \tag{A.6}$$

Next inserting the new variables (A.2-A.4) into (2.40) and (2.43), the matrix and operator

representations for the conservative quantum logic gate become

$$\hat{\Upsilon}(z) = e^{z\hat{H}} \tag{A.7}$$

$$= \begin{pmatrix} 1 & 0 & 0 & 0 \\ 0 & (e^z-1)\mathcal{A}+1 & (e^z-1)\mathcal{B} & 0 \\ 0 & (e^z-1)\mathcal{B}^\dagger & (e^z-1)\mathcal{D}+1 & 0 \\ 0 & 0 & 0 & (e^z-1)\delta+1 \end{pmatrix} \tag{A.8}$$

$$= \mathbf{1} + (e^z-1)\left[\mathcal{B}\hat{a}_2^\dagger\hat{a}_1 + \mathcal{C}\hat{a}_1^\dagger\hat{a}_2 + \mathcal{D}\hat{n}_1(\mathbf{1}-\hat{n}_2) + \mathcal{A}(\mathbf{1}-\hat{n}_1)\hat{n}_2 + \delta\hat{n}_1\hat{n}_2\right].$$

Since the Hamiltonian must be Hermitian, $\hat{H} = \hat{H}^\dagger$, we know that $\mathcal{C} = \mathcal{B}^\dagger$ and $\delta = \delta^\dagger$, so δ must be a real valued number. Also, since the Hamiltonian is idempotent, $\hat{H}^2 = \hat{H}$, we get the additional constraint equations on the components:

$$\mathcal{A}^2 - \mathcal{A} + |\mathcal{B}|^2 = 0 \tag{A.9}$$

$$\mathcal{A} + \mathcal{D} = 1 \tag{A.10}$$

$$\mathcal{D}^2 - \mathcal{D} + |\mathcal{B}|^2 = 0, \tag{A.11}$$

which admit the solutions:

$$\mathcal{A} = \frac{1}{2}\left(1 \pm \sqrt{1-4|\mathcal{B}|^2}\right) \tag{A.12}$$

$$\mathcal{D} = \frac{1}{2}\left(1 \mp \frac{1}{2}\sqrt{1-4|\mathcal{B}|^2}\right). \tag{A.13}$$

Then inserting (A.12) and (A.13) into (A.5) and (A.6), we can specify the idempotent Hamiltonian with only one free complex parameter:

$$\hat{H} = \begin{pmatrix} 0 & 0 & 0 & 0 \\ 0 & \frac{1}{2} \pm \frac{1}{2}\sqrt{1-4|\mathcal{B}|^2} & \mathcal{B} & 0 \\ 0 & \mathcal{B}^\dagger & \frac{1}{2} \mp \frac{1}{2}\sqrt{1-4|\mathcal{B}|^2} & 0 \\ 0 & 0 & 0 & \delta \end{pmatrix} \tag{A.14}$$

$$= \mathcal{B}\hat{a}_2^\dagger\hat{a}_1 + \mathcal{B}^\dagger\hat{a}_1^\dagger\hat{a}_2 + \frac{1}{2}\left(1 \mp \sqrt{1-4|\mathcal{B}|^2}\right)\hat{n}_1(\mathbf{1}-\hat{n}_2)$$

$$+ \frac{1}{2}\left(1 \pm \sqrt{1-4|\mathcal{B}|^2}\right)(\mathbf{1}-\hat{n}_1)\hat{n}_2 + \delta\hat{n}_1\hat{n}_2$$

$$= \mathcal{B}\hat{a}_2^\dagger\hat{a}_1 + \mathcal{B}^\dagger\hat{a}_1^\dagger\hat{a}_2 + \frac{1}{2}\left(1 \mp \sqrt{1-4|\mathcal{B}|^2}\right)\hat{n}_1 + \frac{1}{2}\left(1 \pm \sqrt{1-4|\mathcal{B}|^2}\right)\hat{n}_2 + (\delta-1)\hat{n}_1\hat{n}_2.$$

The associated conservative quantum logic gate can also be rewritten by inserting (A.12) and (A.13) into (A.7):

$$\hat{\Upsilon}(z) = \begin{pmatrix} 1 & 0 & 0 & 0 \\ 0 & \frac{1}{2}(e^z+1) \pm \frac{1}{2}(e^z-1)\sqrt{1-4|\mathcal{B}|^2} & (e^z-1)\mathcal{B} & 0 \\ 0 & (e^z-1)\mathcal{B}^\dagger & \frac{1}{2}(e^z+1) \mp \frac{1}{2}(e^z-1)\sqrt{1-4|\mathcal{B}|^2} & 0 \\ 0 & 0 & 0 & (e^z-1)\delta+1 \end{pmatrix}$$

$$= \mathbf{1} + (e^z-1)\left[\mathcal{B}\hat{a}_2^\dagger\hat{a}_1 + \mathcal{B}^\dagger\hat{a}_1^\dagger\hat{a}_2 + \right.$$

$$\left. \frac{1}{2}\left(1 \mp \sqrt{1-4|\mathcal{B}|^2}\right)\hat{n}_1 + \frac{1}{2}\left(1 \pm \sqrt{1-4|\mathcal{B}|^2}\right)\hat{n}_2 + (\delta-1)\hat{n}_1\hat{n}_2\right]. \tag{A.15}$$

A physical and useful special case occurs if we choose $\mathcal{B} = -\frac{1}{2}e^{-i\xi}$:

$$\begin{aligned}\hat{H} &= \begin{pmatrix} 0 & 0 & 0 & 0 \\ 0 & \frac{1}{2} & -\frac{1}{2}e^{-i\xi} & 0 \\ 0 & -\frac{1}{2}e^{i\xi} & \frac{1}{2} & 0 \\ 0 & 0 & 0 & \delta \end{pmatrix} \\ &= -\frac{1}{2}\left(\hat{a}_1^\dagger \hat{a}_2 e^{i\xi} + \hat{a}_2^\dagger \hat{a}_1 e^{-i\xi} - \hat{n}_1 - \hat{n}_2\right) + (\delta - 1)\hat{n}_1\hat{n}_2. \end{aligned} \tag{A.16}$$

Since $\hat{n}_1 = \hat{a}_1^\dagger \hat{a}_1$ and $\hat{n}_2 = \hat{a}_2^\dagger \hat{a}_2$, we can rewrite the idempotent Hamiltonian as follows

$$\hat{H} = \frac{1}{2}(\hat{a}_1^\dagger - e^{-i\xi}\hat{a}_2^\dagger)(\hat{a}_1 - e^{i\xi}\hat{a}_2) + (\delta - 1)\hat{n}_1\hat{n}_2. \tag{A.17}$$

Also

$$\begin{aligned}\hat{\Upsilon}(z) &= \begin{pmatrix} 1 & 0 & 0 & 0 \\ 0 & \frac{1}{2}(e^z + 1) & -\frac{1}{2}(e^z - 1)e^{-i\xi} & 0 \\ 0 & -\frac{1}{2}(e^z - 1)e^{i\xi} & \frac{1}{2}(e^z + 1) & 0 \\ 0 & 0 & 0 & (e^z - 1)\delta + 1 \end{pmatrix} \\ &= \mathbf{1} + (e^z - 1)\left[\frac{1}{2}\left(\hat{a}_1^\dagger - e^{-i\xi}\hat{a}_2^\dagger\right)\left(\hat{a}_1 - e^{i\xi}\hat{a}_2\right) + (\delta - 1)\hat{n}_1\hat{n}_2\right]. \end{aligned} \tag{A.18, A.19}$$

Finally, for $z = i\pi$ we get the general quantum swap gate

$$\hat{\Upsilon}(i\pi) = \begin{pmatrix} 1 & 0 & 0 & 0 \\ 0 & 0 & e^{-i\xi} & 0 \\ 0 & e^{i\xi} & 0 & 0 \\ 0 & 0 & 0 & 1 - 2\delta \end{pmatrix} = \mathbf{1} - \left(\hat{a}_1^\dagger - e^{-i\xi}\hat{a}_2^\dagger\right)\left(\hat{a}_1 - e^{i\xi}\hat{a}_2\right) - 2(\delta - 1)\hat{n}_1\hat{n}_2. \tag{A.20}$$

For $\xi = 0$, (A.20) is a symmetric quantum swap gate. To satisfy the unitary condition for our quantum logic gate, $\Upsilon\Upsilon^\dagger = 1$, we must restrict the real-valued component δ by the following constraint equation:

$$(1 - 2\delta)^2 = 1, \tag{A.21}$$

which implies that either $\delta = 0$ or $\delta = 1$. Then our quantum swap gate (A.20) can be rewritten as:

$$\hat{\Upsilon}(i\pi) = \begin{pmatrix} 1 & 0 & 0 & 0 \\ 0 & 0 & e^{-i\xi} & 0 \\ 0 & e^{i\xi} & 0 & 0 \\ 0 & 0 & 0 & \pm 1 \end{pmatrix}, \tag{A.22}$$

where the plus sign applies for bosonic particles (the $\delta = 0$ case) and the minus sign for fermionic particles (the $\delta = 1$ case). For $z = \frac{i\pi}{2}$ we get the $\sqrt{\text{swap}}$ gate

$$\begin{aligned}\hat{\Upsilon}\left(\frac{i\pi}{2}\right) &= \begin{pmatrix} 1 & 0 & 0 & 0 \\ 0 & \frac{1}{2} + \frac{i}{2} & \left(\frac{1}{2} - \frac{i}{2}\right)e^{-i\xi} & 0 \\ 0 & \left(\frac{1}{2} - \frac{i}{2}\right)e^{i\xi} & \frac{1}{2} + \frac{i}{2} & 0 \\ 0 & 0 & 0 & (i - 1)\delta + 1 \end{pmatrix} \\ &= \mathbf{1} + (i - 1)\left[\frac{1}{2}\left(\hat{a}_1^\dagger - e^{-i\xi}\hat{a}_2^\dagger\right)\left(\hat{a}_1 - e^{i\xi}\hat{a}_2\right) + (\delta - 1)\hat{n}_1\hat{n}_2\right]. \end{aligned} \tag{A.23, A.24}$$

A.2 $\hat{H}^3 = \hat{H}$ case

There exists an alternative Hamiltonian that is not idempotent but has a similar property at third order, $\hat{H}^3 = \hat{H}$, which can generate a conservative quantum logic gate of the form (2.40).

In this second case, the series expansion of the quantum gate (2.45) reduces to the form (2.47), which is

$$\hat{\Upsilon}(z) = \mathbf{1} + (\cosh z - 1)\hat{H}^2 + \sinh z \hat{H}.$$

Our approach will be to assume the Hamiltonian still has the form (A.5) and that its square has a diagonal matrix form:

$$\begin{aligned}
\hat{H}^2 &= \begin{pmatrix} 0 & 0 & 0 & 0 \\ 0 & \mathcal{A} & \mathcal{B} & 0 \\ 0 & \mathcal{B}^\dagger & \mathcal{D} & 0 \\ 0 & 0 & 0 & \delta \end{pmatrix} \cdot \begin{pmatrix} 0 & 0 & 0 & 0 \\ 0 & \mathcal{A} & \mathcal{B} & 0 \\ 0 & \mathcal{B}^\dagger & \mathcal{D} & 0 \\ 0 & 0 & 0 & \delta \end{pmatrix} && \text{(A.25)} \\
&= \begin{pmatrix} 0 & 0 & 0 & 0 \\ 0 & 1 & 0 & 0 \\ 0 & 0 & 1 & 0 \\ 0 & 0 & 0 & \delta \end{pmatrix} && \text{(A.26)} \\
&= \hat{n}_1(\mathbf{1} - \hat{n}_2) + (\mathbf{1} - \hat{n}_1)\hat{n}_2 + \delta \hat{n}_1 \hat{n}_2 && \text{(A.27)} \\
&= \hat{n}_1 + \hat{n}_2 + (\delta - 2)\hat{n}_1 \hat{n}_2. && \text{(A.28)}
\end{aligned}$$

where as in the previous case either $\delta = 0$ or $\delta = 1$. This imposes the following constraint equations on the components:

$$\begin{aligned}
\mathcal{A}^2 &= 1 - |\mathcal{B}|^2 && \text{(A.29)} \\
\mathcal{A} + \mathcal{D} &= 0 && \text{(A.30)} \\
\mathcal{D}^2 &= 1 - |\mathcal{B}|^2, && \text{(A.31)}
\end{aligned}$$

which admit the solutions:

$$\begin{aligned}
\mathcal{A} &= \pm\sqrt{1 - |\mathcal{B}|^2} && \text{(A.32)} \\
\mathcal{D} &= \mp\sqrt{1 - |\mathcal{B}|^2}. && \text{(A.33)}
\end{aligned}$$

Then the Hamiltonian has the form

$$\begin{aligned}
\hat{H} &= \begin{pmatrix} 0 & 0 & 0 & 0 \\ 0 & \pm\sqrt{1 - |\mathcal{B}|^2} & \mathcal{B} & 0 \\ 0 & \mathcal{B}^\dagger & \mp\sqrt{1 - |\mathcal{B}|^2} & 0 \\ 0 & 0 & 0 & \delta \end{pmatrix} && \text{(A.34)} \\
&= \mathcal{B}\hat{a}_2^\dagger \hat{a}_1 + \mathcal{B}^\dagger \hat{a}_1^\dagger \hat{a}_2 \mp \sqrt{1 - |\mathcal{B}|^2}\hat{n}_1(\mathbf{1} - \hat{n}_2) \pm \sqrt{1 - |\mathcal{B}|^2}(\mathbf{1} - \hat{n}_1)\hat{n}_2 + \delta \hat{n}_1 \hat{n}_2 \\
&= \mathcal{B}\hat{a}_2^\dagger \hat{a}_1 + \mathcal{B}^\dagger \hat{a}_1^\dagger \hat{a}_2 \mp \sqrt{1 - |\mathcal{B}|^2}\hat{n}_1 \pm \sqrt{1 - |\mathcal{B}|^2}\hat{n}_2 + \delta \hat{n}_1 \hat{n}_2.
\end{aligned}$$

and hence, using (2.47), the matrix representation of the conservative quantum gate becomes

$$\hat{\Upsilon}(z) = \begin{pmatrix} 1 & 0 & 0 & 0 \\ 0 & \cosh z \pm \sqrt{1-|\mathcal{B}|^2}\sinh z & \mathcal{B}\sinh z & 0 \\ 0 & \mathcal{B}^\dagger \sinh z & \cosh z \mp \sqrt{1-|\mathcal{B}|^2}\sinh z & 0 \\ 0 & 0 & 0 & (e^z-1)\delta + 1 \end{pmatrix} \tag{A.35a}$$

$$= \mathbf{1} + (\cosh z - 1)\left[\hat{n}_1 + \hat{n}_2 + (\delta - 2)\hat{n}_1\hat{n}_2\right] + \sinh z\left[\mathcal{B}\,\hat{a}_2^\dagger\hat{a}_1 + \mathcal{B}^\dagger\,\hat{a}_1^\dagger\hat{a}_2 \mp \sqrt{1-|\mathcal{B}|^2}\hat{n}_1 \pm \sqrt{1-|\mathcal{B}|^2}\hat{n}_2 + \delta\hat{n}_1\hat{n}_2\right] \tag{A.35b}$$

$$= \mathbf{1} + \sinh z\mathcal{B}\,\hat{a}_2^\dagger\hat{a}_1 + \sinh z\mathcal{B}^\dagger\,\hat{a}_1^\dagger\hat{a}_2 + (\cosh z - 1 \mp \sqrt{1-|\mathcal{B}|^2})\,\hat{n}_1 + (\cosh z - 1 \pm \sqrt{1-|\mathcal{B}|^2})\,\hat{n}_2 + [(e^z-1)\delta + 2(\cosh z - 1)]\,\hat{n}_1\hat{n}_2. \tag{A.35c}$$

A useful special case occurs for $\mathcal{B} = ie^{-i\xi}$. Then

$$\hat{H} = \begin{pmatrix} 0 & 0 & 0 & 0 \\ 0 & 0 & ie^{-i\xi} & 0 \\ 0 & -ie^{i\xi} & 0 & 0 \\ 0 & 0 & 0 & \delta \end{pmatrix} = ie^{-i\xi}\hat{a}_2^\dagger\hat{a}_1 - ie^{i\xi}\hat{a}_1^\dagger\hat{a}_2 + \delta\hat{n}_1\hat{n}_2. \tag{A.36}$$

With the following identity

$$\left(\hat{a}_1^\dagger + ie^{-i\xi}\hat{a}_2^\dagger\right)\left(\hat{a}_1 - ie^{i\xi}\hat{a}_2\right) = ie^{-i\xi}\hat{a}_2^\dagger\hat{a}_1 - ie^{i\xi}\hat{a}_1^\dagger\hat{a}_2 + \hat{n}_1 + \hat{n}_2 \tag{A.37}$$

we can rewrite the Hamiltonian (A.36) as

$$\hat{H} = \begin{pmatrix} 0 & 0 & 0 & 0 \\ 0 & 0 & ie^{-i\xi} & 0 \\ 0 & -ie^{i\xi} & 0 & 0 \\ 0 & 0 & 0 & \delta \end{pmatrix} = \left(\hat{a}_1^\dagger + ie^{-i\xi}\hat{a}_2^\dagger\right)\left(\hat{a}_1 - ie^{i\xi}\hat{a}_2\right) - \hat{n}_1 - \hat{n}_2 + \delta\hat{n}_1\hat{n}_2. \tag{A.38}$$

The quantum gate has the form:

$$\hat{\Upsilon}(z) = \begin{pmatrix} 1 & 0 & 0 & 0 \\ 0 & \cosh z & ie^{-i\xi}\sinh z & 0 \\ 0 & -ie^{i\xi}\sinh z & \cosh z & 0 \\ 0 & 0 & 0 & (e^z-1)\delta + 1 \end{pmatrix} \tag{A.39}$$

$$= \mathbf{1} + i\sinh z\left(e^{-i\xi}\hat{a}_2^\dagger\hat{a}_1 - e^{i\xi}\hat{a}_1^\dagger\hat{a}_2\right) + (\cosh z - 1)(\hat{n}_1 + \hat{n}_2) + [(e^z-1)\delta + 2(\cosh z - 1)]\,\hat{n}_1\hat{n}_2. \tag{A.40}$$

Finally, for $z = i\pi$ we get the general quantum swap gate

$$\hat{\Upsilon}(i\pi) = \begin{pmatrix} 1 & 0 & 0 & 0 \\ 0 & 0 & -e^{-i\xi} & 0 \\ 0 & e^{i\xi} & 0 & 0 \\ 0 & 0 & 0 & 1-2\delta \end{pmatrix} = \mathbf{1} + e^{i\xi}\hat{a}_1^\dagger\hat{a}_2 - e^{-i\xi}\hat{a}_2^\dagger\hat{a}_1 - 2\delta\hat{n}_1\hat{n}_2, \tag{A.41}$$

For $\xi = 0$, (A.41) is an antisymmetric quantum swap gate. For $z = \frac{i\pi}{2}$ we get the antisymmetric quantum $\sqrt{\text{swap}}$ gate

$$\hat{\Upsilon}(z) = \begin{pmatrix} 1 & 0 & 0 & 0 \\ 0 & \frac{1}{\sqrt{2}} & -\frac{1}{\sqrt{2}}e^{-i\xi} & 0 \\ 0 & \frac{1}{\sqrt{2}}e^{i\xi} & \frac{1}{\sqrt{2}} & \\ 0 & 0 & 0 & (i-1)\delta + 1 \end{pmatrix} \tag{A.42}$$

$$= \mathbf{1} + \frac{1}{\sqrt{2}}\left(e^{i\xi}\hat{a}_1^\dagger \hat{a}_2 - e^{-i\xi}\hat{a}_2^\dagger \hat{a}_1\right) + \left(\frac{1}{\sqrt{2}} - 1\right)(\hat{n}_1 + \hat{n}_2) + \left[(i-1)\delta + 2\left(\frac{1}{\sqrt{2}} - 1\right)\right]\hat{n}_1\hat{n}_2. \tag{A.43}$$

Appendix B

Generating function example

$$
\begin{aligned}
\left(\sum_{p=0}^{1}\sum_{m=0}^{1} n^{p+m} s_z^{p-m}\right)^7 \;=\; & \frac{n^7}{{s_z}^7} \\
& + \frac{7\,n^6}{{s_z}^6} + \frac{7\,n^8}{{s_z}^6} \\
& + \frac{21\,n^5}{{s_z}^5} + \frac{49\,n^7}{{s_z}^5} + \frac{21\,n^9}{{s_z}^5} \\
& + \frac{35\,n^4}{{s_z}^4} + \frac{147\,n^6}{{s_z}^4} + \frac{147\,n^8}{{s_z}^4} + \frac{35\,n^{10}}{{s_z}^4} \\
& + \frac{35\,n^3}{{s_z}^3} + \frac{245\,n^5}{{s_z}^3} + \frac{441\,n^7}{{s_z}^3} + \frac{245\,n^9}{{s_z}^3} + \frac{35\,n^{11}}{{s_z}^3} \\
& + \frac{21\,n^2}{{s_z}^2} + \frac{245\,n^4}{{s_z}^2} + \frac{735\,n^6}{{s_z}^2} + \frac{735\,n^8}{{s_z}^2} + \frac{245\,n^{10}}{{s_z}^2} + \frac{21\,n^{12}}{{s_z}^2} \\
& + \frac{7\,n}{s_z} + \frac{147\,n^3}{s_z} + \frac{735\,n^5}{s_z} + \frac{1225\,n^7}{s_z} + \frac{735\,n^9}{s_z} + \frac{147\,n^{11}}{s_z} + \frac{7\,n^{13}}{s_z} \\
& + 1 + 49\,n^2 + 441\,n^4 + 1225\,n^6 + 1225\,n^8 + 441\,n^{10} + 49\,n^{12} + n^{14} \\
& + 7\,n\,s_z + 147\,n^3\,s_z + 735\,n^5\,s_z + 1225\,n^7\,s_z + 735\,n^9\,s_z + 147\,n^{11}\,s_z + 7\,n^{13}\,s_z \\
& + 21\,n^2\,{s_z}^2 + 245\,n^4\,{s_z}^2 + 735\,n^6\,{s_z}^2 + 735\,n^8\,{s_z}^2 + 245\,n^{10}\,{s_z}^2 + 21\,n^{12}\,{s_z}^2 \\
& + 35\,n^3\,{s_z}^3 + 245\,n^5\,{s_z}^3 + 441\,n^7\,{s_z}^3 + 245\,n^9\,{s_z}^3 + 35\,n^{11}\,{s_z}^3 \\
& + 35\,n^4\,{s_z}^4 + 147\,n^6\,{s_z}^4 + 147\,n^8\,{s_z}^4 + 35\,n^{10}\,{s_z}^4 \\
& + 21\,n^5\,{s_z}^5 + 49\,n^7\,{s_z}^5 + 21\,n^9\,{s_z}^5 \\
& + 7\,n^6\,{s_z}^6 + 7\,n^8\,{s_z}^6 \\
& + n^7\,{s_z}^7.
\end{aligned}
$$

Appendix C

Spin operators

The operator $\hat{S}_{nx}$ flips the nth spin:

$$\begin{array}{ll} \hat{S}_{1x}|\downarrow\downarrow\rangle = |\uparrow\downarrow\rangle & \hat{S}_{2x}|\downarrow\downarrow\rangle = |\downarrow\uparrow\rangle \\ \hat{S}_{1x}|\downarrow\uparrow\rangle = |\uparrow\uparrow\rangle & \hat{S}_{2x}|\downarrow\uparrow\rangle = |\downarrow\downarrow\rangle \\ \hat{S}_{1x}|\uparrow\downarrow\rangle = |\downarrow\downarrow\rangle & \hat{S}_{2x}|\uparrow\downarrow\rangle = |\uparrow\uparrow\rangle \\ \hat{S}_{1x}|\uparrow\uparrow\rangle = |\downarrow\uparrow\rangle & \hat{S}_{2x}|\uparrow\uparrow\rangle = |\uparrow\downarrow\rangle \end{array} \tag{C.1}$$

The operator $\hat{S}_{nz}$ flips the phase of the state (multiplies the amplitude by -1) if the nth spin is down and does nothing otherwise:

$$\begin{array}{ll} \hat{S}_{1z}|\downarrow\downarrow\rangle = -|\downarrow\downarrow\rangle & \hat{S}_{2z}|\downarrow\downarrow\rangle = -|\downarrow\downarrow\rangle \\ \hat{S}_{1z}|\downarrow\uparrow\rangle = -|\downarrow\uparrow\rangle & \hat{S}_{2z}|\downarrow\uparrow\rangle = |\downarrow\uparrow\rangle \\ \hat{S}_{1z}|\uparrow\downarrow\rangle = |\uparrow\downarrow\rangle & \hat{S}_{2z}|\uparrow\downarrow\rangle = -|\uparrow\downarrow\rangle \\ \hat{S}_{1z}|\uparrow\uparrow\rangle = |\uparrow\uparrow\rangle & \hat{S}_{2z}|\uparrow\uparrow\rangle = |\uparrow\uparrow\rangle \end{array}. \tag{C.2}$$

The operator $\hat{S}_{ny}$ both flips the nth spin and flips the phase of the state if the nth spin is down and multiplies the amplitude by i since $\hat{S}_{ny} = i\hat{S}_{nz}\hat{S}_{nx}$:

$$\begin{array}{ll} \hat{S}_{1y}|\downarrow\downarrow\rangle = -i|\uparrow\downarrow\rangle & \hat{S}_{2y}|\downarrow\downarrow\rangle = -i|\downarrow\uparrow\rangle \\ \hat{S}_{1y}|\downarrow\uparrow\rangle = -i|\uparrow\uparrow\rangle & \hat{S}_{2y}|\downarrow\uparrow\rangle = i|\downarrow\downarrow\rangle \\ \hat{S}_{1y}|\uparrow\downarrow\rangle = i|\downarrow\downarrow\rangle & \hat{S}_{2y}|\uparrow\downarrow\rangle = -i|\uparrow\uparrow\rangle \\ \hat{S}_{1y}|\uparrow\uparrow\rangle = i|\downarrow\uparrow\rangle & \hat{S}_{2y}|\uparrow\uparrow\rangle = i|\uparrow\downarrow\rangle \end{array}. \tag{C.3}$$

Appendix D

Unfolding the multiqubit number operator

The single qubit number operator ($N = 1$) is

$$\hat{n} = \begin{pmatrix} 1 & 0 \\ 0 & 0 \end{pmatrix}. \tag{D.1}$$

The two qubit number operator ($N = 2$) can be expressed as the following tensor product that depends on $\hat{n}$

$$\begin{aligned} \hat{n}_1^{(2)} &= \begin{pmatrix} 1 & 0 & 0 & 0 \\ 0 & 1 & 0 & 0 \\ 0 & 0 & 0 & 0 \\ 0 & 0 & 0 & 0 \end{pmatrix} \qquad (D.2) \\ &= \begin{pmatrix} 1 & 0 \\ 0 & 0 \end{pmatrix} \otimes \begin{pmatrix} 1 & 0 \\ 0 & 1 \end{pmatrix} = \hat{n} \otimes \mathbf{1} \\ \hat{n}_2^{(2)} &= \begin{pmatrix} 1 & 0 & 0 & 0 \\ 0 & 0 & 0 & 0 \\ 0 & 0 & 1 & 0 \\ 0 & 0 & 0 & 0 \end{pmatrix} \qquad (D.3) \\ &= \begin{pmatrix} 1 & 0 \\ 0 & 1 \end{pmatrix} \otimes \begin{pmatrix} 1 & 0 \\ 0 & 0 \end{pmatrix} = \mathbf{1} \otimes \hat{n}. \end{aligned}$$

The three qubit number operator ($N = 3$) can be expressed as the following tensor product that depends on $\hat{n}$

$$\begin{aligned} \hat{n}_1^{(3)} &= \hat{n} \otimes \mathbf{1} \otimes \mathbf{1} \qquad (D.4) \\ \hat{n}_2^{(3)} &= \mathbf{1} \otimes \hat{n} \otimes \mathbf{1} \qquad (D.5) \\ \hat{n}_3^{(3)} &= \mathbf{1} \otimes \mathbf{1} \otimes \hat{n}. \qquad (D.6) \end{aligned}$$

In general, for a B qubit node, the a^{th} number operator, $\hat{n}_a$ can be expressed in a way that depends on a single $\hat{n}$ placed at the a^{th} position within the following tensor product

$$\hat{n}_a = \overbrace{\mathbf{1} \otimes \mathbf{1} \otimes \cdots \underbrace{\otimes \hat{n} \otimes}_{a^{\text{th}}-\text{term}} \cdots \otimes \mathbf{1}}^{B-\text{terms}}, \tag{D.7}$$

where here $\mathbf{1}$ denotes the 2×2 identity matrix.

Similarly, for a Q qubit system, the α^{th} number operator, $\hat{n}_\alpha$ can be expressed in a way that depends on a single $\hat{n}$ placed at the α^{th} position within the following tensor product

$$\hat{n}_\alpha = \overbrace{\mathbf{1} \otimes \mathbf{1} \otimes \cdots \underbrace{\otimes \hat{n} \otimes}_{\alpha^{\text{th}}-\text{term}} \cdots \otimes \mathbf{1}}^{N-\text{terms}}. \tag{D.8}$$

This tensor product can be partitioned into $L = Q/B$ terms as follows

$$\hat{n}_\alpha = \overbrace{\mathbf{1} \otimes \cdots \otimes \mathbf{1}}^{B-\text{terms}} \otimes \cdots \otimes \overbrace{\mathbf{1} \otimes \cdots \underbrace{\otimes \hat{n} \otimes}_{a^{\text{th}}-\text{term}} \cdots \otimes \mathbf{1}}^{B-\text{terms}} \otimes \cdots \otimes \overbrace{\mathbf{1} \otimes \cdots \otimes \mathbf{1}}^{B-\text{terms}}, \tag{D.9}$$

where $a = (\alpha \ \mathbf{mod}\ B)$. Each set of B-terms $\mathbf{1} \otimes \cdots \otimes \mathbf{1}$ constitutes a $2^B \times 2^B$ identity matrix. The set of B-terms $\mathbf{1} \otimes \cdots \otimes \hat{n} \otimes \cdots \otimes \mathbf{1}$ is the on-site number operator, $\hat{n}_a$ by identity (D.7). Therefore, using these two facts, we have the final result that

$$\hat{n}_\alpha = \overbrace{\mathbf{1} \otimes \mathbf{1} \otimes \cdots \underbrace{\otimes \hat{n}_a \otimes}_{\ell^{\text{th}}-\text{term}} \cdots \otimes \mathbf{1}}^{L-\text{terms}}, \tag{D.10}$$

where here $\mathbf{1}$ denotes the $2^B \times 2^B$ identity matrix. The index ℓ is a site index referring to site $\vec{x}_\ell$ in the lattice. The identity (D.10) represents the unfolding of the Q-qubit system number operator into a tensor product with a B-qubit on-site number operator.

Appendix E

Relativistic path integral

Following Jacobson and Schulman [Jacobson and Schulman, 1984], we may write the Kronecker delta as a continuous integral:

$$\delta\left(M, \sum_{i=0}^{N} \sigma_i\right) = \int_{-\pi}^{\pi} \frac{d\theta}{2\pi} e^{i\theta\left(M - \sum_i \sigma_i\right)}. \tag{E.1}$$

Then inserting (E.1) into (4.15) gives

$$K_{\sigma_0\sigma_N} = \int_{-\pi}^{\pi} \frac{d\theta}{2\pi} e^{i\theta M} \sum_{\{\sigma_1,\ldots,\sigma_{N-1}\}} e^{-\sum_{i=0}^{N}\sigma_i - \nu\sum_{i=0}^{N-1}(1-\sigma_i\sigma_{i+1})}. \tag{E.2}$$

Now since $\sum_{i=0}^{N}\sigma_i = \frac{1}{2}(\sigma_0+\sigma_N) + \frac{1}{2}\sum_{i=0}^{N-1}(\sigma_i+\sigma_{i+1})$, we pull down the summation in the argument of the exponential to form the following product:

$$K_{\sigma_0\sigma_N} = \int_{-\pi}^{\pi} \frac{d\theta}{2\pi} e^{i\theta M} e^{-\frac{i\theta}{2}(\sigma_0+\sigma_N)} \sum_{\{\sigma_1,\ldots,\sigma_{N-1}\}} \prod_{i=0}^{N-1} e^{-\frac{i\theta}{2}(\sigma_i+\sigma_{i+1}) - \nu(1-\sigma_i\sigma_{i+1})}. \tag{E.3}$$

The components of the transfer matrix are

$$\mathscr{U}_{\sigma_i,\sigma_{i+1}} \equiv e^{-\nu(1-\sigma_i\sigma_{i+1}) - \frac{i\theta}{2}(\sigma_i+\sigma_{i+1})}, \tag{E.4}$$

then (E.3) becomes

$$K_{\sigma_0\sigma_N} = \int_{-\pi}^{\pi} \frac{d\theta}{2\pi} e^{i\theta M} e^{-\frac{i\theta}{2}(\sigma_0+\sigma_N)} Z_{\sigma_0\sigma_N}. \tag{E.5}$$

where for convenience we restate the definition (4.21)

$$\mathscr{Z}_{\sigma_0\sigma_N} \equiv \sum_{\sigma_1=\pm1} \cdots \sum_{\sigma_{N-1}=\pm1} \mathscr{U}_{\sigma_0,\sigma_1}\mathscr{U}_{\sigma_1,\sigma_3}\cdots\mathscr{U}_{\sigma_{N-1},\sigma_N}. \tag{E.6}$$

(E.4) in matrix form is

$$\mathscr{U} = \begin{pmatrix} \mathscr{U}_{-1,-1} & \mathscr{U}_{-1,1} \\ \mathscr{U}_{1,-1} & \mathscr{U}_{1,1} \end{pmatrix} = \begin{pmatrix} e^{-i\theta} & e^{-2\nu} \\ e^{-2\nu} & e^{i\theta} \end{pmatrix}. \tag{E.7}$$

and (E.6) is an $(N-1)$-fold matrix multiplication of $\mathscr{U}$:

$$\mathscr{Z} = \begin{pmatrix} \mathscr{Z}_{-1,-1} & \mathscr{Z}_{-1,1} \\ \mathscr{Z}_{1,-1} & \mathscr{Z}_{1,1} \end{pmatrix} = \begin{pmatrix} e^{-i\theta} & e^{-2\nu} \\ e^{-2\nu} & e^{i\theta} \end{pmatrix}^N \tag{E.8}$$

From (4.14), the off-diagonal components of (E.7) are $e^{-2\nu} = i\Delta t\,\frac{mc^2}{\hbar}$, and in turn the eigenvalues of (E.7) are

$$\lambda_\pm = \cos\theta \pm i\left(\sin^2\theta + \Delta t^2 \frac{m^2c^4}{\hbar^2}\right)^{\frac{1}{2}}. \tag{E.9}$$

We can write (E.7) as

$$\mathscr{U} = \lambda_+|+\rangle\langle+| + \lambda_-|-\rangle\langle-|, \tag{E.10}$$

where $|\pm\rangle$ are orthonormal eigenvectors of (E.7). The components of the orthonormal eigenvectors $|\pm\rangle = \begin{pmatrix} x \\ y \end{pmatrix}$ satisfy

$$\begin{pmatrix} e^{-i\theta} & \frac{i\Delta tmc^2}{\hbar} \\ \frac{i\Delta tmc^2}{\hbar} & e^{i\theta} \end{pmatrix} \begin{pmatrix} x \\ y \end{pmatrix} = \left[\cos\theta \pm i\left(\sin^2\theta + \frac{\Delta t^2 m^2 c^4}{\hbar^2}\right)^{\frac{1}{2}}\right] \begin{pmatrix} x \\ y \end{pmatrix}, \tag{E.11}$$

and from which we know the ratio of the components is

$$\frac{y}{x} = \beta \pm \sqrt{1+\beta^2}, \tag{E.12}$$

where $\beta \equiv \frac{\hbar\sin\theta}{\Delta t\, mc^2}$. Notice that $\beta = \tan 2\delta$ is the solution of an equation of the form of (E.12):

$$\frac{\pm 1 + \sin 2\delta}{\cos 2\delta} = \beta \pm \sqrt{1+\beta^2}. \tag{E.13}$$

Since the R.H.S. of (E.13) can be rewritten

$$\frac{\pm\cos\delta + \sin\delta}{\cos\delta \mp \sin\delta} = \beta \pm \sqrt{1+\beta^2}, \tag{E.14}$$

our orthonormal eigenkets are

$$|\pm\rangle = \begin{pmatrix} \cos\delta \mp \sin\delta \\ \pm\cos\delta + \sin\delta \end{pmatrix}. \tag{E.15}$$

Then using (E.15), the projection operators are

$$|\pm\rangle\langle\pm| = \frac{1}{2}\begin{pmatrix} 1 \mp \sin 2\delta & \pm\cos 2\delta \\ \pm\cos 2\delta & 1 \pm \sin 2\delta \end{pmatrix} \tag{E.16a}$$

$$= \frac{1}{2}\left[\mathbf{1} \pm (\sigma_x \cos 2\delta - \sigma_z \sin 2\delta)\right]. \tag{E.16b}$$

As a consistency check, the projection operators are idempotent: $(|\pm\rangle\langle\pm|)^2 = |\pm\rangle\langle\pm|$.

Inserting (E.10) into (4.23), and because of the orthonormality of the eigenvectors, we have

$$\mathscr{Z} = \lambda_+^N |+\rangle\langle +| + \lambda_-^N |-\rangle\langle -|, \tag{E.17}$$

and in turn inserting (E.9) and (E.17) into (E.5), we have

$$K_{\sigma_0\sigma_N} = \sum_{\mu=\pm 1} \int_{-\pi}^{\pi} \frac{d\theta}{2\pi} e^{i\theta M} e^{-\frac{i\theta}{2}(\sigma_0+\sigma_N)} \left[\cos\theta + i\mu \left(\sin^2\theta + \Delta t^2 \frac{m^2c^4}{\hbar^2}\right)^{\frac{1}{2}}\right]^N \left(|\mu\rangle\langle\mu|\right)_{\sigma_0\sigma_N}. \tag{E.18}$$

Inserting (E.16b) into (E.18) gives:

$$\begin{aligned} K_{\sigma_0\sigma_N} &= \frac{1}{2} \sum_{\mu=\pm 1} \int_{-\pi}^{\pi} \frac{d\theta}{2\pi} e^{i\theta M} e^{-\frac{i\theta}{2}(\sigma_0+\sigma_N)} \left[\cos\theta + i\mu \left(\sin^2\theta + \Delta t^2 \frac{m^2c^4}{\hbar^2}\right)^{\frac{1}{2}}\right]^N \\ &\times \left[\mathbf{1} + \mu(\sigma_x \cos 2\delta - \sigma_z \sin 2\delta)\right]_{\sigma_0\sigma_N}. \end{aligned} \tag{E.19}$$

Expanding the trigonometric terms to include only first-order terms, we have

$$\cos\theta = 1 + \mathcal{O}(\Delta z^2) \qquad \sin\theta = \frac{p\Delta z}{\hbar} + \mathcal{O}(\Delta z^3) \tag{E.20}$$

From our definition of $\beta = \tan 2\delta$, we have

$$\begin{aligned} \tan 2\delta &= \frac{\hbar}{\Delta t\, mc^2} \sin\left(\frac{p\Delta z}{\hbar}\right) && \text{(E.21)} \\ &= \frac{p}{mc} + \mathcal{O}(\Delta z^2), && \text{(E.22)} \end{aligned}$$

which in turn implies that

$$\cos 2\delta \simeq \frac{mc}{\sqrt{p^2 + m^2c^2}} \qquad \sin 2\delta \simeq \frac{p}{\sqrt{p^2 + m^2c^2}}. \tag{E.23}$$

$$\begin{aligned} K_{\sigma_0\sigma_N} &= \frac{\Delta z}{2\hbar} \sum_{\mu=\pm 1} \int_{-\frac{\pi\hbar}{c\Delta t}}^{\frac{\pi\hbar}{c\Delta t}} \frac{dp}{2\pi} e^{i\frac{pz}{\hbar}} \left[1 + i\mu \frac{c\Delta t}{\hbar} \left(p^2 + m^2c^2\right)^{\frac{1}{2}} + \mathcal{O}(\Delta t^2)\right]^N e^{-i\frac{p\Delta z}{2\hbar}(\sigma_0+\sigma_N)} \\ &\times \left[\mathbf{1} + \mu \frac{\sigma_x mc - \sigma_z p}{\sqrt{p^2 + m^2c^2}} + \mathcal{O}(\Delta t^2)\right]_{\sigma_0\sigma_N}. \end{aligned} \tag{E.24}$$

With $\Delta t = \frac{t}{N}$ and using $(1 + \frac{x}{N})^N \to e^x$ and $c\Delta t = \Delta z \to dz$ as $N \to \infty$, and keeping only the lowest-order terms, (E.24) becomes the following kernel:

$$K_{\alpha\beta}(z,t) \equiv \lim_{N\to\infty} K_{\sigma_0\sigma_N} = \frac{dz}{2\hbar} \sum_{\mu=\pm 1} \int_{-\infty}^{\infty} \frac{dp}{2\pi} e^{i\frac{pz}{\hbar}} e^{i\frac{\mu E t}{\hbar}} \left[\mathbf{1} + \frac{\sigma_x mc^2 - \sigma_z pc}{\mu E}\right]_{\alpha\beta}, \tag{E.25}$$

where $E \equiv \sqrt{p^2c^2 + m^2c^4}$. For differential time steps, (E.25) takes the form

$$K_{\alpha\beta}(dz, dt) = \frac{dz}{2\hbar} \sum_{\mu=\pm 1} \int_{-\infty}^{\infty} \frac{dp}{2\pi} e^{i\frac{pdz}{\hbar}} \left(1 + i\frac{\mu E dt}{\hbar} + \mathcal{O}(dt^2)\right) \left[\mathbf{1} + \frac{\sigma_x mc^2 - \sigma_z pc}{\mu E}\right]_{\alpha\beta} . \quad \text{(E.26)}$$

Expanding the sum in (E.26) and keeping only first-order terms, the differential kernel can be written in purely exponential form:

$$K_{\alpha\beta}(dz, dt) = \frac{dz}{h} \int_{-\infty}^{\infty} dp \; e^{i\frac{pdz}{\hbar}} \left[e^{i\frac{dt}{\hbar}(\sigma_x mc^2 - \sigma_z pc)}\right]_{\alpha\beta}, \quad \text{(E.27)}$$

which is the Fourier transform of the differential evolution operator $e^{iH/\hbar} = e^{i(\sigma_x mc^2 \delta t - \sigma_z p \delta z)/\hbar}$. The result (E.27) is identical to our quantum lattice-gas formulation of the path integral (4.32).

Appendix F

Finite-difference algorithm for Schroedinger's equation

The full finite-difference equation for the quantum lattice-gas model presented in this chapter is very long. To simplify this expression, we introduce a *local neighborhood vector* with the following 18 components

$$\begin{aligned}\vec{\eta}(x_l,t) &= (\varphi_0(x_l,t),\varphi_1(x_l,t),\\ &\quad \varphi_0(x_{l+1},t),\varphi_1(x_{l+1},t),\varphi_0(x_{l-1},t),\varphi_1(x_{l-1},t),\\ &\quad \varphi_0(x_{l+2},t),\varphi_1(x_{l+2},t),\varphi_0(x_{l-2},t),\varphi_1(x_{l-2},t),\\ &\quad \varphi_0(x_{l+3},t),\varphi_1(x_{l+3},t),\varphi_0(x_{l-3},t),\varphi_1(x_{l-3},t),\\ &\quad \varphi_0(x_{l+4},t),\varphi_1(x_{l+4},t),\varphi_0(x_{l-4},t),\varphi_1(x_{l-4},t)).\end{aligned} \tag{F.1}$$

We define the following two *coefficient vectors*

$$\begin{aligned}\vec{\alpha} &\equiv (-3,-3i,3,i,-3,-5i,1,i,3,3i,-1,i,1,3i,0,0,-1,-i)\\ \vec{\beta} &\equiv (-3i,-3,-5i,-3,i,3,3i,3,i,1,3i,1,i,-1,-i,-1,0,0).\end{aligned} \tag{F.2}$$

The microscopic evolution equation (5.11), explicitly written out, has the following protocol of operations

$$|\psi(t_{16})\rangle \equiv \left(\hat{S}_2^{\mathrm{T}}\hat{C}\hat{S}_2\hat{C}\hat{S}_2^{\mathrm{T}}\hat{C}\hat{S}_2\hat{C}\right)\left(\hat{S}_1^{\mathrm{T}}\hat{C}\hat{S}_1\hat{C}\hat{S}_1^{\mathrm{T}}\hat{C}\hat{S}_1\hat{C}\right)|\psi(t_0)\rangle. \tag{F.3}$$

The corresponding full finite-difference equation can be specified by the following dot product of these vectors

$$\varphi_0(x_l,t_{16}) = \frac{\vec{\alpha}\cdot\vec{\eta}(x_l,t_0)}{16} \tag{F.4}$$

$$\varphi_1(x_l,t_{16}) = \frac{\vec{\beta}\cdot\vec{\eta}(x_l,t_0)}{16}. \tag{F.5}$$

Note that if t_0 is the initial time, then the interval $\tau \equiv t_{16}$ is defined the update time step. The finite-difference equation for $\psi = \varphi_0 + \varphi_1$ is

$$\psi(x_l, t_{16}) = \frac{(\vec{\alpha} + \vec{\beta}) \cdot \vec{\eta}(x_l, t_0)}{16} \tag{F.6}$$

and it has a high degree of numerical accuracy as indicated in Figure 5.2.

Appendix G

Triangular and square symmetry groups

As an example of how to use the finite-point group symmetries of the spatial lattice to reduce to the size of the Hilbert space sectors, we consider very small lattices (clusters) with 3 nodes and 4 nodes, both with 2-qubits/node.

The triangular cluster possesses the C_{3v} point group symmetry and the square cluster possesses C_{4v}.

Table G.1: C_3 and C_{3v} character table

C_3	E	C_3	C_3^2
A	1	1	1
E	1	ϵ	ϵ^*
E	1	ϵ^*	ϵ

C_{3v}	E	$2C_3$	$3\sigma_v$
A_1	1	1	1
A_2	1	1	-1
E	2	-1	0

Table G.2: C_4 and C_{4v} character table

C_4	E	C_4	C_2	C_4^3
A	1	1	1	1
B	1	-1	1	-1
E	1	i	-1	-i
E^*	1	-i	-1	i

C_{4v}	E	$2C_4$	C_2	$2\sigma_v$	$2\sigma_d$
A_1	1	1	1	1	1
A_2	1	1	1	-1	-1
B_1	1	-1	1	1	-1
B_2	1	-1	1	-1	1
E	2	0	-2	0	0

The C_{3v} group has six group operations and three irreducible representations, and C_{4v} has eight and five, respectively. They are shown in Table G.1 and Table G.2 for these example groups.

Specifically, for the case of C_{3v}, we obtain four sets of states in the symmetry basis: $\{\psi_n^{A_1}\}$, $\{\psi_n^{A_2}\}$, $\{\psi_n^{E}\}$, and $\{(\psi_n^{E})^*\}$. For the case of C_{4v}, we obtain six sets of states: $\{\psi_n^{A_1}\}$,

$\{\psi_n^{B_1}\}$, $\{\psi_n^{A_2}\}$, $\{\psi_n^{B_2}\}$, $\{\psi_n^{E}\}$, and $\{(\psi_n^{E})^*\}$. The E-representation always appears twice [1]. In the $\{\psi_n\}$ basis a Hamiltonian system on a triangular lattice therefore decouples into four diagonal blocks and a Hamiltonian system on a square lattice decouples into six diagonal blocks. So this is a good example illustrating how group theory reduces the complexity of the problem by partitioning each s_z-sector of the Hilbert space into smaller sub-sectors.

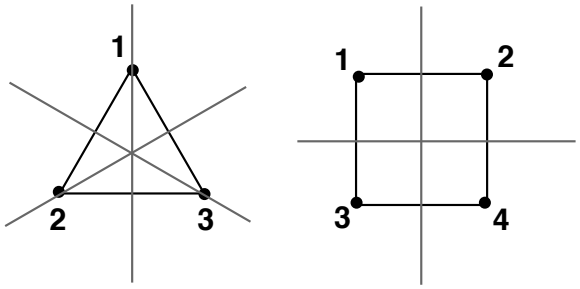

Figure G.1: Symmetry axes for the triangular and square clusters.

For the triangular cluster, using (2.91) we implement the C_{3v} point operators as follows

$$\hat{R}^{C_3} = \hat{\mathcal{X}}_{12}\hat{\mathcal{X}}_{23} \tag{G.1a}$$
$$\hat{R}^{C_3^2} = \hat{\mathcal{X}}_{23}\hat{\mathcal{X}}_{12} \tag{G.1b}$$
$$\hat{R}^{\sigma_v^{(1)}} = \hat{\mathcal{X}}_{23} \tag{G.1c}$$
$$\hat{R}^{\sigma_v^{(2)}} = \hat{\mathcal{X}}_{31} \tag{G.1d}$$
$$\hat{R}^{\sigma_v^{(3)}} = \hat{\mathcal{X}}_{12}, \tag{G.1e}$$

which are 120° and 240° rotations, and reflections about sites 1, 2, and 3, respectively. For the square cluster, we implement the C_{4v} point group operators as follows

$$\hat{R}^{C_4} = \hat{\mathcal{X}}_{34}\hat{\mathcal{X}}_{23}\hat{\mathcal{X}}_{12} \tag{G.2a}$$
$$\hat{R}^{C_2} = \hat{\mathcal{X}}_{23}\hat{\mathcal{X}}_{12} \tag{G.2b}$$
$$\hat{R}^{C_4^3} = \hat{\mathcal{X}}_{12}\hat{\mathcal{X}}_{23}\hat{\mathcal{X}}_{34} \tag{G.2c}$$
$$\hat{R}^{\sigma_v^{(13)}} = \hat{\mathcal{X}}_{24} \tag{G.2d}$$
$$\hat{R}^{\sigma_v^{(24)}} = \hat{\mathcal{X}}_{13} \tag{G.2e}$$
$$\hat{R}^{\sigma_d^{(13)}} = \hat{\mathcal{X}}_{12}\hat{\mathcal{X}}_{34} \tag{G.2f}$$
$$\hat{R}^{\sigma_d^{(24)}} = \hat{\mathcal{X}}_{14}\hat{\mathcal{X}}_{23}, \tag{G.2g}$$

which are 90°, 180° and 270° rotations, and reflections about two diagonals and the vertical and horizontal, respectively.

[1] Using projection operators constructed from the C_3 and C_4 character tables breaks the size of the E-type blocks in two for the half-filling cases

Appendix H

Improved algorithm for the diffusion equation

The algorithm described in this appendix uses a variant of the typical lattice-gas update procedure. First, there are two particles per site, but only one of them is a moving particle. The other is a stationary or rest particle. Second, the moving particle hops in both directions (and this is not typical in lattice-gas models). The collision operator is homogeneously applied across the lattice and then the moving particle hops one lattice unit to the right. The collision operator is then homogeneously applied again across the entire lattice and then the moving particle hops one lattice unit to the left. The moving particle must hop in both directions to keep the macroscopic dynamics unbiased and symmetrical. Therefore, each time step involves two applications of the collision operator and streaming operator.

The factorized quantum lattice-gas algorithm for the one-dimensional diffusion equation can be implemented with two passes as defined in the following six steps (two groups of three). This version of the algorithm is considered to be an improvement over the simpler version given in Section 8.2 because it remedies the problems of coexisting independent sublattices. Spurious high frequency noise is thereby removed from the time variation of the macroscopic mass-density field as well. We assume the initial state of the quantum computer is set as specified in Figure 8.1, where $|q_a(x,t)\rangle = \sqrt{f_a(x,t)}|1\rangle + \sqrt{1-f_a(x,t)}|0\rangle$.

STEP 1: Apply the collision operator simultaneously to all sites

$$|\psi'(x,t)\rangle = \hat{U}|\psi(x,t)\rangle.$$

This step accounts for all the quantum computation that is accomplished in a classically parallel fashion across all nodes of the array.

STEP 2: Measure ("read") all the occupancy probabilities using the following matrix ele-

ments

$$\begin{aligned} f_1'(x,t) &= \langle\psi'(x,t)|\hat{n}_1|\psi'(x,t)\rangle \\ f_2'(x,t) &= \langle\psi'(x,t)|\hat{n}_2|\psi'(x,t)\rangle \end{aligned}$$

on all sites. In practice, f_1 and f_2 must be determined by either repeated measurement of a single realization of the system or by a single measurement over a statistical ensemble of systems.

STEP 3: Reinitialize ("write") the state of the quantum computer as a separable state where each qubit is set as follows

$$\begin{aligned} |q_1(x,t+\tau)\rangle &= \sqrt{f_1'(x,t)}|1\rangle + \sqrt{1-f_1'(x,t)}|0\rangle \\ |q_2(x,t+\tau)\rangle &= \sqrt{f_2'(x+\ell,t)}|1\rangle + \sqrt{1-f_2'(x+\ell,t)}|0\rangle \end{aligned}$$

for all x. Note that qubit $|q_2\rangle$ is shifted to its neighboring node at the right. This step requires nearest-neighbor classical communication between all lattice nodes.

STEP 4: Apply the collision operator again as in STEP 1.

STEP 5: Measure ("read") the occupancy probabilities again as in STEP 2.

STEP 6: Reinitialize ("write") the state of the quantum computer as a separable state where each qubit is set as follows

$$|q_1(x,t)\rangle = \sqrt{f_1(x,t)}|1\rangle + \sqrt{1-f_1(x,t)}|0\rangle \tag{H.1}$$

$$|q_2(x,t)\rangle = \sqrt{f_2(x-\ell,t)}|1\rangle + \sqrt{1-f_2(x-\ell,t)}|0\rangle \tag{H.2}$$

for all x. Note that qubit $|q_2\rangle$ is shifted to its neighboring node at the left. This step requires classical communication between all lattice nodes.

ONE TIME-STEP UPDATE COMPLETED.

With this improved version of the quantum algorithm, the diffusion constant that arises in the effective field theory is $D^{\rm imp} = \frac{1}{4}\frac{\ell^2}{\tau}$, half the value the diffusion constant that arises from the simpler version of the algorithm presented in Section 8.2. The reason for the reduction in dissipation is that the diffusion constant goes as the ratio of the square of the

mean-free path length to the mean-free collision time. In the simple version of the quantum algorithm, the mean-free path length goes as the lattice cell size ℓ and the mean-free collision time is the time of a single update τ. However, in the improved version of the algorithm, the collision frequency is doubled, so effectively both the mean-free path length and the mean-free collision time are halved. Consequently, the value of the transport coefficient is halved, $D^{\rm imp} = \frac{D}{2}$.

H.1 Discrete Fourier transform

Consider a quantity $A(\vec{x})$ defined over the entire lattice. The discrete transform and its inverse in one dimension are

$$A(k_n) = \frac{1}{\sqrt{V}} \sum_{\{x_l\}} e^{ik_n x_l} A(x_l) \tag{H.3}$$

$$A(x_n) = \frac{1}{\sqrt{V}} \sum_{\{k_l\}} e^{-ik_l x_n} A(k_l). \tag{H.4}$$

The possible k-vectors are $k_n = 2n\pi/Vl$ and the lattice vectors are $x_n = \ell n$, where $n = 1, \ldots, V$ and ℓ is the cell size. The generalization to D dimensions is straightforward.

Inserting (H.4) into (H.3) gives

$$\begin{aligned} A(k_n) &= \frac{1}{\sqrt{V}} \sum_{\{x_l\}} e^{ik_n x_l} \left[\frac{1}{\sqrt{V}} \sum_{\{k_m\}} e^{-ik_m x_l} A(k_m) \right] \\ &= \sum_{\{k_m\}} A(k_m) \left[\frac{1}{V} \sum_{\{x_l\}} e^{i(k_n - k_m)x_l} \right] \qquad \text{(H.5)} \\ & \qquad \text{(H.6)} \end{aligned}$$

For the R.H.S. of this last expression to equal $A(k_n)$, the quantity in brackets must be a Kronecker delta. Therefore, the resolution of the identity is

$$\frac{1}{V} \sum_{\{x_l\}} e^{i(k_n - k_m)x_l} = \delta_{nm}. \tag{H.7}$$

Similarly, inserting (H.3) into (H.4) gives

$$\begin{aligned} A(x_n) &= \frac{1}{\sqrt{V}} \sum_{\{k_l\}} e^{-ik_l x_n} \left[\frac{1}{\sqrt{V}} \sum_{\{x_m\}} e^{ik_l x_m} A(x_m) \right] \\ &= \sum_{\{x_m\}} A(x_m) \left[\frac{1}{V} \sum_{\{k_l\}} e^{ik_l(x_m - x_n)} \right]. \qquad \text{(H.8)} \end{aligned}$$

Again, for the R.H.S. of this last expression to equal $A(x_n)$, the quantity in brackets must be a Kronecker delta. Therefore, the resolution of the identity is

$$\frac{1}{V}\sum_{\{k_n\}} e^{ik_n(x_m - x_n)} = \delta_{mn}. \tag{H.9}$$

Appendix I

Single-particle Fermi-Dirac distribution function

The single-particle Fermi-Dirac distribution function has the form

$$f(z_a) = \frac{1}{z_a + 1}, \tag{I.1}$$

where the natural log of the *fugacity*

$$\ln z_a = \alpha\rho + \beta\hat{e}_a \cdot \vec{p} + \gamma E \tag{I.2}$$

is a linear combination of the conserved scalar quantities, the mass ρ,the momentum component $\hat{e}_a \cdot \vec{p}$ along the lattice direction $\hat{e}_a$, and the energy E at a lattice site. The real numbered coefficients α, β, and γ are free parameters that we will determine. It is convenient to define the momentum and energy independent part of the fugacity as

$$z_\circ \equiv e^{\alpha\rho}. \tag{I.3}$$

Since $f_a(z_\circ) = d$ is the reduced density, $d \equiv \frac{\rho}{mB}$, we must set

$$z_\circ = \frac{1-d}{d}. \tag{I.4}$$

This fixes the coefficient α. To fix the coefficients β and γ, we can specify two moments of the single-particle distribution function as constraint conditions. We begin by Taylor expanding the single-particle distribution function $f(z_a)$ about $z_\circ$

$$f(z_a) = d + f'(z_\circ)\delta z + \frac{1}{2}f''(z_\circ)(\delta z^2) + \cdots. \tag{I.5}$$

The derivatives of f evaluated at $z_\circ$ are

$$f'(z) = \frac{-1}{(z+1)^2} \longrightarrow f'(z_\circ) = -d^2 \tag{I.6}$$

and

$$f''(z) = \frac{2}{(z+1)^3} \longrightarrow f''(z_\circ) = 2d^3, \tag{I.7}$$

so

$$f(z_a) \cong d\left[1 - d\delta z + d^2(\delta z)^2\right]. \tag{I.8}$$

To determine δz, we begin by writing the fugacity in series form

$$z_a = z_\circ \left[\sum_{k=0}^{\infty} \frac{(\beta \hat{e}_a \cdot \vec{p})^k}{k!}\right] \left[\sum_{k=0}^{\infty} \frac{(\gamma E)^k}{k!}\right]. \tag{I.9}$$

In the subsonic limit, $\vec{p} \ll mc$, keeping terms only to second order in the velocity, the fugacity becomes

$$z_a = z_\circ \left[1 + \beta \hat{e}_a \cdot \vec{p} + \frac{1}{2}(\beta \hat{e}_a \cdot \vec{p})^2\right](1 + \gamma E) + \mathcal{O}(v^3). \tag{I.10}$$

since $p \sim v$ and $E \sim v^2$. Then to second order in the velocity, the change in z_a is

$$\delta z_a \equiv z_a - z_\circ = \left(\frac{1-d}{d}\right)\left[\beta \hat{e}_a \cdot \vec{p} + \frac{1}{2}(\beta \hat{e}_a \cdot \vec{p})^2 + \gamma E\right] + \mathcal{O}(v^3) \tag{I.11}$$

and the square of the change is

$$(\delta z_a)^2 = \left(\frac{1-d}{d}\right)^2 \beta^2 \left(\hat{e}_a \cdot \vec{p}\right)^2 + \mathcal{O}(v^3). \tag{I.12}$$

Inserting the expressions for δz and $(\delta z)^2$ into the Taylor expansion of $f(z_a)$ we have

$$\begin{aligned} f(z_a) &= d\left\{1 - (1-d)\left[\beta \hat{e}_a \cdot \vec{p} + \frac{1}{2}(\beta \hat{e}_a \cdot \vec{p})^2 + \gamma E\right] + (1-d)^2 \left(\hat{e}_a \cdot \vec{p}\right)^2\right\} \\ &= d\left[1 - (1-d)\left(\beta \hat{e}_a \cdot \vec{p} + \gamma E\right) + \frac{1}{2}(1-d)(1-2d)\beta^2 \left(\hat{e}_a \cdot \vec{p}\right)^2\right]. \end{aligned} \tag{I.13}$$

We have the freedom to choose the coefficients β and γ as free parameters of the distribution function to satisfy any two constraints. Consider fixing the value of the coefficients β and γ by using the following moments for the mass density and momentum density

$$\rho = m \sum_{a=1}^{B} f_a \tag{I.14}$$

$$\rho \vec{v} = mc \sum_{a=1}^{B} \hat{e}_a f_a. \tag{I.15}$$

This choice may be termed the *non-Galilean parametrization*. Constraints (I.14) and (I.15) are typically used in the formulation of classical lattice gases. The single particle distribution function using this non-Galilean parameterization was first found in the mid 1980's by the US

researchers Wolfram and Hasslacher and by the French researchers Frisch, d'Humières, Lallemand, Pomeau, and Rivet [Wolfram, 1986, Frisch et al., 1987]. Their derivation of (I.20) is different then the derivation presented in this section; they used only two free coefficients in the expression for the fugacity, one for the mass and the other for the momentum; whereas we use three free coefficients. The reason for using only two free parameters is that in the standard single-speed classical lattice-gas construction, the energy is degenerate with the mass, so it was deemed unnecessary to keep a separate free coefficient for the energy. However, it is expedient to use a free parameter for E. Using (I.14) and (I.15) as constraint equations gives us a non-unity density-dependent prefactor in the convective term in the hydrodynamic flow equation.

Inserting (I.13) into (I.15), the odd term in the distribution function expansion survives the first moment sum over lattice directions; the odd term is the one linear in the momentum. This fixes the value of β to be

$$\beta = -\frac{D}{1-d} \tag{I.16}$$

so the distribution function becomes

$$f_a = d\left[1 + D\hat{e}_a \cdot \vec{p} + \frac{D^2}{2}\frac{1-2d}{1-d}\left(\hat{e}_a \cdot \vec{p}\right)^2 + (1-d)\gamma E\right]. \tag{I.17}$$

Inserting (I.17) into (I.14), all the even terms that survive the sum over lattice directions must add to zero. This fixes the value of γ as follows

$$\frac{D}{2}\frac{1-2d}{1-d}p^2 - (1-d)\gamma E = 0 \tag{I.18}$$

or

$$\gamma E = D\frac{1-2d}{(1-d)^2}\frac{p^2}{2}. \tag{I.19}$$

Therefore, the non-Galilean distribution function is

$$f_a = d\left[1 + De_{ai}p_i + \frac{D(D+2)}{2}g(d)Q_{aij}p_ip_j\right], \tag{I.20}$$

where the density dependent prefactor $g(d)$ is defined

$$g(d) \equiv \frac{D}{D+2}\frac{1-2d}{1-d} \tag{I.21}$$

and the traceless second-rank tensor $\hat{Q}_a$ is defined

$$Q_{aij} \equiv e_{ai}e_{aj} - \frac{\delta_{ij}}{D}. \tag{I.22}$$

$\hat{Q}_a$ is an isotropic symmetric tensor.

The second moment of (I.20) gives the momentum flux density

$$mc^2 \sum_{a=1}^{B} e_{ai} e_{aj} f_a = P\delta_{ij} + g\rho v_i v_j. \tag{I.23}$$

The density-dependent prefactor g appears in the nonlinear convective term. The pressure in (I.23) has a quadratic velocity dependence

$$P = \rho c_s^2 \left(1 - g\frac{v^2}{c^2}\right). \tag{I.24}$$

Appendix J

Lattice tensors

Let us define an n-th rank tensor composed of a product of lattice displacement vectors $\hat{e}_a$ for a single-speed lattice gas as follows

$$E^{(n)} = E_{i_1 \ldots i_n} = \sum_{a=1}^{B} (e_a)_{i_1} \cdots (e_a)_{i_n}. \tag{J.1}$$

Wolfram's notation is used here [Wolfram, 1986]. For certain lattices all odd-rank E vanish. The Kronecker delta is defined as follows: $\delta_{ij} \equiv 1$ if $i = j$, and $\delta_{ij} \equiv 0$ if $i \neq j$. It is possible to express the even-rank E-tensors in terms of products of Kronecker deltas.

Let $\Delta^{(2n)}$ denote a symmetric tensor with even rank $2n$. For $n = 1$, the symmetric second-rank tensor is Kronecker's delta

$$\Delta^{(2)}_{ij} = \delta_{ij}. \tag{J.2}$$

For $n = 2$ case, a symmetric fourth-rank tensor $\Delta^{(4n)}_{ijkl}$ has three terms

$$\Delta^{(4)}_{ijkl} = \delta_{ij}\delta_{kl} + \delta_{ik}\delta_{jl} + \delta_{il}\delta_{kj}. \tag{J.3}$$

Let's see why this is true. The number of terms in $\Delta^{(4)}$ can be determined by first counting the total number of permutations of the indices (in this case there are 4 indices, so the number of permutations is simply $4! = 24$) and then dividing this by the number of duplicated terms. Duplicate terms arise for two reasons. First, since the Knonecker delta is symmetric in its indices, the following four products are identical: $\delta_{ij}\delta_{kl} = \delta_{ij}\delta_{lk} = \delta_{ji}\delta_{kl} = \delta_{ji}\delta_{lk}$. This duplication is 2^2-fold. Second, the order of the Kronecker deltas also doesn't matter; that is, $\delta_{ij}\delta_{kl} = \delta_{kl}\delta_{ij}$. This duplication is 2!-fold. The number of duplicate terms arising from writing all possible products of two Kronecker deltas is $2^2 2! = 8$, for $n = 2$. Therefore, $\Delta^{(4)}$ consists of $\frac{24}{8} = 3$ terms.

For the general case, for any n, the total number of permutations of the $2n$ indices is $(2n)!$. There are 2^n identical ways of writing the product of n Kronecker deltas. For each

choice of indices, there are $n!$ additional ways of ordering the Kronecker deltas within each term. So, the total number of identical ways to write an $2n^{\text{th}}$-rank tensor as a product of n Kronecker deltas is $2^n n! = (2n)!!$. Since the number of terms can be determined by dividing the total number of permutations of the indices by the number of duplicated identical terms, $\Delta^{(2n)}$ consists of a sum of $\frac{(2n!)}{(2n)!!} = (2n-1)!!$ terms. For example, for $n = 3$, $\Delta^{(6)}$ has 15 terms, for $n = 4$, $\Delta^{(8)}$ has 35 terms, and so forth.

E is proportional to Δ

$$E^{(2n)} = \alpha^{(2n)} \Delta^{(2n)}. \tag{J.4}$$

The constant of proportionality, denoted $\alpha^{(2n)}$, may be obtained by taking the trace successively as follows. Since $e_{ai}e_{ai} = 1$ and $\delta_{ii} = D$, for $n = 1$ it follows that

$$\sum_a e_{ai}e_{ai} = \alpha^{(2)}\delta_{ii} \longrightarrow \alpha^{(2)} = \frac{B}{D}, \tag{J.5}$$

giving the following identity relating the second-rank tensors

$$E^{(2)} = \frac{B}{D}\delta_{ij}. \tag{J.6}$$

Since $\delta_{ijkk} = (D+2)\delta_{ij}$ and consequently $\delta_{iijj} = D(D+2)$, for $n = 2$ it follows that

$$\sum_a e_{ai}e_{ai}e_{aj}e_{aj} = \alpha^{(4)}\delta_{iijj} \longrightarrow \alpha^{(4)} = \frac{B}{D(D+2)}, \tag{J.7}$$

giving the following identity relating the fourth-rank tensors

$$E^{(4)} = \frac{B}{D(D+2)} \left(\delta_{ij}\delta_{kl} + \delta_{ik}\delta_{jl} + \delta_{il}\delta_{kj}\right). \tag{J.8}$$

Continuing this procedure, in general for any n, the lattice tensors are

$$E^{(2n+1)} = 0 \tag{J.9}$$

$$E^{(2n)} = \frac{B}{D(D+2)\cdots(D+2n-2)}\Delta^{2n}. \tag{J.10}$$

In Section 11.5.3, we will need the following four identities

$$\sum_{a=1}^{B} \hat{e}_a = 0 \tag{J.11a}$$

$$\sum_{a=1}^{B} \hat{e}_a\hat{e}_a = \frac{B}{D}\Delta^{(2)} \tag{J.11b}$$

$$\sum_{a=1}^{B} \hat{e}_a\hat{e}_a\hat{e}_a = 0 \tag{J.11c}$$

$$\sum_{a=1}^{B} \hat{e}_a\hat{e}_a\hat{e}_a\hat{e}_a = \frac{B}{D(D+2)}\Delta^{(4)}. \tag{J.11d}$$

Bravais lattices that satisfy these identities are: the two-dimensional triangular lattice with $B = 6$; the three-dimensional icosahedral lattice with $B = 12$; and the four-dimensional face-centered hypercubic lattice with $B = 24$ [Wolfram, 1986]. The identities (J.11) are commonly used in the lattice-gas literature.

Bibliography

[Ansumali et al., 2003] Ansumali, S., Karlin, I., and Oettinger, H. (2003). Minimal entropic kinetic models for hydrodynamics. *Europhysics Letters*, 63(6):798–804.

[Ansumali and Karlin, 2000] Ansumali, S. and Karlin, I. V. (2000). Stabilization of the lattice Boltzmann method by the h theorem: A numerical test. *Physical Review E*, 62(6):7999–8003.

[Ansumali and Karlin, 2002] Ansumali, S. and Karlin, I. V. (2002). Single relaxation time model for entropic lattice Boltzmann methods. *Physical Review E*, 65(056312):9.

[Barenco, 1995] Barenco, A. (1995). A universal two-bit gate for quantum computation. *Proceedings Royal Society London*, 449A:679–683.

[Barenco et al., 1995] Barenco, A., Bennett, C. H., Cleve, R., DeVincenzo, D. P., Margolus, N. H., Shor, P. W., Sleator, T., Smolin, J., and Weinfurter, H. (1995). Elementary gates for quantum computation. *Physical Review A*, 52(5):3457–3467.

[Ben-Naim et al., 1999] Ben-Naim, E., Chen, S., Doolen, G., and Redner, S. (1999). Shock-like dynamics of inelastic gases. *Physical Review Letters*, 83(20):4069–4072.

[Berman et al., 2002] Berman, G., Ezhov, A., Kamenev, D., and Yepez, J. (2002). Simulation of the diffusion equation on a type-II quantum computer. *Physical Review A*, 66(012310):8.

[Bialynicki-Birula, 1994] Bialynicki-Birula, I. (1994). Weyl, Dirac, and Maxwell equations on a lattice as unitary cellular automata. *Physical Review D*, 49(12):6920–6927.

[Binder, 1981] Binder, K. (1981). Finite size scaling analysis of Ising model block distribution functions. *Phys. B - Condensed Matter*, 43:119–140.

[Binder, 1987] Binder, K. (1987). Theory of first-order phase transitions. *Rep. Prog. Phys.*, 50:783–859.

[Binder, 1988] Binder, P. (1988). The properties of tagged lattice fluids: I: Diffusion coefficients. In Monaco, R., editor, *Discrete Kinetic Theory, Lattice Gas Dynamics and Foundations of Hydrodynamics*, pages 28–37. Institute for Scientific Interchange, World Scientific.

[Boghosian et al., 2004a] Boghosian, B., Love, P., and Yepez, J. (2004a). Entropic lattice Boltzmann model for Burgers's equation. *Philosophical Transactions of the Royal Society*, 362(1821):1691–1701.

[Boghosian, 1995] Boghosian, B. M. (1995). Correlations and renormalization in lattice gases. *Physical Review E*, 52(1). comp-gas/9403003.

[Boghosian and IV, 1997] Boghosian, B. M. and IV, W. T. (1997). Quantum lattice gas models for the many-body Schroedinger equation. *International Journal of Modern Physics C*, 8:705–716. quant-ph/9604035.

[Boghosian and IV, 1998a] Boghosian, B. M. and IV, W. T. (1998a). A quantum lattice-gas model for the many-particle Schroedinger equation in d dimensions. *Physical Review E*, 57:54–66.

[Boghosian and IV, 1998b] Boghosian, B. M. and IV, W. T. (1998b). Simulating quantum mechanics on a quantum computer. *Physica D*, 120:30–42.

[Boghosian and Levermore, 1987] Boghosian, B. M. and Levermore, C. D. (1987). A cellular automaton for Burger's equation. *Complex Systems*, 1:17–29.

[Boghosian et al., 2003] Boghosian, B. M., Love, P., Coveney, P. V., Karlin, I. V., Succi, S., and Yepez, J. (2003). Galilean-invariant lattice-Boltzmann models with H theorem. *Physical Review E*, 68(025103(R)).

[Boghosian et al., 2004b] Boghosian, B. M., Love, P., and Yepez, J. (2004b). Galilean-invariant multi-speed entropic lattice Boltzmann models. *Physica D*, 193(1-4):169–181.

[Boghosian et al., 1997] Boghosian, B. M., Yepez, J., Alexander, F. J., and Margolus, N. H. (1997). Integer lattice gas. *Physical Review E*, 55(4):4137–4147. comp-gas/9602001.

[Boghosian et al., 2001] Boghosian, B. M., Yepez, J., Coveney, P., and Wagner, A. (2001). Entropic lattice Boltzmann methods. *Proceedings of the Royal Society A: Mathematical, Physical and Engineering Sciences*, 457(2007):717–766.

[Bouwmeester et al., 2001] Bouwmeester, D., Ekert, A., and Zeilinger, A. (2001). *The Physics of Quantum Information*. Springer. ISBN: 3-540-66778-4.

[Brito and Ernst, 1992] Brito, R. and Ernst, M. (1992). Ring kinetic theory for tagged-particle problems in lattice gases. *Physical Review A*, 46(2):875–887.

[Bussemaker et al., 1995] Bussemaker, H., Ernst, M., and Duffy, J. (1995). Generalized Boltzmann equation for lattice gas automata. *Journal of Statistical Physics*, 78(5/6):1521–1554.

[Buzek and Konôpka, 1998] Buzek, V. and Konôpka, M. (1998). Dynamics of open systems governed by the milburn equation. *Physical Review A*, 58(3):1735–1739.

[Caves, 1986] Caves, C. M. (1986). Quantum mechanics of measurements distributed in time. a path-integral formulation. *Physical Review A*, 33(6):1643–1665.

[Caves and Milburn, 1987] Caves, C. M. and Milburn, G. J. (1987). Quantum-mechanical model for continuous position measurements. *Physical Review A*, 36(12):5543–5555.

[Chen et al., 1988] Chen, C., Reich, A., and Falicov, L. (1988). *Physical Review B*, 38:12823.

[Chen et al., 1989] Chen, H., Chen, S., Doolen, G. D., Lee, Y., and Rose, H. (1989). Multithermodynamic phase lattice-gas automata incorporating interparticle potentials. *Physical Review A*, 40(5):2850–2853. Rapid Communications.

[Chen et al., 1992] Chen, H., Chen, S., and Mattaeus, W. H. (1992). Recovery of the navier-stokes equations using a lattice-gas Boltzmann method. *Physical Review A*, 45(8):R5339–R5342.

[Chen et al., 2006a] Chen, Z., Yepez, J., and Cory, D. G. (2006a). Simulation of the Burgers equation by NMR quantum-information processing. *Physical Review A*, 74(4):042321. arXiv:quant-ph/0410198.

[Chen et al., 2006b] Chen, Z., Yepez, J., and Cory, D. G. (2006b). Simulation of the Burgers equation by NMR quantum-information processing. *Physical Review A*, 74(4):042321.

[Chuang and Nielsen, 2000] Chuang, I. L. and Nielsen, M. A. (2000). *Quantum Computation and Quantum Information*. Cambridge University Press. ISBN: 0521635039.

[Cole, 1951] Cole, J. (1951). *Quarterly of Applied Mathematics*, 9:225.

[Cory et al., 1998] Cory, D. G., Price, M. D., and Havel, T. F. (1998). Nuclear magnetic resonance spectroscopy: An experimentally accessible paradigm for quantum computing. *Physica*, D(120):82–101.

[Cotton, 1964] Cotton, F. (1964). *Chemical applications of group theory.*

[Creutz, 1992] Creutz, M. (1992). Microcanonical cluster Monte Carlo simulation. *Physical Review Letters*, 69(7):1002–1005.

[Das et al., 1993] Das, S., Bussemaker, H., and Ernst, M. (1993). Generalized hydrodynamics and dispersion relations in lattice gases. *Physical Review E*, 48(1):245–255.

[DeVincenzo, 1995] DeVincenzo, D. P. (1995). Two-bit gates are universal for quantum computation. *Physical Review A*, 51:1015–1022.

[Diósi, 1989] Diósi, L. (1989). Models for universal reduction of macroscopic quantum fluctuations. *Physical Review A*, 40(3):1165–1174.

[Dubrulle et al., 1991] Dubrulle, B., Frisch, U., Hénon, M., and Rivet, J. (1991). Low-viscosity lattice gases. *Physica*, D(47):27–29.

[Einstein et al., 1935] Einstein, A., Podolsky, B., and Rosen, N. (1935). Can quantum-mechanical description of physical reality be considered complete? *Physical Review*, 47:777.

[Falicov, 1966] Falicov, L. (1966). *Group theory and its physical applications.*

[Fetter and Walecka, 1971] Fetter, A. L. and Walecka, J. D. (1971). *Quantum Theory of Many-Particle Systems.* International series in pure and applied physics. McGraw-Hill Book Company, New York.

[Feynman, 1948] Feynman, R. P. (1948). Space-time approach to non-relativistic quantum mechanics. *Reviews of Modern Physics*, 20(2):367–387.

[Feynman, 1982] Feynman, R. P. (1982). Simulating physics with computers. *International Journal of Theoretical Physics*, 21(6/7):467–488.

[Feynman, 1985] Feynman, R. P. (1985). Quantum mechanical computers. *Optics News*, 11(2):11–20.

[Feynman, 1946] Feynman, R. P. (February 1946). Geometry of Dirac equ. in 1 dimension. *California Institute of Technology CIT archives*, (13.3).

[Feynman, 1960] Feynman, R. P. (February 1960). There's plenty of room at the bottom. *Caltech Engineering and Science.* This is a transcript of Feynman's talk given on December 29, 1959 at the annual meeting of the American Physical Society.

[Feynman and Hibbs, 1965] Feynman, R. P. and Hibbs, A. (1965). *Quantum Mechanics and Path Integrals*. McGraw-Hill. Problem 2-6 on page 34.

[Fleischer and Diamond, 2000] Fleischer, J. and Diamond, P. (2000). *Physical Review E*, 61:3912.

[Freericks and Falicov, 1991] Freericks, J. and Falicov, L. (1991). *Physical Review B*, 44:2895.

[Freericks et al., 1991] Freericks, J., Falicov, L., and Rokhsar, D. (1991). *Physical Review B*, 44:1458.

[Frisch et al., 1987] Frisch, U., d'Humiéres, D., Hasslacher, B., Lallemand, P., Pomeau, Y., and Rivet, J.-P. (1987). Lattice gas hydrodynamics in two and three dimensions. *Complex Systems*, 1:649–707.

[Frisch et al., 1986] Frisch, U., Hasslacher, B., and Pomeau, Y. (1986). Lattice-gas automata for the navier-stokes equation. *Physical Review Letters*, 56(14):1505–1508.

[Galtier, 1999] Galtier, S. (1999). A 1-d mhd model of solar flares: Emergence of a population of weak events, and a possible road toward nanoflares. *The Astrophysical Journal*, 521:483–489.

[Geppert, 2002] Geppert, L. (October 2002). The amazing vanishing transistor act. *IEEE Spectrum*, pages 28–33.

[Ghirardi et al., 1986] Ghirardi, G., Rimini, A., and Weber, T. (1986). Unified dynamics for microscopic and macroscopic systems. *Physical Review A*, 34(2):470–491.

[Ghirardi et al., 1990] Ghirardi, G. C., Pearle, P., and Rimini, A. (1990). Markov processes in hilbert space and continuous spontaneous localization of systems of identical particles. *Physical Review A*, 42(1):78–89.

[Glauber, 1963] Glauber, R. (1963). *Journal of Mathematical Physics*, 4:294.

[Grosfils et al., 1993] Grosfils, P., Boon, J.-P., Brito, R., and Ernst, M. H. (1993). Statistical hydrodynamics of lattice-gas automata. *Physical Review E*, 48(4):2655–2668.

[Hede and Herrmann, 1991] Hede, B. and Herrmann, H. (1991). Fast simulation of the Ising model using cellular automata. *Journal of Physics A: Math. Gen.*, 24:L691–L697.

[Hey and Allen, 1996] Hey, A. J. and Allen, R. W., editors (1996). *Feynman Lectures on Computation*. The Advanced Book Program. Addison-Wesley Publishing Company, Inc.

[Hohenberg and Halperin, 1977] Hohenberg, P. and Halperin, B. (1977). Theory of dynamic critical phenomena. *Reviews of Modern Physics*, 49(3):435–479.

[Hopf, 1950] Hopf, E. (1950). *Communications on Pure & Applied Mathematics*, 3:201.

[Infeld and Rowlands, 2000] Infeld, E. and Rowlands, G. (2000). *Nonlinear Waves, Solitons, and Chaos*. Cambridge University Press, Cambridge, 2nd edition.

[Jacobson, 1984] Jacobson, T. (1984). Spinor chain path integral for the Dirac equation. *Journal of Physics A: Math. Gen.*, 17:2433–2451.

[Jacobson and Schulman, 1984] Jacobson, T. and Schulman, L. (1984). Quantum stochastics: the passage from a relavistic to a non-relativistic path integral. *Journal of Physics A: Math. Gen.*, 17:375–383.

[Jakubowski et al., 1998] Jakubowski, M., Steiglitz, K., and Squier, R. (1998). State transformations of colliding optical solitons and possible application to computation in bulk media. *Physical Review E*, 58:6752.

[Jakubowski et al., 2001] Jakubowski, M., Steiglitz, K., and Squier, R. (2001). Computing with solitons: A review and prospectus. *Multiple-Valued Logic*, 6:439.

[Jones and Knill, 1999] Jones, J. and Knill, E. (1999). Efficient refocusing of one-spin and two-spin interactions for nmr quantum computation. *Journal of Magnetic Resonance*, 141(2):322–5.

[Kandel et al., 1988] Kandel, D., Domany, E., Ron, D., Brandt, A., and Eugene Loh, J. (1988). Simulations without critical slowing down. *Physical Review Letters*, 60(16):1591–1594.

[Kardar et al., 1986] Kardar, M., Parisi, G., and Zhang, Y.-C. (1986). Dynamic scaling of growing interfaces. *Physical Review Letters*, 56(9):889–892.

[Karlin et al., 1999] Karlin, I., Ferrante, A., and Oettinger, H. (1999). Perfect entropy functions of the lattice Boltzmann method. *Europhysics Letters*, 47(2):182–188.

[Karlin and Gorban, 1998] Karlin, I. V. and Gorban, A. N. (1998). Maximum entropy principle for lattice kinetic equations. *Physical Review Letters*, 81(1-6).

[Kawasaki, 1972] Kawasaki, K. (1972). *Phase Transitions and Critical Phenomena*, volume 4. Academic, London.

[Kida and Murakami, 1987] Kida, S. and Murakami, Y. (1987). Kolmogorov similarity in freely decaying turbulence. *Physics of Fluids*, 30(7):2030–2039.

[Kivshar and Agrawal, 2003] Kivshar, Y. and Agrawal, G. (2003). *Optical Solitons*. Academic Press, New York.

[Knill et al., 1998] Knill, E., Laflamme, R., and Zurek, W. H. (1998). Resilient quantum computation. *Science*, 279:342–345.

[Landau and Lifshitz, 1987] Landau, L. and Lifshitz, E. (1987). *Fluid Mechanics*, volume 6 of *Course of Theoretical Physics*. Pergamon Press, 2nd edition.

[Ma, 1976] Ma, S. (1976). Renormalization group by Monte Carlo methods. *Physical Review Letters*, 37(8):461–464.

[MacIssac et al., 1991] MacIssac, A. B., Hunter, D., Corsten, M., and Jan, N. (1991). Determinism and thermodynamics: Ising cellular automata. *Physical Review A*, 43(6):3190–3193.

[McNamara and Zanetti, 1988] McNamara, G. R. and Zanetti, G. (1988). Use of the Boltzmann equation to simulate lattice-gas automata. *Physical Review Letters*, 61(20):2332–2335.

[Meyer, 1996a] Meyer, D. A. (1996a). From quantum cellular automata to quantum lattice gas. *Journal of Statistical Physics*, 85(5,6):551–574.

[Meyer, 1996b] Meyer, D. A. (1996b). On the absense of homogeneous scalar unitary cellular automatoa. *Physics Letters A*, 223:337–340.

[Meyer, 1997a] Meyer, D. A. (1997a). Quantum lattice gases and their invariants. *International Journal of Modern Physics C*, 8:717–735.

[Meyer, 1997b] Meyer, D. A. (1997b). Quantum mechanics of lattice gas automata ii. boundary conditions and other inhomogeneities. *Quant-Ph*, 9712052:1–24.

[Meyer, 1997c] Meyer, D. A. (1997c). Quantum mechanics of lattice gas automata: One-particle plane waves and potentials. *Physical Review E*, 55(5):5261–5269.

[Meyer, 1998] Meyer, D. A. (1998). Quantum mechanics of lattice gas automata: boundary conditions and other inhomogeneities. *Journal of Physics A: Mathematical and General*, 31:2321–2340.

[Milburn, 1987] Milburn, G. (1987). Kicked quantized cavity mode: An open-systems-theory approach. *Physical Review A*, 36(2):744–749.

[Milburn, 1991] Milburn, G. (1991). Intrinsic decoherence in quantum mechanics. *Physical Review A*, 44(9):5401–5406.

[Mooij et al., 1999] Mooij, J., Orlando, T. P., Levitov, L., Tian, L., van der Wal, C. H., and Lloyd, S. (1999). Josephson persistent-current qubit. *Science*, 285:1036–1039.

[Moore, 1965] Moore, G. E. (April 1965). Cramming more components onto integrated circuits. *Electronics*, 38(8):4 pages.

[Orlando et al., 1999] Orlando, T., Mooij, J., Tian, L., van der Wal, C. H., Levitov, L., Lloyd, S., and Mazo, J. (1999). Superconducting persistent-current qubit. *Physical Review B*, 60(22):15398–15413.

[Orszag and Patterson, 1972] Orszag, S. A. and Patterson, G. S. (1972). *Statistical Models and Turbulence*. Springer-Verlag, New York. editors M. Rosenblatt and C. Van Atta.

[Orszag and Yakhot, 1986] Orszag, S. A. and Yakhot, V. (1986). Reynolds number scaling of cellular-automaton hydrodynamics. *Physical Review Letters*, 56(16):1691–1693.

[Pearle, 1989] Pearle, P. (1989). Combining stochastic dynamical state-vector reduction with spontaneous localization. *Physical Review A*, 39(5):2277–2289.

[Pendleton, 1991] Pendleton, H. (1991). Fermion exchange operator. private note, No. 2448460, Physics Department, Brandeis University.

[Penrose, 1955] Penrose, R. (1955). A generalized inverse for matrices. *Proc. Cambridge Phil. Soc.*, 51:406–413.

[Polley, 2000] Polley, L. (2000). Schroedinger equation as the universal continuum limit of nonrelativistic coherent hopping on a cubic spatial lattice. *Los Alamos National Laboratory Electronic Archive*, quant-ph/9811048:1–6.

[Pravia et al., 2002] Pravia, M., Chen, Z., Yepez, J., and Cory, D. G. (2002). Towards an NMR implementation of a quantum lattice gas algorithm. *Computer Physics Communications*, 146(3):339–344.

[Pravia et al., 2003] Pravia, M., Chen, Z., Yepez, J., and Cory, D. G. (2003). Experimental demonstration of parallel quantum computation. *Quantum Information Processing*, 2:1–19.

[Qian et al., 1992a] Qian, Y., d'Humiéres, D., and Lallemand, P. (1992a). Lattice BGK models for Navier-Stokes equation. *Europhysics Letters*, 17(6BIS):479–484.

[Qian et al., 1992b] Qian, Y. H., d'Humières, D., and Lallemand, P. (1992b). Diffusion simulation with a deterministic one-dimensional lattice-gas model. *Journal of Statistical Physics*, 68(3/4):563–573.

[R. Benzia and Vergassola, 1992] R. Benzia, S. S. and Vergassola, M. (1992). The lattice Boltzmann equation: theory and applications. *Physics Reports*, 222(3):145–197.

[Reich and Falicov, 1988] Reich, A. and Falicov, L. (1988). *Physical Review B*, 37:5560.

[Riazanov, 1958] Riazanov, G. (June 1958). The Feynman path integral for the Dirac equation. *Soviet Physics JETP*, 6 (33)(6):7 pages.

[Sato, 2003] Sato, T. (2003). *Annual Report of the Earth Simulator Center*. International series in pure and applied physics. The Earth Simulator Center, 3173-25 Showa-machi, Kanazawa-ku, Yokohama, 236-0001 Japan. ISSN 1348-5830.

[Schiff, 1968] Schiff, L. I. (1968). *Quantum Mechanics*. International series in pure and applied physics. McGraw-Hill Book Company, New York, 3rd edition.

[Schleier et al., 1992] Schleier, W., Besold, G., and Heinz, K. (1992). Overcoming artificial spatial correlations in simulations of superstructure domain growth with parallel Monte Carlo algorithms. *Journal of Statistical Physics*, 66(3/4):1101–1122.

[Schrodinger, 1926] Schrodinger, E. (1926). *Naturwiss*, 14:664.

[Schweber, 1986] Schweber, S. S. (1986). Feynman and the visualization of space-time processes. *Reviews of Modern Physics*, 449(2):449–508.

[Shandarin and Zeldovich, 1989] Shandarin, S. and Zeldovich, Y. B. (1989). The large-scale structure of the universe: Turbulence, intermittency, structures in a self-gravitating medium. *Reviews of Modern Physics*, 61(2):185–220.

[Shor, 1994] Shor, P. W. (1994). Polynomial-time algorithms for prime factorization and discrete logarithms on a quantum computer. In *Proceedings of the 35th Annual Symposium on Foundations of Computer Science*, pages 124–134. Santa Fe, NM, IEEE Computer Society Press.

[Shor, 1995] Shor, P. W. (1995). Scheme for reducing decoherence in quantum computer memory. *Physical Review A*, 52:R2493–R2496.

[Siskind et al., 2005] Siskind, L. C., Hammer, B. E., Christensen, N. L., and Yepez, J. (2005). Multiple RF coil nuclear magnetic resonance quantum computing. *Quantum Information Processing*, 4(6). Contained in this QCPM special issue of QIP.

[Succi, 1996] Succi, S. (1996). Numerical solution of the Schroedinger equation using discrete kinetic theory. *Physical Review E*, 53(2):1969–1975.

[Succi, 1998] Succi, S. (1998). Lattice quantum mechanics: an application to Bose-Einstein condensation. *International Journal of Modern Physics C*, 9(8):1577–1585.

[Succi, 2002] Succi, S. (2002). Lattice Boltzmann schemes for quantum applications. *Computer Physics Communications*, 146(3):317–323.

[Succi and Benzi, 1993] Succi, S. and Benzi, R. (1993). Lattice Boltzmann equation for quantum mechanics. *Physica D*, 69:327–332.

[Succi et al., 1991] Succi, S., Benzi, R., and Higuera, F. (1991). The lattice Boltzmann equation: A new tool for computational fluid dynamics. *Physica D*, 47:219–230.

[Swendsen, 1979] Swendsen, R. H. (1979). Monte Carlo renormalization group. *Physical Review Letters*, 42(14):859–861.

[Teixeira, 1992] Teixeira, C. (1992). *Continuum Limit Of Lattice Gas Fluid Dynamics*. PhD thesis, Massachusetts Institute of Technology, Department of Nuclear Engineering. Kim Molvig Thesis Supervisor.

[Thaller, 2004] Thaller, B. (2004). Visualizing the kinematics of relativistic wave packets. *arXiv:quant-ph*, (0409079):7.

[Thomas, 1968] Thomas, J. (1968). *Physics of Fluids*, 11:1245.

[Toffoli and Margolus, 1987] Toffoli, T. and Margolus, N. (1987). *Cellular Automata Machines*. MIT Press Series in Scientific Computation. The MIT Press.

[Vahala et al., 2003a] Vahala, G., Vahala, L., and Yepez, J. (2003a). Quantum lattice gas representation for vector solitons. *SPIE*, 5105:187–196.

[Vahala et al., 2003b] Vahala, G., Vahala, L., and Yepez, J. (2003b). Quantum lattice gas representation of some classical solitons. *Physics Letters A*, 310:187–196.

[Vahala et al., 2004a] Vahala, G., Vahala, L., and Yepez, J. (2004a). Inelastic vector soliton collisions: a lattice-based quantum representation. *Philosophical Transactions of the Royal Society*, 362(1821):1677–1690.

[Vahala et al., 2004b] Vahala, G., Vahala, L., and Yepez, J. (2004b). Quantum lattice representation of dark solitons. *SPIE*, 5436:376–385.

[Vahala et al., 2003c] Vahala, L., Vahala, G., and Yepez, J. (2003c). Lattice Boltzmann and quantum lattice representations of one-dimensional magnetohydrodynamic turbulence. *Physics Letters A*, 306:227–234.

[Vichniac, 1984] Vichniac, G. Y. (1984). Simulating physics with cellular automata. *Physica*, 10D:96–116.

[Walls et al., 1985] Walls, D., Collet, M., and Milburn, G. (1985). Analysis of a quantum measurement. *Physical Review D*, 32(12):3208–3215.

[Wolfram, 1986] Wolfram, S. (1986). Cellular automaton fluids 1: Basic theory. *Journal of Statistical Physics*, 45(3/4):471–526.

[Woyczynski, 1998] Woyczynski, W. (1998). In *Burgers-KPZ Turbulence: Gottingen Lectures*, volume 1700. Lecture Notes in Computer Science, Springer-Verlag.

[Yepez, 1998] Yepez, J. (1998). Lattice-gas quantum computation. *International Journal of Modern Physics C*, 9(8):1587–1596. Proceeding of the 7th International Conference on the Discrete Simulation of Fluids, University of Oxford.

[Yepez, 1999] Yepez, J. (1999). Quantum computation of fluid dynamics. In Williams, C. P., editor, *Quantum Computing and Quantum Communications*, pages 34–60. Lecture Notes in Computer Science, Springer-Verlag.

[Yepez, 2001a] Yepez, J. (2001a). Quantum lattice-gas model for computational fluid dynamics. *Physical Review E*, 63(4):046702.

[Yepez, 2001b] Yepez, J. (2001b). Quantum lattice-gas model for the diffusion equation. *International Journal of Modern Physics C*, 12(9):1285–1303.

[Yepez, 2001c] Yepez, J. (2001c). Type-II quantum computers. *International Journal of Modern Physics C*, 12(9):1273–1284.

[Yepez, 2002a] Yepez, J. (2002a). An efficient quantum algorithm for the one-dimensional Burgers equation. *arXiv.org e-Print archive*. quant-ph/0210092.

[Yepez, 2002b] Yepez, J. (2002b). Quantum computation for physical modeling. *Computer Physics Communications*, 146(3):277–279.

[Yepez, 2002c] Yepez, J. (2002c). Quantum lattice-gas model for the Burgers equation. *Journal of Statistical Physics*, 107(1):203–224. Presented at the 9th International Conference on Discrete Simulation of Fluid Dynamics, Santa Fe, NM, August 22, 2000.

[Yepez, 2003] Yepez, J. (2003). An efficient and accurate quantum algorithm for the Dirac equation. *arXiv.org e-Print archive*. quant-ph/0210093.

[Yepez, 2005] Yepez, J. (2005). Relativistic path integral as a lattice-based quantum algorithm. *Quantum Information Processing*, 4(6):471–509.

[Yepez, 2006] Yepez, J. (2006). Open quantum system model of the one-dimensional Burgers equation with tunable shear viscosity. *Physical Review A*, 74(4):042322.

[Yepez and Boghosian, 2002] Yepez, J. and Boghosian, B. (2002). An efficient and accurate quantum lattice-gas model for the many-body Schroedinger wave equation. *Computer Physics Communications*, 146(3):280–294.

[Yepez et al., 2005] Yepez, J., Vahala, G., and Vahala, L. (2005). Quantum lattice representation of 1D MHD turbulence with arbitrary transport coefficients. *SPIE*, 5815(33).

[Zalka, 1996] Zalka, C. (Aug 1996). Efficient simulation of quantum systems by quantum computers. *Los Alamos National Laboratory Archive*, quantum-ph(9603026v2):8 pages.

[Zhang, 1989] Zhang, M. (1989). A fast vectorized multispin coding algorithm for 3d Monte Carlo simulations using Kawasaki spin-exchange dynamics. *Journal of Statistical Physics*, 56(5/6):939–950.

[Zurek, 1981] Zurek, W. H. (1981). Pointer basis of quantum apparatus: Into what mixture does the wave packet collapse? *Physical Review D*, 24(6):1516–1525.

[Zurek, 1982] Zurek, W. H. (1982). Environment-induced superselection rules. *Physical Review D*, 26(8):1862–1880.